

# Topological insulators grown by molecular beam epitaxy (MBE) and related quantum devices

Daniel Portela de Brito

Doutoramento em Física  
Departamento de Física e astronomia, INL  
2024

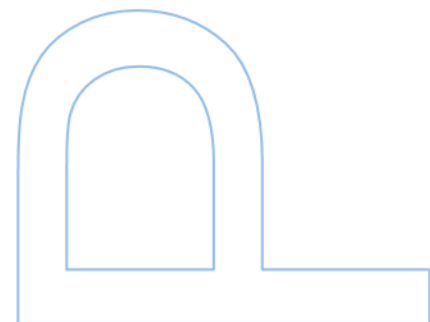
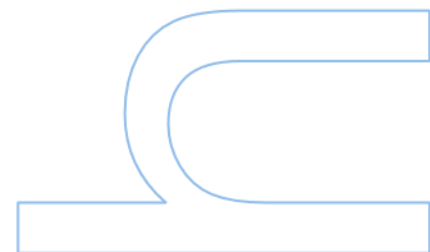
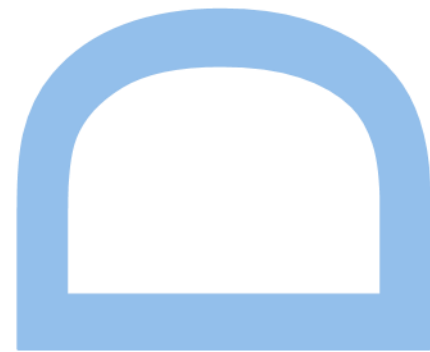
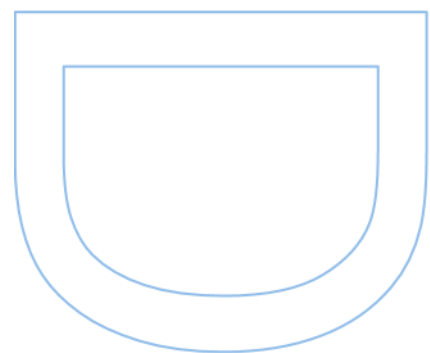
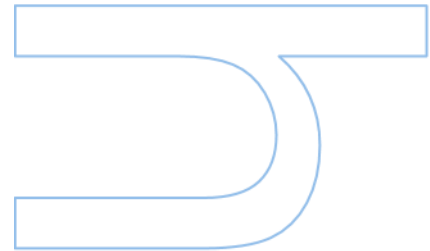
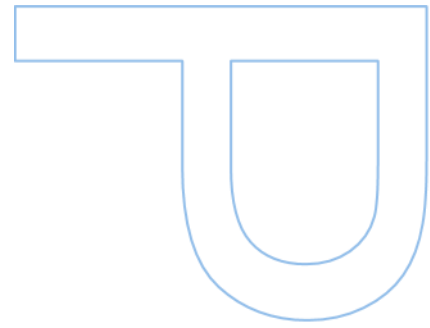
## Supervisor

Prof. Dr. Eduardo Castro, Professor, Faculdade de Ciências,  
Departamento de Física e Astronomia

## Co-supervisors

Dr. Sascha Sadewasser, Principal Investigator, INL  
LaNaSC- Laboratory for Nanostructured Solar Cells

Dr. Marcel Claro Visiting Scholar at Universidade de Santiago de Compostela, Spain  
Centro Singular de Investigación en Química Biológica y Materiales Moleculares (CIQUS)



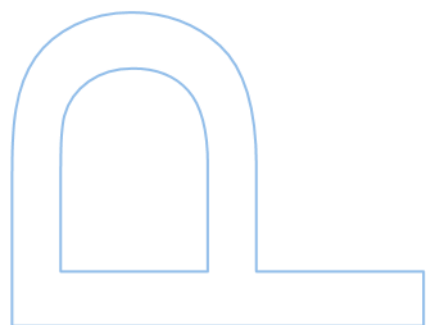
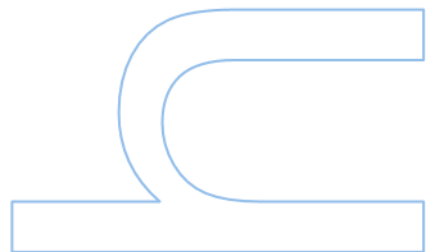


universidade  
de aveiro



Universidade do Minho

**U.** PORTO  
FC FACULDADE DE CIÊNCIAS  
UNIVERSIDADE DO PORTO



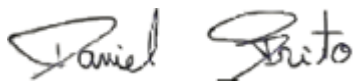
# Sworn Statement

I, Daniel Portela de Brito, enrolled in the Doctor's Degree in Physics at the Faculty of Sciences of the University of Porto hereby declare, in accordance with the provisions of paragraph a) of Article 14 of the Code of Ethical Conduct of the University of Porto, that the content of this thesis reflects perspectives, research work and my own interpretations at the time of its submission.

By submitting this thesis, I also declare that it contains the results of my own research work and contributions that have not been previously submitted to this or any other institution.

I further declare that all references to other authors fully comply with the rules of attribution and are referenced in the text by citation and identified in the bibliographic references section. This thesis does not include any content whose reproduction is protected by copyright laws.

I am aware that the practice of plagiarism and self-plagiarism constitute a form of academic offense.

A handwritten signature in black ink, appearing to read "Daniel Brito". The signature is written in a cursive style with some loops and flourishes.

01/03/2024

# Acknowledgments

The journey of a PhD was an evolution as a person, scientifically and mentally. I would recommend everyone to do a PhD. You will face several challenges and emotions. You will learn how life is in the real world. You will develop skills you didn't know you had. Thank you for making me a better person.

Firstly, I would like to express my sincere thanks to Dr. Sascha Sadewasser and Professor Eduardo Castro for giving me the opportunity to do a PhD. Their deep knowledge of physics, from both experimental and theoretical points of view, combined with assistance and support was an inspiration. I wish to thank them for their guidance and support.

I am extremely grateful to Dr. Marcel Claro for the solid guidance throughout this project. I thank him for sharing his extensive knowledge about the UHV/MBE equipment and for the helpful advice and reviews that contributed to the improvement of my scientific performance. I also wish to thank Dr. Ana Pérez for my collaboration in Salamanca. It was thanks to her that this collaboration was possible. Her enthusiastic nature made every moment always more enjoyable.

I extend my gratitude to James Peters for all the good quality STEM and EDX images for the Ph.D. thesis. Massimo Tallarida and Ji Dai for their help as beamline scientists in collaboration with the ARPES measurements at ALBA. To Prof. Carlos Tavares for the Hall effect measurements at the University of Minho.

To all members of the LANASC group (random order): Dr. Nicoleta Nicoara, Dr. Pedro Anacleto, Marina Alves, José Virtuoso, Dr. Diego Colombara, Deepanjan Sharma, Pedro Santos, Dr. Alessandro Cavali, Diana, Carolina, Fonseca, Dr. Ishwor Katri, Mahdi, Diego Garzon, Dr. Christian Rossi, Pedro Sousa, Maria, Kate, Bruno, Wesley, Patricia, Nuno Rodrigues, Dr. Angelica, Dr. Devaraj, Diogo Costa, Rafael, Cláudia Coelho, Dr. Neha, Dr. Neslihan and all new and previous group members for the enjoyable moments, the coffee breaks, the gossip in the lab and everything! To Mathieu Galliou and Timothé Pabouef, my interns, who helped me and contributed to my thesis work and helped me learn how to supervise a student. To Dr. Carlos Rosário for keeping the knowledge I obtained and supporting the research line of 2D materials and topological insulators at LANASC. To INL for all the available facilities, good organization, and nice people ...

Then, I would like to express great thanks to all my friends from "Power Rangers", "Daniel foi ...", "Weekly Futsal", "Park Volley", "Physics Enthusiasts" and "weekly outside lunch" for all the fun activities performed. To all my family members for all the emotional support.

Finally, to One Piece! Without One Piece life would be boring... Each week I had to wait for an episode/chapter was my motivation to do all my PhD work. To all the animes I have watched for the last 4 years. Every episode I watched motivated me to always be better, and consequently do a successful PhD!

This work was supported by Fundação para a Ciência e Tecnologia (FCT, Portugal) for the Ph.D. Grant (No. SFRH/BD/ 150638/2020) and the FUNLAYERS project.

# Resumo

Os isoladores topológicos são uma nova classe de matéria caracterizada pela sua estrutura eletrônica única, é isolante no interior e possui estados condutores na superfície. A presença de acoplamento spin-órbita e a simetria de inversão temporal são pré-requisitos para esta nova classe de materiais. Os estados de superfície exibem dispersões do tipo cone de Dirac sem massa e bloqueio spin-momento, o que implica a interação proibida de elétrons de spin oposto e que o spin do elétron muda de acordo com o seu momento. Esta combinação confere a propriedade de condutividade sem dissipação aos isoladores topológicos.

O seleneto de bismuto ( $\text{Bi}_2\text{Se}_3$ ) é um isolante topológico promissor devido ao seu hiato energético de 0.3 eV, tornando-o adequado para aplicações à temperatura ambiente. No entanto, uma grande desvantagem é a sua degenerescência do tipo n devido à sua dopagem nativa por vacâncias de Se, que normalmente leva ao transporte no interior, tornando o acesso a estados de superfície condutores uma grande dificuldade. Por conseguinte, a fabricação de  $\text{Bi}_2\text{Se}_3$  sem contribuição elétrica do interior de alta qualidade com condução ao longo da superfície é de alta relevância. Isto poderia ser obtido deslocando o potencial químico para o seu hiato energético, tornando o transporte dos estados de superfície mais pronunciado.

O presente trabalho contribui para o desenvolvimento da fabricação de filmes de isoladores topológicos de alta qualidade, por epitaxia de feixe molecular. Um dos principais objetivos é investigar a dopagem de Ga e Cu em  $\text{Bi}_2\text{Se}_3$ , com vista a identificar o seu potencial papel como impurezas aceitadoras. Além disso, a dopagem com elementos exóticos pode oferecer oportunidades para descobrir novos fenômenos físicos, tais como a supercondutividade topológica ou o efeito Hall quântico anômalo. A segunda estratégia centra-se no ajuste do nível de Fermi através da utilização de uma gate eletrostática. Este método reduziu a concentração de elétrons do  $\text{Bi}_2\text{Se}_3$ , facilitando a deteção do transporte topológico de superfície.

Inicialmente, a investigação começou com a otimização do crescimento filmes finos de  $\text{Bi}_2\text{Se}_3$  em substratos de safira (0001). Foram otimizados diferentes parâmetros de crescimento, obtendo-se uma temperatura de crescimento de 310 °C, uma abertura da válvula de Se em 2 mm e a implementação de um crescimento em duas fases, designado por tratamento de superfície. A caracterização estrutural demonstraram isolador topológico com boa qualidade estrutural e morfologia com número mínimo de defeitos. Os defeitos de geminação (*twinning*) no plano foram atenuados para menos de 15% com a aplicação do tratamento de superfície. O estudo de duas camadas tampão (*buffer*) diferentes foi abordado,  $(\text{Bi}, \text{In})_2\text{Se}_3$  e  $\text{In}_2\text{Se}_3 + (\text{Bi}, \text{In})_2\text{Se}_3$ , com a última a mostrar um melhor isolamento do  $\text{Bi}_2\text{Se}_3$  e uma interface ordenada. A camada tampão  $\text{In}_2\text{Se}_3 + (\text{Bi}, \text{In})_2\text{Se}_3$  levou a concentrações de elétrons de  $\text{Bi}_2\text{Se}_3$  de  $4 \times 10^{18} \text{ cm}^{-3}$  e mobilidades de elétrons de aproximadamente  $600 \text{ cm}^2/\text{Vs}$ .

Foram estudadas as propriedades estruturais, elétricas e de transporte da dopagem com Ga e Cu. Os resultados revelam uma expansão da rede c de 28.66 Å (não dopado) para 28.92 Å (Ga: 7 at.%) e uma dopagem do tipo n, seis vezes maior, atingindo valores de aproximadamente  $6 \times 10^{19} \text{ cm}^{-3}$ . Sugerindo que o Ga possivelmente se intercala no gap de van der Waals. A dopagem de Cu, por outro lado, leva a uma contração da rede c para  $\approx 28.60 \text{ Å}$  (Cu: 2 at.%), em que Cu atua como uma impureza aceitadora com uma redução de

duas vezes da concentração de elétrons. Além disso, a medição de magneto transporte mostraram o efeito da anti localização fraca (*WAL*) através da ponta em campos magnéticos baixos de  $\text{Bi}_2\text{Se}_3$  não dopado. Esta ponta degrada-se após a dopagem com Ga, com uma transição de fase topológica a uma percentagem de Ga de 7 at.%, sugerindo a destruição dos estados de superfície. Por outro lado, a dopagem com Cu mostrou pouca interferência na forma da ponta *WAL*.

As medições de espectroscopia de fotoemissão resolvida em ângulo (*ARPES*) confirmam a presença de estados de superfície em  $\text{Bi}_2\text{Se}_3$  não dopado, em todas as amostras dopadas com Cu e na amostra dopada com Ga até uma dopagem de 2 at.%, enquanto com 7 at.% de Ga não se observam estados de superfície. A dopagem também levou a uma diminuição do nível de Fermi para a dopagem com Cu e um aumento para a dopagem com Ga.

Além disso, exploramos o fabrico e a caracterização de transístores de efeito de campo (*FET*) baseados em filmes finos de  $\text{Bi}_2\text{Se}_3$ . A incorporação de uma camada de cobertura de  $\text{In}_2\text{Se}_3$  e a utilização de alumina como *gate* dielétrica permite a afinação do nível de Fermi e a modulação da concentração de elétrons de  $6 \times 10^{12} \text{ cm}^{-2}$  para  $4 \times 10^{12} \text{ cm}^{-2}$  com uma tensão de *gate* de -10 V, demonstrando o potencial dos FET para controlar as propriedades de transporte.

**Palavras-chave:** ARPES,  $\text{Bi}_2\text{Se}_3$ , dopagem com Cu, dopagem com Ga, efeito de anti localização fraca, epitaxia por feixe molecular, estados de superfície, isoladores topológicos, transístor de efeito de campo.

# Abstract

Topological insulators are a new class of matter characterized by their unique electronic structure, which features insulating bulk and conductive surface states. The presence of spin-orbit coupling, and time-reversal symmetry are prerequisites for this new class of materials. The surface states exhibit massless Dirac cone-like dispersions and spin-momentum locking, which implies the forbidden interaction of electrons with opposite spin and that the electron spin changes according to its momentum. This combination confers the property of dissipationless conductivity for topological insulators.

Bismuth selenide ( $\text{Bi}_2\text{Se}_3$ ) is a promising topological insulator due to its band gap of 0.3 eV, making it suitable for room temperature applications. However, a major drawback is its n-type degeneracy due to its native doping by Se vacancies, which normally leads to bulk transport, making the access to pure conductive surface states a major difficulty. Therefore, the experimental realization of high-quality bulk-insulating  $\text{Bi}_2\text{Se}_3$  with pure conduction along the surface is a critical point in the field. This could be obtained by shifting the chemical potential into the bandgap, turning the transport of the surface states to be more pronounced than the bulk counterpart.

The present work contributes to the ongoing effort to grow high-quality topological insulator films by a molecular beam epitaxy. One of the primary objectives is to explore the doping of  $\text{Bi}_2\text{Se}_3$  with Ga and Cu elements, aiming to identify their potential role as compensating acceptor impurities. Furthermore, doping with exotic elements may offer opportunities to discover novel physical phenomena, such as topological superconductivity or quantum anomalous Hall effect. The second strategy focuses on adjusting the Fermi level through the use of an electrostatic gate. This method reduces the electron concentration of the  $\text{Bi}_2\text{Se}_3$ , thereby unmasking the topological surface transport.

Initially, the research started with the optimization of the  $\text{Bi}_2\text{Se}_3$  thin film growth on sapphire (0001) substrates. Different growth parameters are optimized obtaining a growth temperature of 310 °C, Se valve aperture of 2 mm, and the implementation of a two-step growth, denoted as surface treatment. Structural characterization measurements showed TI films with good structural quality and morphology with reduced defects. In-plane twinning defects were mitigated below 15 % by the implementation of the surface treatment. The study of two different buffer layers was addressed,  $(\text{Bi}, \text{In})_2\text{Se}_3$  and  $\text{In}_2\text{Se}_3 + (\text{Bi}, \text{In})_2\text{Se}_3$ , with the latter showing an improved insulation of the bulk of the  $\text{Bi}_2\text{Se}_3$  and a highly ordered interface. The  $\text{In}_2\text{Se}_3 + (\text{Bi}, \text{In})_2\text{Se}_3$  buffer layer led to the  $\text{Bi}_2\text{Se}_3$  electron concentrations of  $4 \times 10^{18} \text{ cm}^{-3}$  and mobilities of approximately  $600 \text{ cm}^2/\text{Vs}$ .

The structural, electrical, and transport of doping with Ga and Cu were studied. The results reveal a *c* lattice expansion from 28.66 Å (undoped) to 28.92 Å (Ga: 7 at.%) and six-fold n-type doping reaching values of approximately  $6 \times 10^{19} \text{ cm}^{-3}$ . Suggesting that Ga possibly intercalates in the van der Waals gap. Cu doping, on the other hand, leads to a *c* lattice contraction to  $\approx 28.60 \text{ Å}$  (Cu: 2 at.%), wherein Cu acts as an acceptor impurity with a two-fold reduction of the electron concentration. Moreover, magnetotransport measurements showed the weak anti-localization (WAL) cusp at low-magnetic fields of undoped  $\text{Bi}_2\text{Se}_3$ . This cusp degrades upon the doping with Ga, with a topological phase transition at a Ga percentage of 7 at.%, suggesting the destruction of the surface states. Otherwise, the Cu doping showed little interference in the WAL cusp shape.

Angle-resolved photoemission spectroscopy (ARPES) measurements confirm the presence of surface states in undoped  $\text{Bi}_2\text{Se}_3$ , all Cu-doped and Ga-doped up to doping of 2 at.%, whereas at Ga: $\text{Bi}_2\text{Se}_3$  7 at.% no clear surface states are observed. The doping also led to a downward Fermi level shift for Cu doping and an upward shift for doping by Ga.

Furthermore, we explore the fabrication and characterization of field-effect transistor (FET) devices based on  $\text{Bi}_2\text{Se}_3$  thin films. The incorporation of an  $\text{In}_2\text{Se}_3$  capping layer and the use of alumina as a dielectric gate allows the tuning of the Fermi level and modulation of carrier concentration from  $6 \times 10^{12} \text{ cm}^{-2}$  down to  $4 \times 10^{12} \text{ cm}^{-2}$  with a gate voltage of -10 V, demonstrating the potential for FETs to control the transport properties.

**Keywords:** ARPES,  $\text{Bi}_2\text{Se}_3$ , Cu doping, field effect transistor, Ga doping, molecular beam epitaxy, surface states, topological insulators, weak antilocalization effect.

# Table of Contents

List of Tables.....	ix
List of Figures.....	x
List of Abbreviations .....	xvi
<b>Introduction.....</b>	<b>1</b>
<b>1. Topological quantum matter.....</b>	<b>4</b>
1.1. Quantum Hall effect.....	4
1.2. Topological Insulators .....	6
1.2.1. $\mathbb{Z}2$ topological insulators .....	7
1.2.2. 2D Quantum Well HgTe/CdTe.....	8
1.2.3. 3D topological insulator and $A_2B_3$ Family.....	10
1.2.4. Weak (anti)localization effect.....	13
<b>2. Experimental Techniques.....</b>	<b>15</b>
2.1. Molecular Beam Epitaxy.....	15
2.1.1. In-situ characterization .....	19
2.2. Ex-situ characterization.....	22
2.2.1. X-ray diffraction.....	22
2.2.2. Raman spectroscopy.....	24
2.2.3. Atomic Force Microscopy .....	25
2.2.4. Magneto-transport measurements.....	26
2.2.5. X-ray photoelectron spectroscopy.....	28
2.2.6. Angle-resolved photoemission spectroscopy.....	29
2.3. Device fabrication.....	32
<b>3. <math>Bi_2Se_3</math> growth optimization by molecular beam epitaxy.....</b>	<b>35</b>
3.1. Substrate temperature and surface treatment.....	36
3.2. Se overpressure optimization .....	40
3.3. High-resolution x-ray diffraction of $Bi_2Se_3$ .....	42
3.4. Buffer layer introduction.....	45
3.4.1. $Bi_2Se_3$ structural properties.....	47
3.4.2. $Bi_2Se_3$ electrical and transport properties.....	50
3.5. Summary .....	52
<b>4. Structural and electrical properties of Ga and Cu doping of <math>Bi_2Se_3</math>.....</b>	<b>53</b>
4.1. Motivation.....	53
4.2. Structural properties.....	54
4.2.1. <i>In situ</i> RHEED.....	55

4.2.2.	X-ray photoelectron Spectroscopy (XPS).....	56
4.2.3.	XRD and Raman characterization.....	58
4.2.4.	Transmission electron microscopy (TEM) .....	62
4.3.	Electrical properties .....	63
4.3.1.	Transport properties .....	63
4.3.2.	Weak antilocalization effect in doped Bi <sub>2</sub> Se <sub>3</sub> .....	66
4.4.	Summary .....	69
<b>5.</b>	<b>ARPES measurements of the topological insulator, Bi<sub>2</sub>Se<sub>3</sub>, and Ga/Cu-doped Bi<sub>2</sub>Se<sub>3</sub>.....</b>	<b>70</b>
5.1.	Motivation.....	70
5.1.1.	Sample preparation, methodologies, and relevant preliminary information 71	
5.2.	Bi <sub>2</sub> Se <sub>3</sub> electronic band structure concepts .....	73
5.2.1.	Bands bending and fitting model.....	74
5.3.	Ga and Cu doped Bi <sub>2</sub> Se <sub>3</sub> electronic structure.....	77
5.4.	Summary .....	85
<b>6.</b>	<b>Wafer-scale Bi<sub>2</sub>Se<sub>3</sub> top gate field effect devices.....</b>	<b>86</b>
6.1.	Heterostructure growth and field effect transistor fabrication methods .....	86
6.2.	Field effect transistor electrical measurements .....	90
6.2.1.	Gate voltage dependence of channel resistance.....	90
6.2.2.	Gate Dependence of Weak Antilocalization .....	93
6.2.3.	Bi <sub>2</sub> Se <sub>3</sub> transport properties modulation with gate voltage.....	95
6.3.	Summary .....	96
	<b>Conclusion and outlook .....</b>	<b>97</b>
	<b>References.....</b>	<b>99</b>
	<b>Annex.....</b>	<b>104</b>

# List of Tables

<b>Table 3.1</b> Lattice constant of $\text{Bi}_2\text{Se}_3$ and respective lattice mismatch of different types of substrates <sup>8</sup> .....	36
<b>Table 3.2</b> RMS roughness of the $\text{Bi}_2\text{Se}_3$ surface deposited at 270°C and 310°C, and different Se valve apertures with or without a surface treatment. Data is analyzed by the Gwydion software.....	41
<b>Table 3.3</b> FWHM calculated from the Gaussian fitting of the XRD rocking curves of the $\text{Bi}_2\text{Se}_3$ plane (006), for all the $\text{Bi}_2\text{Se}_3$ samples deposited at 310°C.....	43
<b>Table 3.4</b> Peak position of each $\text{Bi}_2\text{Se}_3$ vibrational mode ( $A1g\ 1$ , $Eg2$ and $A1g2$ ) and correspondent FWHM. ....	48
<b>Table 3.5</b> Crystal lattice parameters $a$ and $c$ of the $\text{Bi}_2\text{Se}_3$ layer, for the three types of $\text{Bi}_2\text{Se}_3$ . ....	49
<b>Table 3.6</b> X-ray reflectivity fitting parameters, thickness, and roughness, for each layer of the IS-BIS buffer sample.....	50
<b>Table 3.7</b> X-ray reflectivity fitting parameters, thickness, and roughness, for each layer of the BIS buffer sample. ....	50
<b>Table 3.8</b> Electrical and transport properties of the $\text{Bi}_2\text{Se}_3$ layer, with surface treatment and grown on different buffer layers (IS-BIS or BIS). The measurements are performed at RT. ....	51
<b>Table 4.1</b> Chemical composition of the Ga/Cu-doped $\text{Bi}_2\text{Se}_3$ extracted from the XPS analysis. ....	57
<b>Table 6.1</b> Estimated WAL fitting values from the $\text{Bi}_2\text{Se}_3$ device at 1.5 K for different gate voltages of 0 and -6 V. ....	94

# List of Figures

<b>Figure 0</b>	Schematic of the thesis body for the experimental results (Chapters 3-6).....	3
<b>Figure 1.1</b>	a) Representation of Quantum Hall Effect with chiral edge states. b) Representation of the Landau levels. c) Transverse component from the resistivity showing the quantization of conductivity of units of $e^2/h$ . Edited from <sup>2</sup> .....	5
<b>Figure 1.2</b>	a) Schematics of the energy dispersion for a 2D topological system with 1D spin edge states crossing the Fermi level and b) Illustration of the quantum spin hall effect presenting two helical channels around the edges associated for each spin. ....	7
<b>Figure 1.3</b>	Dispersion of spin texture edge states with a) topological trivial and b) topological nontrivial character (Blue and red colors indicate spin species). ....	8
<b>Figure 1.4</b>	a) Quantum Well structure of the HgTe/CdTe heterostructure. b) Electron energy subbands E1 and E2 and heavy-hole subbands (H1-H4) as a function of thickness d. Edited from <sup>3</sup> .....	9
<b>Figure 1.5</b>	a) Hall bar geometry. b) Longitudinal resistance plotted as a function of $V_g - V_{th}$ for 4 different samples at 30mK: (I) QW with $d=45$ Å and (II, III, IV) $d=73$ Å. The device dimensions are (L/W), $(20.0 \times 13.3) \mu\text{m}^2$ for devices (I) and (II), $(1 \times 1) \mu\text{m}^2$ for device (III), and $(1 \times 0.5) \mu\text{m}^2$ for device (IV) Edited from <sup>3</sup> .....	10
<b>Figure 1.6</b>	a) Illustration of a weak 3D TI being a stack of 2D TI with topological properties and a strong 3D insulator with all surfaces presenting topological properties. b) Full illustration of a Strong 3D TI and the conduction along the TI surface. c) Band diagram of a 3D TI, presenting the topological spin-texture surface states dispersion for 3D systems (Dirac cone) with a spin orientation $S$ rotating along a circle. Edited from <sup>12</sup> .....	11
<b>Figure 1.7</b>	a) Crystal structure of $A_2B_3$ compounds with primitive vectors $(a_1, a_2, a_3)$ . b) Illustration of structural organization along the planes YX and ZX of $\text{Bi}_2\text{Se}_3$ <sup>13</sup> .....	12
<b>Figure 1.8</b>	a) Energy and momentum dependence of the local density of states (LDOS) for $\text{Bi}_2\text{Se}_3$ . b) High resolution ARPES measurements of the surface band structure of $\text{Bi}_2\text{Se}_3$ . Edited from <sup>13</sup> .....	13
<b>Figure 1.9</b>	a) Illustration of a close loop of an electron path. b) Positive conductance of weak localization (WL) and c) typical weak antilocalization curve showing a decreasing in the conductance with magnetic field <sup>159</sup> .....	14
<b>Figure 2.1</b>	MBE diagram showing the growth chamber. This chamber is equipped with 4 Knudsen cells with Cu, Bi, Ga, and In and a valved cracker cell for Se. The system is also equipped with a RHEED and a beam flux monitor.....	16

<b>Figure 2.2</b> Illustration of the three main growth modes a) Volmer-Weber (Island growth), b) Frank-van der Merwe (Layer-by-layer), and c) Stranski-Krastanov.....	17
<b>Figure 2.3</b> Defect representation of a) Stacking fault, b) twin defects (vertical and horizontal), and c) point defects with the representation of interstitial, substitutional and vacancy defects.....	18
<b>Figure 2.4</b> Schematic configuration of a RHEED setup.....	20
<b>Figure 2.5</b> a) Reciprocal space and real space of a RHEED. Reciprocal space presents the Ewald sphere construction. b) Schematics of different types of realistic surface growth and correspondent reciprocal space and their RHEED pattern <sup>34</sup> .....	21
<b>Figure 2.6</b> RHEED intensity oscillation and crystal growth monitor. $\theta$ represents the percentage of the monolayer growth. $\theta=1$ represents 1 monolayer and $\theta=1.5$ represents 1 monolayer and half growth of the following <sup>34</sup> .....	22
<b>Figure 2.7</b> a) Inter-atomic planes with diffraction by the crystal structure. b) Angles and axes relevant for all XRD measurement modes <sup>160</sup> .....	23
<b>Figure 2.8</b> Periodic oscillations observed in an XRR scan and information profile. ....	24
<b>Figure 2.9</b> Schematic diagram of an atomic force microscope (AFM) setup.....	25
<b>Figure 2.10</b> a) Van der Pauw geometry. b) Hall-bar geometry with visualization of measured contacts. c) Example Van der Pauw geometry as realized for a Bi <sub>2</sub> Se <sub>3</sub> sample. b) Hall-bar example.....	26
<b>Figure 2.11</b> Schematic diagram of an XPS instrumentation setup <sup>161</sup> .....	29
<b>Figure 2.12</b> Illustration of ARPES geometry experiment with a hemispherical analyzer in angular mode. Adapted from <sup>21</sup> .....	30
<b>Figure 2.13</b> Illustration of the energy dispersion relation in 1D representing the Fermi level with the corresponding Fermi vector. The Fermi-Dirac distribution for the concept of the Fermi level energy position is observed at the Fermi level. ....	32
<b>Figure 2.14</b> a) Top view and b) cross-section view of the cleanroom fabrication process for the Hall-bar structure top gate device. ....	34
<b>Figure 3.1</b> a) RHEED pattern of a cleaned sapphire substrate after a 900°C annealing for 45 min. b) RHEED pattern of a 30 nm Bi <sub>2</sub> Se <sub>3</sub> layer in the [100] direction.....	37
<b>Figure 3.2</b> AFM image of a 30 nm thick Bi <sub>2</sub> Se <sub>3</sub> surface, deposited at a) 270 °C and Se valve: 5.0 mm and b) 310 °C and Se valve: 5.0 mm. Line profile of Bi <sub>2</sub> Se <sub>3</sub> surface from c) 270 °C and d) 310 °C, as indicated by the black line in a) and b).....	38
<b>Figure 3.3</b> a) AFM image of a 30 nm thick Bi <sub>2</sub> Se <sub>3</sub> surface with a surface treatment deposited at 310°C, Se valve: 5.0 mm. b) Line profile of Bi <sub>2</sub> Se <sub>3</sub> surface as indicated by the black line in a).....	39
<b>Figure 3.4</b> XRD diffractogram for the Bi <sub>2</sub> Se <sub>3</sub> layer with and without surface treatment. ...	39

<b>Figure 3.5</b> AFM images of 30 nm thick Bi <sub>2</sub> Se <sub>3</sub> surfaces. The substrates were subjected to a surface treatment. The Bi <sub>2</sub> Se <sub>3</sub> growth was performed at 310 °C and with a Se valve aperture of a) 1.0 mm, b) 2.0 mm and c) 5.0 mm. Line profiles of Bi <sub>2</sub> Se <sub>3</sub> surfaces grown at a Se aperture of d) 1.0 mm, e) 2.0 mm and f) 5.0 mm, as indicated by the black line. ....	41
<b>Figure 3.6</b> XRD rocking curves of Bi <sub>2</sub> Se <sub>3</sub> grown at 310°C along the plane (006) of Bi <sub>2</sub> Se <sub>3</sub> .	43
<b>Figure 3.7</b> XRD $\varphi$ scan of Bi <sub>2</sub> Se <sub>3</sub> grown at 310°C along the plane (015) of Bi <sub>2</sub> Se <sub>3</sub> . The black dotted lines denote the crystal 3-fold symmetry by the repetition of the peak every 120°. The green dotted lines denote the presence of twinning by the appearance of a peak every 60° .....	44
<b>Figure 3.8</b> Schematic of the IS-BIS buffer layer deposition adapted from Koirala et al. b) RHEED patterns for each individual layer in the direction [100]. c) Schematic of the BIS buffer layer deposition adapted from Wang et al. d) RHEED patterns for each individual layer. The first RHEED is in the direction [110] and the second is in the direction [100], showing that there is a 3-fold rotational symmetry.....	46
<b>Figure 3.9</b> a) Room temperature Raman signal of Bi <sub>2</sub> Se <sub>3</sub> with a surface treatment and with a buffer layer showing three characteristic vibrational peaks. b) Illustration of the vibrational modes present in Bi <sub>2</sub> Se <sub>3</sub> . ....	47
<b>Figure 3.10</b> a) XRD diffractogram for the Bi <sub>2</sub> Se <sub>3</sub> layer with a surface treatment and Bi <sub>2</sub> Se <sub>3</sub> grown with an IS-BIS or BIS buffer layer. b) High-resolution x-ray diffraction of the (006) plane of Bi <sub>2</sub> Se <sub>3</sub> . ....	48
<b>Figure 3.11</b> X-ray reflectivity measurements for the Bi <sub>2</sub> Se <sub>3</sub> grown on a a) IS-BIS buffer layer (orange line), b) BIS buffer layer (orange line). Both images present the fitting profile calculated from the software REFLEX extracted in MATLAB (blue lines).....	50
<b>Figure 4.1</b> Unit cell of a) Bi <sub>2</sub> Se <sub>3</sub> crystal structure and possible doping atoms site in the crystal: b) Bi substitution, c) interstitial in the quintuple layer or d) intercalated into the Van der Waals gap. Edited from Daniel Brito et al. <sup>121</sup> .....	54
<b>Figure 4.2</b> RHEED pattern of a) undoped Bi <sub>2</sub> Se <sub>3</sub> , Ga-doped with b) 2 at.%, c) 7 at.%, d) 14 at.% in the [110] direction. RHEED pattern of e) undoped Bi <sub>2</sub> Se <sub>3</sub> and Cu doped with f) 2 at.%, g) 4 at.% and h) 7 at.% in the [100] direction. Pannels (a)-(d) are edited from Daniel Brito et al. <sup>121</sup> .....	56
<b>Figure 4.3</b> XPS spectra for Ga-doped Bi <sub>2</sub> Se <sub>3</sub> with the respective high-resolution spectra for a) Ga 3d, b) Bi 4f and c) Se 3d core lines for all doping percentages. XPS spectra for the Cu-doped Bi <sub>2</sub> Se <sub>3</sub> with the respective high-resolution spectra for d) Cu 2p, e) Bi 4f and f) Se 3d core lines for all doping percentages. Edited from Daniel Brito et al. <sup>121</sup> . ....	57

<b>Figure 4.4</b> XRD pattern for the a) Ga-doped $\text{Bi}_2\text{Se}_3$ with b) high-resolution XRD pattern for the (0015) plane. XRD pattern for the c) Cu-doped $\text{Bi}_2\text{Se}_3$ with d) high-resolution XRD pattern for the (0015) plane. Edited from Daniel Brito et al. <sup>121</sup> .....	58
<b>Figure 4.5</b> Crystal lattice parameters a) c and b) a as a function of the Ga atomic doping percentage. Crystal lattice parameters c) c and d) a as a function of the Cu atomic doping percentage. The calculated values are extracted from XRD by Eq. (2.2) Edited from Daniel Brito et al. <sup>121</sup> .....	60
<b>Figure 4.6</b> Room temperature Raman spectroscopy for a) undoped and Ga-doped $\text{Bi}_2\text{Se}_3$ and b) peak position as a function of the nominal Ga percentage. Raman spectroscopy for c) undoped and Cu-doped $\text{Bi}_2\text{Se}_3$ and b) peak position as a function of the nominal Cu percentage. Edited from Daniel Brito et al. <sup>121</sup> .....	61
<b>Figure 4.7</b> STEM images along the [100] direction of $\text{Bi}_2\text{Se}_3$ doped with a) 2 at.% and b) 7 at.% of Cu grown on a sapphire substrate.....	62
<b>Figure 4.8</b> a) Resistivity, b) sheet concentration, c) bulk concentration, d) mobility of undoped and Ga-doped $\text{Bi}_2\text{Se}_3$ as a function of the temperature extracted from the Hall effect measurements. All samples are n-type. Edited from Daniel Brito et al. <sup>121</sup> . ....	64
<b>Figure 4.9</b> a) Resistivity, b) sheet concentration, c) bulk concentration, d) mobility of undoped and Cu-doped $\text{Bi}_2\text{Se}_3$ as a function of the temperature extracted from Hall effect measurements. All samples are n-type.....	66
<b>Figure 4.10</b> WAL measurements for undoped $\text{Bi}_2\text{Se}_3$ (black dots) and doped samples with 2 at.% (red dots) and 7 at.% (blue dots) of a) Ga and c) Cu doped $\text{Bi}_2\text{Se}_3$ , as a function of low magnetic field with the corresponding HLN model fittings (dashed lines). The sharp cusp is a typical feature of the presence of surface states. Fitting parameters $\alpha$ and phase coherence length ( $L\phi$ ) as a function of b) Ga or d) Cu doping level. Edited from Daniel Brito et al. <sup>121</sup> . ....	67
<b>Figure 5.1</b> Configuration of the $\text{Bi}_2\text{Se}_3$ substrate for the ARPES measurements. It is visible the sample with a gold line on the surface of it. The sample is held on the holder by a washer, which also provides the metallic contact to the film surface.....	72
<b>Figure 5.2</b> a) $\text{Bi}_2\text{Se}_3$ surface Brillouin zone with a hexagonal structure with visualization of the relevant symmetry points( $\Gamma$ , K and M). b) Energy dispersion of $\text{Bi}_2\text{Se}_3$ . c) The fitting model applied to the band dispersion of the $\text{Bi}_2\text{Se}_3$ , observing the surface states (Dirac cone, red dash), conduction band (Black dash) and valence band (Gray dash). Additionally, as yellow dash line is observed a confined quantum well level, as new conduction and valence bands.....	74
<b>Figure 5.3</b> a) 2DEG illustration and the respective b) band diagram as a function of the depth of the material.....	75

<b>Figure 5.4</b> Energy dispersion of $\text{Bi}_2\text{Se}_3$ with a) long scan mode and b) integrated fast scan in different spots of the sample. The fitting model is applied on both signals where the simulated fitting signal of b) is observed in c).....	76
<b>Figure 5.5</b> Core levels from the $\text{Bi}_2\text{Se}_3$ and the Cu/Ga doped $\text{Bi}_2\text{Se}_3$ .....	77
<b>Figure 5.6</b> Energy dispersion by the point scan of a) 2 at.% Ga-doped $\text{Bi}_2\text{Se}_3$ , b) 7 at.% Ga-doped $\text{Bi}_2\text{Se}_3$ , c) 2 at.% Cu-doped $\text{Bi}_2\text{Se}_3$ and d) 7 at.% Cu-doped $\text{Bi}_2\text{Se}_3$ with the fitting model as dashed lines. Black dashed line corresponds the conduction band, red dashed lines to the Dirac surface states and the gray dashed line to the valence band. ....	79
<b>Figure 5.7</b> Evolution of the conduction band minimum, valence band maximum, and Dirac point of the surface states as a function of a) Ga and b) Cu doping. ....	80
<b>Figure 5.8</b> Evolution of the conduction and valence electron effective masses as a function of a) Ga and b) Cu doping. ....	81
<b>Figure 5.9</b> Evolution of the Fermi velocity of the surface states as a function of a) Ga and b) Cu doping. ....	81
<b>Figure 5.10</b> Fermi map for the reference $\text{Bi}_2\text{Se}_3$ , Ga-doped $\text{Bi}_2\text{Se}_3$ and Cu-doped $\text{Bi}_2\text{Se}_3$ at energies from the Fermi level (0, -200, -300, -400, -500, -800 meV). The signal is obtained by a long scan to improve the signal-to-noise ratio. ....	83
<b>Figure 5.11</b> Surface charge carrier density of $\text{Bi}_2\text{Se}_3$ extracted from ARPES as a function of doping of Cu or Ga. ....	84
<b>Figure 6.1</b> a) Devices heterostructure composed by an IS-BIS buffer layer deposition, a 12 nm thick $\text{Bi}_2\text{Se}_3$ and a 40 nm thick $\text{In}_2\text{Se}_3$ capping layer. b) Photograph of a sapphire wafer with the deposited heterostructure. c) XRD spectrum of the device heterostructure on a sapphire substrate. d) High-resolution XRD for the (0015) diffraction peak.....	87
<b>Figure 6.2</b> $\text{In}_2\text{Se}_3$ and $\text{Bi}_2\text{Se}_3$ samples a) in a 0.5% HCl + 30% $\text{H}_2\text{O}_2$ etching solution (4:50), and b) wafer removed from the etching solution after 30 min. ....	88
<b>Figure 6.3</b> Microscope image of the individual steps of the FET device cleanroom fabrication. a) Hall-bar patterning lithography, b) physical etching by ion milling, c) lithography of the metallic contacts, d) dielectric deposition by PVD, e) contact exposure by lift-off, f) chemical etching of the capping layer, g) Gold deposition on the contact area with the lithography for the h) metallic contacts and metallic gate on top of the channel. i) Wafer visualization of the 36 FET devices. The distinct colors are due to the optical interference of the layers.....	89
<b>Figure 6.4</b> Cross-sectional illustration of the $\text{Bi}_2\text{Se}_3$ FET devices. b) Full wafer with 36 FET devices and magnification of a 300/150 $\mu\text{m}$ device with the wire bonding configuration, as used for the electrical measurements at low temperatures. ....	90

**Figure 6.5** a) Gate I-V curves for different sweep voltages. The measurements start with smaller voltage and increase slowly to higher voltage sweeps. b) Bi<sub>2</sub>Se<sub>3</sub> channel I-V curve with the gate I-V curve observing a minimal leakage current. The measurements are performed at RT.....92

**Figure 6.6** Bi<sub>2</sub>Se<sub>3</sub> channel resistance as a function of the gate voltage for a) temperatures from 200 K to 1.55 K and b) different magnetic fields of 0 and 2 T at 1.5 K. ....93

**Figure 6.7** Gate dependence of the WAL in the Bi<sub>2</sub>Se<sub>3</sub> device for the gate voltage of 0 and -6 V as a function of the magnetic field. The fitting is shown as dashed lines for each gate voltage. ....94

**Figure 6.8** a) Linear response of the transverse resistance (R<sub>xy</sub>) as a function of the magnetic field for different gate voltages. b) Extracted electron concentration and mobility for the different gate voltages. The measurements are performed at a temperature of 1.5 K. ....95

# List of Abbreviations

AFM	Atomic force microscopy
ARPES	Angle-resolved photoelectron spectroscopy
BEP	Beam equivalent pressure
BIS	(Bi,In) <sub>2</sub> Se <sub>3</sub> buffer layer
CB	Conduction band
EBIN	Binding energy
DP	Dirac point
EC	Conduction band minimum
ED	Dirac equation
EF	Fermi level
EV	Valence band maximum
FET	Field effect transistor
FWHM	Full width half maximum
HLN	Hikami-Larkin-Nagaoka
IS-BIS	In <sub>2</sub> Se <sub>3</sub> + (Bi,In) <sub>2</sub> Se <sub>3</sub> buffer layer
KF	Fermi vector
MBE	Molecular beam epitaxy
QAHE	Quantum anomalous hall effect
QHE	Quantum hall effect
QSHE	Quantum spin hall effect
QL	Quintuple layer
RHA	Rashba splitting
RHEED	Reflection high-energy electron diffraction
SOC	Spin-orbit coupling
RS	Sheet resistance
RT	Room temperature
SS	Surface states
ST	Surface treatment
TEM	Transmission electron microscopy
TI	Topological insulator
TRS	Time reversal symmetry
TSC	Topological superconductor

UHV	Ultra-high vacuum
VB	Valence band
VF	Fermi velocity
VDW	Van der Waals
XPS	X-ray photoemission spectroscopy
XRD	X-ray diffraction
XRR	X-ray reflectivity
WAL	Weak antilocalization
2DEG	2-Dimensional electron gas



# Introduction

In the society we live in, the world is extremely dependent on technology, which has grown exponentially since the discovery of transistors. The transistor is the key to developing new technologies in the modern world because of its efficiency, reliability, and compact size. Even with their compact size, over the years, the world has demanded faster and more efficient electronics. The solution for the problem consisted of transistor size reduction with the purpose of increasing the transistor density in integrated circuits. However, Moore's law predicts that the continuous reduction of the transistor size would eventually approach the physical limit of miniaturization. Simultaneously, the high density and integration of transistors are leading to a high-power consumption. Therefore, alternative materials for semiconductor technologies must be investigated to address this problem. The introduction of topological insulators has attracted considerable attention to the possibility of a dissipationless material, which could minimize the constraints and improve the power consumption of future technologies.

Topological insulators have recently been introduced in the field of condensed matter physics based on the predictions of Kane and Mele<sup>1</sup>. The topic increased exponentially after the first experimental discovery due to their promising properties. They are a new class of materials that exhibit insulating behavior in bulk, combined with conductive surfaces or edges. These conductive surfaces arise from strong spin-orbit coupling and are protected by time-reversal symmetry (TRS) to perturbations like disorder or impurities, as long as TRS is preserved. The combination of spin-orbit coupling and TRS leads to the spin-locked momentum of electrons, which implies that electrons with opposite momentum are required to have opposite spin. The spin momentum locking allied with TRS implies the absence of scattering between states with opposite momentum, which leads to a decrease in scattering probability. Hence, the surface states of topological insulator materials assure more efficient transport and can pave the way for the fabrication of electronics with reduced power consumption.

One promising topological insulator candidate is the  $\text{Bi}_2\text{Se}_3$  compound because of its relatively large band gap (0.3 eV), which is suitable for applications at room temperature. However, a major challenge in exploring the topological properties of these materials is unintentional doping (n-type). Doping leads to bulk conductivity, which masks the effects of dissipationless surface states.

To address this challenge, various strategies have been discovered, such as reverse doping with different elements to compensate (by p-type doping) for unintentional doping by moving the Fermi level of the material into the band gap. This has been implemented by molecular beam epitaxy (MBE) which allows for a controllable composition, a good material quality, and has a crucial advantage for the fabrication of devices on a wafer scale.

The primary goal here is to obtain a material with insulating bulk and conductive surface states on the topological insulator  $\text{Bi}_2\text{Se}_3$ . Two approaches were used in this study. The first is the study of  $\text{Bi}_2\text{Se}_3$  doped with Ga and Cu to understand if they could act as acceptor impurities. Additionally, doping could also be beneficial for the discovery of new physical properties such as the anomalous quantum Hall effect or topological superconductivity. The second approach to insulate the bulk by tuning the Fermi level involves the implementation of an electrostatic gate that decreases the electron

concentration of the material and consequently facilitates the exploitation of the topological surface state properties.

The thesis starts (**Chapter 1**) by introducing the topic of quantum topological matter and the state of the art. Here, we explain the theoretical concepts used to understand the subject and the experimental results obtained. Moreover, it shows what has already been obtained to date. This is followed by **Chapter 2**, in which the experimental growth technique (MBE) and several characterization techniques implemented throughout the thesis are explained in more detail.

The experimental results of the thesis start from **Chapter 3**. The research presented in this thesis is as follows (see Fig. 0): Firstly, in **Chapter 3**, the optimization of the growth of the topological insulator  $\text{Bi}_2\text{Se}_3$  is addressed for the first time at INL by an MBE growth. The substrate temperature, growth rate, and surface treatment were optimized to obtain the best structural properties with minimal defect formation. Moreover, a buffer layer was studied, which leads to a highly oriented interface with the  $\text{Bi}_2\text{Se}_3$ , and consequently an enhancement of the  $\text{Bi}_2\text{Se}_3$  electrical and transport properties.

After establishing the procedure for the growth of good-quality  $\text{Bi}_2\text{Se}_3$ , the doping of  $\text{Bi}_2\text{Se}_3$  by gallium and copper was studied with the aim of understanding the effect from the structural and electrical points of view (**Chapter 4**). The doped material was studied using Raman spectroscopy, X-ray diffraction (XRD), and X-ray photoelectron spectroscopy (XPS) to obtain information about the structural and compositional evolution upon doping. The Hall effect and weak antilocalization effect were studied to obtain the electrical and transport properties upon doping as a 2D transport effect. Owing to the difficulty in distinguishing the 2D transport from the surfaces and bulk through electrical characterization techniques, ARPES is implemented in **Chapter 5**. An electronic study of the doping effect is achieved, which allows for obtaining detailed information about 2D transport.

Finally, because MBE growth allows the fabrication of several devices on a wafer scale, including heterostructures, the fabrication of field effect transistors (FET) is studied (**Chapter 6**). FET devices have been successfully developed, allowing the tuning of the Fermi level of the material closer to the band gap.

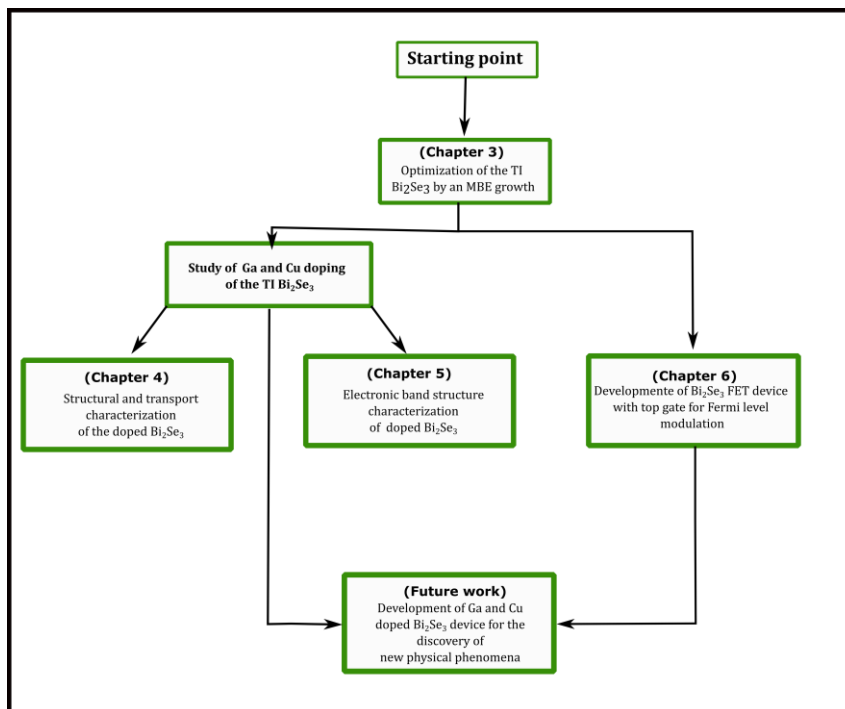


**Figure 0** Schematic of the thesis body for the experimental results (Chapters 3-6).

# Chapter 1

## 1. Topological quantum matter

The concept of topology was introduced to condensed matter physics in the 80's by David J. Thouless among others, which led to the Nobel Prize in Physics in 2016. The concept of topological phases of matter has then emerged. These phases are not characterized by local order parameters such as magnetization, polarization, etc.... They are associated with certain properties that are robust to perturbations, meaning there is no spontaneous symmetry breaking. In fact, topological phases are protected by a combination of symmetry and dimensionality, and the robustness of characteristic properties holds as long as, for the given dimensionality, perturbations do not break the protecting symmetry. These properties are characterized by topological invariants, which do not change under smooth, continuous variations of the system's Hamiltonian. Such topological distinct phases can appear in solid-state systems where the topology is related to the crystal's band structure. Topological states were first observed in the quantum Hall effect (QHE)<sup>2</sup>, but most recently the discovery of topological insulators has attracted a lot of attention<sup>3,4</sup>. This chapter aims to review some aspects to understand the origin of topological matter and its state of the art.

### 1.1. Quantum Hall effect

In a 2D electron system, within the classical picture, at low temperatures, the presence of a magnetic field perpendicular to the plane of the system and an external electric field, causes electrons to move along circular orbits, due to the Lorentz force. With high magnetic fields, these orbits are localized in the bulk of the material, but close to the edge, these circular orbital motions are incomplete, leading to the movement of electrons along the system edge (Fig. 1.1 a). Quantum mechanically, the system is described by quantized Landau levels, with  $n \geq 0$ :

$$E_n = \left(n + \frac{1}{2}\right) \hbar\omega_c, \quad n = 0, 1, 2, \dots \quad (1.1)$$

where  $\omega_c = \frac{eB}{m}$  is the cyclotron frequency. The Landau levels are illustrated in Fig. 1.1 b). The system behaves as an insulator in the bulk, due to the presence of an energy band gap.

However, due to the confining potential, there are states crossing the Fermi level near the edges of the sample, as also indicated in Fig. 1.1 b) by red circles. The presence of an electric field causes the orbits to drift (classical picture), or the edge states to conduct (quantum picture), which leads to a Hall current along the edges associated with a transverse Hall tension. Experimentally, Von Klitzing et al. <sup>2</sup> discovered that the transverse conductivity  $\sigma_{xy}$  is quantized in multiples of  $e^2/h$  <sup>5</sup>:

$$\sigma_{xy} = n \frac{e^2}{h}, \quad n = 0, 1, 2, \dots \quad (1.2)$$

The behavior of the Hall conductivity as a function of the magnetic field is shown in Fig. 1.1 c). The characteristic plateaus associated with the quantized Hall conductivity are observed.

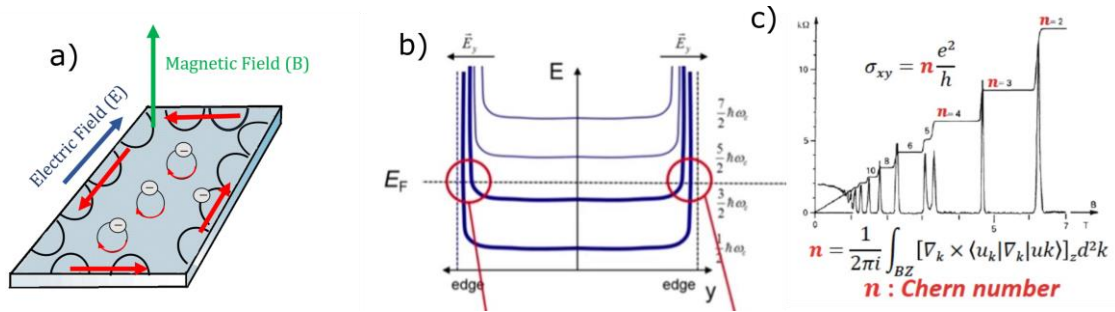


**Figure 1.1** a) Representation of Quantum Hall Effect with chiral edge states. b) Representation of the Landau levels. c) Transverse component from the resistivity showing the quantization of conductivity of units of  $e^2/h$ . Edited from <sup>2</sup>.

It was soon realized by Laughlin<sup>6</sup>, Halperin<sup>7</sup>, among others, that the edge states play a determinant role. The presence of a bulk quantized property along with metallic (crossing the Fermi level) boundary states is the hallmark of a topological insulator, known as the bulk-boundary correspondence. Thouless, Kohmoto, Nightingale, and den Njjs<sup>8</sup> made an important further step in this relation, discovering that the quantized conductivity was topological, meaning that it can be described by an integer topological invariant, the first Chern Number ( $C_n$ ).

$$\sigma_{xy} = C_n \left( \frac{e^2}{h} \right) \quad (1.3)$$

With  $C_n$  given by the expression shown in Fig 1.1 c) in terms of the periodic art of the Bloch wave function,  $u_k$ . The robustness of the quantized conductivity is explained by the topological invariant, in the sense that it cannot be changed under smooth variations of the Hamiltonian. The topological nature of the quantum Hall effect is characterized by the two-dimensionality of the system and the lack of time reversal symmetry (TRS). For time-reversal symmetric systems, the first Chern number is necessarily zero, implying zero Hall

conductivity. In the quantum Hall effect, the time reversal symmetry is broken by the presence of a magnetic field.

## 1.2. Topological Insulators

Topological phases of matter differ from conventional matter because the former feature a nontrivial topological invariant on its electronic structure. Topological insulators (TIs) are electronic materials with a band gap in the bulk like an insulator material while being electrically conductive along its boundaries, due to topologically unavoidable gapless boundary states<sup>5</sup>.

The formation of conducting edge states in the QHE requires a magnetic field to break the time-reversal symmetry so that the Chern number is different from zero. Topological states can also exist in systems that do not break time reversal symmetry. An important example of an intrinsic effect that causes the formation of nontrivial topological states without the need to break TRS is the spin-orbit coupling.

The spin-orbit coupling allows a different topological class of insulator with TRS unbroken. The presence of spin-orbit coupling leads to a band inversion in the electronic structure of the material between the conduction and the valence band<sup>5</sup>, resulting from the coupling of an electron's magnetic spin to the intrinsic magnetic field set up by the electron's motion around its orbital. The band inversion without TRS breaking is the key ingredient in the new class of topological insulators.

### Quantum Spin Hall effect

Kane and Mele<sup>1</sup> proposed a model displaying the so-called quantum spin hall effect (QSHE), which does not break TRS. It can be understood as two copies of the QHE with spin-filtered (spin current  $\neq 0$ ) counter-propagating (total current = 0) edge states pair (Fig 1.2), where each has a different spin and propagation direction (helical edge states). Considering both edges, a two-terminal conductance of  $2 \frac{e^2}{h}$  is expected<sup>5</sup>, but taking into account the spin edge channels, it is expected a nonzero spin Hall conductance of  $\frac{e^2}{2h}$  for each channel<sup>4</sup>.

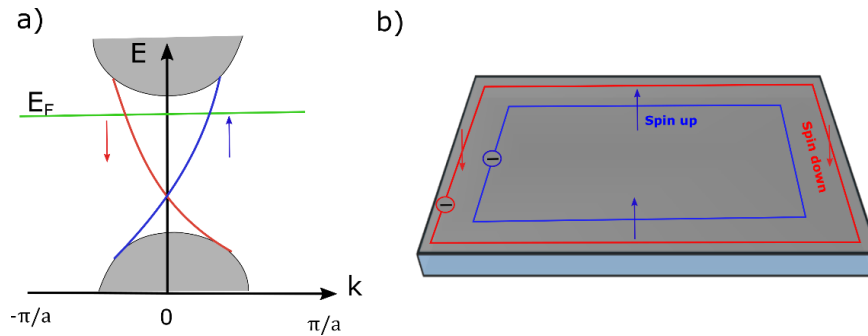


**Figure 1.2** a) Schematics of the energy dispersion for a 2D topological system with 1D spin edge states crossing the Fermi level and b) Illustration of the quantum spin hall effect presenting two helical channels around the edges associated for each spin.

Furthermore, due to the absence of a magnetic field, the TRS is maintained. Therefore, backscattering is not allowed since it would require an electron spin to flip. The spin of an electron cannot be changed due to the protection of the TRS, which gives robustness to the edge states. This holds in the presence of disorder or impurities, as long as they do not break TRS. Spin-orbit coupling requires a distinct topological invariant from the Chern number,  $C_n$ , because time-reversal invariant systems present a zero Chern number. Thus, a new topological invariant ( $\nu$ ) was introduced for this class of  $\mathbb{Z}_2$  topological insulators<sup>9</sup>. A more detailed discussion about the spin-orbit coupling is explained later in the context of 3D topological insulators.

### 1.2.1. $\mathbb{Z}_2$ topological insulators

2D topological insulators (TIs) with TRS are characterized by a  $\mathbb{Z}_2$  topological invariant,  $\nu_0$ , which can only take two values, 0 or 1, where 0 would correspond to a topologically trivial and 1 to a topologically nontrivial system<sup>10</sup>. This classification derives from the conservation of TRS. The Bloch Hamiltonian should be time-reversal invariant (TRI), consequently, imposing a restriction on the band structure called Kramer's theorem. The theorem states that all eigenstates of a TRI Hamiltonian must be at least two-fold degenerate for spin  $\frac{1}{2}$  particles<sup>5</sup>. In particular, at the so-called time-reversal invariant momenta (TRIM) ( $k=0, \pi/a$ ), two bands must meet corresponding to states related by TRS.

As an example, Fig. 1.3 a) shows the dispersion of spin edge states. The special points  $k=0$  and  $k=\pi/a$  are degenerate as a consequence of Kramer's theorem, but the spin-orbit coupling splits the degeneracy in momentum as we move away from these points. There are two ways for these states to connect. In Fig. 1.3 a) the same pair of edge-state bands are shared between the TRI points. In this case, the edge states can be eliminated with disorder, by tuning the Fermi energy or pushing them out of the band gap, therefore the topological invariant  $\nu_0 = 0$  (topological trivial system). In Fig. 1.3 b), the states cannot be removed from the band gap, as there is always an odd number of pairs of states crossing the Fermi level, so that  $\nu_0 = 1$  (topological nontrivial system). In conclusion, a topological insulator is

characterized by having topologically protected edge states, when there is an odd number of times the states cross the Fermi level.

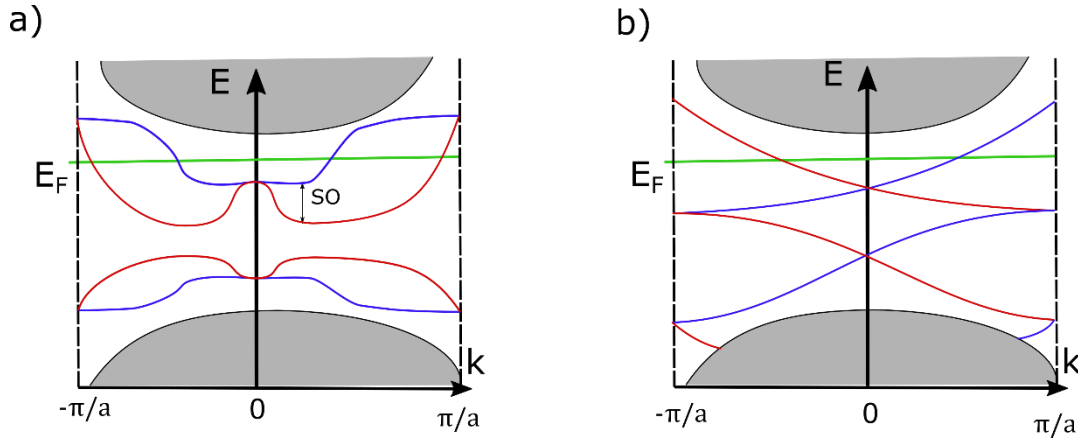


**Figure 1.3** Dispersion of spin texture edge states with a) topological trivial and b) topological nontrivial character (Blue and red colors indicate spin species).

### 1.2.2. 2D Quantum Well HgTe/CdTe

The quantum spin Hall effect was observed experimentally on inverted HgTe/CdTe quantum wells (QWs)<sup>3</sup>. The compound HgTe is a zero-gap semiconductor with a degeneracy of the valence and conduction bands at the  $\Gamma_8$  point and which features an inverted band structure, representing a “negative band gap”. This material is combined, as a sandwich, with a semiconductor,  $\text{Hg}_{0.32}\text{Cd}_{0.68}\text{Te}$ , which has a positive energy gap, meaning that there is no inversion of the conduction and valence bands. Consequently, a QW is formed as illustrated in Fig 1.4. a).

The crucial parameter in the QW is the HgTe layer thickness ( $d$ ). An evolution of the energy band with the thickness can be seen in Fig. 1.4 b). The s-type band E1 and the p-type H1 band cross each other by increasing the thickness  $d$ , reaching a critical value  $d_c = 63 \text{ \AA}$ , resulting in a zero-gap semiconductor<sup>3</sup>. For a thickness  $d_c < 63 \text{ \AA}$ , the material is a normal semiconductor with a valence band below the conducting band and a positive band gap. However, for thickness  $d_c > 63 \text{ \AA}$ , the band structure is inverted resulting in a “negative band gap”, and a quantum phase transition occurs at  $d = d_c$ <sup>3</sup>.

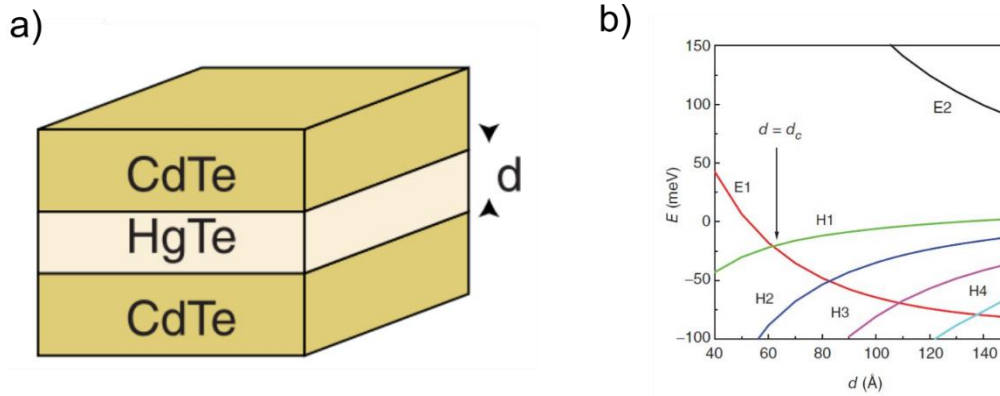


**Figure 1.4** a) Quantum Well structure of the HgTe/CdTe heterostructure. b) Electron energy subbands E1 and E2 and heavy-hole subbands (H1-H4) as a function of thickness  $d$ . Edited from <sup>3</sup>.

Considering an inverted QW band structure, if the Fermi level is in the bulk band gap, there are edge states crossing the  $E_F$ , giving rise to a non-trivial insulator, referred to as the quantum spin Hall effect (QSH). The system is characterized by the existence of two spin-polarized conducting channels at the edge, each one owning a characteristic quantum conductance of  $\frac{e^2}{h}$ . Furthermore, due to the crossing of states of the inverted band structures, a QSH cannot be adiabatically deformed into a trivial insulating state without closing the gap, so the system is topologically protected.

Experimentally, the  $\frac{2e^2}{h}$  conductance, the helical character of the edge channels, and the electrical detection of their spin polarization were demonstrated <sup>3</sup>. For the conductance measurement, a four-terminal resistance  $R_{14,23} = V_{23} / I_{14}$  of a sample was measured as a function of a gate voltage (Fig. 1.5). The gate voltage enables tuning the Fermi energy from the bulk conduction to the bulk valence band, by shifting the Fermi level.

Sample (I), with a thickness smaller than the critical thickness ( $d_c$ ), presents a conventional semiconductor behavior, whereas sample (II), with a thickness larger than the critical thickness ( $d_c$ ) and an inverted band structure exhibits a conductance of  $\frac{0.3e^2}{h}$ . If the length ( $L$ ) of the device is shorter, as for samples (III and IV) the conductance reaches the predicted value of  $\frac{2e^2}{h}$  and curiously, changing the width ( $W$ ) does not change the conductance of the material, demonstrating the existence of counterpropagating edge states<sup>3</sup>.

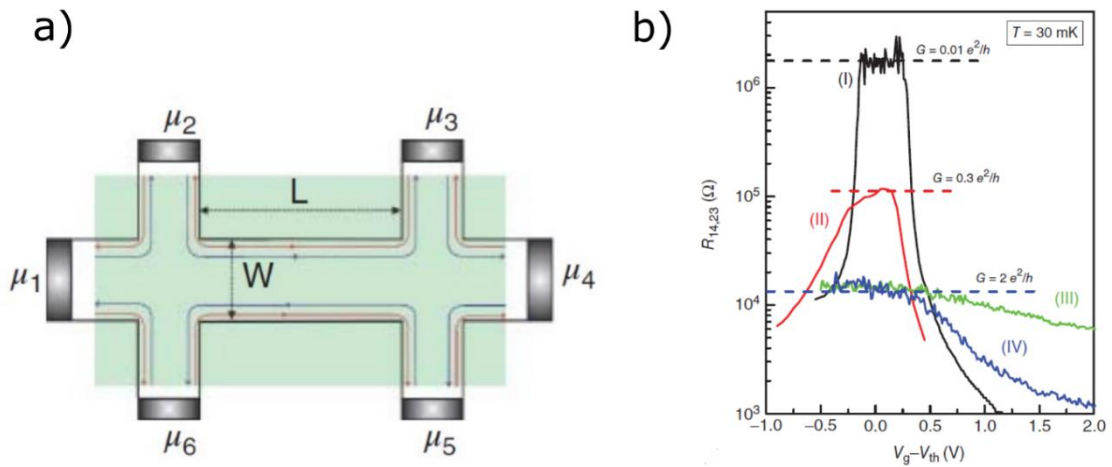


**Figure 1.5** a) Hall bar geometry. b) Longitudinal resistance plotted as a function of  $V_g - V_{th}$  for 4 different samples at 30mK: (I) QW with  $d=45$  Å and (II, III, IV)  $d=73$  Å. The device dimensions are  $(L/W)$ ,  $(20.0 \times 13.3) \mu\text{m}^2$  for devices (I) and (II),  $(1 \times 1) \mu\text{m}^2$  for device (III), and  $(1 \times 0.5) \mu\text{m}^2$  for device (IV) Edited from <sup>3</sup>.

### 1.2.3.3D topological insulator and $A_2B_3$ Family

Subsequently, it was possible to extend the quantum spin hall insulator to three dimensions (3D), establishing a new bulk topological order and the presence of conducting surface states instead of edge states. 3D TIs are characterized by four  $\mathbb{Z}_2$  topological invariants  $(\nu_0; \nu_1\nu_2\nu_3)$ , where  $\nu_0$  is the strong topological invariant and  $\nu_1 - \nu_3$  are the weak topological invariants<sup>10</sup>. The 2D surface Brillouin zone has 4 different TRIM points. These points give rise to Kramer's pairs, whereas for the rest of the Brillouin zone points the degeneracy is split in momentum due to spin-orbit coupling (SOC). For energy bands connecting these points, it could occur a crossing of the Fermi level an even or odd number of times, corresponding to a trivial insulator and a topological insulator, respectively. Since these TRIM points also belong to other 2D surface Brillouin zones, we arrive at the set of four  $\mathbb{Z}_2$  integers, with a single combination guaranteeing the presence of surface states over all the surfaces of the sample<sup>11</sup>. This combination is identified by the strong topological invariant  $\nu_0$ , which can take the values 0 or 1, corresponding to a weak or strong insulator, respectively.

A weak TI ( $\nu_0 = 0$ ) can be seen as a stack of 2D TIs layers (Fig. 1.6 a) left), while the weak topological invariants  $(\nu_1\nu_2\nu_3)$  can be seen as the miller indices corresponding to the TI layer. However, the surface states of this type of 3D TI are not protected by TRS and therefore are not robust. A strong TI ( $\nu_0 = 1$ ) presents topologically protected metallic surface states as illustrated in Fig. 1.6 b). Kramer's degeneracy ensures that surface state bands cross at TRIM points, giving rise to the characteristic Dirac cone dispersion shown in Fig. 1.6 c). Furthermore, due to TRS, 3D TIs present opposite spins at opposite momenta,  $k$  and  $-k$ , which leads to the spin-momentum locking also illustrated in Fig. 1.6 c), also referred

to a spin texture. Integrating the phase around the Dirac point, where the spin orientation is fully revolving, gives rise to a Berry phase of  $\pi$ <sup>5</sup> and has important consequences for the weak anti-localization effect. This effect is introduced in section 1.2.4.

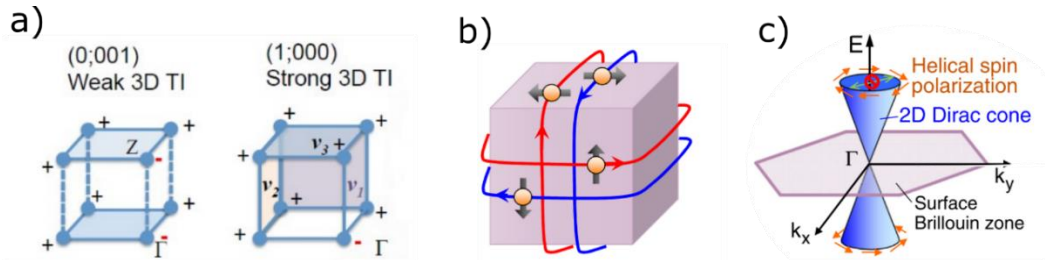


**Figure 1.6** a) Illustration of a weak 3D TI being a stack of 2D TI with topological properties and a strong 3D insulator with all surfaces presenting topological properties. b) Full illustration of a Strong 3D TI and the conduction along the TI surface. c) Band diagram of a 3D TI, presenting the topological spin-texture surface states dispersion for 3D systems (Dirac cone) with a spin orientation  $S$  rotating along a circle. Edited from <sup>159</sup>.

### $A_2B_3$ Family

It was theoretically proposed by Zhang et al. that binary compounds with elements, such as Bi, Sb, Se, and Te, could lead to a 3D topological insulator with 2D conductive surface states<sup>4</sup>. It was shown that the  $A_2B_3$  family is a candidate for the detection of topological effects with  $A = \text{Bi, Sb}$  (Elements of Group V), and  $B = \text{Te, Se}$  (Elements of Group VI). Later, these compounds were studied confirming the existence of the topological surface states in  $\text{Bi}_2\text{Se}_3$ <sup>12</sup>,  $\text{Bi}_2\text{Te}_3$ <sup>13</sup>, .... Among them,  $\text{Bi}_2\text{Se}_3$  offers the potential topologically protected behavior in ordinary crystals at room temperature, due to the large band gap (0.3 eV)<sup>5</sup>.

$\text{Bi}_2\text{Se}_3$  presents a rhombohedral crystal structure with a space group ( $R\bar{3}m$ ). The unit cell consists of 15 atomic layers as illustrated in Fig 1.7. 5 atomic layers arranged along the Z-axis are known as quintuple layers (QLs) stacked as  $\text{Se}1'-\text{Bi}1'-\text{Se}2-\text{Bi}1-\text{Se}1$ . Two QLs are bound by Van der Waals (VdW) forces, whereas within a QL, intralayers are bonded by strong covalent bonding<sup>4</sup>. A stack of 3 QL forms the unit cell.

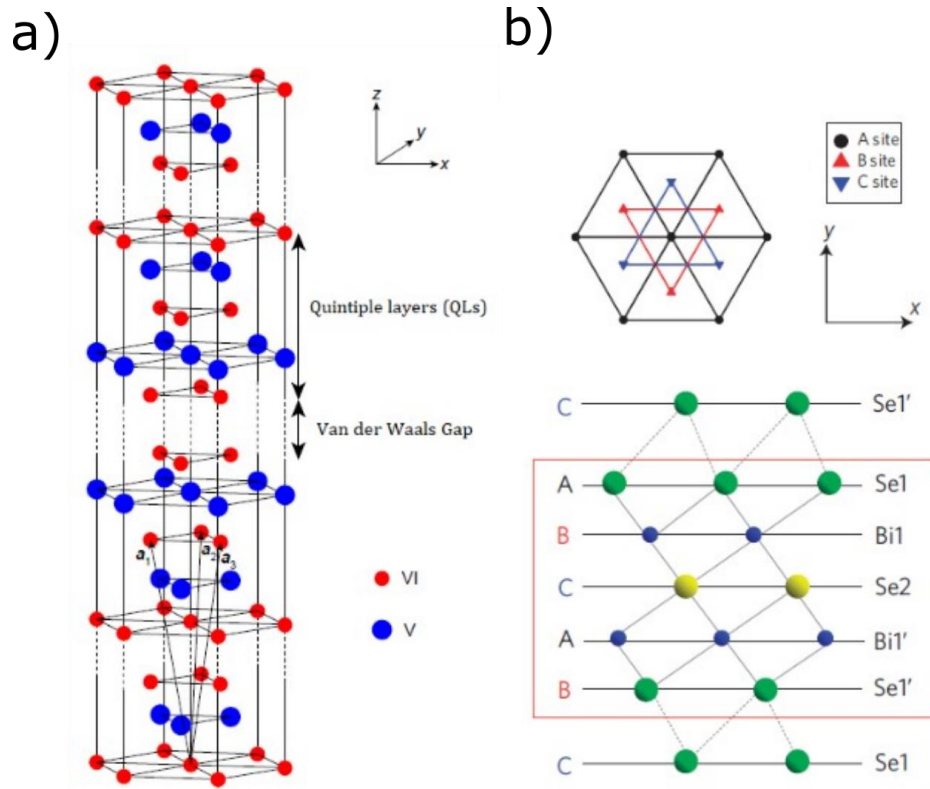


**Figure 1.7** a) Crystal structure of  $A_2B_3$  compounds with primitive vectors ( $a_1, a_2, a_3$ ). b) Illustration of structural organization along the planes YX and ZX of  $Bi_2Se_3$  <sup>12</sup>.

The  $Bi_2Se_3$  band structure is characterized by a large band gap up to 0.3 eV and a robust, almost idealized surface Dirac cone at the  $\Gamma$  point, where the topological surface states are crossing the band gap<sup>4</sup>, see Fig. 1.8 a). The presence of strong spin-orbit coupling, owing to the heavy element Bi, allows the band inversion, splitting the energy levels, and creating the surface states.

Due to the relatively large band gap,  $Bi_2Se_3$  is one candidate suitable for studying the topologically protected states at room temperature ( $k_B T = 25$  meV). Furthermore, the surface states are spin non-degenerate and helically spin polarized. The constant energy contour is nearly spherical, while the spin vector is perpendicular to the wave vector. Similar to a 2D TI, where 2 spin channels with opposite spin and propagation directions are present at the edge, for a 3D TI, two opposite spins propagate in opposite directions on a surface instead of a 1D channel. The relation between the spin and the propagation direction is such that the spin direction lies on the surface, but is perpendicular to the propagation direction, an example of the spin-momentum locking. These properties enable efficient spin manipulation for spintronic applications, by modifying the momentum of the electrons.

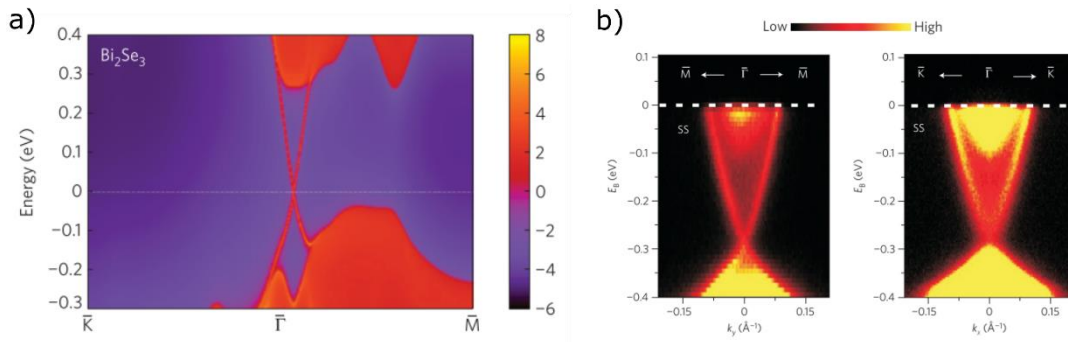


**Figure 1.8** a) Energy and momentum dependence of the local density of states (LDOS) for Bi<sub>2</sub>Se<sub>3</sub>. b) High resolution ARPES measurements of the surface band structure of Bi<sub>2</sub>Se<sub>3</sub>. Edited from <sup>12</sup>.

### 1.2.4. Weak (anti)localization effect

Weak anti-localization (WAL) is a manifestation of the phase coherence of charge carriers in a material with intrinsic spin-orbit coupling in two-dimensions. For systems in the quantum diffusive regime, the electron maintains its phase coherence after being scattered multiple times, since the mean free path is smaller than the phase coherence length. In a closed time-reversed loop (Fig. 1.9 a), a quantum interference of the phase coherence occurs, causing a quantum correction of the conductivity. In TIs, the time-reversed paths interfere destructively, due to the existence of spin-momentum locking. Whenever an electron is scattered its momentum changes and consequently, the spin rotates accordingly. A phase shift of  $\pi$  (Berry phase) occurs when the electron moves along a closed path, which leads to destructive interference with its original position. This destructive interference increases electron delocalization, meaning that the conductivity is enhanced<sup>10</sup>. The application of a perpendicular magnetic field destroys the time-reversal symmetry of the system, and it affects the Berry phase in a way that increases the localization. Therefore, the conductivity decreases sharply, as a cusp, by increasing the magnetic field. This effect is known as the weak anti-localization effect, Fig. 1.9 c). For conventional two-dimensional electron systems with zero Berry phase, a characteristic weak localization is seen instead, as illustrated in Fig. 1.9 b).

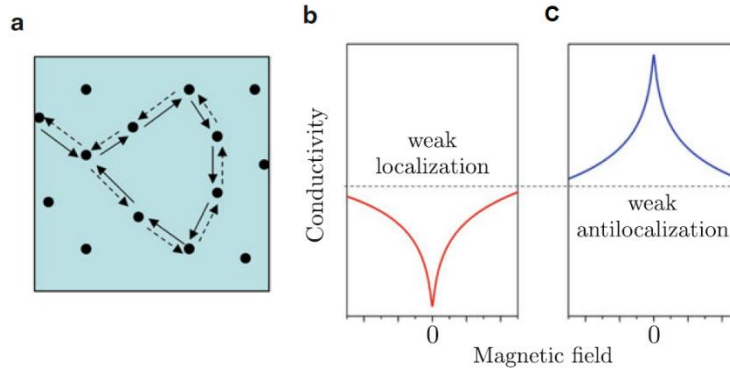


**Figure 1.9** a) Illustration of a close loop of an electron path. b) Positive conductance of weak localization (WL) and c) typical weak antilocalization curve showing a decreasing in the conductance with magnetic field <sup>160</sup>.

At low temperatures, in the quantum transport regime, the WAL manifests itself in magnetoresistance (MR) measurements, as a resistance cusp in low fields. This effect arises in TIs due to the presence of strong spin-orbit coupling in the bulk and 2D Dirac-like physics at the edges. The sharp cusp in the magnetoconductance can be described by the following Hikami–Larkin–Nagaoka (HLN) equation<sup>14</sup>:

$$\Delta G(B) = \alpha \frac{e^2}{\pi h} \left[ \ln \left( \frac{B\phi}{B} \right) - \psi \left( \frac{1}{2} + \frac{B\phi}{B} \right) \right] + \beta B^2 \quad (1.4),$$

where  $G$  is the magneto conductance,  $e$  and  $h$  are the electron charge and Planck constant, respectively.  $B\phi = \frac{\hbar}{4eL_\phi^2}$ , where  $L_\phi$  is the phase coherent length and  $\psi(x)$  is the digamma function.  $\alpha$  “alpha” is the prefactor, a coefficient related to the scattering events that can affect the phase. The value can be either positive for the Weak localization (WL) or negative for the weak antilocalization. For the WAL  $\alpha$  is expected to acquire a value of -0.5 per conductive channel. An ideal TI should hold a prefactor of -1 due to the existence of two decoupled surfaces grasping topological surface states. The  $\beta B^2$  term is representing the magnetic background, being  $\beta$  the quadratic component<sup>14</sup>.

# Chapter 2

## 2. Experimental Techniques

In the following chapter, the experimental setups used here are introduced. Firstly, the molecular beam epitaxy (MBE) is discussed such as all components present in the deposition equipment. *In-situ* characterization is possible by reflection high energy electron diffraction (RHEED). The *ex-situ* characterization techniques applied were X-ray diffraction (XRD), X-ray Reflectivity (XRR), Raman spectroscopy, atomic force microscopy (AFM), magneto-transport measurements, X-ray photoelectron spectroscopy (XPS) and angle-resolved photoemission spectroscopy (ARPES). Finally, the fabrication of the Hall-bar field effect transistors is explained.

### 2.1. Molecular Beam Epitaxy

There are several deposition techniques for the growth of thin films, such as physical vapor deposition, chemical vapor deposition, and molecular beam epitaxy. Molecular beam epitaxy (MBE) presents several advantages, such as a clean growth environment, good controllability, slow growth rates (1 nm/min), easy to dope, and wafer-scale growth, hence allowing the growth of 2D epitaxial materials<sup>15</sup>.

An MBE presents an environment free from contamination due to ultra-high vacuum (UHV) conditions with a low background pressure of  $1 \times 10^{-10}$  mbar and a loading lock pressure of around  $1 \times 10^{-9}$  mbar. Such low pressures are possible due to the combination of a turbo pump, ionic pump, and titanium sublimation pump. Moreover, the low background pressure, in the growth chamber, allows the growth of large-area thin films with good uniformity.

The MBE at INL (Fig. 2.1) (Omicron Nanotechnology EVO-50) has two chambers, the growth chamber, and a loading lock. The latter is used for the storage of substrates before being introduced into the growth chamber, separated by a gate valve. The following elements can be evaporated from the effusion cells: Cu, Bi, Ga, and In. Each element is contained in a non-reactive crucible in Knudsen cells, where a filament surrounding the cell heats the material until it evaporates, creating a molecular beam. The MBE also presents the Se element contained in a valved cracker source. In this case, the Se besides being

evaporated thermally, a cracker at higher temperatures is present to break the large Se molecules into smaller molecules. Subsequently, an adjustable valve is incorporated into the cell, which permits to change of valve aperture from 0 to 5 mm, and consequently changes the Se flux without changing the cell temperature. A beam flux monitor is installed into the system. This movable equipment can be placed directly below the substrate to measure the beam equivalent pressure (BEP) or element fluxes to control the growth rate and the stoichiometry of the deposited compound. Moreover, the substrate holder can be rotated to provide good uniformity throughout the substrate, which can be heated to very high temperatures (max 1000 °C). Finally, an *in-situ* RHEED<sup>16</sup> system is also installed to supply real-time information about the growth, such as crystal structure, and growth rate, as explained in section 2.1.1. The MBE provides good control and high-quality growth of thin films due to the accurate thickness, slow growth rate, and controllable stoichiometry by adjusting the cell temperature. The growth parameters for optimized Bi<sub>2</sub>Se<sub>3</sub> were studied in the initial part of the thesis.

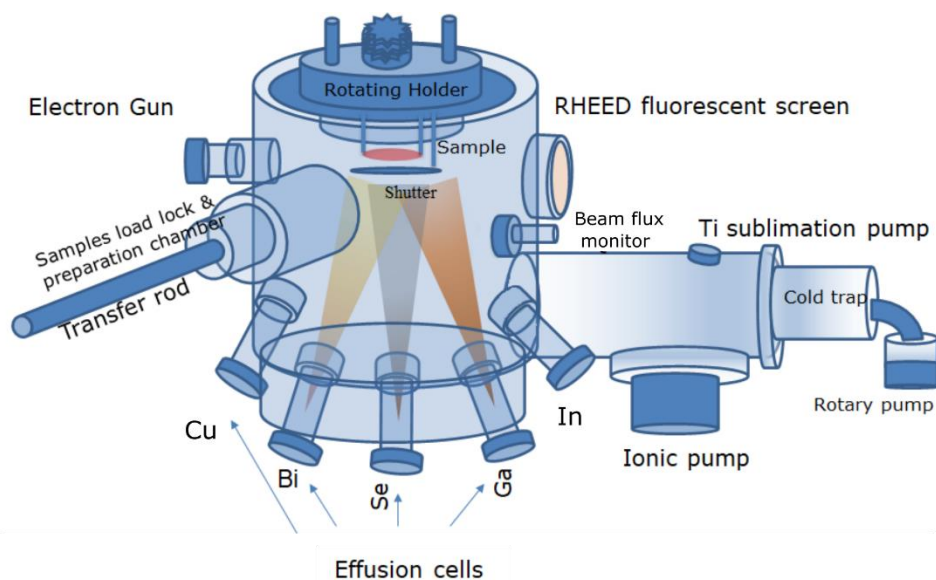


**Figure 2.1** MBE diagram showing the growth chamber. This chamber is equipped with 4 Knudsen cells with Cu, Bi, Ga, and In and a valved cracker cell for Se. The system is also equipped with a RHEED and a beam flux monitor.

## Epitaxy

MBE allows a slow rate, enabling the epitaxial growth of 2D materials, meaning that the growth material orientation is well-defined concerning the substrate surface, resulting in a single-crystal material<sup>15</sup>.

The element flux is controlled by the effusion cell temperature, which either sublimates or evaporates the atoms/molecules of specific elements with low kinetic energy. The growth is dominated by the kinetic energy at the substrate material (substrate temperature). Atoms reaching the surface of the crystal substrate, adatoms, are weakly

bonded to it. They reach with an energy that allows them to move freely parallel to the plane surface to the energetically favorable site of the layer. At this point, they bound and become energetically stable and act as nucleation centers.

There are three distinct growth modes, as presented in Fig 2.2, the Volmer-Weber, the Frank-van der Merwe, and the Stranski-Krastanov<sup>17</sup>. These growth modes are dependent on the interface energies and lattice mismatch. However, in lattice-matched systems, the growth modes are mainly dependent on the interface and surface energies.

The Volmer-Weber growth (island growth) (Fig. 2.2 a) takes place as an agglomeration of adatoms in a preferential region on the sample, because the sum of the epilayer surface energy and the interface energy is higher than the energy of the substrate surface, and consequently this nucleation results in 3D islands. On the other hand, Frank-van der Merwe (layer-by-layer) (Fig. 2.2 b) occurs when the energy of the substrate surface is higher, hence the material can be seen as a wet deposition, and a layer-by-layer growth occurs. Finally, the last mode called Stranski-Krastanov, is a mixture of the two previous modes with 2D layers and 3D islands (Fig. 2.2 c), due to a strained epilayer energy with small interface energy.

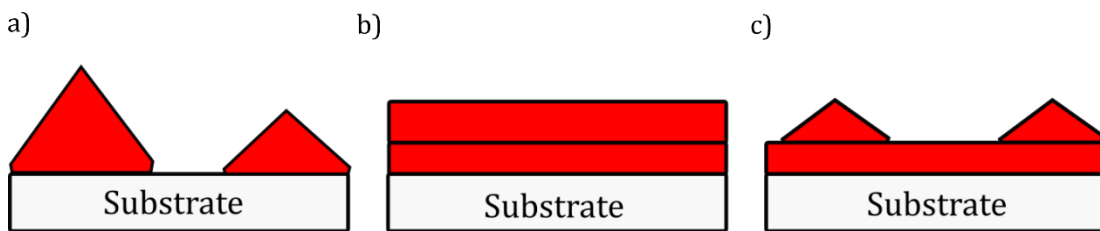


**Figure 2.2** Illustration of the three main growth modes a) Volmer-Weber (Island growth), b) Frank-van der Merwe (Layer-by-layer), and c) Stranski-Krastanov.

As introduced in section 1.2.3, the topological insulator studied in the current thesis consists of the  $A_2B_3$  family TI. This family consists of Van der Waals layers stacked by Van der Waals forces. The growth of these materials (Van der Waals) can be understood as layer-by-layer growth (Fig. 2.2 b). Due to the weak bonding of these materials to the substrate through Van der Waals forces, a distinct gap forms. This unique growth characteristic allows for layer-by-layer growth, where each subsequent layer retains structural information from the preceding layer (epitaxial).

### Defects

Besides the growth temperature, the substrate surface roughness, lattice mismatch, and other parameters also influence the growth of these thin films, which play an important role in defect minimization. Lattice mismatch is one of the most important factors for the growth of those materials because if the substrate lattice parameter is significantly different from the material lattice parameter, it leads to stress in the thin film. The stress stimulates the formation of defects. As the film is deposited, the formation of defects can accumulate, and consequently, decrease the material quality.

A variety of structural defects exists, such as stacking faults, twin defects, antiphase domain boundaries, point defects, and mosaicity-tilt(twist). As illustrated in Fig 1.7, the stacking sequence of the  $\text{Bi}_2\text{Se}_3$  in the growth direction would be  $ABCABC$ , with a rotation of  $120^\circ$  to the previous layer. A stacking fault occurs when a layer is removed or added, leading to a sequence e.g.,  $ABCBCABC$  or  $ABCABBC$  (FIG 2.3a). Studies have shown that stacking faults can be responsible for shifts of the Dirac point concerning the pristine band structure<sup>15</sup>. Twin defects occur when two different domains meet, where the stacking sequences are different (Fig 2.3 b). This effect can be in-plane (horizontal twinning) or in the growth direction (vertical twinning). Due to the higher surface/thickness ratio, the probability of an in-plane twinning is larger than a vertical twinning. It can be seen as a triangular rotation between two different domains. Details about the reduction of twinning are studied in Chapter 3.

Finally, point defects are characteristic of single atoms in the lattice sites. There are three types of point defects as shown in Fig. 2.3 c). 1) There are interstitial defects by the nucleation of atoms inside the crystal structure randomly, not adapting to a site of the crystal. 2) If the defect is replacing an element in the lattice, it is called a substitutional defect. In some cases, these defects are introduced on purpose to study doping in the material. 3) In case an element is missing in the site it is called a vacancy.

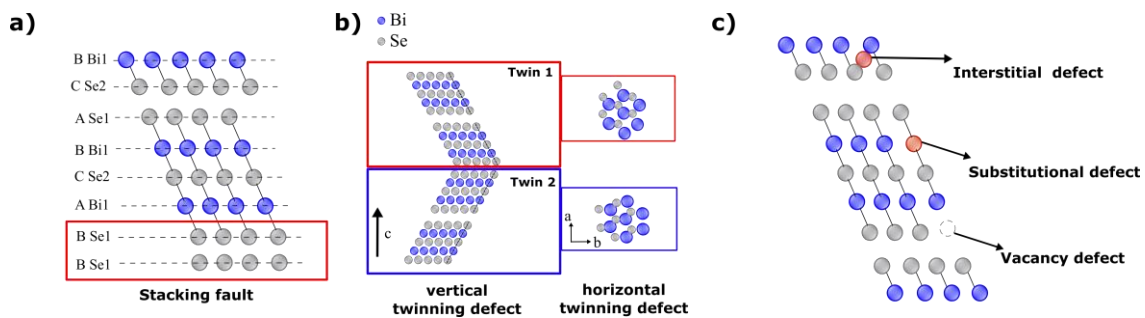


**Figure 2.3** Defect representation of a) Stacking fault, b) twin defects (vertical and horizontal), and c) point defects with the representation of interstitial, substitutional and vacancy defects.

### Preparation of substrates and growth procedure

Before the 2D material growth, we subjected the substrate to specific annealing steps and surface treatments.  $\text{Bi}_2\text{Se}_3$  and  $\text{In}_2\text{Se}_3$  are the 2D materials deposited during the presented thesis. The growth of these materials was optimized on c-oriented (0001) sapphire substrates ( $\text{Al}_2\text{O}_3$ ) due to the similar lattice parameter with a lattice mismatch percentage of 15%<sup>15</sup>. The substrate is a 2-inch wafer with a thickness of 0.43 mm and a maximum miscut of  $0.2^\circ$ , purchased from University Wafer.

Prior to the material deposition, the substrates are introduced in the UHV system, where they undergo an annealing process at  $900^\circ\text{C}$  for 45-60 minutes, to remove all contaminations on the substrate surface.

The  $\text{Bi}_2\text{Se}_3$  growth procedure optimization is studied in Chapter 3. Bi is evaporated with a cell temperature of  $535^\circ\text{C}$ , with a Se cell temperature of  $285^\circ\text{C}$  and a Se valve aperture of 2 mm (BEP =  $1 \times 10^{-5}$  mBar). The Se source also presents a cracker at  $900^\circ\text{C}$  to break the large Se molecules into smaller molecules, hence improving the reactivity of the Se atoms. The  $\text{Bi}_2\text{Se}_3$  growth rate ranges between 1-1.4 nm/min. The Bi cell temperature used for the first growth was around  $520^\circ\text{C}$ . After a stabilization of over 5 growths, it was necessary to increase the Bi cell temperature to maintain the growth rate. In Chapter 3, the Bi cell temperature was  $520^\circ\text{C}$ , which was increased to  $535^\circ\text{C}$  in Chapter 4 and forward. Each element flux is measured by a Bayard-Alpert pressure gauge, beam equivalent pressure (BEP) in front of the substrate. The BEP can be different each growth day which might lead to a small variation in the growth rate.

The  $\text{In}_2\text{Se}_3$  layer is introduced in Chapter 3 for the implementation of a buffer layer. The growth of  $\text{In}_2\text{Se}_3$  is of considerable difficulty due to the large phase variety ( $\text{InSe}$ ,  $\gamma\text{-In}_2\text{Se}_3$ ,  $\alpha\text{-In}_2\text{Se}_3$ , ...) with different crystal forms. Marcel Claro et al. developed the optimization of the  $\beta\text{-In}_2\text{Se}_3$  growth by controlling the substrate temperature ( $550^\circ\text{C}$ ) and the Se valve aperture 5 mm (BEP =  $2.5 \times 10^{-5}$  mBar)<sup>18</sup>. The In and Se cell temperatures are  $740^\circ\text{C}$  and  $285^\circ\text{C}$ , respectively, leading to a growth rate of 1.2 nm/min.  $\beta\text{-In}_2\text{Se}_3$  resembles the crystal structure of  $\text{Bi}_2\text{Se}_3$  with a similar lattice parameter<sup>18</sup>. Furthermore,  $\beta\text{-In}_2\text{Se}_3$  is a semiconductor material with a 1.38 eV band gap which acts as an insulating material without contributions to the  $\text{Bi}_2\text{Se}_3$  transport properties when in contact.

### 2.1.1. In-situ characterization

#### Reflection high-energy electron diffraction (RHEED)

The growth of epitaxial materials by MBE is commonly monitored by in-situ characterization techniques, such as reflection high-energy electron diffraction (RHEED) to provide good material quality. RHEED is a surface-sensitive technique that offers information about the crystal structure. Fig. 2.4 illustrates the configuration of a RHEED system. It consists of an electron gun to generate a flux of high-energy electrons, which can range between 5-100 keV. Electrons hit the sample at grazing angles ( $1\text{-}5^\circ$ ), which only allows them to interact with the topmost surface layer of the sample. The beam is deflected from the sample surface, and it creates a pattern on a fluorescent screen. Additionally, a rotation stage for the sample is required to allow the azimuthal rotation of the sample for the visualization at different azimuthal directions.

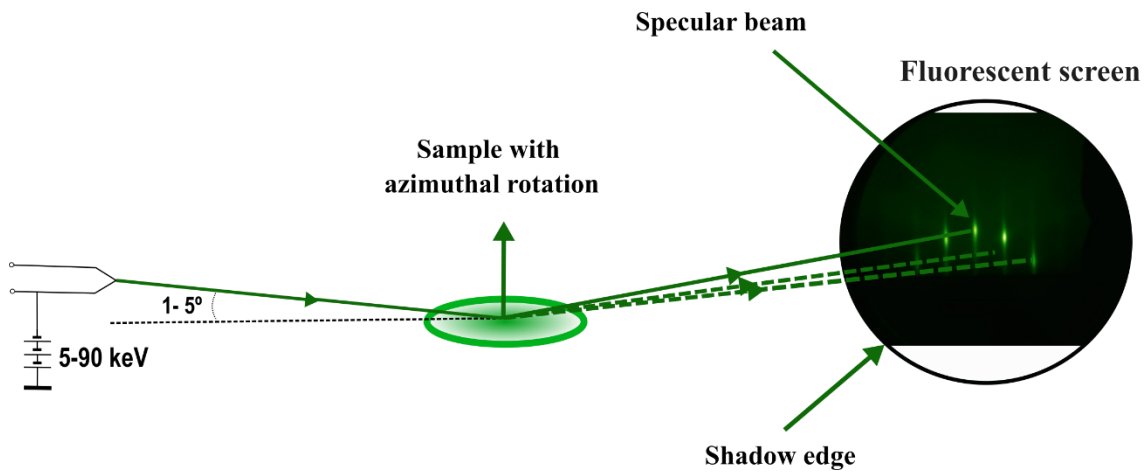


**Figure 2.4** Schematic configuration of a RHEED setup.

The Ewald sphere is used to understand the diffraction pattern (Fig 2.5 a). The atoms arranged in the real space are transformed into perpendicular reciprocal planes. The intersection of these planes with the Ewald sphere creates a pattern that is observable on the fluorescent screen. Fig 2.5 b) illustrates possible configurations of realistic surface constructions and their respective RHEED pattern. This information is important for section 4.2.1. For a flat and perfect single crystalline surface, the electron beam diffracts into spots. However, imperfections and the formation of small domains generate an elongation of the spots into streaky lines. On the other hand, if the surface is not flat, e.g. island growth, a regular spot pattern is formed. Finally, if the sample is not a single crystal and presents some polycrystallinity, this leads to the formation of concentric rings.

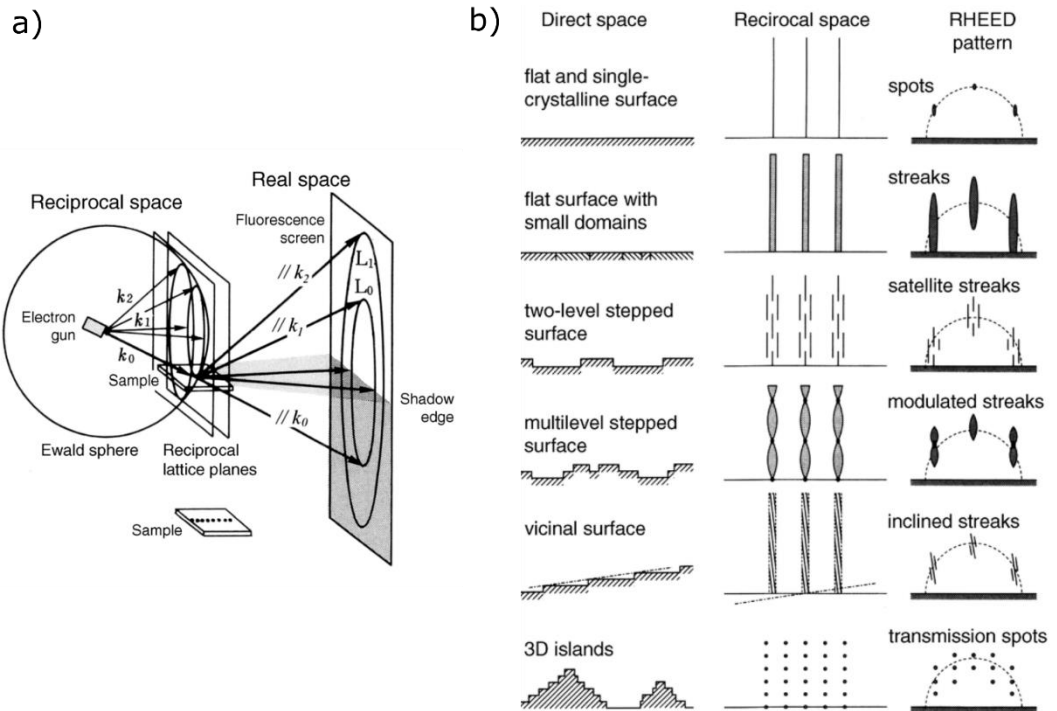


**Figure 2.5** a) Reciprocal space and real space of a RHEED. Reciprocal space presents the Ewald sphere construction. b) Schematics of different types of realistic surface growth and correspondent reciprocal space and their RHEED pattern<sup>34</sup>.

RHEED is also used to monitor the growth in real-time of thin films by measuring the oscillations of the reflection intensity. The oscillations can be used to calculate the growth rate of different materials because a monolayer deposition ( $\theta=1$ ) represents a period oscillation as illustrated in Fig. 2.6.

A KSA from STAIB Instruments is used. The system was operated at a filament current of 1.54 A and accelerating voltages of 15 keV. The RHEED pattern was recorded by a camera.

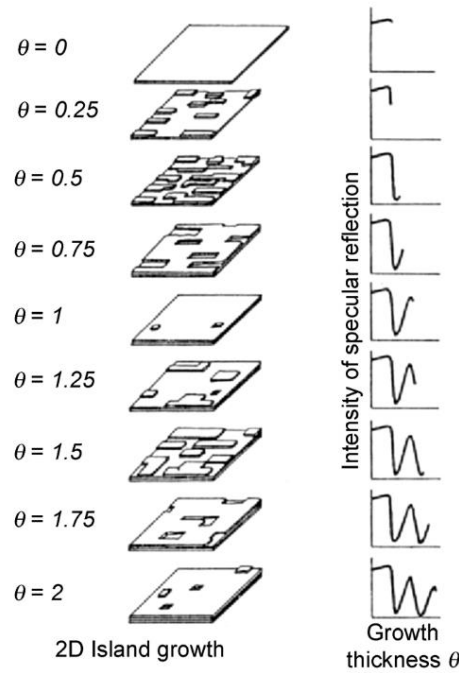


**Figure 2.6** RHEED intensity oscillation and crystal growth monitor.  $\theta$  represents the percentage of the monolayer growth.  $\theta=1$  represents 1 monolayer and  $\theta=1.5$  represents 1 monolayer and half growth of the following<sup>34</sup>.

## 2.2. Ex-situ characterization

### 2.2.1. X-ray diffraction

X-ray diffraction (XRD) is a common characterization technique used to identify crystal structure, its lattice parameters, material phase, and orientation. The crystal structure study is possible due to the similar range of X-ray wavelength and the inter-atomic distances from the crystal structure, as illustrated in Fig 2.7 a). When an X-ray beam hits a crystalline material, it can be reflected from the material crystalline plane, and consequently interfere with the X-ray beam reflected in the material surface. This process is called diffraction. We have a constructive interference if Bragg's law is satisfied.

$$2d_{hkl} \sin \theta = n\lambda \quad (2.1)$$

where  $d_{hkl}$  is the inter-atomic distance between two planes,  $\theta$  is the incident angle, and  $\lambda$  is the X-ray wavelength. A schematic configuration of the XRD can be seen in Fig. 2.7 b).

Single crystals and epitaxial materials can be identified by XRD, due to the existence of only one set of parallel planes to the surface of the material. These types of materials should present all peaks of the same family (00n, nnn, etc) in the Bragg-Brentano configuration geometry. Epitaxial thin films require different mode XRD geometries for the in-plane lattice

information. In addition to the  $\theta$  angle,  $\omega$ ,  $\varphi$ ,  $\psi$ , and  $\chi$  (Fig 2.7 b) angles are also variable. A  $\varphi$  scan is used to have in-plane information by fixing a  $\omega$ ,  $\theta$  and  $\chi$  correspondent to a diffracted plane (hkl), with  $h/k \neq 0$  such as the (015) plane. The  $\varphi$  scan is performed by an azimuthal rotation and registers the diffracted intensity. This mode has information about the crystal symmetry, and it can be implemented to study twinning defects.

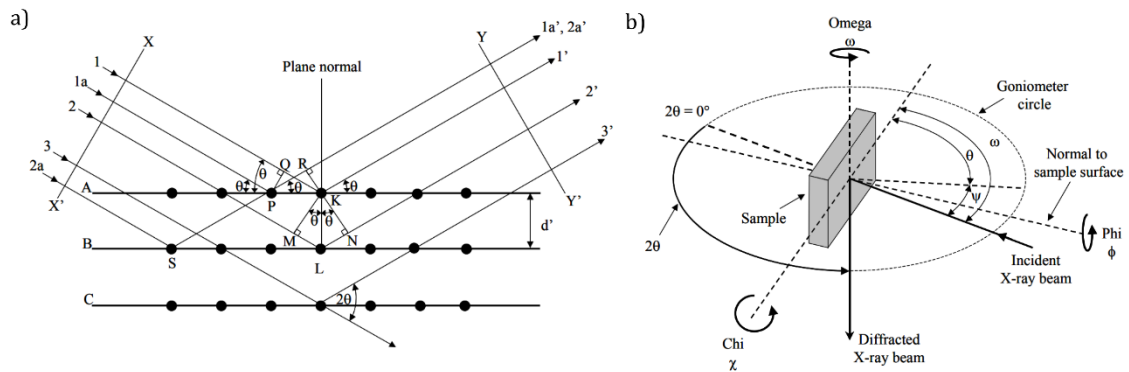


**Figure 2.7** a) Inter-atomic planes with diffraction by the crystal structure. b) Angles and axes relevant for all XRD measurement modes <sup>161</sup>.

A PANalytical X'Pert system was used to perform the XRD measurements, using a wavelength of 1.54 Å. The Bi<sub>2</sub>Se<sub>3</sub> lattice parameter  $c$  was calculated with the simplified Eq. (2.2) for a hexagonal crystal structure:

$$\frac{1}{d^2} = \frac{4}{3} \left( \frac{h^2 + hk + k^2}{a^2} \right) + \frac{l^2}{c^2} = \frac{4}{3} \frac{l^2}{c^2} \quad (2.2)$$

### Reflectivity

X-ray studies also offer the mode of X-ray reflectivity (XRR) used on flat materials to obtain information about the thickness, roughness, and density of the film. Similar to XRD, an X-ray beam hits the sample at grazing angles, which creates a specular reflected wave. When the incident angle is higher than the critical angle ( $\theta_c$ ) the beam penetrates the material. XRR is focused on the interference at grazing angles which leads to periodic oscillation about the Fresnel reflectivity. Fig. 2.8 explains these oscillations and the respective information acquired.

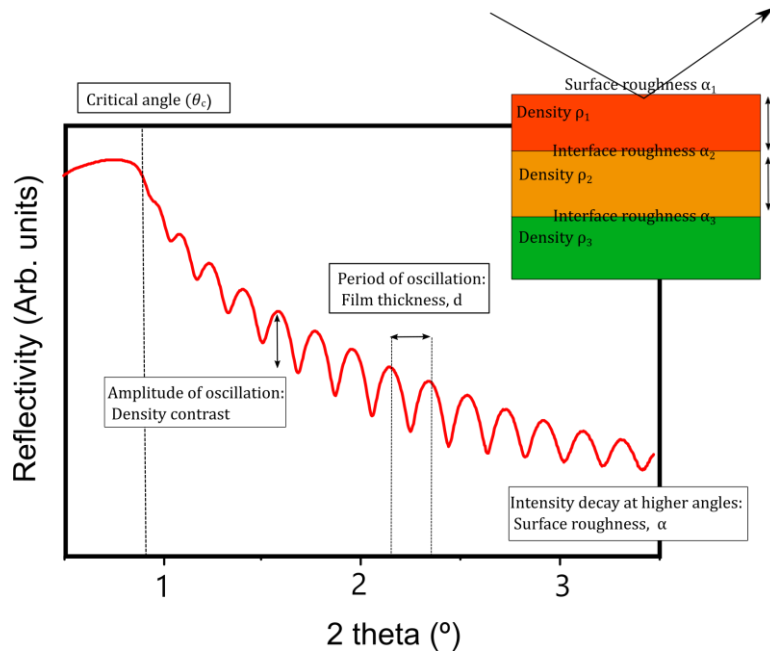


**Figure 2.8** Periodic oscillations observed in an XRR scan and information profile.

The reflectivity oscillation period is linked to the thickness of the thin layer, which allows us to estimate the thickness of thin films. The signal amplitude provides information about the materials density, between the thin film and the substrate. Finally, the roughness affects the rate as the oscillation decreases in intensity. Larger roughness leads to a faster decay rate of the reflectivity signal. In case we have more than one layer, the interface roughness also affects the oscillation decay rate. The film thickness can be calculated with the following formula:

$$d = \frac{\lambda}{2(\theta_2 - \theta_1)} \tag{2.3}$$

where  $\theta_1, \theta_2$  are two consecutive angular positions of maximum or minimum peaks. The fitting analysis of XRR data was achieved by the software REFLEX<sup>19</sup> to obtain an approximate value of the thickness and roughness.

### 2.2.2. Raman spectroscopy

Raman spectroscopy is a characterization technique to study the vibrational modes of molecules, which permits the extraction of structural information from the material. Raman spectroscopy relies on the measurement of inelastic scattered photons. The vibrational mode of the molecule affects its polarizability. The incident radiation interacts with the polarizability, inducing a dipole moment in the material. This induces the emission of characteristic radiation through the scattering of the incident radiation. Raman scattering

produces two signals, Anti-Stokes and Stokes, symmetrically shifted in frequency relative to the excitation light. The frequency shift correlates directly with the vibrational frequency of the crystal.

The analysis was performed by a confocal Raman microscopy system (WITec alpha300 R) equipped with an optical microscope. The laser wavelength was 532 nm and the power of approximately 0.8 - 2 mW to prevent sample damage. The grating line is 1800 g/mm and the CCD resolution of  $0.1 \text{ cm}^{-1}$ .

### 2.2.3. Atomic Force Microscopy

Atomic force microscopy (AFM) is a surface topography mapping technique that allows studying the morphology, growth modes, and surface roughness. A sharp tip supported at the end of a cantilever is used to scan the material surface by measuring the deflection of the cantilever. The beam laser that is reflected in the cantilever moves accordingly and the deflection movement is measured by photodiodes. The tapping mode focuses on a resonance frequency oscillation by a piezoelectric that slightly taps the sample. The force between the sample surface and the tip creates a modulation of the oscillation amplitude, and consequently, a 3D image of the material surface topography is obtained. A configuration of an AFM system can be illustrated in Fig 2.9. The data analysis to obtain the roughness and morphological line profile is obtained with the Gwydion software.

The measurements are performed by a Bruker Dimension AFM in tapping mode.

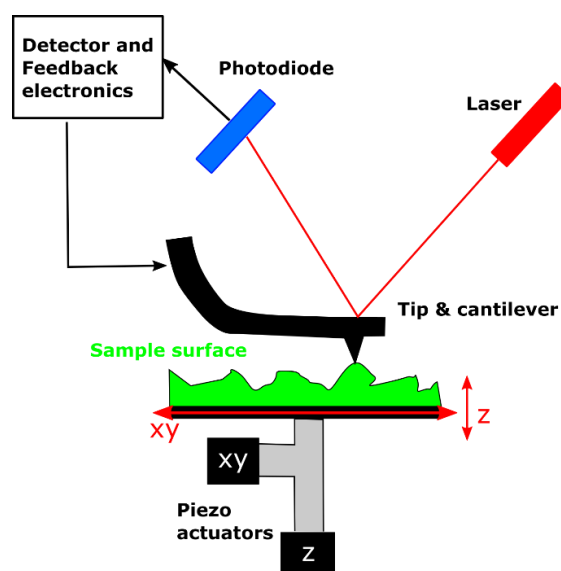


Figure 2.9 Schematic diagram of an atomic force microscope (AFM) setup.

## 2.2.4. Magneto-transport measurements

To analyze and investigate the electrical and transport properties of topological insulators, magneto-transport measurements are used. Through a variation of the magnetic field at cryogenic temperatures it is possible to obtain topological information. Furthermore, variation in the resistance due to magnetic fields is a crucial characterization for topological insulators to investigate electrical transport.

### Geometries

There are two main geometries for these measurements, Van der Pauw and Hall-bar. Both of them were implemented throughout the thesis. Fig. 2.10 shows an example of both geometries. The van der Pauw geometry (Fig. 2.10 a and c) permits the measurement with a smaller preparation time by soldering small indium pellets on top of the material. The Hall-bar geometry (Fig. 2.10 b and d) was implemented by a cleanroom fabrication process, which is explained in section 2.3. This geometry provides a more reliable measurement due to the elimination of contact asymmetries.

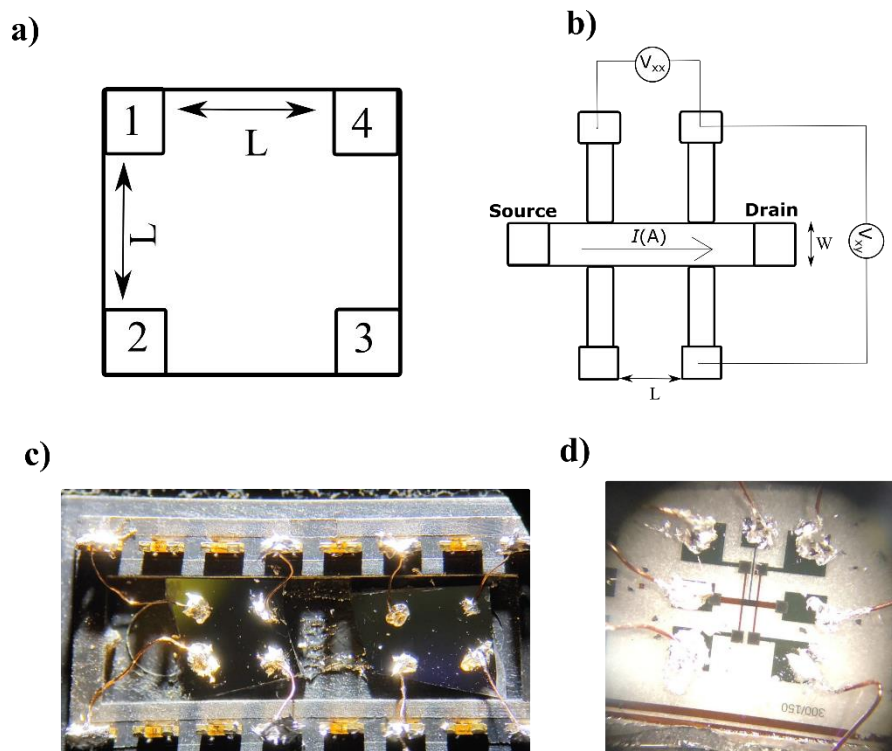


**Figure 2.10** a) Van der Pauw geometry. b) Hall-bar geometry with visualization of measured contacts. c) Example Van der Pauw geometry as realized for a  $Bi_2Se_3$  sample. d) Hall-bar example.

### Van der Pauw geometry

For a Van der Pauw geometry 4-point contacts ( $V_1, V_2, V_3, V_4$ ) are considered, where the respective resistances  $R_A$  and  $R_B$  can be given by:

$$R_A = \frac{1}{2} \left( \frac{V_{43}}{I_{12}} + \frac{V_{12}}{I_{43}} \right) \quad (2.4),$$

$$R_B = \frac{1}{2} \left( \frac{V_{14}}{I_{23}} + \frac{V_{23}}{I_{14}} \right) \quad (2.5),$$

The sheet resistance ( $R_S$ ) and the resistivity ( $\rho$ ) are then calculated as follows:

$$e^{\left(\frac{-\pi R_A}{R_S}\right)} + e^{\left(\frac{-\pi R_B}{R_S}\right)} = 1 \quad (2.6),$$

$$\rho = R_S t \quad (2.7),$$

where  $t$  is the thin film thickness.

### Hall Effect

The transport properties, such as electron concentration and electron mobility, are measured by applying a magnetic field. The magnetic field moves the charged particles perpendicularly both to the field and velocity vector (Lorentz Force). The transverse charge accumulation results in a Hall voltage ( $V_H$ ). The electron concentration ( $n_{2d}$ ) and the mobility ( $\mu$ ) are determined as follows:

$$n_{2d} = \frac{|\vec{B}|I}{e|V_H|} \quad (2.8),$$

$$n_{3d} = \frac{n_{2d}}{t} \quad (2.9),$$

$$\mu = \frac{1}{e n_{2d} R_S} \quad (2.10),$$

Where  $V_H = \frac{(V^{+24} - V^{-24}) + (V^{+42} - V^{-42}) + (V^{+13} - V^{-13}) + (V^{+31} - V^{-31})}{8}$ . The magnetic field is applied in different directions ( $V^+$  and  $V^-$ ) to obtain a higher resolution of the Hall voltage.

### Hall-bar geometry

For the Hall-bar geometry, a different approach can be implemented to calculate the transport properties. As illustrated in Fig. 2.10 b), the current is applied along the source-drain channels. Two different voltages are measured,  $V_{xx}$  and  $V_{xy}$  to obtain the  $R_S$  as follows:

$$R_s = \left(\frac{V_{xx}}{I}\right) \frac{W}{L} \quad (2.11 \text{ a}),$$

$$R_{xy} = \left(\frac{V_{xy}}{I}\right) \quad (2.11 \text{ b}),$$

The electron densities for the Hall-bar geometry were calculated by a linear fitting of the Hall resistance as a function of the magnetic field:

$$n_{2D} = \frac{1}{\left(\frac{\partial R_{xy}}{\partial B}\right)e} \quad (2.12),$$

The equipment used is a Teslatron at the Universidad de Salamanca (through a collaboration). It allows the application of a perpendicular magnetic field to study transport measurements, in a temperature range of 1.5 - 300 K and with magnetic fields up to 10 T. The measurements are performed by a standard lock-in technique with frequencies of 10-20 Hz and a driving current of 0.5  $\mu\text{A}$ , which keeps low heating and good signal detection. All signals proceeded under a low-pass filter in order to minimize the high-frequency noise.

## 2.2.5. X-ray photoelectron spectroscopy

X-ray photoelectron spectroscopy (XPS) is a surface-sensitive technique that relies on the photoelectric effect to obtain quantitative composition and chemical information. The sample is subjected to electromagnetic X-ray radiation. Due to the photoelectron effect, photoelectrons are excited from the material. The kinetic energies of these photoelectrons are measured by a hemispherical analyzer as follows:

$$E_{kin} = h\nu - \phi - E_{bin} \quad (2.13),$$

Where  $h$  is Planck's constant,  $\nu$  is the radiation frequency,  $\phi$  is the work function of the detector, and  $E_{bin}$  is the binding energy characteristic of the element present in the sample. The binding energy of each element is unique and depends on the chemical bond to the neighbor atom. Thus, it is possible to identify the elements and chemical compounds. An XPS measurement consists of the collection of these photoelectrons from the spectrometer, based on Eq. 2.13, the spectra show a signal of the photoemission intensity as a function of the binding energy. A schematic diagram of an XPS system is shown in Fig. 2.11.

The XPS system used in this work is an ESCALAB250Xi UHV system (Thermo Fisher Scientific). The samples are treated with a plasma of  $\text{Ar}^+$  ions for 2 min to etch any surface oxides. The atomic composition quantification is performed by a fitting of the element peak by a Voigt function and the detection of the signal baseline. The software Avantage (Thermo Fisher Scientific) provides a quantification by the integration of each peak area and the sensitivity factor provided by the Avantage library.

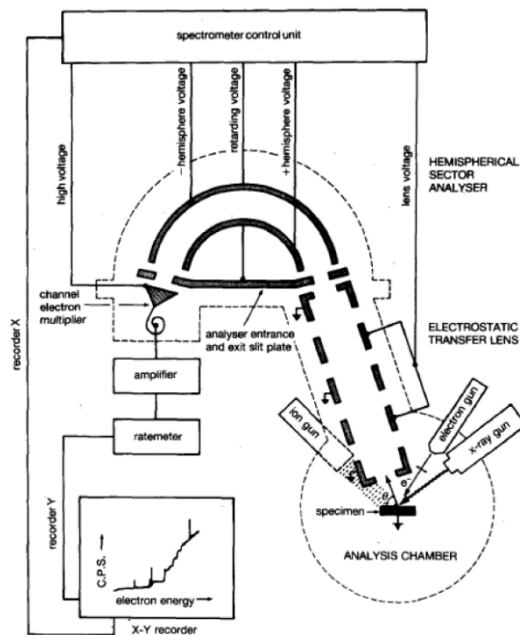
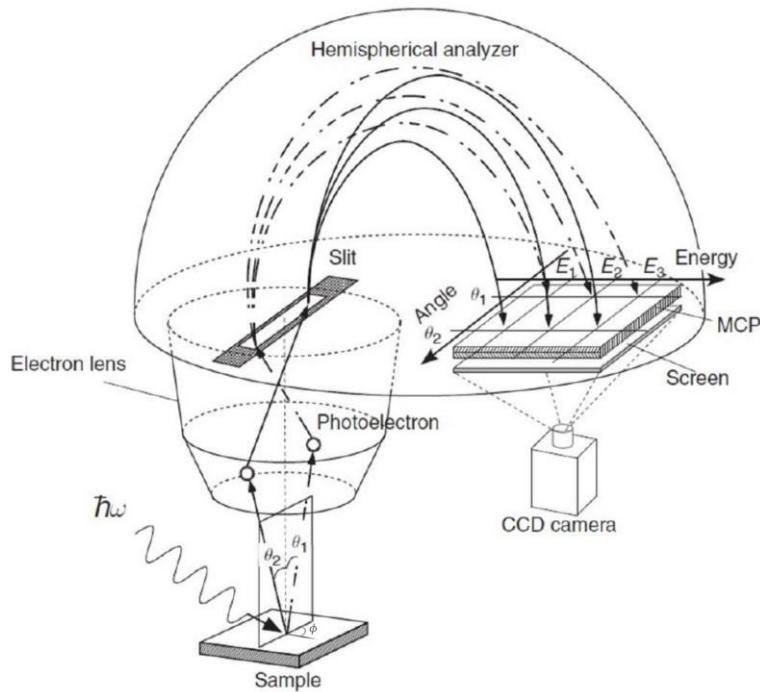


Figure 2.11 Schematic diagram of an XPS instrumentation setup <sup>162</sup>.

### 2.2.6. Angle-resolved photoemission spectroscopy

Angle-Resolved PhotoEmission Spectroscopy (ARPES) is a characterization technique based on the same principle as XPS, the photoelectric effect. The electronic energy states are studied based on Eq. (2.13), similarly to XPS, with an incorporation of precise measurements of the electron angular distribution. The electron propagation angles ( $\theta$ ,  $\phi$ ), (Fig 2.12) carry the information of the electron momenta, which is also connected to the material momentum due to the conservation of momentum laws <sup>20</sup>. The electron energy and angle provide information about the material energy and momentum space, and thus a band dispersion is obtained  $E(k)$ .



**Figure 2.12** Illustration of ARPES geometry experiment with a hemispherical analyzer in angular mode. Adapted from <sup>20</sup>.

ARPES starts with a light source with enough energy, typically 20-40 eV, to overcome the work function. Electrons are emitted and collected by electron lenses which collimate the electrons. The slit is used to select the angular ratio of electrons. The hemispherical analyzer can select the specific range of energies by a capacitor voltage. Electrons are then detected by the detector in the multi-channel plate (MCP). The electron position detected by the MCP is transformed into momentum as a function of the angles by the following relations:

$$k_x = \frac{1}{\hbar} \sqrt{2mE_{kin}} \sin \theta \cos \phi \quad (2.14),$$

$$k_y = \frac{1}{\hbar} \sqrt{2mE_{kin}} \sin \theta \sin \phi \quad (2.15),$$

$$k_z = \frac{1}{\hbar} \sqrt{2mE_{kin}} \cos \theta \quad (2.16),$$

Where  $m$  is the electron mass and  $\theta$ ,  $\phi$  are the polar and azimuthal emission angles, respectively. The photoemission process conserves the momentum, thus the in-plane parallel momentum can be written as:

$$k_{||} = \frac{1}{\hbar} \sqrt{2mE_{kin}} \sin \theta \quad (2.17),$$

For 2D materials, as our topological insulators, the perpendicular dispersion ( $k_z$ ) can be negligible. Therefore, the electronic dispersion can be determined according to  $k_{||}$ .

Topological insulators can be compared to semiconductors because the band gap is small to create few electrons in the lowest or highest bands. The unoccupied band is called the conduction band ( $CB$ ), and the occupied band is called the valence band ( $VB$ ). These band dispersions can be approximated as parabolic bands as:

$$CB(k) = E_c + \frac{\hbar^2 k^2}{2m_c} + R_{ha} k \quad (2.18),$$

$$VB(k) = E_v - \frac{\hbar^2 k^2}{2m_v} + R_{ha} k \quad (2.19),$$

Where  $E_c$  and  $E_v$  are the conduction band minimum and valence band maximum, respectively.  $m_c$  and  $m_v$  are the correspondent electron conduction mass or electron valence mass. Finally, an additional parameter, the Rashba effect contribution ( $R_{ha}$ ), is characteristic of topological insulators, due to the presence of spin-orbit coupling that splits the bands, known as the Rashba splitting. This effect was visually more pronounced for the valence band here, meaning that this contribution is adjusted only for the valence band.

Another characteristic property of topological insulators is the formation of surface states like Dirac cones. These surface states can also be approximated as a massless Dirac fermion in 2D systems as the Dirac cone equation ( $E_D$ ):

$$E_D(K) = D_p \pm \hbar V_F |k| \quad (2.20),$$

Where,  $D_p$  is the Dirac point and  $V_F$  is the electron Fermi velocity. Furthermore, the energy dispersion obtained here is fitted with the previous equations to achieve approximated values for the fermi velocities, electron masses, and band positions.

Additionally, the surface charge carrier density ( $n_s$ ) can be estimated from the Fermi vector ( $k_F$ ) established in the ARPES measurements<sup>21-23</sup> :

$$n_s = \frac{\pi}{(2\pi)^2} k_F^2 \quad (2.21),$$

The Fermi level is determined by the Fermi-Dirac distribution. The Fermi vector is calculated as observed in Fig 2.13. Electrons occupy the area in the reciprocal space from the lowest energies up to the highest energy, the Fermi level ( $E_F$ ).

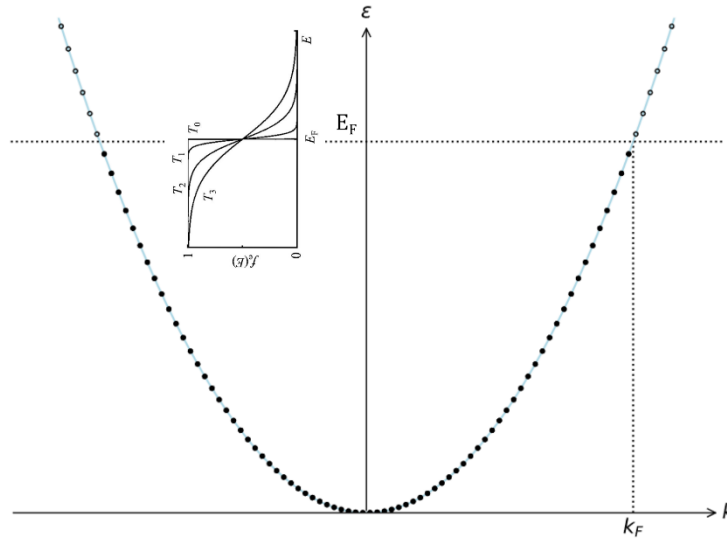


**Figure 2.13** Illustration of the energy dispersion relation in 1D representing the Fermi level with the corresponding Fermi vector. The Fermi-Dirac distribution for the concept of the Fermi level energy position is observed at the Fermi level.

Where the Fermi-Dirac distribution is characterized by  $f(E) = \frac{1}{e^{(E-E_F)/k_B T} + 1}$ .

All ARPES data in the thesis presented were acquired at the ALBA Synchrotron in Barcelona at the LOREA beamline through the grant “AV-2023027322”. LOREA presents an MBS A-1 hemispherical analyzer with a linear polarization and photon energies ranging between 15 - 40 eV with the optimal condition found to be 18 eV<sup>24</sup>. The source is an Apple II with a photon flux of approximately  $10^{12}$  photons/s and a spot size at the sample of  $50 \times 25 \mu\text{m}^2$ . The measurements were performed at a base temperature of 12 K and a base pressure of  $10^{-11}$  mbar. The ARPES data is analyzed using a custom Python script to generate ARPES images and to apply the fitting models (Annex S4).

## 2.3. Device fabrication

In this section, the cleanroom Hall-bar fabrication process to study the electrical and transport properties is presented. Moreover, by deposition of a dielectric material on top of the  $\text{Bi}_2\text{Se}_3$  channel with a metallic contact (gate), we formed an electrostatic gate to tune the  $\text{Bi}_2\text{Se}_3$  Fermi level position. This device can be understood as a field effect transistor (FET).

## Solid gate field effect transistor

$\text{Bi}_2\text{Se}_3$  is deposited on sapphire substrates ( $\text{Al}_2\text{O}_3$ ) by an MBE following the methods described in section 2.1. Different  $\text{Bi}_2\text{Se}_3$  thicknesses are used depending on the application of the device. On top of the  $\text{Bi}_2\text{Se}_3$  layer, a 40 nm capping layer of  $\beta\text{-In}_2\text{Se}_3$  is deposited to act as a protective layer (capping layer).  $\text{Bi}_2\text{Se}_3$  is prone to Se vacancy formation that leads to n-type degeneracy and exposure to air leads to an oxygen diffusion that increases the n-type degeneracy. Our work led to the conclusion that  $\beta\text{-In}_2\text{Se}_3$  can be used effectively as a capping layer with an insulating/semiconductor electrical contribution (Chapter 6). The  $\text{Bi}_2\text{Se}_3$  is the only layer with an electrical contribution for the electrical and transport characterization.

The samples are removed from the MBE system to perform the fabrication process of the Hall-bar structures. All the steps used for the fabrication process are illustrated in Fig 2.14. Usual lithography is performed to create the Hall bar or the metal contacts pattern, by direct laser writing (DWL Heidelberg 2000). Several lithography steps are required to achieve the full working FET device. All steps used the same positive photoresist Az1505 (Merck KGaA) approximately 1  $\mu\text{m}$  thick. The exposure is performed with a laser wavelength of 405 nm and with a laser power within the range of 40-60% of the maximum intensity. The developer used to reveal the pattern is a standard Az400 developer by 30 sec.

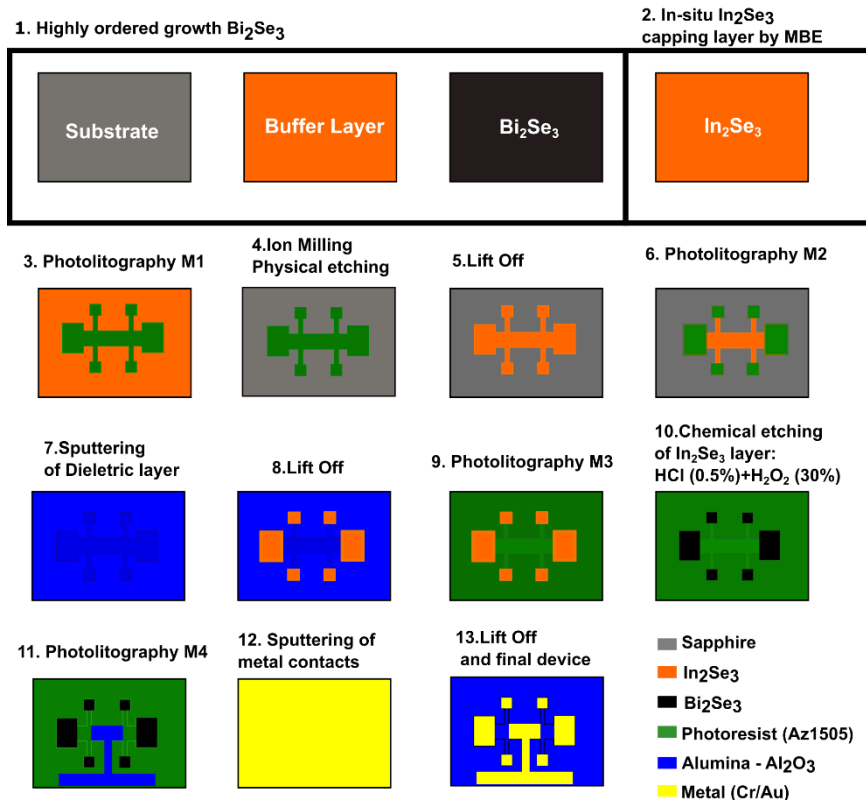
The Hall-bar pattern is molded onto the  $\text{Bi}_2\text{Se}_3$  by a physical etching (Ion milling-Nordiko) with an  $\text{Ar}^+$  plasma with an incident angle of  $130^\circ$  to the sample, to avoid the accumulation of material on the sides of the channel. Further etching is performed for 1 min at  $174^\circ$  to remove the extra material accumulated in the channel lateral. This step is crucial to avoid the creation of short circuits between the gate contact and the channel.

The implementation of an electrostatic gate on top of the channel is studied in Chapter 6.  $\text{Al}_2\text{O}_3$  is the material used for the dielectric layer, due to its good properties as an insulating material with a high dielectric constant.  $\text{Al}_2\text{O}_3$  is deposited by sputtering aiming at a thickness of 100 nm, and the dielectric layer on the metallic contact area is later removed by a lift-off process.

The metallic contacts, to be in contact with the  $\text{Bi}_2\text{Se}_3$  layer, require the removal of the  $\beta\text{-In}_2\text{Se}_3$  layer selectively without damaging the  $\text{Bi}_2\text{Se}_3$  layer. Several tests were performed to achieve a wet chemical etch that selectively etched the  $\beta\text{-In}_2\text{Se}_3$ <sup>18</sup>. The chemical used is a solution with a volume ratio of  $\text{HCl}$  (0.5%)+ $\text{H}_2\text{O}_2$ (30%) (4:50). The solution etches selectively the  $\beta\text{-In}_2\text{Se}_3$  layer in 3-5 min. Additional  $\beta\text{-In}_2\text{Se}_3$  samples are used to verify the complete etching of the  $\beta\text{-In}_2\text{Se}_3$  layer. An additional 30 s of over-etch is performed to ensure the  $\beta\text{-In}_2\text{Se}_3$  is etched completely since the  $\text{Bi}_2\text{Se}_3$  is not severely affected by the chemical solution. To stop the etch process we perform an immersion of the samples in DI  $\text{H}_2\text{O}$  for a maximum of 30 s to avoid the  $\text{Bi}_2\text{Se}_3$  oxidation. Studies also predict that water is not as harmful as air or alcohol<sup>25</sup>.

Finally, the metallic contact can be deposited on top of the  $\text{Bi}_2\text{Se}_3$  layer and onto the dielectric material for the electrostatic gate. The electrodes are a combination of 15 nm of an adhesion layer of Cr and 35 nm of Au by sputtering.

a)



b)

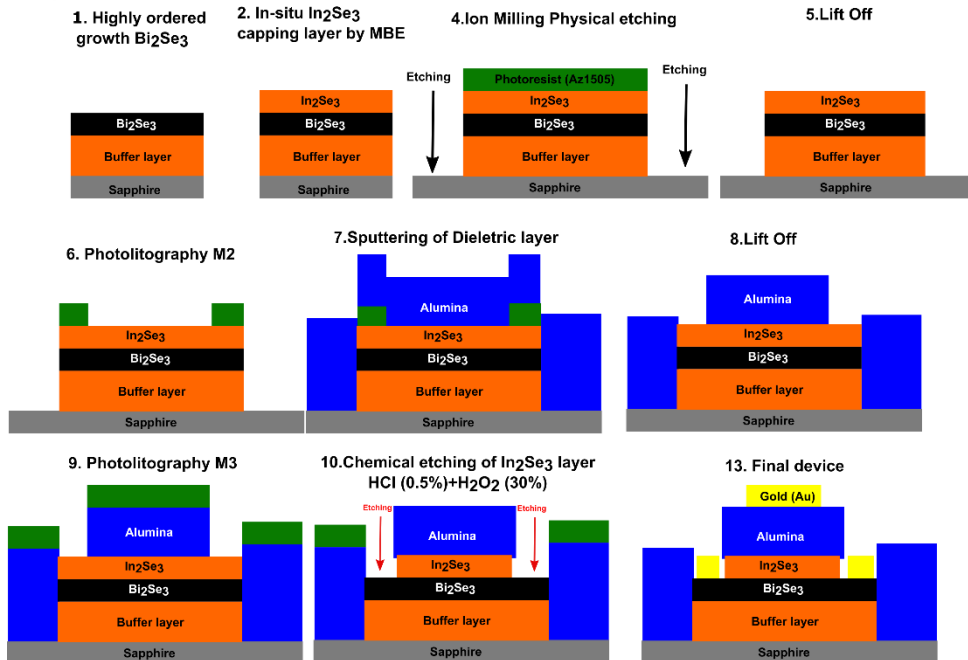


Figure 2.14 a) Top view and b) cross-section view of the cleanroom fabrication process for the Hall-bar structure top gate device.

# Chapter 3

## 3. Bi<sub>2</sub>Se<sub>3</sub> growth optimization by molecular beam epitaxy

As mentioned previously, Bi<sub>2</sub>Se<sub>3</sub> stands out among the 3D topological insulators due to the large band gap of 0.3 eV and possessing robust semi-Dirac surface states crossing the band gap<sup>5</sup>. The presence of a strong spin-orbit coupling, and the protection of time-reversal symmetry offers the property of a spin-momentum locking of the electron spin, meaning the spin is connected to the momentum space<sup>5</sup>. The surface states similarity to the Dirac cone also resembles the electronic properties of those materials, such as relatively low electron densities and high mobilities<sup>12</sup>. The protection offered by the system symmetry leads to the robustness of these properties, which ideally should produce a dissipationless material<sup>5</sup>. Those properties suggest that TIs are relevant in the field of low-power consumption electronics, spintronics, and quantum computation. A key to achieving such good properties is of keen importance that the TI exhibits good crystallinity, minor roughness, low defect densities, and high electron mobility<sup>26</sup>.

MBE is identified as a deposition technique of high-quality single crystals. The growth of Bi<sub>2</sub>Se<sub>3</sub> was reported in several studies showing good properties by MBE<sup>27-31</sup>. However, Bi<sub>2</sub>Se<sub>3</sub> tends to grow with an n-type degeneracy due to the existence of Se vacancies<sup>29,32</sup>. Se has a low vapor pressure at low pressures and standard temperatures which leads to desorption of the material and acts as a donor impurity. Thus, the bulk material contributes to the electrical properties, which compromises the topological properties of TI and the detection of the surface state properties.

At INL, the growth of TIs was implemented for the first time during this thesis work. This chapter reports the growth of Bi<sub>2</sub>Se<sub>3</sub>, investigated and optimized by changing different growth parameters such as growth temperature, and Se background. The Bi<sub>2</sub>Se<sub>3</sub> growth quality depends on the interface between the layer below and the Bi<sub>2</sub>Se<sub>3</sub>. To improve the interface a surface treatment (ST) and different buffer layers are studied. The Bi<sub>2</sub>Se<sub>3</sub> is studied in terms of structural, electrical, and transport properties.

### 3.1. Substrate temperature and surface treatment

The first point to consider for the growth was the Se vacancies which represent a critical factor for the growth of a good quality topological insulator with an insulating bulk. Studies have observed that the use of overpressure of selenium reduces the desorption of Se from the deposited material<sup>27</sup>. The excess Se is re-evaporated due to the relatively high temperatures of the substrate. Theresa Ginley et al. optimized the growth conditions for a selenium cracked source, which allows the use of reduced Se fluxes<sup>27</sup>. It is reported an optimal ratio Bi/Se of 1:4. Due to the MBE similarities, it is the starting point, where the ratio Bi/Se was kept approximately at 1:4, achieving a growth rate of 1 - 1.4 nm/min.

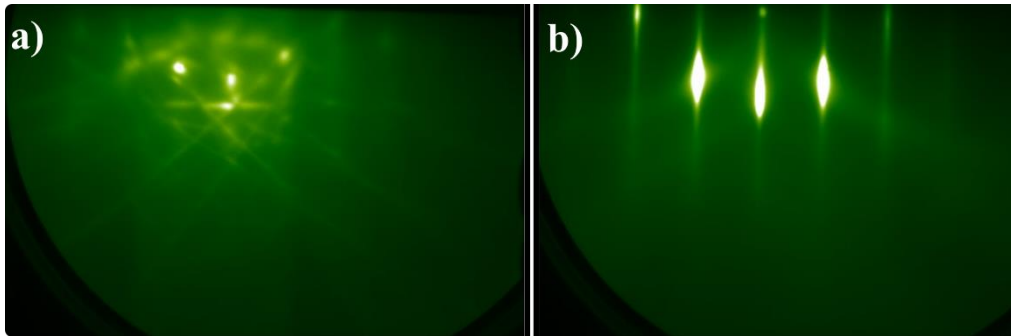
The growth of Bi<sub>2</sub>Se<sub>3</sub> is reported in several substrates, such as InP<sup>33</sup>, Si (111)<sup>31,34,35</sup>, GaAs<sup>36</sup>, SrTiO<sub>3</sub><sup>37</sup>, and sapphire (Al<sub>2</sub>O<sub>3</sub>)<sup>28-30,38,39</sup>. Van der Waals (VdW) 2D materials possess the ability to couple weakly to the substrate due to the weak VdW forces. It permits the growth of these materials in a large variety of substrates with relatively large lattice mismatch compared to covalent layers. Nevertheless, we selected substrates with small lattice mismatches, chemically compatible, and ideally with a matching hexagonal surface structure.

Table 3.1 shows the lattice parameters of Bi<sub>2</sub>Se<sub>3</sub> and the lattice mismatch between Bi<sub>2</sub>Se<sub>3</sub> and different types of substrates. The best candidates for the growth of lattice match Bi<sub>2</sub>Se<sub>3</sub> are InP and GaAs substrates, but they are commercially expensive. Thus, sapphire substrates are chosen due to their cost-effectiveness while exhibiting a comparable small lattice mismatch (13%) and the inert chemical nature<sup>40</sup>. Furthermore, sapphire substrates are commercially available, extensively studied in the literature with optimized Bi<sub>2</sub>Se<sub>3</sub> growth reported and present an electrical insulating behavior that facilitates the study of transport properties without any substrate contribution.

**Table 3.1** Lattice constant of Bi<sub>2</sub>Se<sub>3</sub> and respective lattice mismatch of different types of substrates<sup>10</sup>.

Material	Lattice constants		Lattice mismatch (%)				
	a (Å)	c (Å)	Si (111)	GaAs (111)	InP (111)	Sapphire (0001)	SrTiO <sub>3</sub> (111)
Bi <sub>2</sub> Se <sub>3</sub>	4.14	28.64	7.80	3.54	-0.24	-12.9	-25.0

Fig. 3.1 shows the RHEED pattern for the sapphire substrate and the Bi<sub>2</sub>Se<sub>3</sub> calibration sample. In Fig. 3.1 a), the sapphire RHEED is shown with the presence of the Kikuchi lines which indicates a high-quality flat surface<sup>41,42</sup>. The Bi<sub>2</sub>Se<sub>3</sub> pattern is observed in Fig. 3.1 b). The pattern confirms the high single crystal quality by the presence of streaky lines with high intensity, corresponding to a flat surface with small domains<sup>34,43-47</sup>.



**Figure 3.1** a) RHEED pattern of a cleaned sapphire substrate after a 900°C annealing for 45 min. b) RHEED pattern of a 30 nm Bi<sub>2</sub>Se<sub>3</sub> layer in the [100] direction.

The first parameter optimization studied is the substrate temperature during the Bi<sub>2</sub>Se<sub>3</sub> deposition. Selenium outgasses easily from the thin-film material even at low temperatures between 250-350 °C<sup>15</sup>. The consequence of a low substrate temperature is low material mobility and induces defect formation. Consequently, it deteriorates the electrical properties of the film. Conversely, temperatures higher than 400 °C were implausible due to the desorption of Bi and Se atoms. Two different temperatures are used, 270 °C and 310 °C to obtain the best material quality. As mentioned before, the MBE at INL offers a Se flux regulation by the adjustable valve aperture. The valve aperture can vary between 0 – 5 mm. The overpressure of Se is proven to help the Se vacancies minimization. Thus, we decided to implement the higher value of 5.0 mm for the growth of the Bi<sub>2</sub>Se<sub>3</sub>. The growth time was set to 30 min which led to a 30 nm thick Bi<sub>2</sub>Se<sub>3</sub>.

Fig. 3.2 shows the AFM image of a 30 nm thick Bi<sub>2</sub>Se<sub>3</sub> surface topography for both deposition temperatures with the correspondent line profile. For the first temperature used 270°C (Fig. 3.2 a), it is observed the formation of triangular pyramidal structures characteristic of a hexagonal crystal structure. However, the triangular crystals present a vast number of domains. Furthermore, the crystal size is fairly small with values smaller than 500 nm. Conversely, by increasing the temperature to 310 °C (Fig. 3.2 b), the triangular crystals grew in a more organized orientation showing a formation of small domains. These domains are characterized by the presence of undesired twinning. In terms of the crystal size, there is no visible difference. In Fig. 3.2 c) and d) are shown a random line profile on the Bi<sub>2</sub>Se<sub>3</sub> surface. The quintuple layer steps are not easily distinguished due to the poor surface quality. The presence of crystal heights approaching nearly 7 nm height induces a large roughness. Table 3.2 presents the roughness obtained from Gwydion software. At a higher temperature (310 °C) a 0.84 nm roughness is observed, whereas at a lower temperature (270 °C) the roughness is 1.14 nm. Both temperatures showed a roughness similar to the literature, where the temperature of 310 °C demonstrated to be the preferred deposition temperature, because of reduced roughness and twinning.

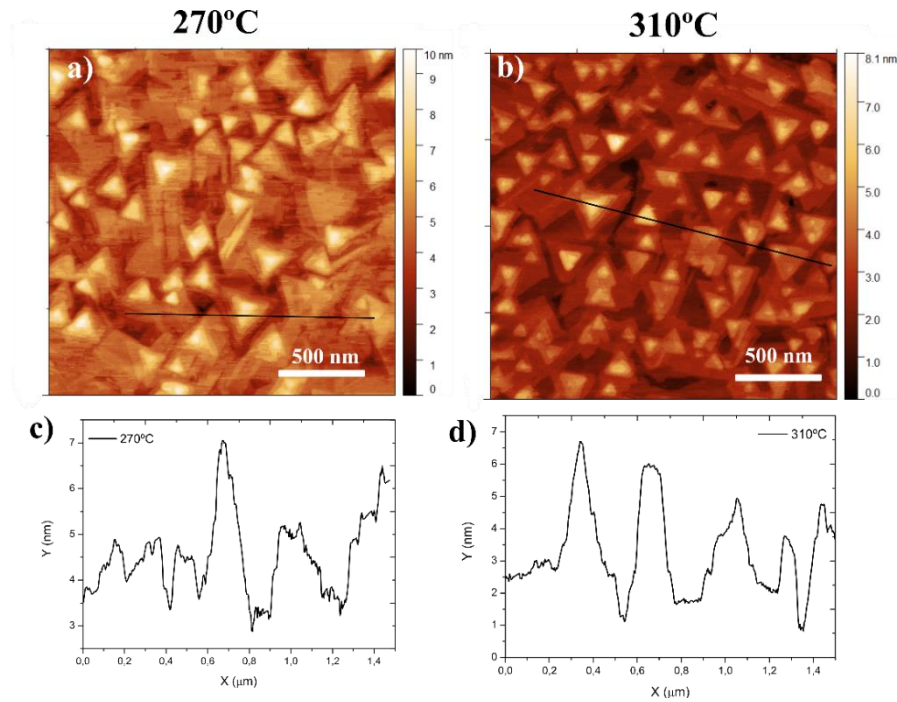


**Figure 3.2** AFM image of a 30 nm thick Bi<sub>2</sub>Se<sub>3</sub> surface, deposited at a) 270 °C and Se valve: 5.0 mm and b) 310 °C and Se valve: 5.0 mm. Line profile of Bi<sub>2</sub>Se<sub>3</sub> surface from c) 270 °C and d) 310 °C, as indicated by the black line in a) and b).

Although the AFM image of the Bi<sub>2</sub>Se<sub>3</sub> showed pyramidal structures, there is still room for improvement concerning the twinning in the Bi<sub>2</sub>Se<sub>3</sub>. Studies concluded that the initial stage or layer is of high importance for the interface quality. The growth of the first layers at lower temperatures increases the uniformity and the larger structural domains<sup>34</sup>. Ido Levy et al. performed a surface treatment before the Bi<sub>2</sub>Se<sub>3</sub> deposition, which led to a twinning suppression. Consequently, the suppression of the twinning can lead to an improvement of the electrical and structural properties<sup>28</sup>. Here, we implemented this surface treatment by adjusting the conditions reported to our MBE system. The surface treatment consisted of exposure to Bi atoms for 2 min to improve the sapphire interface at 140°C. Subsequently, a sacrificial 2-3 quintuple layers of Bi<sub>2</sub>Se<sub>3</sub> are deposited at this low temperature to improve the adhesion to the substrate. The temperature is then increased up to 500°C for the layer to be evaporated from the substrate. The second step is repeated (2-3 quintuple layers of Bi<sub>2</sub>Se<sub>3</sub> at 140°C). The Bi<sub>2</sub>Se<sub>3</sub> is then deposited after the temperature is increased to 310°C, which is the preferred growth temperature. To prevent the Se evaporation of the initial 2-3 QL Bi<sub>2</sub>Se<sub>3</sub> already deposited, the Se shutter is kept open during the substrate warm-up.

The Bi<sub>2</sub>Se<sub>3</sub> growth conditions such as growth rates, temperature of the substrate, Se valve aperture, and thin-film thickness are kept the same as before. We observed a significant improvement in the crystal size, reaching up to 1 μm (Fig. 3.3). The twinning seems to be reduced, indicated by the diminished presence of different domains (triangular terraces pointing to the same direction). This effect is described in more detail in section 3.3. The terraces are more defined, and it is possible to identify the QL height of around 1 nm (Fig 3.3 b). On the other hand, the roughness of this sample increased from 0.81 nm to 1.13 nm (Table 3.2), because since more layers are forming at once the crystal size is

increased, and consequently the crystal height, which leads to a slight increase in the roughness.

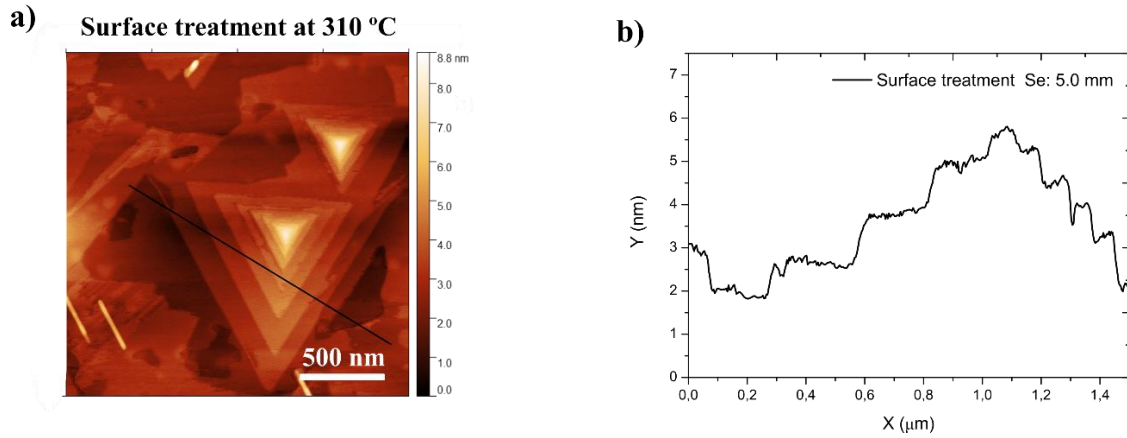


**Figure 3.3** a) AFM image of a 30 nm thick Bi<sub>2</sub>Se<sub>3</sub> surface with a surface treatment deposited at 310°C, Se valve: 5.0 mm. b) Line profile of Bi<sub>2</sub>Se<sub>3</sub> surface as indicated by the black line in a).

Structural characterization of the Bi<sub>2</sub>Se<sub>3</sub> layer was performed by X-ray diffraction measurements. The diffractogram (Fig. 3.4) of the Bi<sub>2</sub>Se<sub>3</sub> samples deposited at 310°C with and without surface treatment, shows characteristic peaks from the diffraction family {0 0 3n} due to the crystal structure and symmetry of the system. The Bi<sub>2</sub>Se<sub>3</sub> presents an epitaxial growth with a rhombohedral crystal structure (R $\bar{3}$ m), which is consistent with literature<sup>34,40,44,48</sup> and without any contaminations. No significant difference is observed for both samples by this scan. However, a  $\varphi$  scan is used in section 3.3 for the quantitative study of twinning.

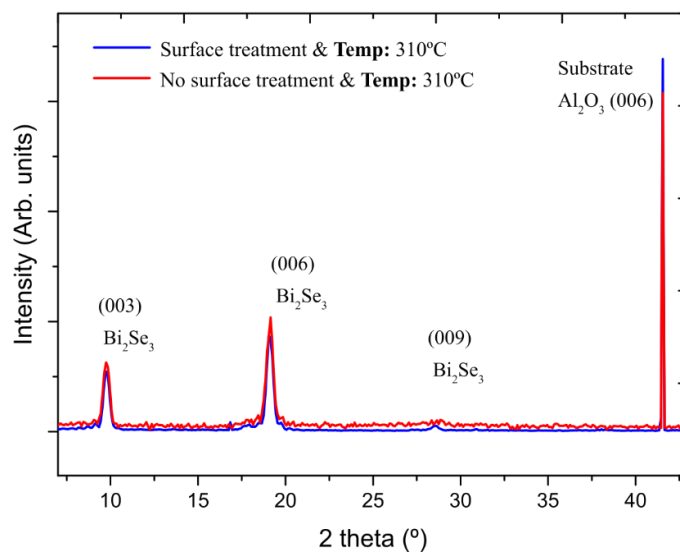


**Figure 3.4** XRD diffractogram for the Bi<sub>2</sub>Se<sub>3</sub> layer with and without surface treatment.

## 3.2. Se overpressure optimization

Continuing the growth optimization, the influence of the Se partial pressure is studied. The overpressure of Se has been shown to avoid the formation of Se vacancies. On the other hand, the Se flux could be exaggeratedly higher than it should be.

In the present section, the Bi<sub>2</sub>Se<sub>3</sub> is grown with the same optimized conditions reached until now. The sapphire was subjected to surface treatment as explained previously, and the growth temperature was set at 310°C. The Se apertures used are 1 mm and 2 mm to add information to the previous 5 mm.

The AFM images for the three different Se valve settings are shown in Fig. 3.5 with the respective line profile. The AFM image of the Se valve of 1.0 mm (Fig. 3.5 a), presents a similar crystal size as observed previously, but with less defined QLs. The profile line observed in Fig. 3.5 d) indicates the presence of pyramidal triangular islands but with less distinctive single QL steps, as observed in Fig. 3.5 f). Increasing the Se valve to 2.0 mm results in a smoother and more uniform surface as shown in Fig. 3.5 b). The pyramidal growth is maintained, nevertheless, more atomic flat terraces are prone to grow, which indicates a better layer-by-layer growth mode. Furthermore, the twinning can be noticed to be minimized compared to the previous Bi<sub>2</sub>Se<sub>3</sub>, with a slight proportion of rotated domains. Finally, a profile line shown in Fig. 3.5 e) shows a flat and smooth Bi<sub>2</sub>Se<sub>3</sub> surface with well-defined QLs at approximately 1 nm height. The Bi<sub>2</sub>Se<sub>3</sub> surface roughness for each sample is shown in Table 3.2. As expected from the AFM images, a lower value of 1.05 nm is observed for the Se valve setting of 2.0 mm. The Se valve setting of 1.0 mm presented the highest value of 1.34 nm, which reveals a relatively rough surface. The optimized Bi<sub>2</sub>Se<sub>3</sub> obtained is similar to that reported in the literature with smaller roughness and less twinning<sup>28,36</sup>.

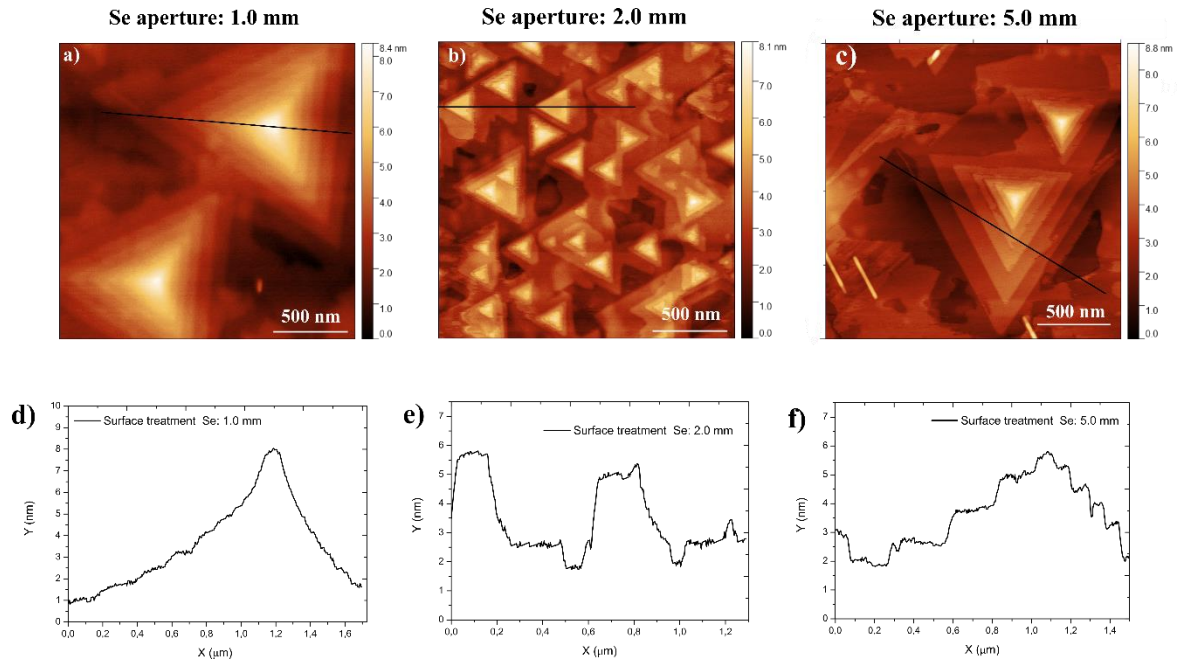


**Figure 3.5** AFM images of 30 nm thick Bi<sub>2</sub>Se<sub>3</sub> surfaces. The substrates were subjected to a surface treatment. The Bi<sub>2</sub>Se<sub>3</sub> growth was performed at 310 °C and with a Se valve aperture of a) 1.0 mm, b) 2.0 mm and c) 5.0 mm. Line profiles of Bi<sub>2</sub>Se<sub>3</sub> surfaces grown at a Se aperture of d) 1.0 mm, e) 2.0 mm and f) 5.0 mm, as indicated by the black line.

**Table 3.2** RMS roughness of the Bi<sub>2</sub>Se<sub>3</sub> surface deposited at 270°C and 310°C, and different Se valve apertures with or without a surface treatment. Data is analyzed by the Gwydion software.

	Samples				
	Se: 5.0 mm without Surface Treatment		Surface treatment at 310 °C		
	270 °C	310 °C	Se: 1.0 mm	Se: 2.0 mm	Se: 5.0 mm
<b>RMS</b>					
<b>Roughness</b>	1.14	0.84	1.34	1.05	1.13
<b>(nm)</b>					

### 3.3. High-resolution x-ray diffraction of Bi<sub>2</sub>Se<sub>3</sub>

The topological properties of TIs are dependent on the crystalline quality<sup>33</sup>, thus, the structural quality of Bi<sub>2</sub>Se<sub>3</sub> needs to be studied in detail. A high-resolution X-ray characterization technique, known as XRD rocking curves, can aid in receiving more detailed information. Rocking curves can study the perfection of the crystal when the crystal planes are not parallel. The scan is performed by fixing the angle in a diffraction plane, in our case the most intense peak (006), and afterward, the sample is tilted. A perfect crystal with parallel planes should decrease the intensity of the diffraction peak sharply with a minimal full-width half maximum (FWHM). The presence of defects such as dislocations and mosaicity disrupts the crystal and consequently, the peak intensity is not as sharp as it should be.

Fig. 3.6 displays the rocking curves of the plane (006) for all the Bi<sub>2</sub>Se<sub>3</sub> samples grown at 310°C. Due to the reduced quality of the sample grown at 270°C, this characterization was not performed in this sample. By observing the figure, it is possible to conclude that all samples present similar quality by small differences in intensity and FWHM. To compare these values Table 3.3 shows the FWHM for all the presented samples. The only notable difference observed is that performing a treatment of the surface produces a higher-quality crystal. The FWHM for the sample without a surface treatment is approximately 0.23° whereas the samples with a surface treatment exhibit a relatively lower value of approximately 0.22°. Additionally, those samples with a surface treatment obtained good crystal quality with extremely similar results of FWHM. These values are comparable to the literature ranging between 0.003-0.33°. In a substrate of InP it was achieved an FWHM of 0.003°<sup>33</sup>, from Table 3.1, the lattice mismatch of InP is 0.24% which explains the highly crystalline quality from the Bi<sub>2</sub>Se<sub>3</sub>. Whereas on sapphire the values vary between 0.1-0.33°<sup>28,48-50</sup>, due to the lattice mismatch of 13%. The experimental result suggests that the Bi<sub>2</sub>Se<sub>3</sub> quality relies more on the substrate than on the starting layer<sup>33,49</sup>.

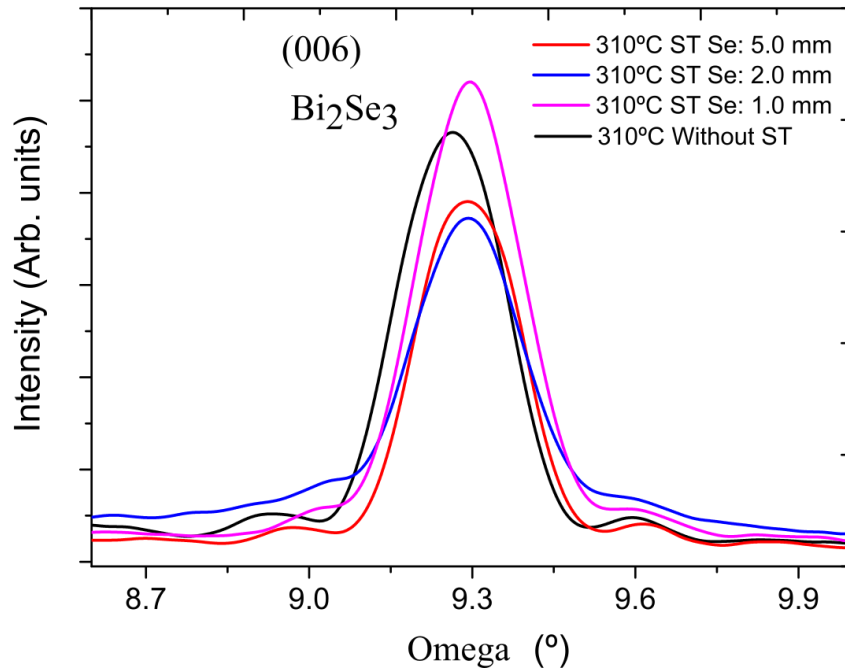


**Figure 3.6** XRD rocking curves of Bi<sub>2</sub>Se<sub>3</sub> grown at 310°C along the plane (006) of Bi<sub>2</sub>Se<sub>3</sub>.

**Table 3.3** FWHM calculated from the Gaussian fitting of the XRD rocking curves of the Bi<sub>2</sub>Se<sub>3</sub> plane (006), for all the Bi<sub>2</sub>Se<sub>3</sub> samples deposited at 310°C.

Temperature (°)	Surface treatment	Se valve (mm)	FWHM (°)	Twinning ratio (%)
310	No	5.0	0.229 ± 0.001	44.2
310	Yes	5.0	0.221 ± 0.001	17.5
310	Yes	2.0	0.220 ± 0.001	15.4
310	Yes	1.0	0.219 ± 0.001	18.6

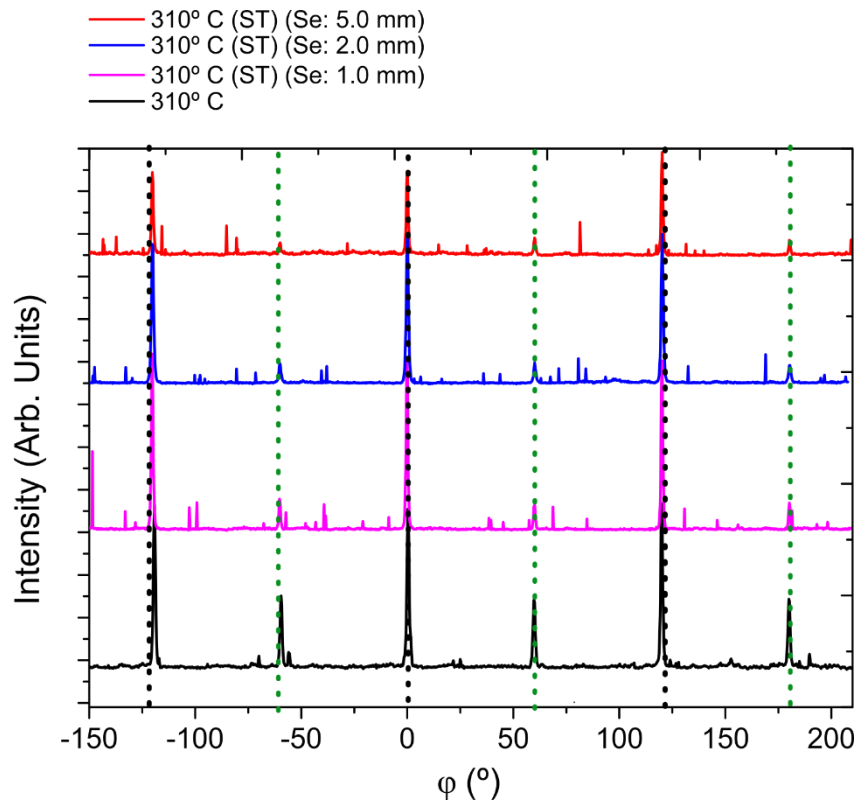
Another characterization technique used to study the crystal quality to give more detail about the percentage of defects in the Bi<sub>2</sub>Se<sub>3</sub> layer is  $\varphi$ -scan X-ray diffraction. The  $\varphi$ -scan allows quantifying the percentage of twinning parallel to the surface (in-plane). Similar to the previous characterization technique, the detector is fixed at an angle corresponding to a diffraction spot (of a plane). The  $\varphi$ -scan is performed along the Bi<sub>2</sub>Se<sub>3</sub> diffraction spot corresponding to the plane (015), which requires a sample rotation of approximately 57° in the  $\chi$  axis, as commonly used in the literature<sup>28,49,51,52</sup>. The sample undergoes a full azimuthal rotation ( $\varphi$ -scan), perpendicular to the sample.

Fig 3.7 shows the  $\varphi$ -scan for all grown samples, which presents a set of high-intensity peaks centered at 0° and repeating every 120° (vertical black dot line) since the system presents a 3-fold symmetry<sup>28,49</sup>. However, when two different domains are present (twinning), results in the emergence of smaller intensity peaks after 60° of the high-

intensity peaks, as illustrated in Fig 3.7 at  $-60^\circ$ ,  $60^\circ$ , and  $-180^\circ$  (can be understood as a 6-fold symmetry). This minority domain repeats every  $120^\circ$  (vertical green dot line) since the new domain also exhibits a 3-fold symmetry.

An ideal twinning-free crystal would present a minimal intensity for those peaks. By comparing the spectra from all samples, we confirm the existence of twinning due to the presence of the second peak intensity, as expected from the AFM images. The sample without surface treatment (ST) demonstrates a more intense peak at  $-90^\circ$  and the remaining peaks every  $120^\circ$ , compared to the other samples that have undergone surface treatment. A small intensity peak is observed at those angles compared to the high-intensity peaks. The ratio of twinning is calculated between both peak intensities and is shown in Table 3.3. The percentage of the twinning of around 44% is reduced to values of around 17.5% by performing the surface treatment, which confirmed the work performed by Ido Levy et al.<sup>28</sup>. Nonetheless, from all the samples subjected to the ST, the Se valve aperture of 2 mm demonstrates a twinning suppression with a ratio of 15.4%. It can be concluded, taking attention to all the sections studied up to now, that the optimal growth conditions for the Bi<sub>2</sub>Se<sub>3</sub> are a growth temperature of  $310^\circ\text{C}$  and a Se valve aperture of 2.0 mm.

Henceforward, the sapphire substrates are subjected to the surface treatment to improve the interface sapphire/ Bi<sub>2</sub>Se<sub>3</sub>. While the Bi<sub>2</sub>Se<sub>3</sub> is deposited at  $310^\circ\text{C}$  and with a Se valve aperture of 2.0 mm.



**Figure 3.7** XRD  $\phi$  scan of Bi<sub>2</sub>Se<sub>3</sub> grown at  $310^\circ\text{C}$  along the plane (015) of Bi<sub>2</sub>Se<sub>3</sub>. The black dotted lines denote the crystal 3-fold symmetry by the repetition of the peak every  $120^\circ$ . The green dotted lines denote the presence of twinning by the appearance of a peak every  $60^\circ$ .

### 3.4. Buffer layer introduction

The Bi<sub>2</sub>Se<sub>3</sub> quality achieved previously showed a low percentage of twinning defects. Nevertheless, there is still room for improvement in terms of interfacial and bulk defects that affect the transport properties of the topological insulator. The growth of these Van der Waal materials requires chemically compatible substrates in preference for lattice-matched ones<sup>53</sup>. The use of chemically and lattice-matched substrates should lead to the suppression of bulk and interfacial defects, which are the principal cause of low mobilities and high bulk carrier densities in TI films<sup>54–56</sup>. The use of a buffer layer below the Bi<sub>2</sub>Se<sub>3</sub> layer has been shown to lead to a more insulating TI with less bulk electrical contributions<sup>54–56</sup>.

This section focuses on the reproduction of two research articles where different buffer layers were implemented to achieve a TI with favorable transport properties. In order to analyze the electronic properties of the Bi<sub>2</sub>Se<sub>3</sub> layer, the buffer layer is required to not contribute electrically. The key material is the Van der Waal material  $\beta$ -In<sub>2</sub>Se<sub>3</sub>, which presents a 1.4 eV band gap, a trivial band insulator, meaning that it does not contribute to the transport properties. Additionally, the material presents an identical rhombohedral crystal structure and a similar lattice parameter (3.4% lattice mismatch)<sup>56</sup>. The hybridization of the  $\beta$ -In<sub>2</sub>Se<sub>3</sub> layer with Bi atoms can lead to an even more chemically stable layer and the “doping” of Bi transforms the lattice parameter to values closer to the Bi<sub>2</sub>Se<sub>3</sub> layer. Studies also confirmed that the (Bi<sub>1-x</sub>In<sub>x</sub>)<sub>2</sub>Se<sub>3</sub> layer (BIS) is a trivial insulating material as long as the percentage of In is higher than 30%<sup>56</sup>.

Koirala et al.<sup>55</sup> and Wang et al.<sup>56</sup> implemented the deposition of a buffer (Bi<sub>1-x</sub>In<sub>x</sub>)<sub>2</sub>Se<sub>3</sub> layer prior to the growth of the Bi<sub>2</sub>Se<sub>3</sub> layer obtaining the improvement of the transport properties for the TI material. A schematic of each buffer layer growth adapted for the Bi<sub>2</sub>Se<sub>3</sub> growth is illustrated in Fig 3.8 a and c. Koirala et al. implemented the growth of a  $\beta$ -In<sub>2</sub>Se<sub>3</sub> and a (Bi<sub>1-x</sub>In<sub>x</sub>)<sub>2</sub>Se<sub>3</sub> to form the buffer layer IS-BIS (Fig 3.8 a). The initial problem is the large variety of phases of In<sub>2</sub>Se<sub>3</sub>. Thus, the buffer layer starts with a 3 QL sacrificial layer of Bi<sub>2</sub>Se<sub>3</sub> to favor the 20 QL  $\beta$ -In<sub>2</sub>Se<sub>3</sub> growth. Later on, the sacrificial layer of Bi<sub>2</sub>Se<sub>3</sub> is removed by annealing the substrate to temperatures around 600°C to prevent the creation of electrical shorts between the Bi<sub>2</sub>Se<sub>3</sub> layer that is deposited later. After the In<sub>2</sub>Se<sub>3</sub> layer, a 20 QL BIS layer is deposited which leads to a highly ordered Bi<sub>2</sub>Se<sub>3</sub> layer.

The RHEED pattern was recorded during the buffer growth (Fig 3.8 b). The In<sub>2</sub>Se<sub>3</sub> shows the same pattern as the Bi<sub>2</sub>Se<sub>3</sub> since they possess an identical crystal structure. The main difference is the intensity of the signal, it presents a more diffuse signal compared to the Bi<sub>2</sub>Se<sub>3</sub>. The incorporation of Bi atoms leads to a less diffuse signal, where brighter streaky lines are seen for the Bi<sub>2</sub>Se<sub>3</sub> RHEED since Bi atoms present a higher atomic number than In atoms. A larger atomic number tends to scatter electrons more effectively, which results in a brighter RHEED signal.

On the other hand, Wang et al. created the (Bi<sub>1-x</sub>In<sub>x</sub>)<sub>2</sub>Se<sub>3</sub> layer (FIG 3.8 c) by depositing a 5 QL layer of Bi<sub>2</sub>Se<sub>3</sub> and In<sub>2</sub>Se<sub>3</sub> separately. This layer is subjected to an annealing process at high temperatures (425°C). The high volatility of Bi<sub>2</sub>Se<sub>3</sub> enables the diffusion into the In<sub>2</sub>Se<sub>3</sub> layer to form the (Bi<sub>1-x</sub>In<sub>x</sub>)<sub>2</sub>Se<sub>3</sub>. The RHEED pattern of this buffer layer is shown in Fig 3.8 d). The pattern of the buffer layer is similar to the previous method. Likewise, the Bi<sub>2</sub>Se<sub>3</sub> layer shows the characteristic streaky lines with good single-crystal quality.

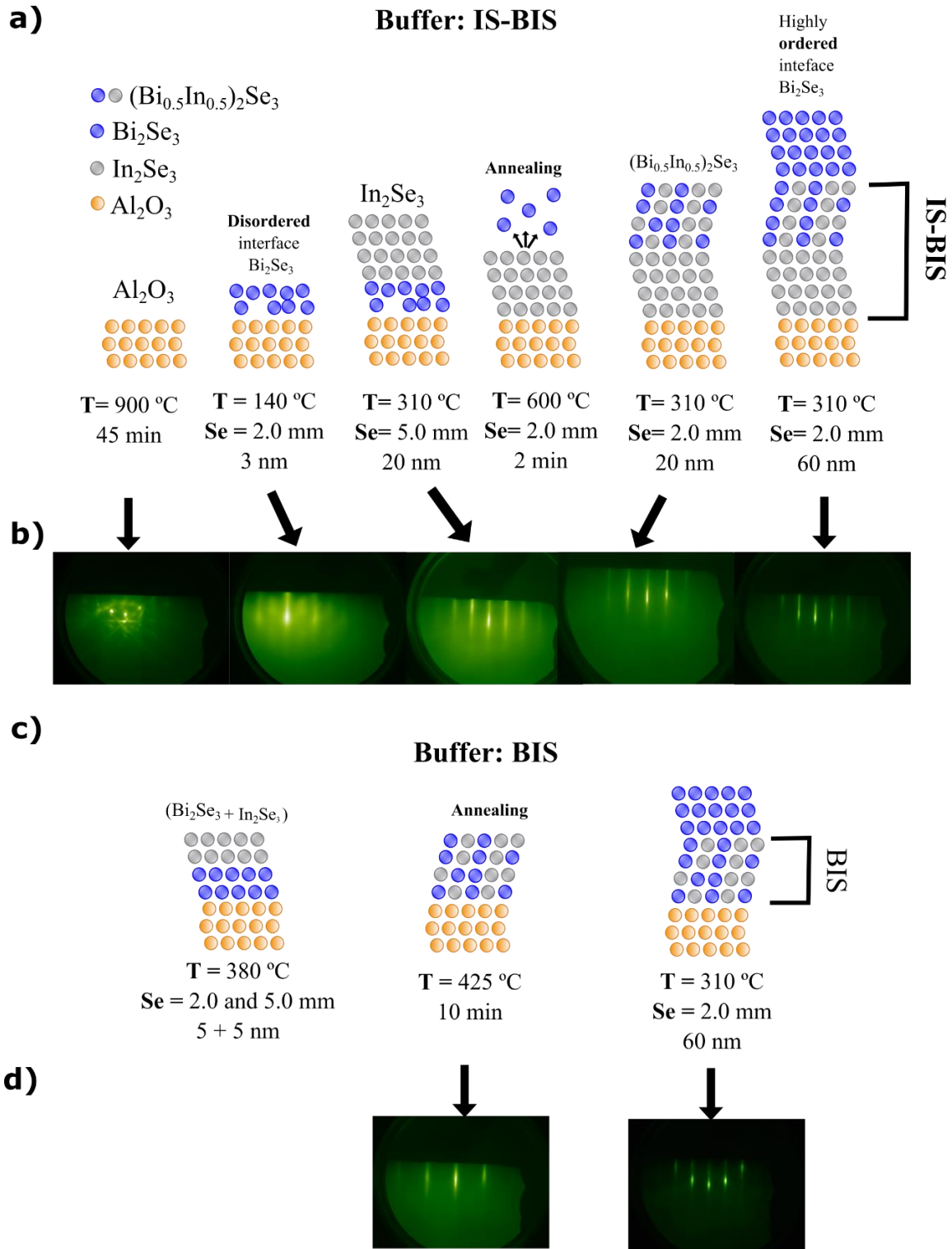


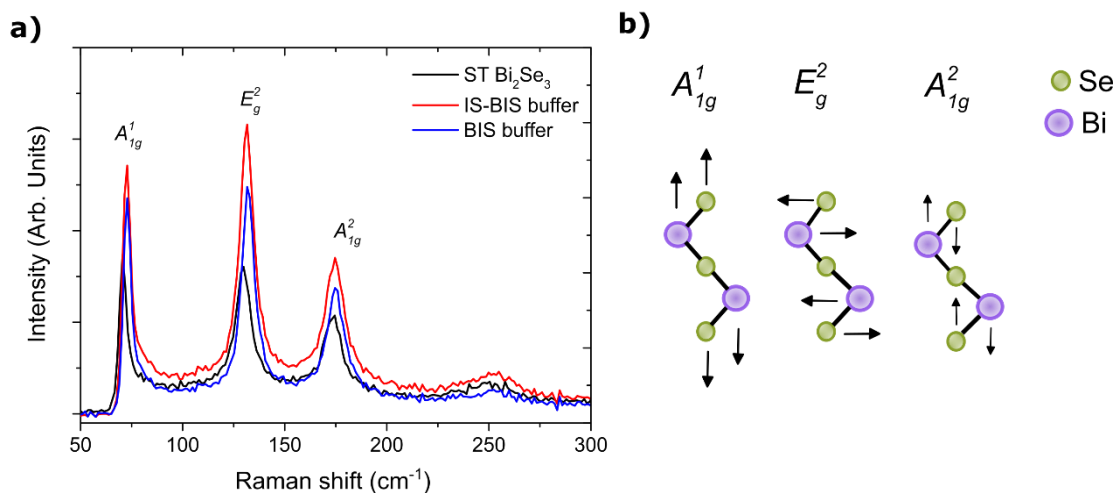
**Figure 3.8** Schematic of the IS-BIS buffer layer deposition adapted from Koirala et al. b) RHEED patterns for each individual layer in the direction [100]. c) Schematic of the BIS buffer layer deposition adapted from Wang et al. d) RHEED patterns for each individual layer. The first RHEED is in the direction [110] and the second is in the direction [100], showing that there is a 3-fold rotational symmetry.

Both buffer layers seem to lead to a good Bi<sub>2</sub>Se<sub>3</sub> crystal quality concerning the pattern from the RHEED. Following, it is studied in more detail the crystal structure of each Bi<sub>2</sub>Se<sub>3</sub> which can be compared to the previous Bi<sub>2</sub>Se<sub>3</sub> wherein only a surface treatment is performed before the TI growth. The conditions for the Bi<sub>2</sub>Se<sub>3</sub> with a buffer layer had the same growth conditions as the previous Bi<sub>2</sub>Se<sub>3</sub>, such as a growth temperature of 310°C, and a Se valve opening of 2.0 mm.

### 3.4.1. Bi<sub>2</sub>Se<sub>3</sub> structural properties

The vibrational modes are studied by Raman spectroscopy. The spectra obtained for all samples are shown in Fig 3.9 a) and an illustration of the characteristic Bi<sub>2</sub>Se<sub>3</sub> vibrational modes is displayed in Fig 3.9 b). Three main characteristic peaks of Bi<sub>2</sub>Se<sub>3</sub> are detected,  $A_{1g}^1$ ,  $E_g^2$ ,  $A_{1g}^2$  similar to the literature<sup>57-60</sup>. The main difference observed for the signal is the intensity. A pronounced peak intensity Bi<sub>2</sub>Se<sub>3</sub> with a buffer IS-BIS is observed whereas a less intense signal is observed for the Bi<sub>2</sub>Se<sub>3</sub> with an ST.

The peak position and the FWHM are extracted by a Gaussian fitting (Table 3.4). The Raman modes,  $A_{1g}^1$ ,  $E_g^2$  and  $A_{1g}^2$  are detected at approximately 71, 131, and 174 cm<sup>-1</sup>, respectively. The sample with an ST presents vibrational peak positions closer to the literature<sup>57-60</sup>. Conversely, the Bi<sub>2</sub>Se<sub>3</sub> growth onto a buffer layer led to a small peak deviation to higher frequencies, a blue shift of  $1.9 \pm 0.3$  cm<sup>-1</sup>. This deviation could represent a small modification of the lattice parameter due to the buffer layer influence. The reduced FWHM is correlated to an improved crystal quality<sup>57</sup>. An additional small and broad peak is detected around 250 cm<sup>-1</sup> representing atomic Se that is commonly evaporated as reported in the literature<sup>61</sup>.

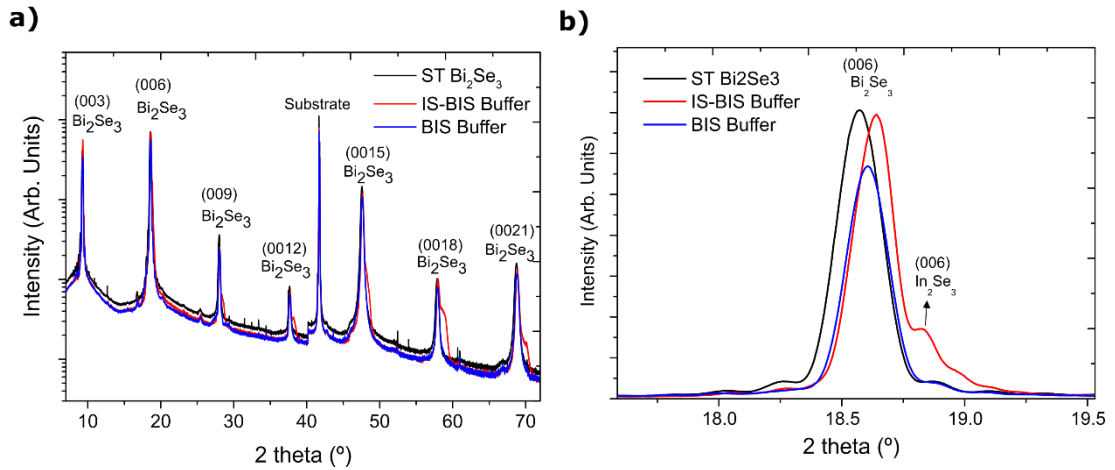


**Figure 3.9** a) Room temperature Raman signal of Bi<sub>2</sub>Se<sub>3</sub> with a surface treatment and with a buffer layer showing three characteristic vibrational peaks. b) Illustration of the vibrational modes present in Bi<sub>2</sub>Se<sub>3</sub>.

**Table 3.4** Peak position of each Bi<sub>2</sub>Se<sub>3</sub> vibrational mode ( $A_{1g}^1$ ,  $E_g^2$  and  $A_{1g}^2$ ) and correspondent FWHM.

	$A_{1g}^1$		$E_g^2$		$A_{1g}^2$	
	Peak position (cm <sup>-1</sup> )	FWHM (cm <sup>-1</sup> )	Peak position (cm <sup>-1</sup> )	FWHM (cm <sup>-1</sup> )	Peak position (cm <sup>-1</sup> )	FWHM (cm <sup>-1</sup> )
Literature <sup>58</sup>	71	(4 – 5)	131	(7-8)	174	(9-10)
ST Bi <sub>2</sub> Se <sub>3</sub>	70.9 ± 0.2	3.7 ± 0.4	129.7 ± 0.2	7.7 ± 0.4	173.3 ± 0.3	10 ± 1
IS-BIS Buffer	72.8 ± 0.3	4.5 ± 0.5	131.3 ± 0.4	6.6 ± 0.2	174.4 ± 0.8	9.2 ± 0.4
BIS Buffer	72.9 ± 0.1	4.2 ± 0.7	132.1 ± 0.1	6.8 ± 0.3	174.9 ± 0.2	8.6 ± 0.5

Further details about the structure of the films can be obtained by X-ray diffraction measurements. The  $2\theta$  scan XRD, shown in Fig 3.10 a), exhibits a single crystal family {00L} rhombohedral crystal structure for all samples. There is no relevant difference between the samples confirming the good Bi<sub>2</sub>Se<sub>3</sub> quality. However, by performing a high-resolution scan for the (006) plane, small differences can be detected. A peak shift is observed for all the samples due to a difference in the crystal lattice parameters as predicted from the Raman data. The (006) plane is detected at 18.57° for a single ST Bi<sub>2</sub>Se<sub>3</sub> whereas for the IS-BIS Bi<sub>2</sub>Se<sub>3</sub> it is detected at 18.64°. Additionally, for the buffer layer, IS-BIS an additional peak is also detected at 18.83 ° correspondent to the In<sub>2</sub>Se<sub>3</sub> layer. Through the XRD diffraction pattern, the lattice parameter of the Bi<sub>2</sub>Se<sub>3</sub> unit cell was calculated (Table 3.5). An additional X-ray scan of the peak (015) is performed to make it possible to calculate the lattice parameter  $a$ , as described in Eq. (3.1). The uncertainty is calculated by Eq. (3.2) through error propagation.


**Figure 3.10** a) XRD diffractogram for the Bi<sub>2</sub>Se<sub>3</sub> layer with a surface treatment and Bi<sub>2</sub>Se<sub>3</sub> grown with an IS-BIS or BIS buffer layer. b) High-resolution x-ray diffraction of the (006) plane of Bi<sub>2</sub>Se<sub>3</sub>.

$$a = \frac{2\sqrt{3}}{3} \sqrt{\frac{c^2 d^2}{c^2 - 25d^2}} \quad (3.1)$$

$$\Delta_a = \frac{2\sqrt{3} \sqrt{\frac{c^6 \Delta_d^2 + 625d^6 \Delta_c^2}{(c^2 - 25d^2)^3}}}{3} \quad (3.2)$$

Table 3.5 indicates a decrease in the  $c$  lattice parameter as a buffer layer is introduced. A value of  $28.66 \pm 0.02 \text{ \AA}$  is obtained for an ST Bi<sub>2</sub>Se<sub>3</sub> which is in agreement with the literature  $c=28.64 \text{ \AA}$  (*ICSD 617072*) and experimental reports<sup>62-65</sup>. This  $c$  value changed to a value of  $28.6 \pm 0.06 \text{ \AA}$  with an IS-BIS buffer layer and  $28.63 \pm 0.03$  with a BIS buffer layer. Moreover, the  $a$  lattice parameter presented a similar value to the literature of around  $4.14 \text{ \AA}$ <sup>62,63,65</sup>, whereas for an IS-BIS buffer, there was an increase of 0.4%.

**Table 3.5** Crystal lattice parameters  $a$  and  $c$  of the Bi<sub>2</sub>Se<sub>3</sub> layer, for the three types of Bi<sub>2</sub>Se<sub>3</sub>.

	$a \text{ (\AA)}$	$c \text{ (\AA)}$
ST Bi <sub>2</sub> Se <sub>3</sub>	$4.139 \pm 0.001$	$28.66 \pm 0.02$
IS-BIS Buffer	$4.158 \pm 0.003$	$28.60 \pm 0.06$
BIS Buffer	$4.141 \pm 0.002$	$28.63 \pm 0.03$

X-ray characterization techniques also offer the analysis of the interfaces of each layer through X-ray reflectivity (XRR), which provides information about film thickness and roughness. XRR analysis was performed for the Bi<sub>2</sub>Se<sub>3</sub> grown onto the different buffer layers, IS-BIS and BIS. Fig 3.11 shows both spectra (orange lines) and the fitting profiles (blue lines) by the software REFLEX. In addition, the thickness and roughness of all layers from the fitting are presented in Tables 3.6 and 3.7. A thickness of around 20 nm for both layers of In<sub>2</sub>Se<sub>3</sub> and BIS is found. In terms of roughness, they present a slightly rough interface. This buffer layer led to a Bi<sub>2</sub>Se<sub>3</sub> layer of around 38 nm thick and a roughness of 1.1 nm, which is comparable to previous Bi<sub>2</sub>Se<sub>3</sub> roughness (Table 3.2).

Fig 3.11 b) presents the XRR data and the fitting profile for the BIS buffer layer with a Bi<sub>2</sub>Se<sub>3</sub> layer on top. Two oscillations are clearly distinguished concerning the BIS and the Bi<sub>2</sub>Se<sub>3</sub> layer with different thicknesses. Table 3.7 shows the fitting parameters. The BIS layer was successfully achieved by the annealing of the Bi<sub>2</sub>Se<sub>3</sub> and the In<sub>2</sub>Se<sub>3</sub>, by the accomplishment of a 10 nm thick layer with a low roughness of 0.6 nm. Despite the good buffer layer, the following Bi<sub>2</sub>Se<sub>3</sub> layer resulted in a rough film of 1.7 nm and a thickness of 41 nm.

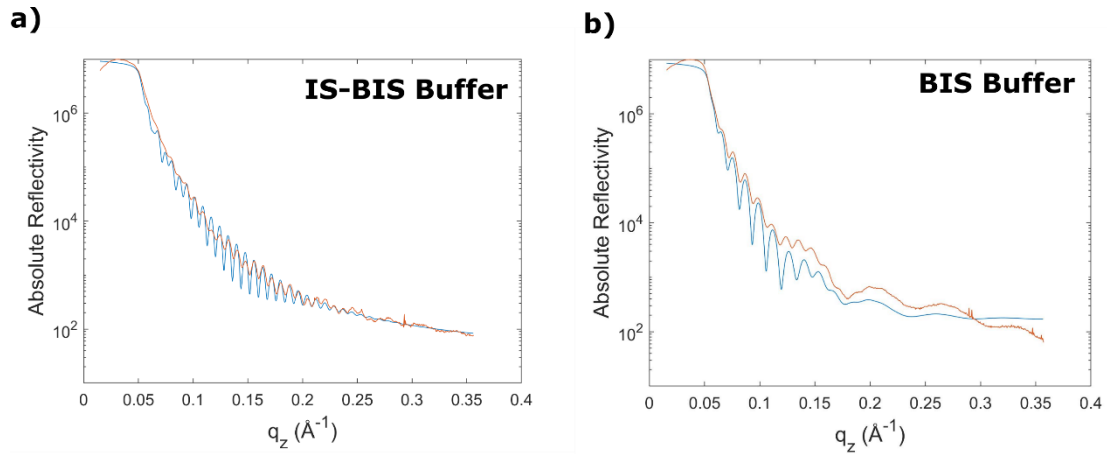


**Figure 3.11** X-ray reflectivity measurements for the Bi<sub>2</sub>Se<sub>3</sub> grown on a) IS-BIS buffer layer (orange line), b) BIS buffer layer (orange line). Both images present the fitting profile calculated from the software REFLEX extracted in MATLAB (blue lines).

**Table 3.6** X-ray reflectivity fitting parameters, thickness, and roughness, for each layer of the IS-BIS buffer sample.

	Roughness (nm)	Thickness (nm)
In <sub>2</sub> Se <sub>3</sub>	3.5	20
BIS	2.2	17
Bi <sub>2</sub> Se <sub>3</sub>	1.1	38

**Table 3.7** X-ray reflectivity fitting parameters, thickness, and roughness, for each layer of the BIS buffer sample.

	Roughness (nm)	Thickness (nm)
BIS	0.6	10.5
Bi <sub>2</sub> Se <sub>3</sub>	1.7	41.1

### 3.4.2. Bi<sub>2</sub>Se<sub>3</sub> electrical and transport properties

One important factor of TIs is their electrical and transport properties. An ideal TI should be an insulator in the bulk, have low bulk electron concentration, and possess conductive surface states due to the semi-Dirac-cone surface states, which can be understood as a high electron mobility material. Even in a defective material, the surface

states of a TI are still present due to their robustness. However, some of their transport properties are going to be affected, such as the bulk mobility and the electron concentration.

The transport study of the Bi<sub>2</sub>Se<sub>3</sub> layer was performed at room temperature (RT) in a Van der Pauw configuration. The layer oxidation cannot be avoided since it is exposed to air for a long period of time (one day).

The electrical and transport properties (resistivity, electron concentration, and mobility) of the Bi<sub>2</sub>Se<sub>3</sub> with ST and buffer layer are shown in Table 3.8. It can be concluded that the introduction of a buffer layer produces a more resistive layer of Bi<sub>2</sub>Se<sub>3</sub> compared to the ST Bi<sub>2</sub>Se<sub>3</sub>, indicating the growth of a highly ordered layer with fewer defects. The most resistive Bi<sub>2</sub>Se<sub>3</sub> film obtained was the sample IS-BIS with a resistivity of  $24.83 \pm 0.04 \text{ } \Omega \text{ } \mu\text{m}$ . The Bi<sub>2</sub>Se<sub>3</sub> can also be affected by an In diffusion into the Bi<sub>2</sub>Se<sub>3</sub> layer that reduces the bulk concentration and consequently increases the resistivity, as proposed in the literature<sup>66</sup>. In fact, for the IS-BIS buffer layer sample, the sheet electron concentration is reduced five times compared to the reference ST Bi<sub>2</sub>Se<sub>3</sub>, from  $5.911 \pm 0.003 \times 10^{13}$  to  $1.69 \pm 0.04 \times 10^{13} \text{ cm}^{-2}$ . In contrast, the BIS buffer sample showed an electron concentration of  $2.23 \pm 0.04 \times 10^{13} \text{ cm}^{-2}$ . These values are still high, likely because Bi<sub>2</sub>Se<sub>3</sub> has the tendency to grow n-type degenerate, due to Se vacancies. These electron concentrations are comparable to the previous research work<sup>55,56</sup>.

In terms of mobility, the literature demonstrated that Bi<sub>2</sub>Se<sub>3</sub> at RT presents values around 600-1000 cm<sup>2</sup>/Vs<sup>27,39,55,56</sup>. The ST Bi<sub>2</sub>Se<sub>3</sub> exhibited a mobility of 420.7 cm<sup>2</sup>/Vs which was improved to values closer to 600 cm<sup>2</sup>/Vs by preparing the Bi<sub>2</sub>Se<sub>3</sub> layer on top of a buffer layer. The highest mobility achieved was  $592.5 \pm 0.6 \text{ cm}^2/\text{Vs}$  for the IS-BIS buffer sample.

To summarize, the transport properties are enhanced by the buffer layer implementation before the Bi<sub>2</sub>Se<sub>3</sub> layer growth. In addition, the IS-BIS buffer layer was demonstrated to achieve better transport properties, such as lower electron concentration and higher mobilities.

**Table 3.8** Electrical and transport properties of the Bi<sub>2</sub>Se<sub>3</sub> layer, with surface treatment and grown on different buffer layers (IS-BIS or BIS). The measurements are performed at RT.

	Resistivity ( $\Omega \text{ } \mu\text{m}$ )	Bulk Concentration ( $\times 10^{18} \text{ cm}^{-3}$ )	Sheet Concentration ( $\times 10^{13} \text{ cm}^{-2}$ )	Mobility ( $\text{cm}^2/\text{Vs}$ )
ST Bi <sub>2</sub> Se <sub>3</sub> (60 nm)	$15.06 \pm 0.01$	$9.851 \pm 0.005$	$5.911 \pm 0.003$	$420.7 \pm 0.1$
IS-BIS Buffer (40 nm)	$24.83 \pm 0.04$	$4.23 \pm 0.01$	$1.69 \pm 0.04$	$592.5 \pm 0.6$
BIS Buffer (40 nm)	$19.80 \pm 0.04$	$5.68 \pm 0.02$	$2.23 \pm 0.04$	$554.8 \pm 0.4$

### 3.5. Summary

Growth conditions for the topological insulator Bi<sub>2</sub>Se<sub>3</sub>, are optimized by adjusting growth temperature and the Se valve aperture. The simple Bi<sub>2</sub>Se<sub>3</sub> layer presented the best crystal quality for a growth temperature of 310 °C and a Se aperture of 2.0 mm. The twinning defects were successfully reduced by the sapphire surface treatment according to high resolutions of x-ray analysis. The transport properties of Bi<sub>2</sub>Se<sub>3</sub> are further enhanced improving the interface between the Bi<sub>2</sub>Se<sub>3</sub> and an added semi-insulating buffer layer. The IS-BIS buffer layer technique, previously, studied by Koirala et al. was shown to reduce the electron concentration and increase the Bi<sub>2</sub>Se<sub>3</sub> mobilities, which leads to an improved topological insulator overall.

# Chapter 4

## 4. Structural and electrical properties of Ga and Cu doping of Bi<sub>2</sub>Se<sub>3</sub>

Parts of the results presented in this chapter have appeared in the *Daniel Brito et al. Journal of Applied Physics (2022) 132(11)*.

### 4.1. Motivation

A major difficulty for the exploitation of the Bi<sub>2</sub>Se<sub>3</sub> surface states is the n-type degeneracy formed due to Se vacancies. It is of extreme importance to reduce the bulk carrier concentration in order to reduce their contribution to electrical transport. One approach commonly used is through the doping of Bi<sub>2</sub>Se<sub>3</sub> with specific elements to achieve p-type doping. The doping of Bi<sub>2</sub>Se<sub>3</sub> with Sn<sup>67</sup>, Ag<sup>68,69</sup>, or In<sup>66,70</sup>, can shift the Fermi level ( $E_F$ ) into the band gap and closer to the Dirac point. Sn doping resulted in an  $E_F$  shift towards the Dirac point without destroying the surface states, whereas In doping showed a topological phase transition destroying the surface states for doping higher than 7%. The Ag-doped Bi<sub>2</sub>Se<sub>3</sub> accomplished a bulk electron concentration reduction with a minimum  $n_{3d}$  of  $4.7 \times 10^{18} \text{ cm}^{-3}$ , which is still higher than the maximum desired value for pure surface state transport at RT ( $10^{15} \text{ cm}^{-3}$ )<sup>71</sup>.

Furthermore, Bi<sub>2</sub>Se<sub>3</sub> has been doped with exotic elements to obtain new physical phenomena such as magnetic dopants to achieve a magnetic topological insulator. Manganese (Mn) brought a lot of attention recently, due to the presence of ferromagnetism that can lead to the quantum anomalous Hall effect (QAHE) in Bi<sub>2</sub>Te<sub>3</sub><sup>72</sup>. Instead of an integer quantum Hall effect with a broken time-reversal symmetry by an external magnetic field, the QAHE creates spinful chiral edge states due to doping magnetization and spin-orbit coupling. Other elements, such as Cr<sup>73</sup>, Co<sup>62</sup>, or Fe<sup>74</sup> are being studied to achieve the QAHE. From a different perspective, Cu<sup>75,76</sup>, Sr<sup>77,78</sup>, and Nb<sup>79,80</sup> doped Bi<sub>2</sub>Se<sub>3</sub> reveal another novel phenomenon: topological superconductivity. This effect takes place due to the rotational symmetry breaking owing to the intercalation of doping atoms in the Van der Waal gap that leads to a zero-resistance material without destroying the surface states. The topological superconductivity (TSC) brought, as well, a lot of interest since it has the capability to host the quasi-particle Majorana fermions<sup>5,81</sup>, which is a key to the future of quantum computation<sup>82,83</sup>. The superconductivity achieved by Cu-doped Bi<sub>2</sub>Se<sub>3</sub> presented a critical

temperature of approximately 4 K by a melt-growth technique. Likewise, other elements (Sr, Nb) can lead to the superconductivity corresponding to the family  $\text{A}_x\text{Bi}_2\text{Se}_3$  (where A= Cu, Sr, Nb).

The exploration of new doping elements is of meaningful value, which can lead to different physical phenomena. Recently, B. Wiendlocha et al.<sup>84</sup> predicted resonant levels peaks from the density of states inside the gap in Ga-doped  $\text{Bi}_2\text{Se}_3$ , which could indicate a p-type doping impurity. In a different approach, Ankita Phutela et al. predicted that  $\text{GaBiSe}_2$  should form a strong topological insulator<sup>85</sup>. Considering the lack of experimental data on Ga-doped  $\text{Bi}_2\text{Se}_3$ , it is of crucial importance to investigate the influence of Ga as a dopant and to provide insight into the theoretical aspect. In the present section, Ga-doping  $\text{Bi}_2\text{Se}_3$  is implemented due to the lack of previous experimental research. Additionally, in a similar way, the doping of  $\text{Bi}_2\text{Se}_3$  by Cu is motivated by a lack of experimental studies of doping by Cu in MBE growth<sup>86</sup>. MBE offers the fabrication of wafer-scale and uniform films that are crucial for device fabrication, however, the topological superconductivity in  $\text{Cu}_x\text{Bi}_2\text{Se}_3$  was never achieved by MBE growth. Cu doping nematic superconductivity was reported for percentages between 2 – 12 at.%<sup>87</sup>.

## 4.2. Structural properties

Fig. 4.1 illustrates the unit cell, rhombohedral crystal structure, of the  $\text{Bi}_2\text{Se}_3$ . The doping element has 3 possible sites in the crystal structure (Fig. 4.1 b, c, d). First, Cu and Ga atoms are prone to replace Bi atoms (Fig 4.1 b) due to their similar valence. Moreover, the Pauling electronegativity of Ga (1.81) or Cu (1.9) is closer to the Bi (2.02) instead of the Se (2.55). The doping element can be interstitial in the quintuple layers sites (Fig 4.1 c) or they can be intercalated in the Van der Waals gap (Fig 4.1 d). It is important to highlight that the topological superconductivity achieved in  $\text{Cu-Bi}_2\text{Se}_3$  is attributed to the intercalation of Cu atoms in the Van der Waal gap<sup>75</sup>.

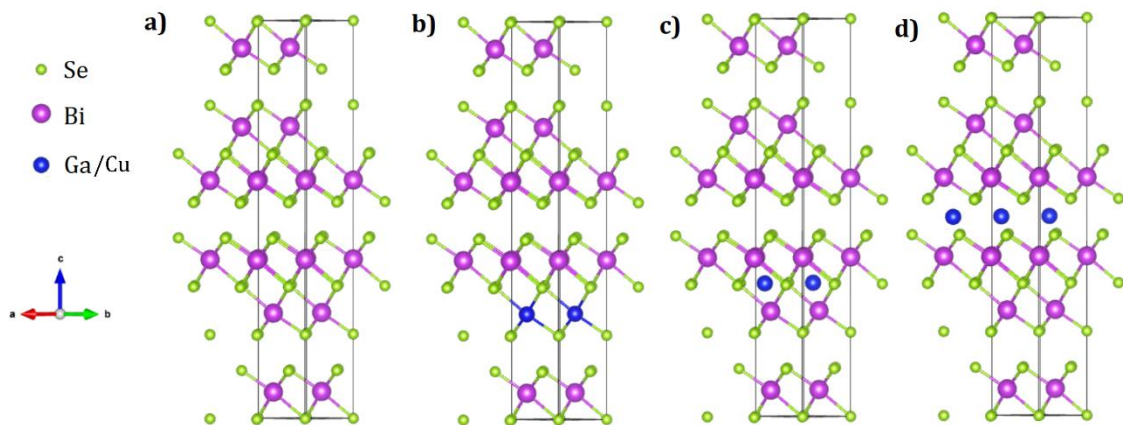


**Figure 4.1** Unit cell of a)  $\text{Bi}_2\text{Se}_3$  crystal structure and possible doping atoms site in the crystal: b) Bi substitution, c) interstitial in the quintuple layer or d) intercalated into the Van der Waals gap. Edited from Daniel Brito et al. <sup>120</sup>.

#### 4.2.1. *In situ* RHEED

To perform the doping of Bi<sub>2</sub>Se<sub>3</sub>, Ga or Cu is evaporated simultaneously during the Bi<sub>2</sub>Se<sub>3</sub> growth. Different doping percentages are implemented by simply changing the doping element cell temperature. The Ga cell temperature varies from 680 to 765 °C and the Cu cell temperature varies from 830 to 860 °C. The remaining growth parameters are kept the same as in Chapter 3, such as substrate temperature, growth rate, and Se valve, .... The sapphire substrate is treated with surface treatment as explained in section 3.1 instead of the buffer layer, to prevent the diffusion of In atoms into the Bi<sub>2</sub>Se<sub>3</sub> layer. The doping element beam fluxes are measured for each cell (Ga and Cu), by the beam flux monitor to control the doping percentage. Since the substrate temperature (310°C) is higher than the Se cell temperature (285°C), the growth rate depends only on the Bi flux<sup>88</sup>. The doping is controlled by adjusting the (Ga: Bi) or (Cu: Bi) flux ratio, aiming for the nominal doping percentages of (Ga: 0.8 at.%, 2 at.%, 7 at.%, 14 at.%) and (Cu: 2 at.%, 4 at.%, 7 at.%). Further compositional characterization technique (XPS) was used to quantify the doping. A higher doping (14 at.%) of Ga is selected to obtain a systematic study of the Ga doping, and hence comprehend wherein the material starts to deteriorate the Bi<sub>2</sub>Se<sub>3</sub> quality. The Ga-doped Bi<sub>2</sub>Se<sub>3</sub> film thickness is 60 nm and the Cu-doped Bi<sub>2</sub>Se<sub>3</sub> thickness is 40 nm due to a change in the growth rate over time.

During the deposition, the morphology and crystallographic information can be extracted *in situ* by the RHEED. The RHEED patterns are shown in Fig. 4.2 for different doping levels of Bi<sub>2</sub>Se<sub>3</sub> for Ga (Fig 4.2 b-d) and Cu (Fig 4.2 f-h). Two distinct undoped samples of Bi<sub>2</sub>Se<sub>3</sub> are grown for each doping batch (Fig 4.2 a and e) as reference. The good quality Bi<sub>2</sub>Se<sub>3</sub> pattern is characterized by sharp streaky lines and a sixfold symmetry under sample azimuthal rotation. This pattern is preserved with doping up to 2 at.% of Ga Fig 4.2 b. However, at 7 at.% Ga doping Bi<sub>2</sub>Se<sub>3</sub> pattern (Fig 4.2 c) starts to exhibit spare dots in the lines, which can be related to a 3D growth or an increase in the film roughness by the incorporation of Ga. When doping increases to 14 at.% (Fig 4.2 d) it destroys the single crystallinity of the Bi<sub>2</sub>Se<sub>3</sub>, observed by the presence of concentric rings characteristic of polycrystalline films.

The Cu-doped Bi<sub>2</sub>Se<sub>3</sub> RHEED patterns do not show a significant difference upon Cu doping. The pattern is unchanged up to a doping of 7 at.% (Fig 4.2 h). The signal intensity, however, seems to increase upon doping. This effect can be attributed to the doping of metallic elements, which can increase the reflectivity. Thus, it could indicate an accumulation of Cu elemental on the surface. In terms of roughness, the pattern is spot free meaning that the roughness is not altered.

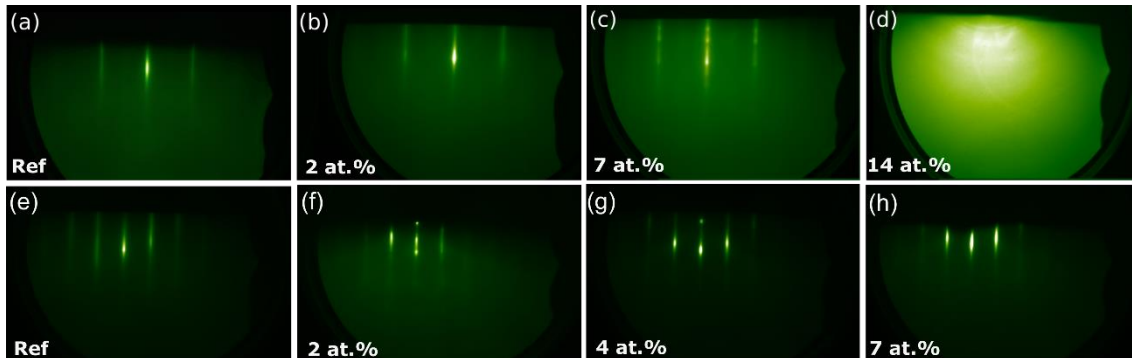


**Figure 4.2** RHEED pattern of a) undoped  $\text{Bi}_2\text{Se}_3$ , Ga-doped with b) 2 at.%, c) 7 at.%, d) 14 at.% in the [110] direction. RHEED pattern of e) undoped  $\text{Bi}_2\text{Se}_3$  and Cu doped with f) 2 at.%, g) 4 at.% and h) 7 at.% in the [100] direction. Pannels (a)-(d) are edited from Daniel Brito et al. <sup>120</sup>

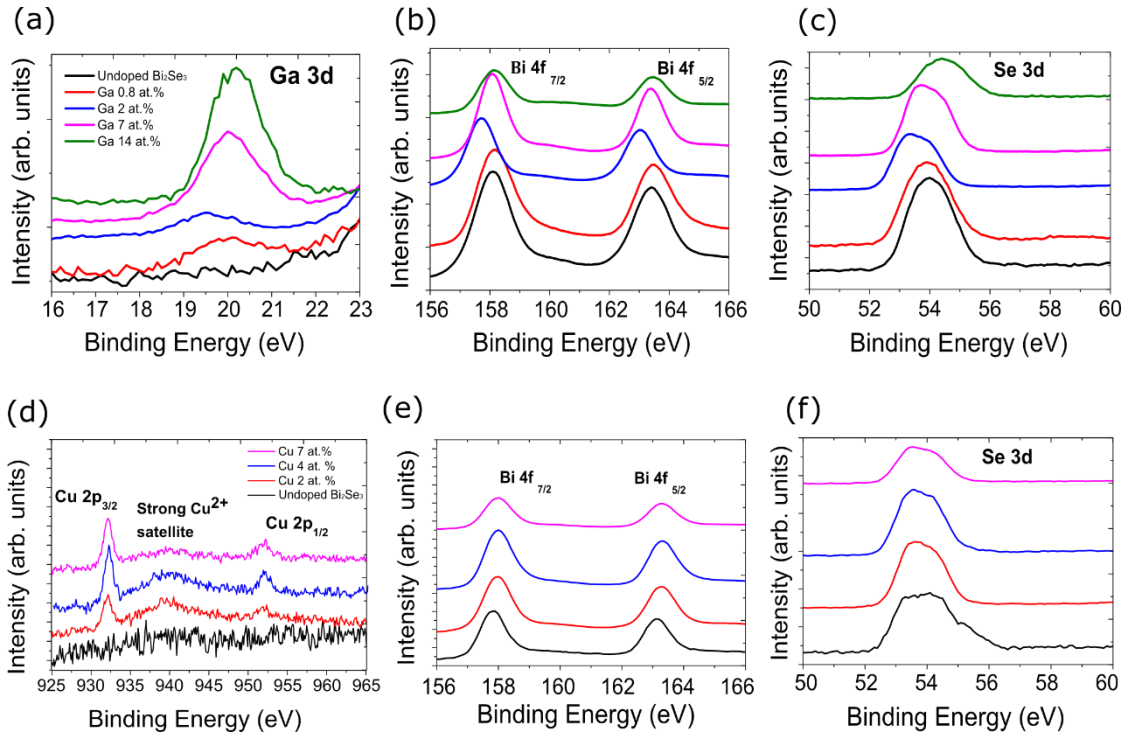
#### 4.2.2. X-ray photoelectron Spectroscopy (XPS)

Fig. 4.3 shows high-resolution XPS spectra of  $\text{Bi}_2\text{Se}_3$  used to quantify the thin film composition of doped samples with different levels of doping. The Ga signal is observed in Fig 4.3 a) for all the Ga- $\text{Bi}_2\text{Se}_3$  samples, where the presence of the Ga binding energy (BE) peak confirmed the successful incorporation in  $\text{Bi}_2\text{Se}_3$ . The BE of Ga  $3d$  is detected around 20 eV for all the samples. The peak intensity increases with the percentage of Ga. However, the characteristic oxide BE peak is close to the Ga peak of  $\approx 20.5$  eV. Furthermore, the surface of Ga-doped  $\text{Bi}_2\text{Se}_3$  presented a higher concentration of Ga, which indicates a segregation of Ga atoms toward the surface. Annex S1 shows the Ga spectra before and after  $\text{Ar}^+$  ion etching.

The XPS peaks of the Bi are presented in Fig 4.3 b) and e), for the Ga-doped and Cu-doped  $\text{Bi}_2\text{Se}_3$ , respectively. The doublets Bi  $4f_{7/2}$  and  $4f_{5/2}$  are localized at 158.1 and 163.4 eV, respectively. Additionally, for the Cu-doped  $\text{Bi}_2\text{Se}_3$  (Fig 4.3 e), a shift to higher energies is visible as the doping is increased, which points to a Bi substitution with Cu atoms <sup>89</sup>. Both signals presented a small percentage of oxides, such as  $\text{Bi}_2\text{O}_3$  <sup>89</sup>. The Se  $3d$  peak doublet (Fig 4.3 c) and f)) is not discerned due to the superposition of both peaks at  $\sim 54$  eV. Analogous to the Bi signal, the characteristic Se oxides, at 58.9 eV<sup>63</sup>, were minimal.

Finally, the Cu spectra are shown in Fig 4.3 d) for the Cu-doped  $\text{Bi}_2\text{Se}_3$ . Two Cu peaks are observed,  $2p_{3/2}$  and  $2p_{1/2}$  at 932.1 eV and 952 eV, respectively. Similarly to the Ga signal, the intensity increases with the Cu doping. Moreover, a strong and broad  $\text{Cu}^{2+}$  satellite peak appears approximately at 940 eV, as reported in the literature <sup>90</sup>. The strong satellite peak presence indicates the existence of divalent  $\text{Cu}^{2+}$  in the film, which is an indication of the Bi atom being replaced with Cu atoms <sup>91–93</sup>.

Table 4.1 shows the composition of each element extracted from the XPS data. The nominal percentages for the Ga and Cu doping agree with the measured doping with a small deviation. From this point forward the nominal percentage is used to facilitate the reading.



**Figure 4.3** XPS spectra for Ga-doped Bi<sub>2</sub>Se<sub>3</sub> with the respective high-resolution spectra for a) Ga 3d, b) Bi 4f and c) Se 3d core lines for all doping percentages. XPS spectra for the Cu-doped Bi<sub>2</sub>Se<sub>3</sub> with the respective high-resolution spectra for d) Cu 2p, e) Bi 4f and f) Se 3d core lines for all doping percentages. Edited from Daniel Brito et al. <sup>120</sup>.

**Table 4.1** Chemical composition of the Ga/Cu-doped Bi<sub>2</sub>Se<sub>3</sub> extracted from the XPS analysis.

Elements	Chemical composition (at.%)							
	Undoped	0.8	2 at.%	7 at.%	14 at.%	2 at.%	4 at.%	7 at.%
	Bi <sub>2</sub> Se <sub>3</sub>	at.% Ga	Ga	Ga	Ga	Cu	Cu	Cu
Bi	33.4	35.3	31.8	29.6	21.1	34.8	31.5	32.1
Se	66.6	63.9	66.8	64.5	65.5	63.0	64.1	62.0
Ga	...	0.8	1.4	5.9	13.4	...	...	...
Cu	...	...	...	...	...	2.2	4.4	5.9

### 4.2.3. XRD and Raman characterization

Fig 4.4 presents the XRD pattern for the Ga (Fig 4.4 a) and b)) and Cu (Fig 4.4 c) and d)) doped Bi<sub>2</sub>Se<sub>3</sub> with nominal doping percentage increasing from bottom to top. All the data is performed with the same scan recipe, integration of time, and sample thickness. All the samples presented a single crystal pattern referent to the Bi<sub>2</sub>Se<sub>3</sub> as the pure Bi<sub>2</sub>Se<sub>3</sub> in the previous chapter and reported in the literature<sup>73</sup>. Lastly, none of the samples present any contaminations such as GaSe<sup>94</sup> ( $\theta \approx 12^\circ$ ,  $22^\circ$  or  $46^\circ$ ) or CuSe<sup>95</sup> ( $\theta \approx 30^\circ$  or  $45^\circ$ ). Fig 4.4 b) shows a high-resolution diffractogram of the (0015) plane for the Ga-doped samples to distinguish the Ga doping influence on the lattice parameter with more details. The peak intensity is reduced by more than 50% upon doping, which suggests a deterioration of the crystal quality, in agreement with the RHEED pattern (Fig. 4.2 b-d). Concerning the peak position, there is a shift towards lower angles with the Ga doping. Moreover, for the Ga percentage of 2 and 7 at.% a split double peak towards lower angles occurs. The double peak formation can indicate the formation of a new competing phase while the shift towards lower angles is related to the expansion of the c lattice parameter. The double peak is later converged into a single peak for a Ga doping of 14 at.%.

For the Cu-doped Bi<sub>2</sub>Se<sub>3</sub>, the high-resolution diffractogram of the (0015) plane is shown in Fig 4.4 d). Contrary to the Ga-doped Bi<sub>2</sub>Se<sub>3</sub>, doping with Cu does not influence the peak intensity. This information supports the RHEED spectra (Fig. 4.2 e-h ), where Cu doping leads to brighter streaky lines compared to the Ga-doped samples. Similarly, there is an observable small shift towards lower angles for the Cu-doped samples compared to the reference Bi<sub>2</sub>Se<sub>3</sub>.

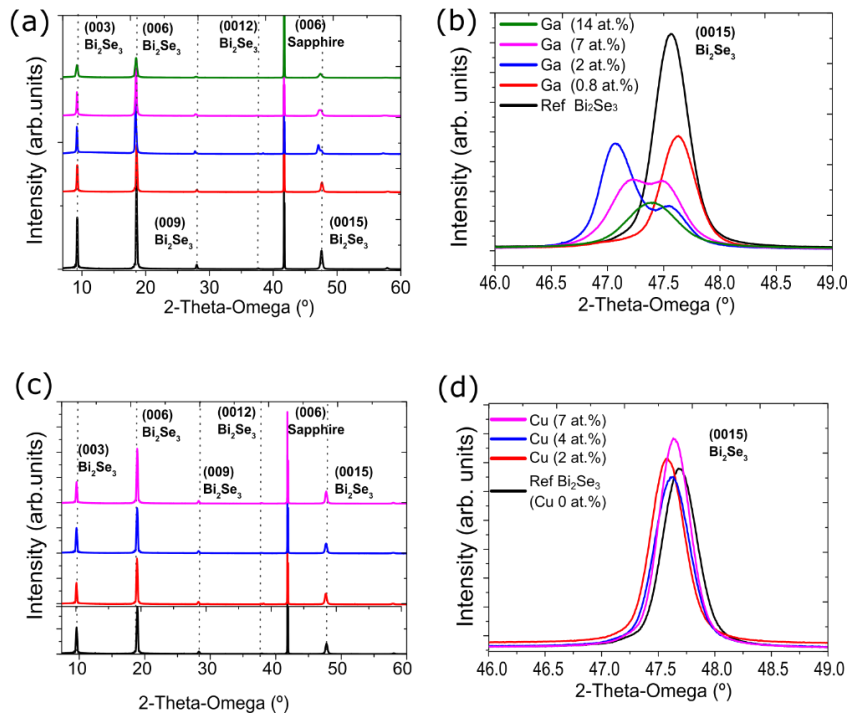


**Figure 4.4** XRD pattern for the a) Ga-doped Bi<sub>2</sub>Se<sub>3</sub> with b) high-resolution XRD pattern for the (0015) plane. XRD pattern for the c) Cu-doped Bi<sub>2</sub>Se<sub>3</sub> with d) high-resolution XRD pattern for the (0015) plane. Edited from Daniel Brito et al.<sup>120</sup>

The XRD peak shift with Ga and Cu doping suggested a modification in the crystal lattice parameter. Based on the XRD data, the  $c$  and  $a$  lattice parameters are calculated as described in sections 2.2.1 and 3.4.1. The results are shown in Fig 4.5. The Ga-doped Bi<sub>2</sub>Se<sub>3</sub>  $c$  and  $a$  lattice parameter are presented in Fig 4.5 a and b, respectively. An  $a$  of 4.14 Å and  $c$  of 28.66 Å for the undoped Bi<sub>2</sub>Se<sub>3</sub> is obtained, in agreement with the literature<sup>62-65</sup>. Previous studies from In-doped Bi<sub>2</sub>Se<sub>3</sub> reported the decrease in the  $c$  lattice parameter due to the Bi atoms substitution with In atoms<sup>63,64</sup>. Likewise, Ga<sup>3+</sup> ions exhibit a smaller radius (0.62 Å) compared to the Bi<sup>3+</sup> (1.03 Å)<sup>96</sup>, then the replacement of Bi atoms with Ga should lead to a decrease in the crystal lattice. The  $c$  lattice tends to increase with the percentage of Ga higher than 7 at.%. Furthermore, the second peak formation is treated as a new phase, thus a new lattice parameter is required to be calculated as a different lattice, as illustrated with a blue dot, produces a maximum  $c$  lattice parameter of 28.92 Å. The intercalation of Ga atoms in the Van der Waals gap is speculated to be occurring since it would lead to the expansion of the  $c$  lattice. The intercalation of different atoms was previously reported for Cu/Ag/Co/Sr-Bi<sub>2</sub>Se<sub>3</sub><sup>62,68,78,91</sup>, where an expansion of the lattice is observed. The value starts to decrease compared to smaller doping percentages but is still higher than the reference. For a higher concentration of Ga (14 at.%), the peak is converged to a single one with a value of 28.77 Å. This behavior is hypothesized to be happening because of a mixture of Ga intercalation and substitutional Ga atoms with Bi.

On the other hand, Cu-doped samples presented a similar behavior as the Ga-doping by an increase in the  $c$  lattice parameter with Cu doping. Firstly, the undoped Bi<sub>2</sub>Se<sub>3</sub> showed a reduced  $c$  lattice parameter of 28.60 Å compared to the reference sample of the Ga-doped batch. It is assumed that the high Cu cell temperature (~ 900 °C) can be prejudicial for the Bi<sub>2</sub>Se<sub>3</sub> film quality by the evaporation of undesired elements. Fig 4.5 c and d show the lattice parameter evolution with Cu doping. The Bi<sub>2</sub>Se<sub>3</sub> unit cell volume decreases as the Cu doping is increased up to 2 at.%, whereas with doping higher than 2 at.%, it starts to increase. Similar to Ga doping there is an increment of the unit cell volume, which indicates an expansion of the crystal structure. However, the values are significantly smaller than the Ga-doped samples. In terms of lower Cu doping (2 at.%), the reduced volume can indicate that the Cu can replace the Bi atoms as observed in the literature<sup>97</sup>.

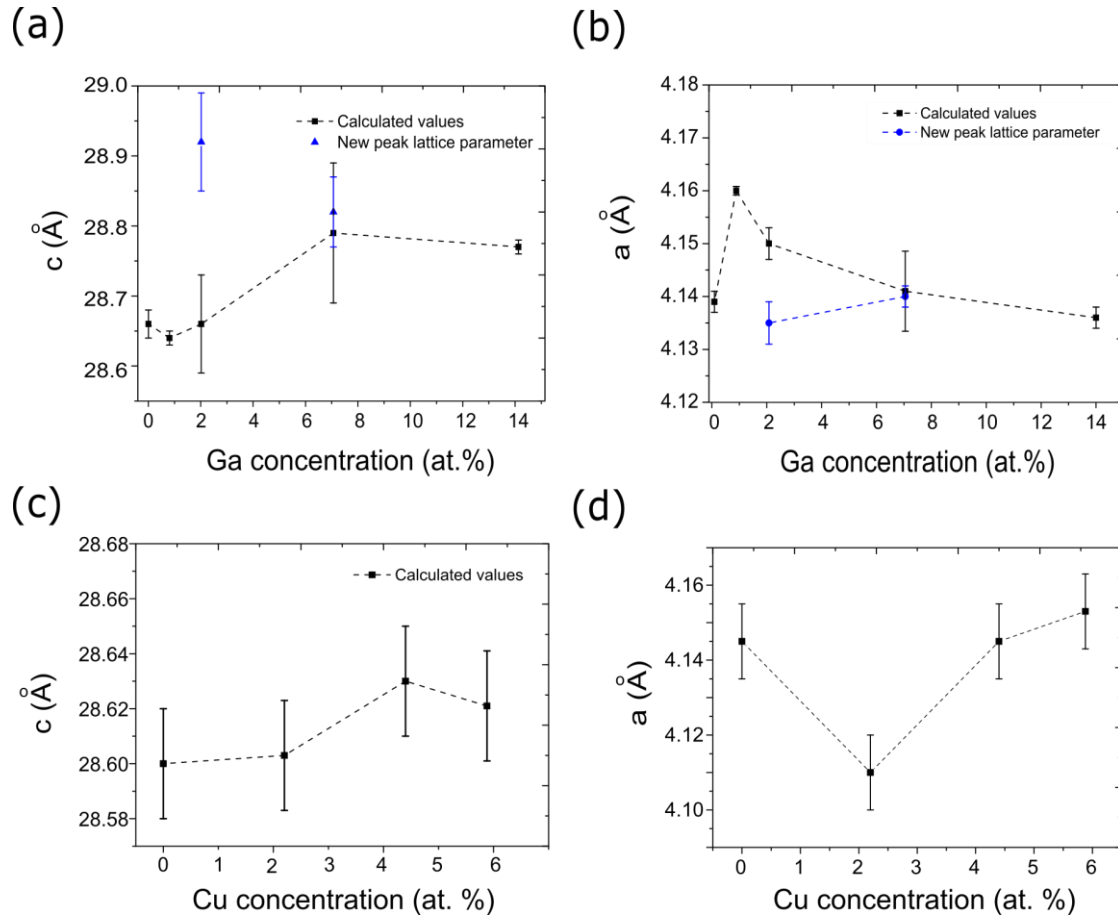


**Figure 4.5** Crystal lattice parameters a)  $c$  and b)  $a$  as a function of the Ga atomic doping percentage. Crystal lattice parameters c)  $c$  and d)  $a$  as a function of the Cu atomic doping percentage. The calculated values are extracted from XRD by Eq. (2.2) Edited from Daniel Brito et al. <sup>120</sup>.

Raman spectroscopy is commonly used as a structural and compositional characterization technique. The Bi<sub>2</sub>Se<sub>3</sub> vibrational modes are studied by Raman spectroscopy at room temperature and the Ga/Cu doping influence is studied by examining the behavior of the vibrational modes upon doping. Fig. 4.6 shows the Raman spectra for increasing Ga (Fig. 4.6 a) and Cu (Fig. 4.6 c) doping from bottom to top and the evolution of the peak position as a function of the doping concentration (Fig. 4.6 b and d). Three vibrational peaks are observed as characteristic of the Bi<sub>2</sub>Se<sub>3</sub> belonging to the  $A_{1g}^1$ ,  $E_g^2$  and  $A_{1g}^2$  vibrational modes, at 71, 130, and 174 cm<sup>-1</sup>, respectively <sup>62,98</sup>.

As observed in Fig. 4.6 a), the incorporation of Ga produces a small shift towards lower frequencies. Furthermore, as observed in the XRD pattern, a double peak for the percentage of 2 at.% of Ga forms a small double peak for the  $E_g^2$  vibrational mode at lower frequencies, which leads to a significant new peak deviated of  $\approx 7.6$  cm<sup>-1</sup> (Fig. 4.6 b pink dot) from the reference peak position. For the remaining doping concentrations, no doublet and undesired phase, such as GaSe is observed. The peak position as a function of the Ga doping

is presented in Fig 4.6 b). Earlier studies performed in intercalated Cu-Bi<sub>2</sub>Se<sub>3</sub> have shown that the intercalation of Cu in the van der Waals gap leads to a red shift in the vibrational modes<sup>91</sup>. The redshift in Ga doping that we observe corroborates the XRD hypothesis that Ga atoms can be intercalated in the Van der Waals gap, despite the shift being small compared to the error margin.

On the other hand, the shift to higher frequencies in Bi<sub>2</sub>Se<sub>3</sub> is reported to occur when Bi atoms are replaced with lighter elements and stronger binding forces<sup>64</sup>. Both 0.8 at.% Ga and 2 at.% Cu showed a blue shift that can be explained as a competitive substitution of Bi atoms for this small doping. Likewise, Cu-doped Bi<sub>2</sub>Se<sub>3</sub> (Fig 4.6 d) showed doping with Cu leads to a blue shift.

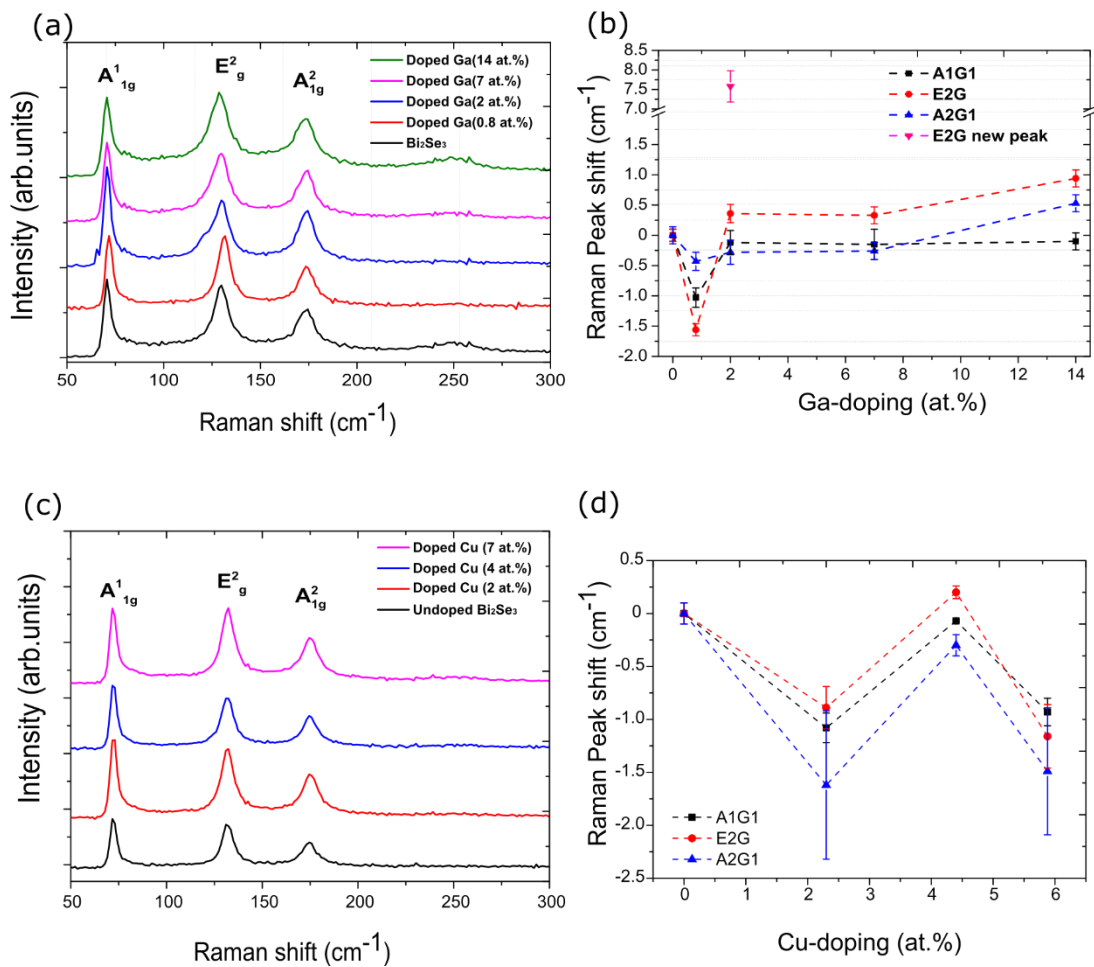


**Figure 4.6** Room temperature Raman spectroscopy for a) undoped and Ga-doped Bi<sub>2</sub>Se<sub>3</sub> and b) peak position as a function of the nominal Ga percentage. Raman spectroscopy for c) undoped and Cu-doped Bi<sub>2</sub>Se<sub>3</sub> and b) peak position as a function of the nominal Cu percentage. Edited from Daniel Brito et al.<sup>120</sup>

#### 4.2.4. Transmission electron microscopy (TEM)

Finally, to conclude the structural analysis of the doped  $\text{Bi}_2\text{Se}_3$ , transmission electron microscopy (TEM) is implemented, which offers a direct visualization of the crystal structure with spatial resolution. Moreover, the dopant localization and distribution can be mapped in conjunction with an energy-dispersive x-ray spectroscopy.

A STEM cross-sectional image of the Cu-doped  $\text{Bi}_2\text{Se}_3$  for both doping percentages is shown in Fig. 4.7(a) 2 at.% and b) 7 at. %). The samples are prepared with a Ga ion irradiation via FIB to cut a lamella to obtain the STEM images. However, the Ga-doped  $\text{Bi}_2\text{Se}_3$  is not measured due to the possible contamination during the preparation of the sample with Ga atoms, which can compromise the STEM images.

The Cu- $\text{Bi}_2\text{Se}_3$  (Fig. 4.7) reveals an atomically ordered structure by the visualization of a stack of 5 atoms bonded vertically (quintuple layers, QL), separated by a Van der Waals gap, confirming the rhombohedral crystal structure of the  $\text{Bi}_2\text{Se}_3$ . The images do not present significant defect percentages, such as twinning or dislocations, even at lower magnification.

The good crystallinity of the  $\text{Bi}_2\text{Se}_3$  is obtained even upon a high Cu percentage of 7 at.%. Thus, the incorporation of Cu atoms in the lattice does not disrupt the crystal quality and does not increase the number of defects. Cu atoms are not distinguished from Bi and Se atoms. Nonetheless, energy-dispersive X-ray spectroscopy can identify atomic localization (Annex S3). As observed in the image in the annex, Bi and Se atoms are well-defined and localized in the crystal structure, whereas Cu atoms are randomly distributed in the crystal structure which reinforces the idea that Cu atoms are replacing Bi atoms in the lattice rather than intercalation.

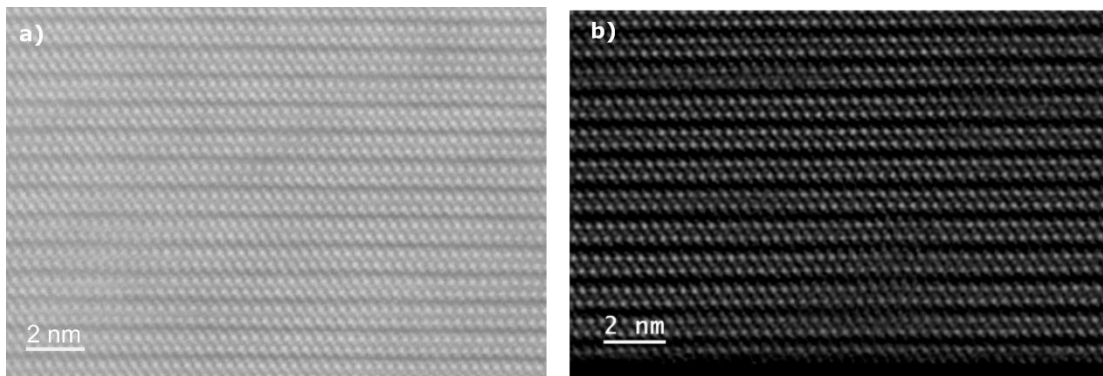


**Figure 4.7** STEM images along the [100] direction of  $\text{Bi}_2\text{Se}_3$  doped with a) 2 at.% and b) 7 at.% of Cu grown on a sapphire substrate.

## 4.3. Electrical properties

### 4.3.1. Transport properties

To minimize the effect of the bulk contributions, the electrical properties are measured at low temperatures. Hall effect measurements can provide information on the level of defects and the impact in terms of the transport properties measurements.

#### Ga-doped Bi<sub>2</sub>Se<sub>3</sub>

Fig 4.8 presents the transport properties of undoped and Ga-doped Bi<sub>2</sub>Se<sub>3</sub> extracted from Hall effect measurements. The resistivity, bulk, sheet electron concentration, and mobility are shown as a function of the temperature. The doping percentages used are 2 and 7 at.%. The 0.8 and 14 at.% doping samples are not studied due to the reduced effect of the doping on observable properties and the reduced crystal quality of the samples, respectively.

Fig 4.8 a) shows the resistivity as a function of the temperature. Both samples present a metallic behavior, which means a decrease of the resistivity with the decrease of the temperature which suggests that the material conductance is mainly dominated by the bulk conductance. The undoped Bi<sub>2</sub>Se<sub>3</sub> exhibits a larger resistivity for temperatures higher than 100 K than the Ga-doped samples, reverted as the temperature decreased. This increase of the resistivity upon doping reveals a greater degree of crystal disorder as the Ga concentration is increased.

In terms of the electron concentration and mobility (Fig 4.8 b) and d)), undoped Bi<sub>2</sub>Se<sub>3</sub> shows a sheet concentration of  $\sim 7 \times 10^{13} \text{ cm}^{-2}$  and a mobility of  $423.5 \text{ cm}^2 \text{ V}^{-1} \text{ s}^{-1}$  at RT, which is in agreement with previous reports for pure MBE-grown Bi<sub>2</sub>Se<sub>3</sub><sup>39,54,58</sup>. The 60 nm thick Bi<sub>2</sub>Se<sub>3</sub> exhibits a bulk electron concentration of  $\sim 1 \times 10^{19} \text{ cm}^{-3}$  (Fig 4.8 c), which increases sixfold to  $\sim 6 \times 10^{19} \text{ cm}^{-3}$  for both Ga percentages. The high concentration is accompanied by a reduced mobility of  $119.2 \text{ cm}^2 \text{ V}^{-1} \text{ s}^{-1}$  with Ga doping. Therefore, Ga acts as a donor impurity, which reinforces the assumption of the intercalation of Ga atoms in the Van der Waals gap since free Ga atoms in the Van der Waals gap contribute with free electrons for the transport. The substitution of Bi atoms with Ga should not produce such notable influence in the concentration of electrons due to their similar valence. Furthermore, the introduction of defects into the VdW gap, meaning intercalation of atoms, produces potential barriers, leading to a sudden decrease in mobility<sup>99</sup>. Nonetheless, the substitution of Bi atoms with dopant atoms can also decrease the mobility due to ionized impurity scattering. Thus, the decrease in mobility supports the hypothesis of the intercalation of Ga atoms and the substitution in the crystal.

As a function of the temperature the electron concentration and the mobility have opposite tendencies. The undoped Bi<sub>2</sub>Se<sub>3</sub> electron concentration increases with the

temperature, whereas the Ga-doped Bi<sub>2</sub>Se<sub>3</sub> electron concentration decreases as the temperature increases. This behavior is observed in Sr intercalated Bi<sub>2</sub>Se<sub>3</sub> and Nb-Bi<sub>2</sub>Se<sub>3</sub><sup>100</sup> which are known to exhibit superconductivity at low temperatures<sup>78,101,102</sup>. This behavior is in accordance with the resistivity since the linear behavior is expected due to the electron-phonon scattering. The Ga-Bi<sub>2</sub>Se<sub>3</sub> presented a reduced slope for the resistivity, as a result of the high carrier concentration, producing an increase in the screening of the deformation potential and thus a reduced electron-phonon coupling. Finally, mobility has a similar tendency for all samples, because it decreases with the temperature for the undoped Bi<sub>2</sub>Se<sub>3</sub> since the electron-phonon scattering is more pronounced for lower temperatures. Hence, the drift velocity is reduced which reaches a maximum mobility of 1700 cm<sup>2</sup> V<sup>-1</sup> s<sup>-1</sup> for the undoped Bi<sub>2</sub>Se<sub>3</sub>.

In conclusion, the electrical properties of the Ga-Bi<sub>2</sub>Se<sub>3</sub> reinforce the hypothesis of Ga atoms being intercalated, acting as donor impurities. Furthermore, the intercalation of atoms in the VdW gap is known to lead to a rotational symmetry breaking and consequently can lead to superconductivity. The electron concentration trend observed is similar to the previously reported Sr/Nb-Bi<sub>2</sub>Se<sub>3</sub> superconductors. However, the zero resistivity is not observed in the resistivity graph down to temperatures of 1.5 K, meaning that the superconductivity is not observed.

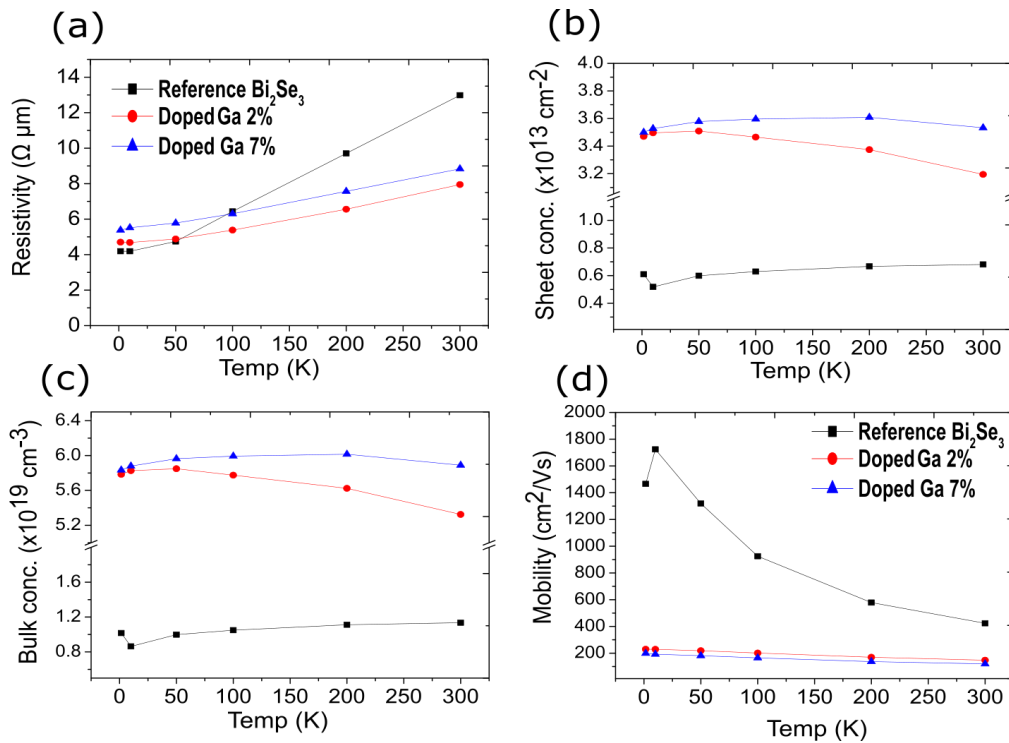


**Figure 4.8** a) Resistivity, b) sheet concentration, c) bulk concentration, d) mobility of undoped and Ga-doped Bi<sub>2</sub>Se<sub>3</sub> as a function of the temperature extracted from the Hall effect measurements. All samples are n-type. Edited from Daniel Brito et al.<sup>120</sup>.

### Cu-doped Bi<sub>2</sub>Se<sub>3</sub>

Fig 4.9 presents the transport properties of undoped and Cu-doped Bi<sub>2</sub>Se<sub>3</sub> extracted from Hall effect measurements. It shows the resistivity, bulk, sheet electron concentration, and mobility as a function of the temperature up to 100 K. In order to compare the different types of doping, the same doping concentrations (Cu 2 and 7 at.%) are used. As previously observed, all the samples exhibit a decrease in resistivity with a decrease in the temperature (Fig 4.9 a). It reveals a weak metallic behavior, which suggests that the transport is controlled by the bulk conductance. As opposed to Ga-doping, doping with Cu produces a systematic increase in resistivity. The increase in resistivity can also be associated with the substitution of Bi atoms with Cu atoms (Cu<sup>2+</sup>), which could act as an acceptor impurity, and consequently increase the resistivity<sup>95,103,104</sup>. Indeed, as observed for the electron concentration (Fig 4.9 b), the Cu acts as an acceptor impurity. Undoped Bi<sub>2</sub>Se<sub>3</sub> presents a sheet concentration of  $\sim 8 \times 10^{13} \text{ cm}^{-2}$ , which upon Cu doping decreases by almost a factor of 2, to  $\sim 5 \times 10^{13} \text{ cm}^{-2}$  with Cu of 7%. The TSC in Cu-doped Bi<sub>2</sub>Se<sub>3</sub> requires the intercalation of Cu in the VdW gap, but Cu atoms tend to bind in the crystal structure, replacing Bi atoms<sup>95,97,103</sup>. The electron concentration shows little dependence on the temperature. The mobility of the undoped Bi<sub>2</sub>Se<sub>3</sub> at 100 K is  $\approx 450 \text{ cm}^2 \text{ V}^{-1} \text{ s}^{-1}$  with a maximum of  $\sim 625 \text{ cm}^2 \text{ V}^{-1} \text{ s}^{-1}$  at 1.5 K. Contrary to the electron concentration, the mobility does not show an improvement upon Cu doping. The mobility was expected to be increased upon Cu doping as a consequence of the lower electron concentration of the Cu-doped Bi<sub>2</sub>Se<sub>3</sub>. The values are reduced from  $625 \text{ cm}^2 \text{ V}^{-1} \text{ s}^{-1}$  to  $\sim 450 \text{ cm}^2 \text{ V}^{-1} \text{ s}^{-1}$  at 1.5 K with a Cu doping of 7 at.%. This can be a consequence of the scattering mechanism due to the presence of Cu impurities.

In conclusion, Cu doping affects positively the transport properties of the topological insulator by reducing the bulk concentration, though, the TSC was not achieved in Cu-Bi<sub>2</sub>Se<sub>3</sub> (lack of a 0  $\Omega$  resistivity at low temperatures) as the Cu impurity worked as an acceptor replacing Bi atoms and not as an intercalated impurity which is a crucial point to earlier observations of the topological superconductivity<sup>75</sup>.

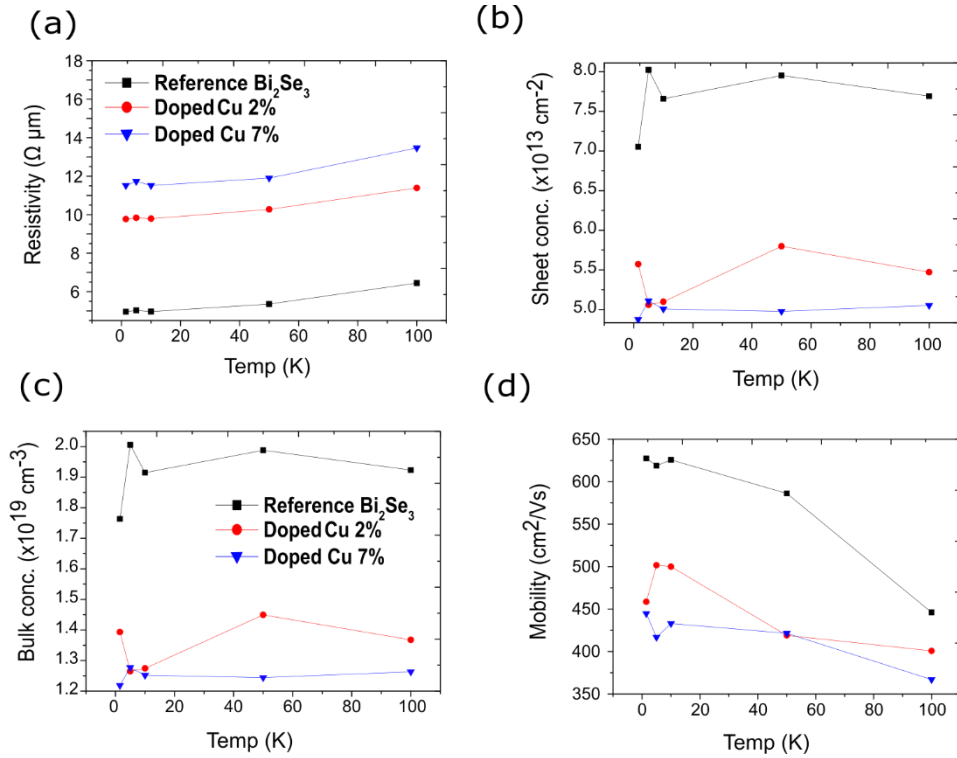


**Figure 4.9** a) Resistivity, b) sheet concentration, c) bulk concentration, d) mobility of undoped and Cu-doped  $\text{Bi}_2\text{Se}_3$  as a function of the temperature extracted from Hall effect measurements. All samples are n-type.

### 4.3.2. Weak antilocalization effect in doped $\text{Bi}_2\text{Se}_3$

As described in section 1.2.4, the weak antilocalization effect (WAL) is a physical phenomenon characteristic of TIs due to the presence of strong spin-orbit coupling in the bulk and 2D Dirac-like physics at the edges<sup>14,105</sup>. This effect was experimentally observed in  $\text{Bi}_2\text{Se}_3$ <sup>49,67,93</sup>.

Fig 4.10 a and c show the magnetoconductance of the Ga and Cu-doped  $\text{Bi}_2\text{Se}_3$ , respectively, showing the symmetric cusp typical for a WAL response to small magnetic fields at 1.5 K. The dash lines represent the fitting by the HLN model. The fitting parameters are presented in Fig 4.10 b and d for the Ga and Cu-doped  $\text{Bi}_2\text{Se}_3$ , respectively. In terms of the Ga doping (Fig 4.10 a and b), the undoped  $\text{Bi}_2\text{Se}_3$  showed a sharp cusp of the magnetoconductance indicating the presence of conductive surface states. The prefactor ( $\alpha$ ) obtained is -0.96, which is extremely close to the ideal value of -1, which represents two decoupled surfaces holding topological states. The coherence length ( $L_\phi$ ) obtained is 804 nm, which is in agreement with previous reports of  $\text{Bi}_2\text{Se}_3$ <sup>49,61,67,106,107</sup> and denotes good  $\text{Bi}_2\text{Se}_3$  quality. On the contrary, the undoped sample in the batch of the Cu doping (Fig 4.10 c and d), shows a less pronounced cusp, even though both are undoped  $\text{Bi}_2\text{Se}_3$ . The principal reason is attributed to the different thicknesses of (60 nm and 40 nm), where studies indicated a transition thickness to occur between 20 and 60 nm referent to the decoupling of the surfaces<sup>107–109</sup>. Consequently, the decoupling of the surface decreases the value of the prefactor from -0.5 to -1.

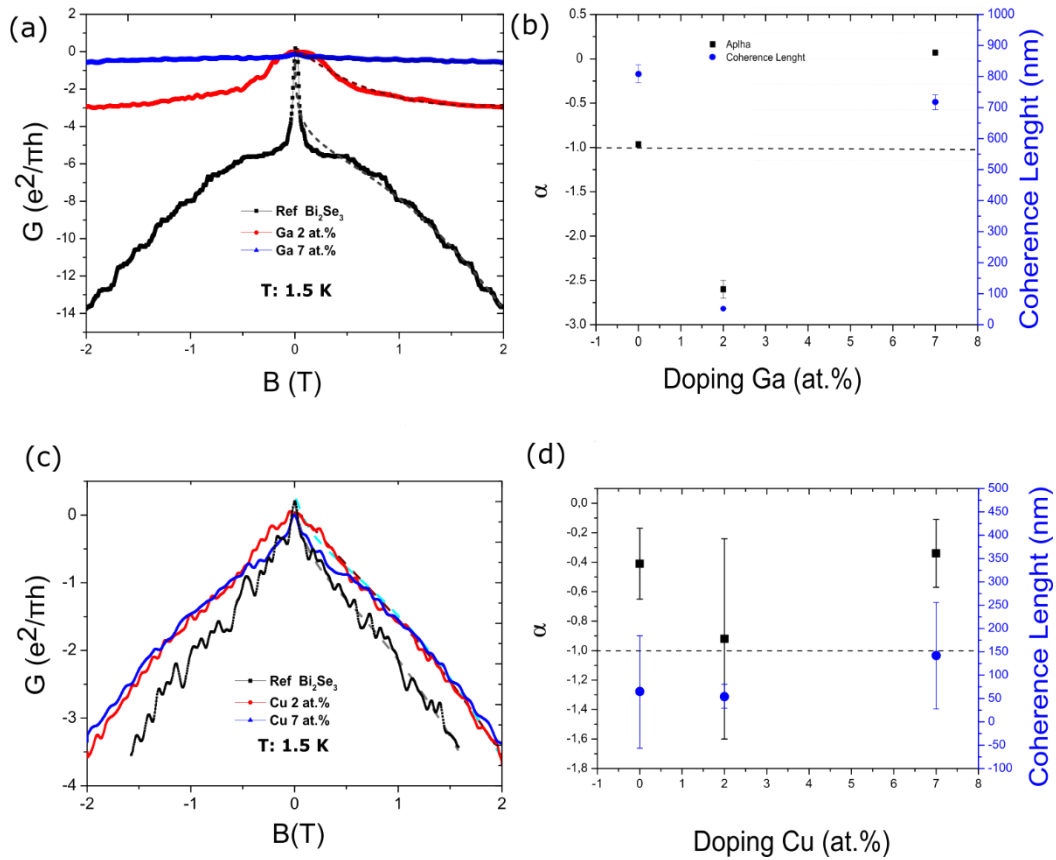


**Figure 4.10** WAL measurements for undoped Bi<sub>2</sub>Se<sub>3</sub> (black dots) and doped samples with 2 at.% (red dots) and 7 at.% (blue dots) of a) Ga and c) Cu doped Bi<sub>2</sub>Se<sub>3</sub>, as a function of low magnetic field with the corresponding HLN model fittings (dashed lines). The sharp cusp is a typical feature of the presence of surface states. Fitting parameters  $\alpha$  and phase coherence length ( $L_\phi$ ) as a function of b) Ga or d) Cu doping level. Edited from Daniel Brito et al. <sup>120</sup>.

By introducing 2 at.% of Ga (Fig 4.10 a), the WAL cusp becomes less visible compared to the reference. Moreover, the magnetoconductance presents a slight plateau at low magnetic fields, meaning a quantized conductance, that sharply decreases at a critical magnetic field of approximately 0.2 T (Signal before filter is shown annex S2). The presence of a critical magnetic field is commonly observed in superconductors<sup>79,92,110</sup> (Sc). Moreover, WAL studies in Sc showed higher values than -1 of the prefactor, for temperatures near the superconducting critical temperature<sup>111,112</sup>. In our case the  $\alpha$  is -2.6 (Fig 4.10 b), suggesting that Ga forms two extra channels with weaker phase coherence compared to the surface states<sup>67</sup>. Castro et al.<sup>113</sup> observed a sudden transition from -0.7 to -2 of the  $\alpha$  at a specific critical temperature of 4K in SnTe QWs. It is assumed that the increase in the prefactor is related to the creation of an additional conductive channel. This prefactor increase is accompanied by a reduction of the coherence length with a relatively higher disorder level by doping, presenting a  $L_\phi$  of 52 nm. As an indication concerning the Ga doping, studies on a atomic monolayer of Ga concluded that atomic Ga leads to superconductivity<sup>114–117</sup> around 4 K, which could explain the superconductor-like behavior of 2 at.% Ga-doped Bi<sub>2</sub>Se<sub>3</sub>. The

intercalation of Ga atoms in the VdW gap might induce superconductivity by a proximity effect with the Bi<sub>2</sub>Se<sub>3</sub> layer, which was experimentally realized by Cequn Li<sup>115</sup> on Bi<sub>2</sub>Te<sub>3</sub>.

By increasing the doping to 7 at.% the disordered material is also confirmed by the WAL signal. The cusp has completely vanished with a conductance being unchanged with the magnetic field. The fitting parameters obtained for  $\alpha$  is -0.07 and  $L_\phi$  of 717 nm. The higher concentration of Ga and possibly the disorder generated a reduction of the prefactor, and consequently, a disappearance of the surface states, meaning a topological phase transition. This destruction of the surface states is also known to occur in In-doped Bi<sub>2</sub>Se<sub>3</sub> for concentrations higher than 7%<sup>66</sup>.

The doping with Cu (Fig 4.10 c and d) produced different behavior compared to the Ga-doped Bi<sub>2</sub>Se<sub>3</sub> since all magnetoresistance signals are fairly similar. The fitting parameters obtained for the undoped Bi<sub>2</sub>Se<sub>3</sub> are  $\alpha = -0.41$  and  $L_\phi = 64$  nm. The prefactor value is close to the value corresponding to one conductive surface of -0.5, meaning that there is one coupled conductive surface state. The reduced coherence length indicates the reduced crystal quality. Even though the topological insulator presented lower quality, the surface states are preserved, and the doping influence of Cu can be studied.

Upon Cu doping, the WAL cusp is still present for both doping concentrations. Cu 2 at.% is slightly different from the WAL behavior of Ga-Bi<sub>2</sub>Se<sub>3</sub> (2 at%). The signal presents a pronounced quadratic shape but without the presence of the plateau. The fitting parameters obtained are  $\alpha = -0.92$  and  $L_\phi = 54$  nm. The results suggest a decoupling of the surfaces which produces two decoupled conductive surface states by a  $\alpha$  near the ideal value of -1.

Finally, Cu doping of 7 at.% produced fitting parameters  $\alpha = -0.34$  and  $L_\phi = 141$  nm. Contrary to the Ga doping of 7 at.%, the high concentration of Cu does not produce a phase transition by the destruction of the surface states. The prefactor is relatively close to -0.5, which confirms the presence of a conductive channel. The WAL signal is identical to the reference which indicates a minimal influence of the Cu doping. However, the coherence length is improved from 64 to 141 nm, which might imply the improvement of the material quality. These results are in accordance with the Hall effect measurements, where the TI's 2D transport should be improved by the reduction of the electron concentration and consequently the reduction of the bulk contribution.

## 4.4. Summary

The epitaxial growth of Ga and Cu-doped Bi<sub>2</sub>Se<sub>3</sub> with various doping concentrations is achieved and the influence on the structural, vibrational, and electrical properties is discussed. XPS, Raman, and XRD measurements are used to confirm the effective incorporation of Ga or Cu dopants. The discernible expansion of the crystal lattice and the slight redshift of the vibrational modes suggest that at low concentrations, most Ga atoms can be intercalated in the van der Waals gap between the Bi<sub>2</sub>Se<sub>3</sub> QLs. Oppositely, at higher concentrations, the lattice contraction and small blueshift of the vibrational modes observed for the Cu doping suggest a substitution effect, where Cu replaces Bi atoms. Furthermore, n-type doping was observed for all Ga concentrations tested, which excludes Ga as a good candidate for acceptor impurity and reinforces the hypothesis of intercalation. In contrast, the Cu dopant can lead to a reduction of the carrier concentration pointing towards a good acceptor impurity by substitution of Bi atoms.

Finally, as observed for intrinsic band insulators, the lack of WAL suggests the annihilation of the topological surface states as the Ga doping concentration is increased. The persistence of the cusp in Cu-doped samples indicates potential topological behavior. At low Ga doping, the supposed intercalation leads to an increased prefactor, similar to the achieved nematic topological superconductivity. Thus, the present study opens up the possibility of a different dopant to achieve topological superconductivity. Meanwhile, the topological superconductivity of Cu-doped Bi<sub>2</sub>Se<sub>3</sub> grown by an MBE is still not achieved.

# Chapter 5

## 5. ARPES measurements of the topological insulator, Bi<sub>2</sub>Se<sub>3</sub>, and Ga/Cu-doped Bi<sub>2</sub>Se<sub>3</sub>

### 5.1. Motivation

Topological insulators (TI) are characterized by massless Dirac surface states (SS). The Bi<sub>2</sub>Se<sub>3</sub> band structure is characterized by a large band gap up to 0.3 eV and a robust almost idealized Dirac cone at the  $\Gamma$  point, where the topological surface states are crossing the band gap. The existence of Bi<sub>2</sub>Se<sub>3</sub> topological surface states was previously confirmed by Angle-Resolved Photoemission Spectroscopy (ARPES)<sup>12</sup> (Fig 1.8 b). Heretofore, the SS existence was experimentally verified by the WAL effect. However, this 2D transport effect is commonly masked by bulk conductivity due to the Bi<sub>2</sub>Se<sub>3</sub> n-type degeneracy. The observation of the WAL effect due to the presence of the SS is necessary but not sufficient to prove the existence of the SS<sup>118</sup>, since trivial surface states can also produce a WAL effect. Nonetheless, WAL cannot evaluate the SS properties. ARPES, on the contrary, provides direct observation of the electronic structure of the material, which allows the visualization of the SS in the momentum space and the topological properties can be studied (Fermi velocity and Dirac point). ARPES was found to be an ideal characterization technique for the observation of the SS, even for samples with a bulk transport domination<sup>119</sup>.

Our previous work demonstrated that Ga doping leads to an increase of the electron density by almost six-fold ( $n \approx 6 \times 10^{19} \text{ cm}^{-3}$ ) in Bi<sub>2</sub>Se<sub>3</sub><sup>120</sup>. Additionally, Fig. 4.10 showed the WAL upon Ga doping, where the cusp starts to disappear as the Ga concentration increases. These observations could indicate a topological phase transition. We also found evidence that Ga atoms, similarly to Cu, intercalated in the van der Waals gap. Together with the WAL studies, it could predict a new member of the topological superconductivity (TSC) family. Likewise, the WAL upon Cu doping showed the presence of a cusp for both doping and consequently the presence of conductive surface states.

ARPES has been used to study Bi<sub>2</sub>Se<sub>3</sub> magnetic dopants<sup>121</sup>, rare earth dopants<sup>122</sup>, and other exotic elements<sup>21,77,79</sup> that can lead to the TSC. Magnetic and TSC dopants may open a gap at the Dirac point of the surface states<sup>77,123</sup>, which can be observed and confirmed by ARPES measurements, in case it presents enough resolution. The effect of the doping of Ga-Bi<sub>2</sub>Se<sub>3</sub> on the surface states was first implemented within this thesis (Chapter 4). Furthermore, ARPES can complement the knowledge about Ga doping and confirm our previous assumptions. Additionally, as previously studied, the growth of topological superconductor Cu-doped Bi<sub>2</sub>Se<sub>3</sub> cannot be achieved by an MBE growth. Up to now, ARPES

measurements have been mainly performed on this superconductive doped material<sup>124–126</sup>. However, ARPES could provide valuable insights into the challenges associated with growing TSC materials via MBE.

This chapter describes experiments with two goals. Firstly, the surface states from the TI  $\text{Bi}_2\text{Se}_3$  are measured and their topological properties (Fermi velocity, Dirac point, ...) are studied. Secondly, the doping with Ga and Cu is studied to provide additional information about the surface states, such as topological properties and evolution upon doping.

### 5.1.1. Sample preparation, methodologies, and relevant preliminary information

ARPES is highly sensitive to the surface properties of materials, and thus, meticulous surface preparation is fundamental for accurate measurements. Any impurities, adsorbates, or defects on the surface can significantly influence the observed electronic structure. This sensitivity underscores the need for pristine surfaces to reveal the intrinsic electronic states. Rigorous surface preparation methods, such as in-situ cleaving or annealing, are employed to ensure reliability in ARPES experiments, thereby providing insights into the fundamental electronic properties of materials. Besides the surface sensitivity, the technique is also affected by the material crystallinity, since polycrystalline samples cannot guarantee momentum conservations, thus making it difficult to extract information from poor single crystals.

#### Sample preparation

The single crystal layer of  $\text{Bi}_2\text{Se}_3$ , Ga-doped  $\text{Bi}_2\text{Se}_3$ , and Cu-doped  $\text{Bi}_2\text{Se}_3$  are grown on sapphire substrates ( $\text{Al}_2\text{O}_3$ ) by MBE. Ga and Cu doping percentages were chosen to be 2 and 7 at.%. Later on, gold contact pads are deposited on the surface of the sample to prevent charging effects at the detector. The lack of a path for photoexcited charges (worsened by insulating substrate) could lead to a surface charging effect that would jeopardize the ARPES measurements as those surface charges interact with the photoexcited electrons of interest. Even though, the problem can also be easily solved by providing good electrical contact between the film and the sample holder by a *washer*. As shown in Fig. 5.1.

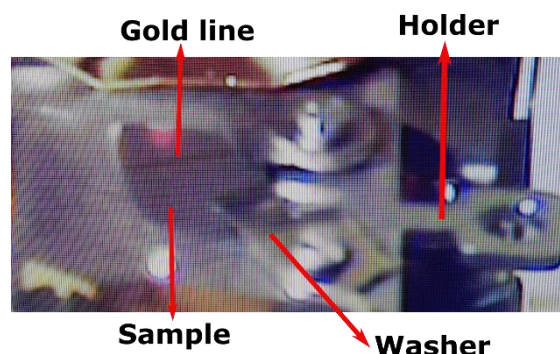


**Figure 5.1** Configuration of the Bi<sub>2</sub>Se<sub>3</sub> substrate for the ARPES measurements. It is visible the sample with a gold line on the surface of it. The sample is held on the holder by a washer, which also provides the metallic contact to the film surface.

Due to the surface sensitivity of this technique, it is important to protect the surface from any contaminations, impurities, or oxidation reactions. Therefore, the surface of the Bi<sub>2</sub>Se<sub>3</sub> is covered with a 20-100 nm amorphous Se capping layer after the MBE growth at a sample temperature of 30-35°C for approximately 10 min. Afterward, the samples are transferred to ALBA synchrotron in Barcelona with the minimal air exposure as possible in a sealed box in vacuum.

After introducing the Bi<sub>2</sub>Se<sub>3</sub> samples into the preparation chamber at the LOREA beamline, the Se layer is then removed (Se decapping) by annealing the sample. Several experimental procedures were tested to remove the Se capping layer. The Se capping layer was already implemented in previous studies<sup>29,127,128</sup>. Nonetheless, the Se decapping depends on various factors such as real temperature, chamber pressure, Se sticking coefficient, and thickness....

Our decapping experiments started by annealing the sample up to 80 °C and staying at this temperature until it is observed a pressure improvement (~2h). Core levels or XPS analysis are implemented to detect the Bi signal to identify the full Se decapping. The core levels could indicate a not-perfect surface cleaning due to the presence of tails in the Bi element peaks, mainly by some Se remnants. Alternatively, a different approach is tested by increasing the temperature to 110 °C and a duration time between 4-6 h. As a result, ARPES intensity showed an improvement in signal-to-noise, and the core level tails were reduced. Finally, a “flash decapping” was performed by annealing at the maximum temperature of 180 °C for the shortest time (5-10 min) wherein the Se seems, by visual inspection, to be fully removed from the surface of the sample. The Se is distinguished by a blueish color. As soon as the surface starts to appear metallic-like the temperature is reduced to avoid the unintentional removal of the Se atoms from the Bi<sub>2</sub>Se<sub>3</sub> layer. This last decapping showed to be the ideal annealing where the best signal-to-noise is observed. Therefore, all samples are subjected to a “flash Se decapping” at 180 °C between 5-10 min until an alteration in the surface of the sample is observed.

## Preliminary information and results

The ARPES measurements start with the scan of the undoped Bi<sub>2</sub>Se<sub>3</sub> band structure at the  $\Gamma$  (gamma point) with different beam source energies (15 – 40 eV). The ideal beam source energy is dependent on the material measured. Thus, different beam source energies from 15 – 40 eV are tested to spot the ideal source energy in order to obtain the best resolution and discern the topological surface states. Lower energies provide the best resolution, and the optimal signal is achieved with a beam source energy of 18 eV.

Furthermore, the beam polarization is studied by using both vertical and planar polarization to understand the preferential polarization. The surface states are detected with a planar polarization, whereas with vertical polarization no signal is detected.

Henceforward, the energy used for ARPES (band dispersion, Fermi map, ...) is 18 eV. Energies higher than 30 eV showed an increased noise-to-signal and reduced resolution. The temperature of all measurements is about 10 - 15 K to minimize thermal broadening effects allowing a higher energy resolution.

## 5.2. Bi<sub>2</sub>Se<sub>3</sub> electronic band structure concepts

The band structure of the Bi<sub>2</sub>Se<sub>3</sub> is composed of a band inversion at the  $\Gamma$  point, related to the non-trivial topology, which creates the crossing surface states. The surface Brillouin zone is composed of a hexagonal structure (Fig 5.2 a), where the  $\Gamma$  point is the center (0,0,0) and the  $\bar{K}$  and  $\bar{M}$  points are at the corners and the mid-edge of two corners, respectively. The surface states are detected from the gamma point to any momentum direction since the Dirac dispersion is symmetric across different momentum directions.

The energy band dispersion of the Bi<sub>2</sub>Se<sub>3</sub> reference sample is shown in Fig 5.2 b). The conduction band (CB) is observed below the Fermi level, demonstrating that the Fermi level resides within the conduction band. This observation confirms the inherent n-type degeneracy attributed to the presence of Se vacancies. The valence band (VB) is observed at higher binding energies as an M-like shape, resulting in the strong split of the band by the spin-orbit coupling. The surface states characteristic of the 3D topological insulator Bi<sub>2</sub>Se<sub>3</sub> is observed as a semi-Dirac cone crossing the band gap connecting the CB to the VB, where they merge with the valence band right underneath the Dirac point ( $D_p$ ), making them only visible on the upper part of the  $D_p$ .

Furthermore, the conduction and valence band can be approximated as a parabolic band, the solution of the Hamiltonian for semiconductors. However, the valence band can be approximated as an inverse parabolic with an incorporation of the strong spin-orbit coupling to produce the M-shape. By performing the fitting model, explained previously in section 2.2.6, it is possible to extract the Dirac point position ( $D_p$ ), Fermi velocity ( $V_f$ ), the electron mass ( $m_{ev}$ ,  $m_{ec}$ ), the conduction band minimum ( $E_c$ ), and the valence band maximum ( $E_v$ ). The fitting model is applied to the ARPES of the undoped Bi<sub>2</sub>Se<sub>3</sub> (Fig. 5.2 b) and presented in Fig 5.2 c).

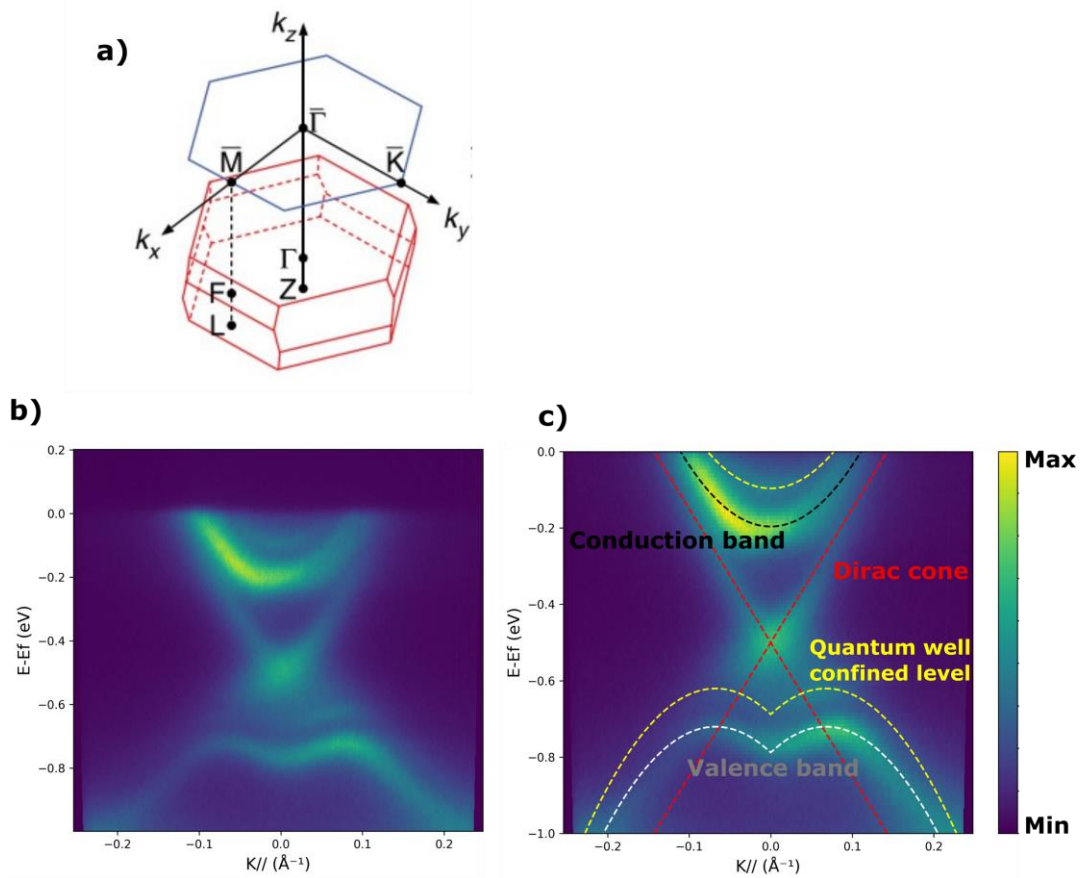


**Figure 5.2** a) Bi<sub>2</sub>Se<sub>3</sub> surface Brillouin zone with a hexagonal structure with visualization of the relevant symmetry points (Γ, K and M). b) Energy dispersion of Bi<sub>2</sub>Se<sub>3</sub>. c) The fitting model applied to the band dispersion of the Bi<sub>2</sub>Se<sub>3</sub>, observing the surface states (Dirac cone, red dash), conduction band (Black dash) and valence band (Gray dash). Additionally, as yellow dash line is observed a confined quantum well level, as new conduction and valence bands.

### 5.2.1. Bands bending and fitting model

Fig 5.2 c) shows sub-bands as quantum well-confined levels by the visualization of extra energy states of the conduction band, and the valence band shifted downwards, which produces an n-type doping of the material.

The downward shift is caused by the Bi<sub>2</sub>Se<sub>3</sub> energy band dispersion with scanning time due to the formation of a two-dimensional electron gas (2DEG) on the surface of the material, as illustrated in Fig 5.3 a). The downward shift bending occurs due to an electron accumulation in the surface, by populating metallic states labeled as 2DEG. The 2DEG transforms quantized in discrete levels and the effect can be observed upon a source photoexcitation in Fig 5.2 c) or as a function of the material depth (Fig 5.3 b). It shows the effect as a band shift, with the yellow dash lines being the quantum well-confined level. The black and gray lines correspond to the final conduction and valence band, respectively. This effect is commonly observed in Bi<sub>2</sub>Se<sub>3</sub><sup>129-131</sup> and impairs the analysis of the signal.

a)



b)

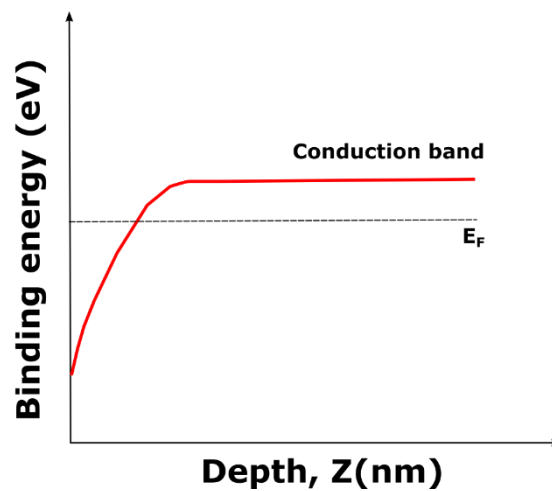


Figure 5.3 a) 2DEG illustration and the respective b) band diagram as a function of the depth of the material.

An alternative scan is used by scanning different spots of the sample and integrating them into a single scan (Fig. 5.4 b), to achieve reliable ARPES data analysis, because the conduction and valence bands are closer to the Fermi level and no sub-bands are visible. This point-integrated signal measurement showed a reduced 2DEG effect contribution. Even though the ARPES becomes more reliable, the signal-to-noise ratio is reduced.

In Fig. 5.4 b) the fitting models are also implemented, where the shift is easier to visualize by comparing the signal to the previous scan (Fig. 5.4 a). The fitting parameters for the reference sample  $\text{Bi}_2\text{Se}_3$  with both scans (Full scan and point integrated signal) are shown in Table 5.1. Based on the fitting values from Table 5.1, Fig. 5.4 c) presents the simulated signal of the fitting curves as an ARPES data image.

The fitting parameters of both scans are compared. The Fermi velocity from the  $\text{Bi}_2\text{Se}_3$  surface states are similar, in the range of  $3 - 4 \times 10^7$  cm/s, and comparable to the literature<sup>21,132,133</sup>. The Dirac point position varies from -0.31 to -0.52 eV, by changing the scan mode. As a result, the downward shift is evident, with a 0.21 eV difference. The same effect is visible for the conduction and valence band, where a valence band maximum of -0.67 eV (point scan) and a -0.79 eV (Full scan) is obtained. Likewise, the conduction band minimum

is -0.06 and -0.19 eV for the point scan and the full scan, respectively. There is a shift of approximately 0.13 and 0.12 eV for the conduction band minimum and valence band maximum, respectively.

In terms of the electron and hole effective mass, there is a slight variation, with values varying in the range of 0.11 - 0.31  $m_e$ . Such variation can be associated with the 2DEG which creates an n-type doping and consequently impacts the effective mass. The fitting parameters are in agreement with the literature where the electron effective mass is expected to be around 0.2  $m_e$ <sup>21,133</sup> and the Dirac point usually appears at 0.3 eV<sup>125,126,129,131,132,134</sup>. In conclusion, the point scan presented a more reliable energy band dispersion with a reduced contribution from the 2DEG.

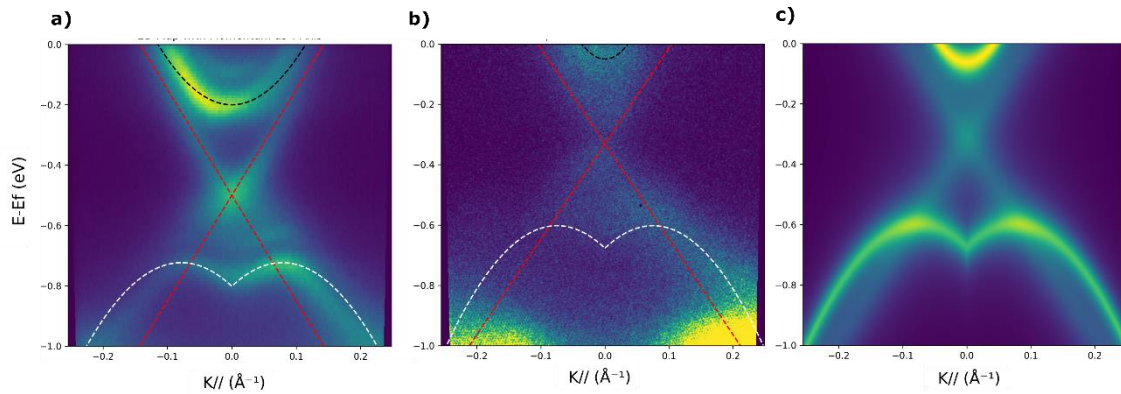


**Figure 5.4** Energy dispersion of Bi<sub>2</sub>Se<sub>3</sub> with a) long scan mode and b) integrated fast scan in different spots of the sample. The fitting model is applied on both signals where the simulated fitting signal of b) is observed in c).

**Table 5.1.** Fitting parameters for the Bi<sub>2</sub>Se<sub>3</sub> with the 2 different scans, the long scan, and the point integrated scan.

Bi <sub>2</sub> Se <sub>3</sub> Sample	$V_f$		$D_p$ (eV)	$m_{ev}$ ( $m_e$ )	$m_{ec}$ ( $m_e$ )	$E_v$ (eV)	$E_c$ (eV)
	$(\times 10^7)$	cm/s)					
Point scans	$3.3 \pm 0.2$		$-0.31 \pm 0.05$	$0.28 \pm 0.01$	$0.11 \pm 0.01$	$-0.67 \pm 0.05$	$-0.06 \pm 0.05$
Full long scan	$4.0 \pm 0.1$		$-0.52 \pm 0.05$	$0.249 \pm 0.01$	$0.31 \pm 0.01$	$-0.792 \pm 0.05$	$-0.191 \pm 0.05$

### 5.3. Ga and Cu doped $\text{Bi}_2\text{Se}_3$ electronic structure

Core levels are measured for all samples post-Se decapping to determine the material composition (Fig 5.5). This technique is identical to XPS spectroscopy. Unfortunately, the binding energy of the Se peak was not measured due to equipment limitations, which did not allow a precise quantification of each element. The  $\text{Bi}_2\text{Se}_3$  presents strong Bi  $5d$  characteristic peaks for all samples at approximately -25 and -27 eV. Moreover, the Ga signal is detected at -21 eV for the Ga-doped samples, with peak intensity increasing with doping percentage, which confirms the presence and proportionality of the doping element. The Cu-doped  $\text{Bi}_2\text{Se}_3$  samples do not detect any Cu, because the Cu binding energy is out of the range.

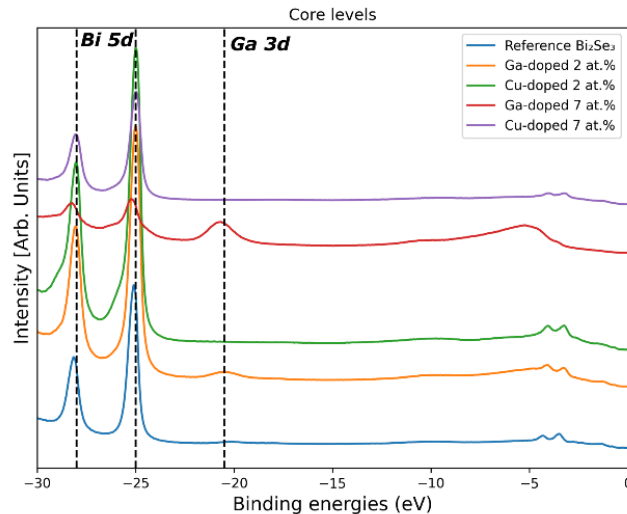


**Figure 5.5** Core levels from the  $\text{Bi}_2\text{Se}_3$  and the Cu/Ga doped  $\text{Bi}_2\text{Se}_3$ .

In Fig. 5.6, the Ga-doped and Cu-doped  $\text{Bi}_2\text{Se}_3$  (2 and 7 at.%) energy dispersions are shown. The Ga and Cu doping presented different tendencies of the band structure, corroborating the findings presented in Chapter 4. For a Ga doping of 2 at.% (Fig. 5.6 a), the surface states are not destroyed. The spectrum confirms the existence of surface states crossing the band gap as projected from the Ga-doped  $\text{Bi}_2\text{Se}_3$  study section 4.3.2 (Fig 4.10). On the other hand, the WAL signal prefactor ( $\alpha$ ) of -2.5 obtained could suggest the creation of additional surface states (trivial or non-trivial), however, the direct visualization of the band structure rejected this possibility since those states are not observed.

As the Ga concentration is increased to 7 at.% (Fig. 5.6 b) the band dispersion becomes less distinguishable due to the poor crystallinity of the material. The doping with 7 at.% leads to a higher concentration of defects in the material surface that prohibit signal acquisition. The band structure of the Ga-doped  $\text{Bi}_2\text{Se}_3$  (7at.%) indicates possible

destruction of the surface states, as a consequence of the higher defect concentration. This is in agreement with our previous assumption that the material undergoes a topological phase transition manifested by the lack of the cusp in the WAL effect (Fig 4.10). This destruction of the surface states was also observed for the doping of In with higher percentages than 7 at.%<sup>66</sup> because In atoms were reducing the spin-orbit coupling and consequently the band inversion was not present in the material.

In the case of Cu doping Bi<sub>2</sub>Se<sub>3</sub> (Fig. 5.6 c and d), the surface states are preserved upon the highest concentration of Cu (7 at.%) without deterioration of the signal intensity. The persistence of the surface states even with higher concentrations of Cu is in agreement with the literature<sup>116,117,136</sup>. The band dispersion quality indicates that the Cu-doped Bi<sub>2</sub>Se<sub>3</sub> maintains the single-crystal nature with a low concentration of defects.

In terms of the doping effect, Cu introduction was shown to cause an upward shift of the bands. The conduction band, valence band, and Dirac point move to higher energies by increasing the percentage of Cu, meaning that it moves closer to the Fermi level. This effect is possibly caused by the substitution of Cu atoms with Bi atoms in the crystal lattice, which leads to a reduction of the electron concentration<sup>95,137,138</sup>. The doping by Cu can improve the topological properties of the topological insulator Bi<sub>2</sub>Se<sub>3</sub> by tuning the Fermi level into the band gap as stated in previous reports of Cu-doped Bi<sub>2</sub>Se<sub>3</sub><sup>124</sup> and Pb/Sb-doped Bi<sub>2</sub>Se<sub>3</sub><sup>88</sup>. The high single-crystal quality growth by MBE seems to lead to a substitution of Cu atoms, which can be the cause of the impossibility of achieving the TSC of Cu-doped Bi<sub>2</sub>Se<sub>3</sub>.

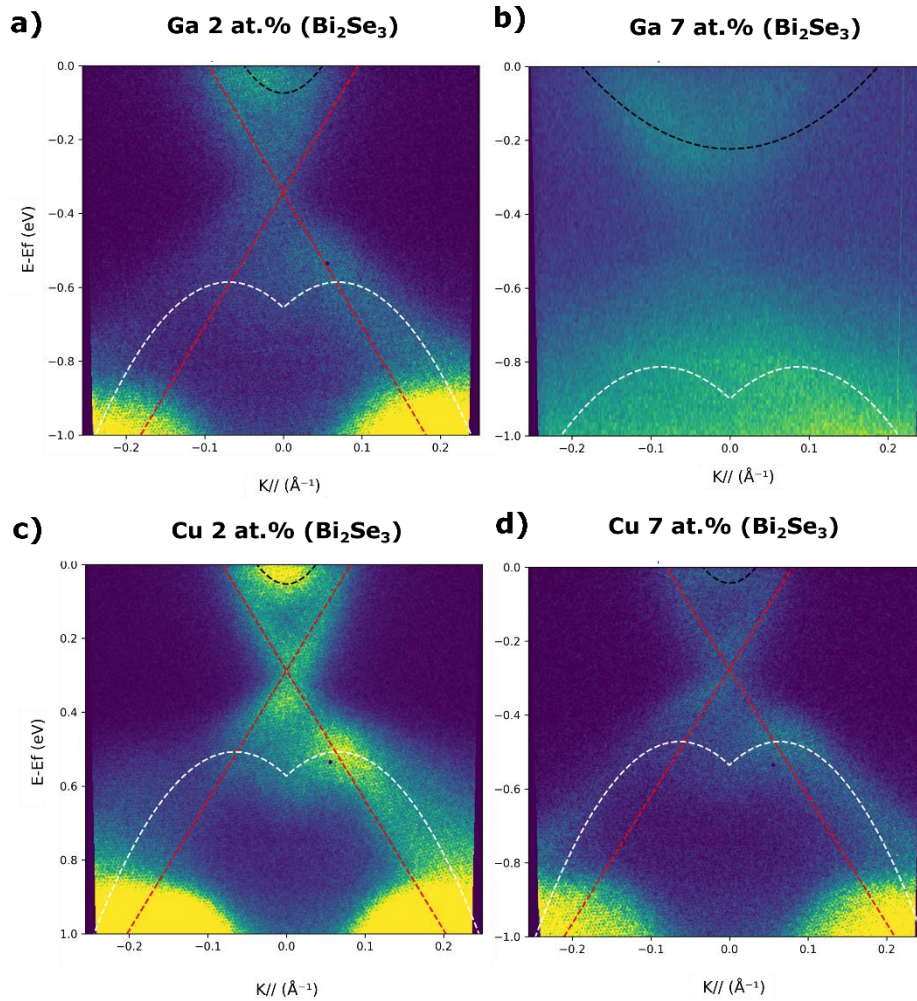


**Figure 5.6** Energy dispersion by the point scan of a) 2 at.% Ga-doped  $\text{Bi}_2\text{Se}_3$ , b) 7 at.% Ga-doped  $\text{Bi}_2\text{Se}_3$ , c) 2 at.% Cu-doped  $\text{Bi}_2\text{Se}_3$  and d) 7 at.% Cu-doped  $\text{Bi}_2\text{Se}_3$  with the fitting model as dashed lines. Black dashed line corresponds the conduction band, red dashed lines to the Dirac surface states and the gray dashed line to the valence band.

The fitting parameters, from the fitting model shown in Fig 5.6, of all the samples are presented in Fig 5.7, Fig 5.8, and Fig 5.9, as a function of the doping. The fitting model is performed for the point-integrated scan where less influence of the 2DEG is found.

The conduction and valence band positions are altered by the introduction of Ga (Fig 5.7 a). The conduction band is moving downwards further from the Fermi level, thus the Fermi level is moving into the conduction band confirming the observation above (Fig 4.8), meaning that the electron concentration is increased. As a consequence, the Dirac point position and the valence band maximum appear to change according to the conduction band. A similar shift in doped  $\text{Bi}_2\text{Se}_3$  was also observed previously with Co, Mn,  $\text{Eu}^{121}$ , and  $\text{Fe}^{134}$ , and in the superconductivity candidates  $\text{Sr}^{77}$ , and  $\text{Ag}^{21}$ .

Oppositely, Cu doping (Fig 5.7 b) leads to a conduction band minimum and valence band maximum moving closer to the Fermi level as Cu doping is increased. However, the shift is within the experimental error, which cannot confirm the shift in the conduction band. The shift is more noticeable in the valence band than in the conduction band. Likewise, the Dirac

point also moves towards the Fermi level, which affects positively the transport properties with reduced transport contributions from the bulk conduction band and increased surface states transport. This effect is also stated in the literature<sup>95,124,137,138</sup> when substitution by Cu atoms occurs.

The conduction and valence electron masses (Fig 5.8) have changed significantly by introducing the doping element. The Ga doping leads to an increase in the hole mass and electron mass. In the case of the conduction electron mass, it changes from approximately 0.11 to almost 0.25  $m_e$ , and the valence electron mass changes from 0.27  $m_e$  up to almost 0.35  $m_e$ . Conversely, the masses in the Cu-doped  $\text{Bi}_2\text{Se}_3$  decrease by doping with the lower percentage of Cu (2 at.%), and it stays constant up to 7 at.% of Cu. These changes are affected by two factors: the change in the chemical composition and the consequence of changing the crystal lattice parameter. The higher effective electron mass was accompanied by an increase in the crystal lattice parameter (Ga doping), whereas the decrease in the lattice parameter corresponded to the decrease in the effective electron masses (Cu doping). Moreover, the evolution of the effective mass is consistent with the carrier concentration<sup>139</sup>.

The surface states Fermi velocity (Fig 5.9) does not change significantly upon any type of doping, varying between  $3.2 - 3.6 \times 10^7$  cm/s. A slight increase is observed for both dopants with 2 at.%, even though the value is within the experimental error. There is the exception of the Ga 7 at.% sample, which does not display a Fermi velocity due to the “non-existence” of the surface states.

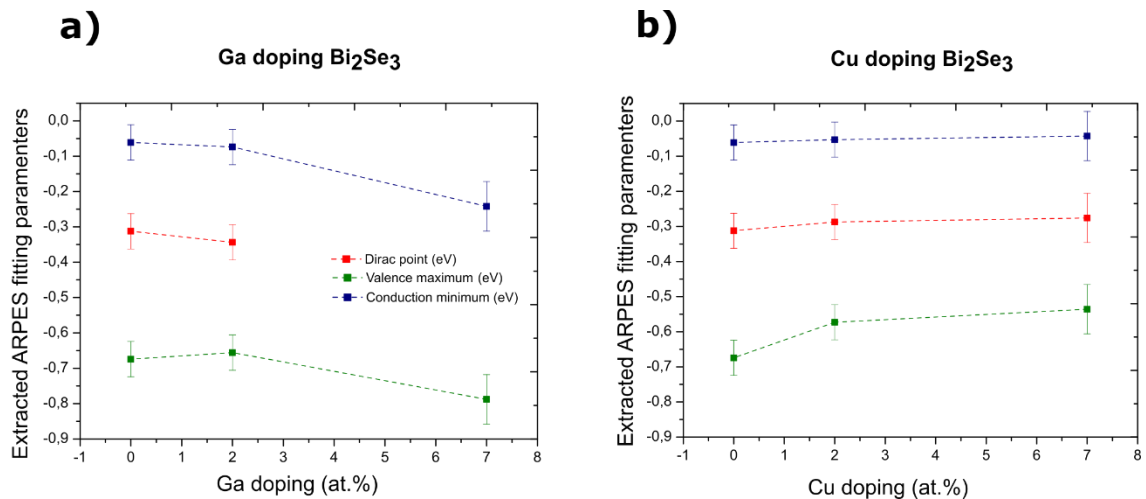


**Figure 5.7** Evolution of the conduction band minimum, valence band maximum, and Dirac point of the surface states as a function of a) Ga and b) Cu doping.

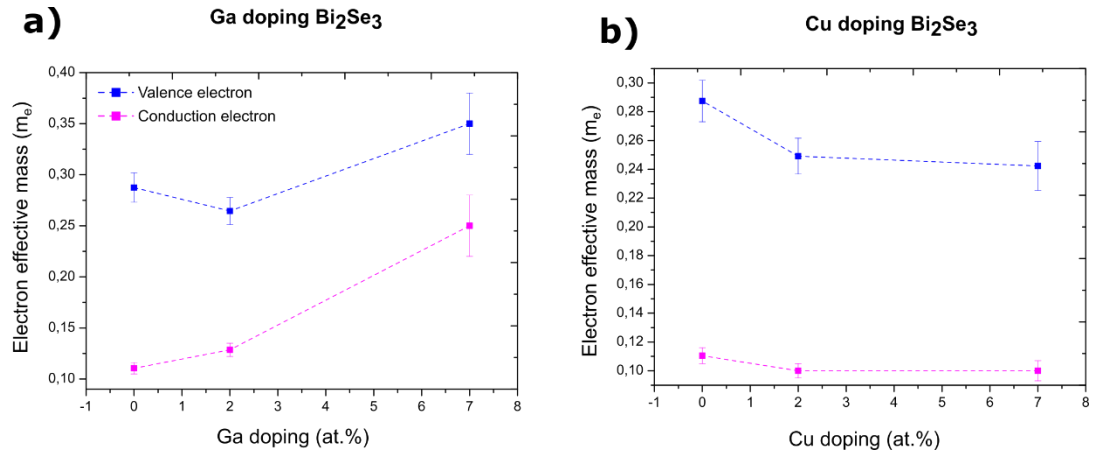


**Figure 5.8** Evolution of the conduction and valence electron effective masses as a function of a) Ga and b) Cu doping.

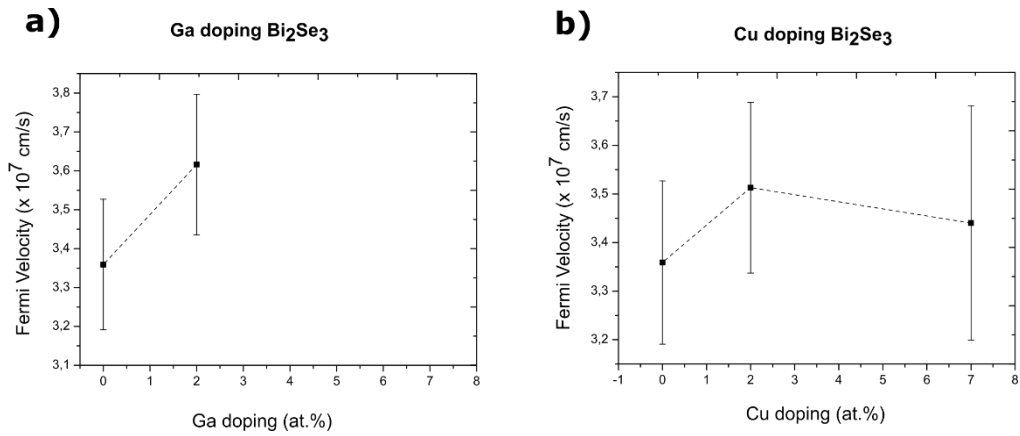


**Figure 5.9** Evolution of the Fermi velocity of the surface states as a function of a) Ga and b) Cu doping.

The  $\text{Bi}_2\text{Se}_3$  and doped  $\text{Bi}_2\text{Se}_3$  Fermi maps are shown in Fig 5.10. Heretofore, the ARPES band spectrum has been shown in the parallel momentum space ( $K_{//}$ ) with the contribution of  $K_x$  and  $K_y$ , while the Fermi map is a 3D energy distribution of the electron energy states across different momentum directions ( $K_x, K_y$ ). The signal is shown for different energy slices 0, -200, -300, -400, -500, and -800 meV related to the Fermi level to have a 2D visualization of the energy distribution as a function of  $k_x$  and  $k_y$ . However, the Fermi map is measured for a prolonged period, which produces the 2DEG and consequently, the band shift. This full scan produces better signal-to-noise and improves the analysis of the Fermi map.

Overall, the 3D Fermi map is similar for all the samples with minimal differences, similar to the previously observed ARPES data. At the Fermi level, far from the Dirac point, it is observed the conduction band and the Dirac cone contours. The effective Dirac Hamiltonian presents a rotational symmetry in  $x$  and  $y$ , which should expect a circular Fermi surface for the surface states<sup>129</sup>. However, the Fermi map contours show a hexagonal shape, as a consequence of the hexagonal warping from the 2DEG<sup>129,121</sup>.

As we move closer to the Dirac point, this previous wrapping effect is less pronounced and the circular shape from the surface states is more noticeable. As a consequence of the full scan, the Dirac point visualization is observed approximately at -500 meV, which explains the difference in the Dirac point position from the previous fitted values. Finally, the  $\text{Bi}_2\text{Se}_3$  valence band is observed at lower energies (-800 meV). Unfortunately, as explained before, the poor material quality of the Ga-doped  $\text{Bi}_2\text{Se}_3$  (7 at.%) implies the difficulty in measuring the surface map. As a consequence, the topological phase transition assumption is not possible to confirm due to the non-observed trivial band gap in the Fermi map.

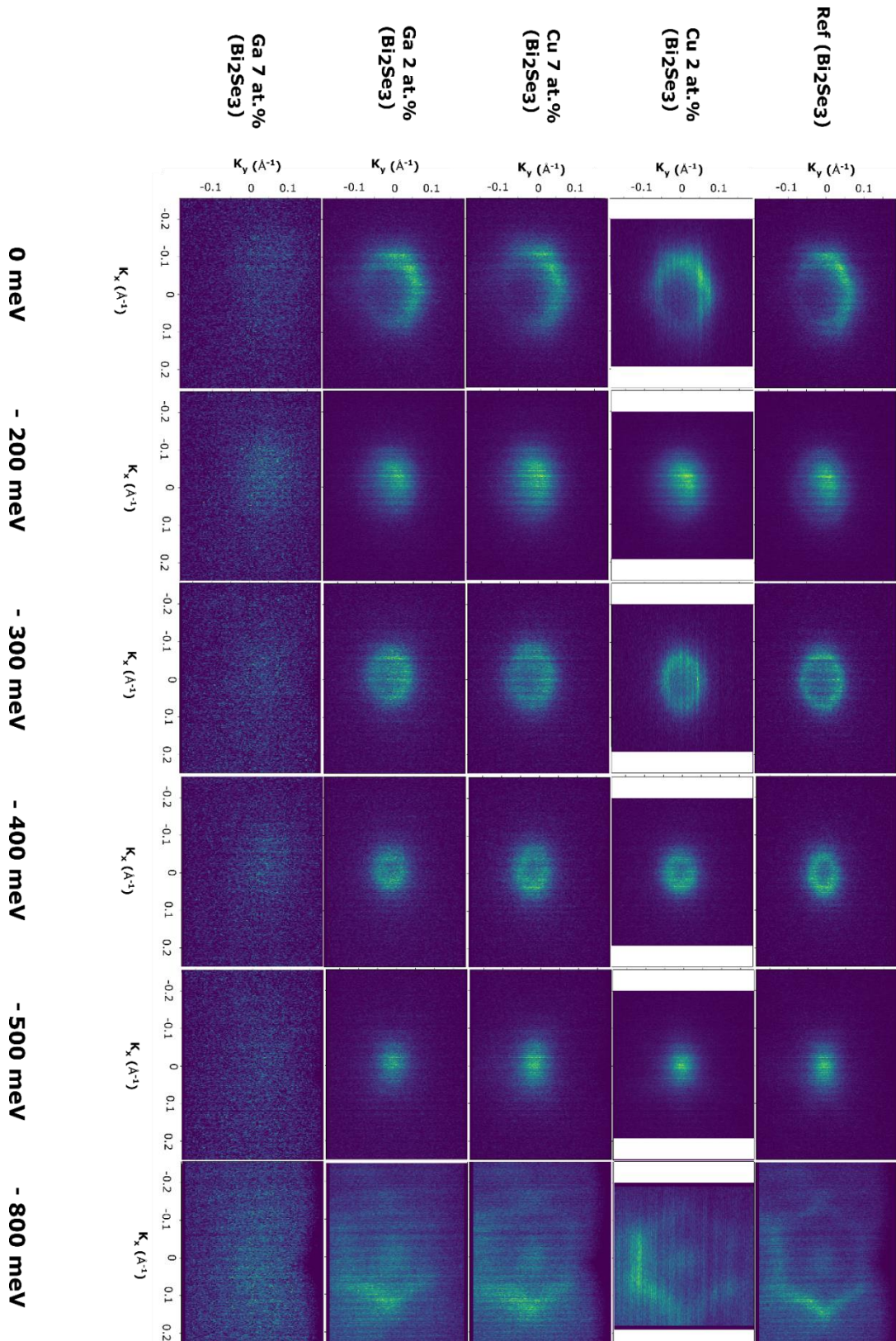


**Figure 5.10** Fermi map for the reference  $\text{Bi}_2\text{Se}_3$ , Ga-doped  $\text{Bi}_2\text{Se}_3$  and Cu-doped  $\text{Bi}_2\text{Se}_3$  at energies from the Fermi level (0, -200, -300, -400, -500, -800 meV). The signal is obtained by a long scan to improve the signal-to-noise ratio.

Lastly, as shown in section 2.2.6, Eq. (2.21), the surface charge carrier density ( $n_s$ ) can be extracted and estimated from the ARPES. In Fig 5.11, the estimated surface carrier density is shown as a function of the Ga and Cu doping.

The concentration for the undoped Bi<sub>2</sub>Se<sub>3</sub> is approximately  $7 \times 10^{12} \text{ cm}^{-2}$ , which is one order of magnitude smaller than that previously obtained in section 4.3.1 of  $7 \times 10^{13} \text{ cm}^{-2}$  by Hall effect measurements. This difference demonstrates that the  $n_{2d}$  calculated from the Hall measurements presents contributions from the bulk and not only from the surface states. As the doping is increased, the surface electron concentration changes. Ga doping leads to a slight increase up to  $\sim 1.3 \times 10^{13} \text{ cm}^{-2}$ , for the highest percentage of 7 at.%, which is double the electron concentration of undoped Bi<sub>2</sub>Se<sub>3</sub>. The increase in the charge carrier concentration was also observed in Ag-Bi<sub>2</sub>Se<sub>3</sub><sup>21</sup>. The transport properties extracted from the Hall effect for the Ga doping concluded that there was a six-fold increase, meaning that the electron concentration was mainly increasing the bulk concentration.

In terms of Cu doping, the effect is the opposite, with the electron concentration decreasing slightly up to  $\sim 5 \times 10^{12} \text{ cm}^{-2}$ , which is in agreement with the previously observed in the hall effect measurements (section 4.3.1).

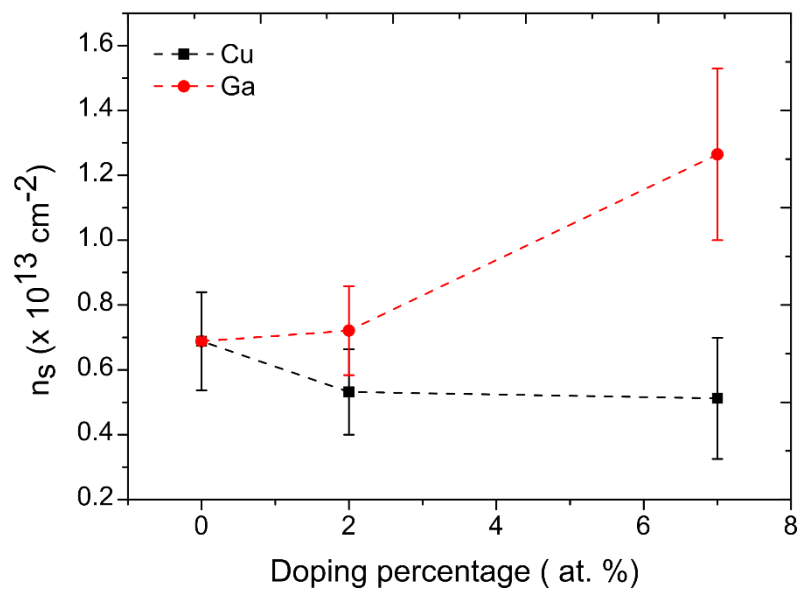


**Figure 5.11** Surface charge carrier density of Bi<sub>2</sub>Se<sub>3</sub> extracted from ARPES as a function of doping of Cu or Ga.

#### 5.4. Summary

In conclusion, ARPES was conducted on the topological insulator  $\text{Bi}_2\text{Se}_3$ , including Ga and Cu-doped  $\text{Bi}_2\text{Se}_3$ , to explore their electronic structures. The experimental procedures involved accurate sample preparation, and annealing, such as systematic annealing experiments to optimize the Se decapping process to enable the ARPES measurements.

The energy spectrum scan of the reference  $\text{Bi}_2\text{Se}_3$  sample revealed surface states, and subsequent measurements on doped samples demonstrated varied effects. Long scans led to a downward band shift due to the emergence of a 2DEG on the surface, which is reduced by the integration of the measurement at different points on the sample. Cu doping preserved the surface states with an upward Fermi level shift, indicative of improved topological properties by the reduced carrier concentration. Conversely, Ga doping at higher concentrations leads to poor crystallinity and degradation of the signal, suggesting a topological phase transition. The fitting parameters showed an independent variation of the surface states Fermi velocity and electron effective masses. Overall, these findings reinforce our hypothesis that the surface states are destroyed upon concentrations of 7 at.% of Ga. The Cu doping exhibits a systematic topological transport improvement by the Fermi level tuning into the band gap and closer to the Dirac point.

# Chapter 6

## 6. Wafer-scale Bi<sub>2</sub>Se<sub>3</sub> top gate field effect devices

A major problem faced in the field of topological insulators is that the bulk is not fully insulating. The use of these materials for applications requires only a residual bulk conductivity. As previously discussed, and concluded in Chapter 3, the use of an IS-BIS buffer layer studied by Koirala et al. improved the transport properties of the topological insulator Bi<sub>2</sub>Se<sub>3</sub>. Despite the reduction of the electron concentration and increase in mobility, the exploitation of its topological properties at room temperature is still unsuitable. The Mott criteria assign a critical density of carriers for an insulator to become a metal. In the case of the TI Bi<sub>2</sub>Se<sub>3</sub>, the critical carrier density is relatively low at  $n_{3d} = 10^{14}$ - $10^{15}$  cm<sup>-3</sup><sup>71</sup> which is orders of magnitude smaller than the previously obtained  $10^{18}$  cm<sup>-3</sup>. Furthermore, air exposure results in the diffusion of oxygen which leads to further n-type doping of the material<sup>140,141</sup>, and consequently raises the bulk transport contribution.

Another approach to reduce the carrier concentration is by tuning the Fermi level into the band gap by the application of an electrostatic gate<sup>142</sup>. This chapter describes the development of a top gate device fabrication process for epitaxial TI Bi<sub>2</sub>Se<sub>3</sub> aiming for the reduction of carrier concentration and to reduce bulk contribution for transport.

### 6.1. Heterostructure growth and field effect transistor fabrication methods

The starting point is the conclusions obtained in section 3.4, where a highly ordered and good interface Bi<sub>2</sub>Se<sub>3</sub> topological insulator with improved transport properties is obtained by the prior deposition of an IS-BIS buffer layer. Furthermore, aiming for the fabrication of quantum devices, it is important to protect the surfaces of TI to prevent the deterioration of the surface states. Kong et al. and Edmonds et al.<sup>140,141</sup> concluded that Bi<sub>2</sub>Se<sub>3</sub> exposure to air results in the formation of defects, such as Se vacancies, and it can increase the bulk charge carrier by oxygen diffusion. Thus, the topological states transport properties are suppressed by the bulk contributions.

MBE presents the opportunity to deposit an *in-situ* capping layer after the TI deposition avoiding the detrimental effect of air exposure. There are two possible solutions for the capping layer. Studies demonstrated that amorphous Se is a semiconducting layer with minimal transport contributions and prevents surface oxidation<sup>43</sup>. The Se layer can be easily

removed by annealing the Bi<sub>2</sub>Se<sub>3</sub> at higher temperatures, as discussed previously in section 5.1.1. However, annealing can be harmful to the Bi<sub>2</sub>Se<sub>3</sub> layer by the formation of Se vacancies, because Se has high volatility.

The second option, for the capping layer is β-In<sub>2</sub>Se<sub>3</sub>. It is a semiconductor with a band gap of 1.4 eV<sup>18</sup>, thus, in its intrinsic form, it should not contribute to the transport properties. Furthermore, it has good chemical and structural compatibility, which should lead to a highly ordered interface without damaging the TI surface. Thus, a 40 nm β-In<sub>2</sub>Se<sub>3</sub> is tested for the first time as a capping layer, and it is studied the feasibility of it for the fabrication of FET devices.

The heterostructure for the fabrication of the FET devices consisted of a 40 nm *IS-BIS* buffer layer, a 12 nm Bi<sub>2</sub>Se<sub>3</sub> layer as the FET channel, and finally, the β-In<sub>2</sub>Se<sub>3</sub> capping layer, as illustrated in Fig 6.1 a). A complete heterostructure fabricated on a sapphire substrate wafer is observed in Fig 6.1 b), by a blueish color due to optical interference.

The heterostructure crystallography is analyzed by XRD (Fig 6.1 c and d). The reduced thickness of the Bi<sub>2</sub>Se<sub>3</sub>, compared to the previous section 3.4, reduces the diffraction peak intensity enabling the detection of the In<sub>2</sub>Se<sub>3</sub> peaks. Both layers present a rhombohedral crystal structure with a diffraction family {00L} but with different crystal lattice parameters. Fig 6.1 d) shows a high-resolution scan of the (0015) plane of both materials where it is possible to distinguish both peaks.

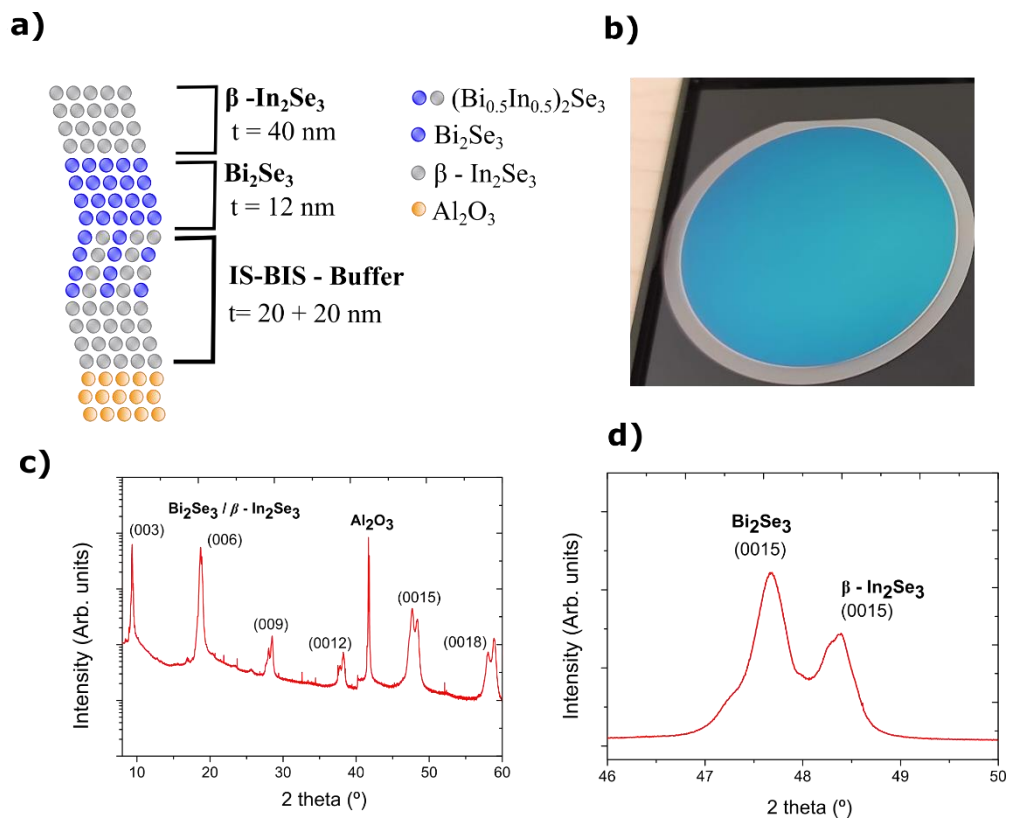


**Figure 6.1** a) Devices heterostructure composed by an IS-BIS buffer layer deposition, a 12 nm thick Bi<sub>2</sub>Se<sub>3</sub> and a 40 nm thick In<sub>2</sub>Se<sub>3</sub> capping layer. b) Photograph of a sapphire wafer with the deposited heterostructure. c) XRD spectrum of the device heterostructure on a sapphire substrate. d) High-resolution XRD for the (0015) diffraction peak.

The capping layer is later removed to provide metallic contact with the Bi<sub>2</sub>Se<sub>3</sub>. Contrary to the Se capping layer, the  $\beta$ -In<sub>2</sub>Se<sub>3</sub> capping layer cannot be removed by increasing the temperature. Diverse etching methods can be used to etch  $\beta$ -In<sub>2</sub>Se<sub>3</sub>, such as physical etching or wet chemical etching. However, since the thickness of 2D materials does not allow the use of physical etching in a precise condition, meaning that it is extremely difficult to selectively etch the  $\beta$ -In<sub>2</sub>Se<sub>3</sub> layer without damaging the Bi<sub>2</sub>Se<sub>3</sub>. By contrast, wet etching is suitable to remove layers selectively by the use of specific chemicals.

A wet chemical process to etch  $\beta$ -In<sub>2</sub>Se<sub>3</sub> was previously developed in the group<sup>18</sup>. However, the etching process effect on Bi<sub>2</sub>Se<sub>3</sub> was unknown. The etching process uses a diluted solution of 0.5% HCl with 30% H<sub>2</sub>O<sub>2</sub> with a proportion of 4:50. The H<sub>2</sub>O<sub>2</sub> acts as an In<sub>2</sub>Se<sub>3</sub> layer oxidation process while the HCl solution acts in the oxide layer by dissolving it in a liquid form. The etching process is quite fast, within a few minutes to etch 40 nm, and it can be visually monitored by the removal of the In<sub>2</sub>Se<sub>3</sub> layer on an additional control In<sub>2</sub>Se<sub>3</sub> sample.

The following experiment demonstrates the selectivity of the etching solution. The experiment consisted of two samples, 40 nm  $\beta$ -In<sub>2</sub>Se<sub>3</sub> and a 10 nm Bi<sub>2</sub>Se<sub>3</sub> being immersed in the etching solution of 0.5% HCl with 30% H<sub>2</sub>O<sub>2</sub> (Fig. 6.2 a) for about 30 min. Fig 6.2 b) shows the thinner  $\beta$ -In<sub>2</sub>Se<sub>3</sub> and Bi<sub>2</sub>Se<sub>3</sub> samples at the end of the etching process. The  $\beta$ -In<sub>2</sub>Se<sub>3</sub> is almost completely removed with a few residual layers in some areas of the wafer, whereas the Bi<sub>2</sub>Se<sub>3</sub> layer showed to withstand the chemical solution after a 30 min etching process even presenting a reduced thickness when compared to the  $\beta$ -In<sub>2</sub>Se<sub>3</sub> layer.

In conclusion, a selective chemical etching is developed to only remove the capping layer without damaging the TI layer. It is important to note that the Bi<sub>2</sub>Se<sub>3</sub> layer is only affected by the chemical for a few seconds, due to the over-etching performed to confirm the complete capping layer removal. Furthermore, a recent study presented a TI surface cleaning with diluted HCl to improve the surface<sup>143</sup> without destroying the surface states.

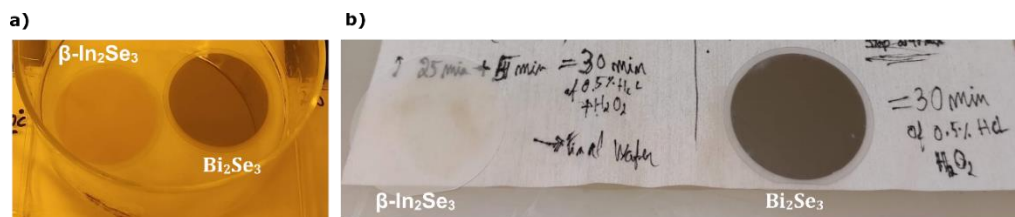


**Figure 6.2** In<sub>2</sub>Se<sub>3</sub> and Bi<sub>2</sub>Se<sub>3</sub> samples a) in a 0.5% HCl + 30% H<sub>2</sub>O<sub>2</sub> etching solution (4:50), and b) wafer removed from the etching solution after 30 min.

With an optimized heterostructure deposited, we proceed with the fabrication of the FET device with a top gate. The geometry used for the device is a four-terminal Hall-bar geometry as commonly used in the literature<sup>43,133,144</sup>. The FET fabrication procedure is explained in detail in section 2.3 and a visual inspection is shown in Fig. 6.3. The fabrication starts with the patterning into a micron-scale Hall bar structure by a physical etching. A 100 nm Al<sub>2</sub>O<sub>3</sub> dielectric is deposited by sputtering in order to protect the whole structure from air exposure and to act as the dielectric material in the FET device. The gate dielectric has shown a high dielectric coefficient and is efficient for the fabrication of Bi<sub>2</sub>Se<sub>3</sub><sup>133,143,145–147</sup>. The Al<sub>2</sub>O<sub>3</sub> is removed from the contact areas (Fig. 6.3 e) to allow the ohmic contact with the Bi<sub>2</sub>Se<sub>3</sub> layer. The etching process discussed previously is successful in removing the capping layer and not affecting the Bi<sub>2</sub>Se<sub>3</sub> layer (Fig. 6.3 f). The sample is rapidly transferred to the sputtering system to avoid Bi<sub>2</sub>Se<sub>3</sub> oxidation. A 15 nm metal layer (Cr/Au) is deposited as a preliminary contact just to protect the Bi<sub>2</sub>Se<sub>3</sub> from air exposure. Gold was shown to be a compatible element to form the ohmic contact without destroying the surface states<sup>148</sup>. The top gate FET devices are finalized by the metal deposition with a total thickness of 50 nm, as exhibited in Fig. 6.3 h). The final wafer is observed in Fig. 6.3 i) with 36 FET devices with different dimensions.

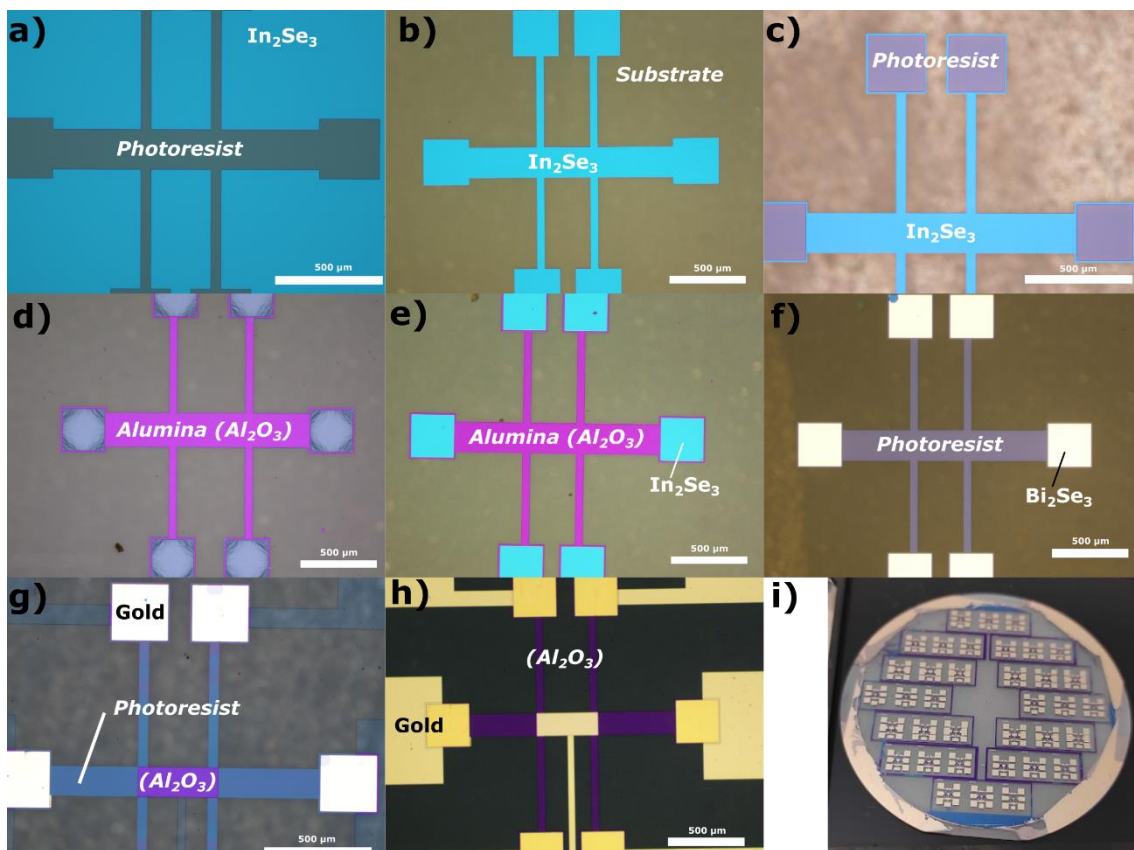


**Figure 6.3** Microscope image of the individual steps of the FET device cleanroom fabrication. a) Hall-bar patterning lithography, b) physical etching by ion milling, c) lithography of the metallic contacts, d) dielectric deposition by PVD, e) contact exposure by lift-off, f) chemical etching of the capping layer, g) Gold deposition on the contact area with the lithography for the h) metallic contacts and metallic gate on top of the channel. i) Wafer visualization of the 36 FET devices. The distinct colors are due to the optical interference of the layers.

A cross-section of the Bi<sub>2</sub>Se<sub>3</sub> FET device is illustrated in Fig 6.4 a). The Bi<sub>2</sub>Se<sub>3</sub> thickness is reduced to 12 nm compared to the previous chapters (40-60 nm) since the bulk transport domination can be reduced by reducing the layer thickness<sup>107,142,145,149</sup>. The increased surface/bulk ratio suppresses the bulk contribution and highlights the surface state transport.

The following sections describe the electrical measurements of one device as shown in Fig 6.4 b). The measurement of the remaining devices was not performed due to the lack of encouraging results to invest the time of our collaborators in Salamanca. A device from the middle of the substrate is expected to present more uniform layers. The dimensions of this Hall-bar structure are 300/150  $\mu\text{m}$  ( $L/W$ ), which means that the channel width is 150  $\mu\text{m}$  and the two terminals in the middle have a 300  $\mu\text{m}$  distance from each other, this dimensions are similar to the ones reported in the literature<sup>150,151</sup>. The electrical measurements are performed at low temperatures (1.5 K) with an indium wire bonding as shown in Fig 6.4 b).

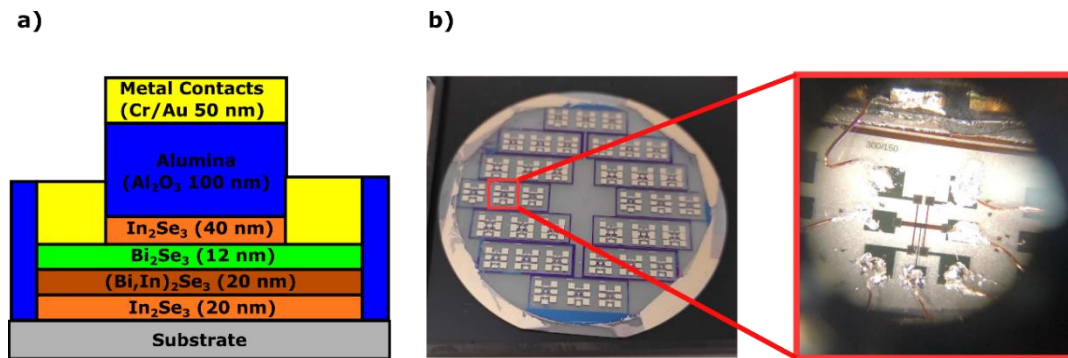


**Figure 6.4** Cross-sectional illustration of the Bi<sub>2</sub>Se<sub>3</sub> FET devices. b) Full wafer with 36 FET devices and magnification of a 300/150  $\mu\text{m}$  device with the wire bonding configuration, as used for the electrical measurements at low temperatures.

## 6.2. Field effect transistor electrical measurements

### 6.2.1. Gate voltage dependence of channel resistance

An operational FET device presents a functional gate without short circuits between the gate contact and the Bi<sub>2</sub>Se<sub>3</sub> channel (gate-source I-V curve). The dielectric gate behaves as an insulator, meaning that it should not conduct electricity. Therefore, the application of an electric field should produce a negligible leak current flowing to the channel. However, the application of high electric field or voltages leads to an increase in the oxide layer conductivity, and consequently a dielectric breakdown. This phenomenon can result in permanent damage to the dielectric material and to the functional FET. This gate behavior can be characterized by the Schottky-Frenkel (Eq. 6.1):

$$J = AE^2 e^{\left(\frac{B}{E}\right)} \quad (6.1)$$

Where  $J$  is the current density,  $E$  is the applied electric field and  $A$  and  $B$  are constants related to the system geometry and dielectric properties. The gate leak current is negligible until a breakdown voltage where the current starts to increase exponentially like with voltage.

The gate-source I-V was performed at room temperature (RT) with different sweeps from 2 - 15 V. It starts with a sweep from -2 V up to 2 V and carefully measures the current flowing along the gate dielectric. The sweep voltage is increased carefully to detect the breakdown voltage, meaning, the maximum voltage that the gate dielectric can withstand without breaking it.

Fig. 6.5 a) shows the gate-source I-V curves for different voltage sweeps. These measurements were performed in a sacrificial device, in order to detect the breakdown voltage, since after reaching the breakdown voltage the device is not operational anymore. As is observed for all curves, an exponential like behavior is successfully achieved confirming the insulating gate behavior. The leak current contribution to the channel current can be disregarded because it is smaller than  $10^{-10}$ A and the channel currents are higher than  $10^{-6}$ A. For a sweep range of 15 V, the leak current starts to increase exponentially between 10 - 12 V, implying that the breakdown voltage is approximately 10 V. The inset image of Fig. 6.5 a) shows the I-V curves with a logarithmic scale to compare with more detail the evolution of the current. The leak current is approximately  $1 \times 10^{-12}$  A and starts increasing up to  $1 \times 10^{-11}$ A as the number of sweeps is increased. Thus, the gate leak current is not stable, and it changes the contribution of the channel with the time of use, due to the defective amorphous insulating layer.

The Bi<sub>2</sub>Se<sub>3</sub> channel between the source and drain is also tested to confirm the ohmic contact between the metal contact and the topological insulator (Fig. 6.5 b). An RT linear response is obtained for the channel I-V curve. The gate I-V curve is shown in the same graph to confirm that the leak current does not have short circuits. Thus, the field effect transistor should be functional to modulate the Fermi level position of the Bi<sub>2</sub>Se<sub>3</sub> channel by the application of different gate voltages.

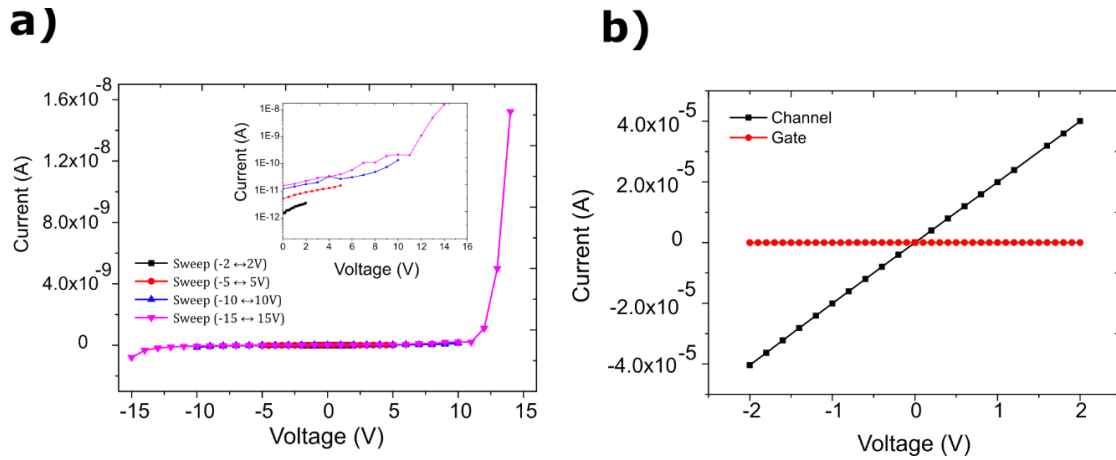


**Figure 6.5** a) Gate I-V curves for different sweep voltages. The measurements start with smaller voltage and increase slowly to higher voltage sweeps. b) Bi<sub>2</sub>Se<sub>3</sub> channel I-V curve with the gate I-V curve observing a minimal leakage current. The measurements are performed at RT.

The gate voltage is applied to understand the effect that the Fermi level variation has on the Bi<sub>2</sub>Se<sub>3</sub> channel. Unfortunately, at RT, residual conductivity is activated thermally creating excited carriers from impurity bands<sup>152</sup>, and consequently masking the topological surface states. To reduce the thermal effect in the topological insulator, the electrical measurements were performed at lower temperatures. These measurements were performed in the device shown in Fig 6.4 b), after confirming the insulating behavior of the dielectric layer.

The channel  $R_{xx}$  at different temperatures as a function of the gate voltage is shown in Fig 6.6 a). The gate voltage ranges from -5 V to 5 V to avoid gate breakdown. In the temperature range of 200 K - 120 K, the channel resistance is unchanged with voltage, due to the Fermi level lying deep in the conduction band. At a temperature of 90 K (light blue curve), an electrical transition occurs, since the channel resistance starts to be affected by the negative gate voltage. Channel resistivity increases for gate voltages lower than -2 V, which means that the Fermi level is approaching the conduction band minimum. The resistance modulation becomes more pronounced as the temperature is decreased. For temperatures lower than 20 K, the channel resistance can be changed between 12 k $\Omega$  to approximately 8 k $\Omega$ , a 30% difference, by applying a gate voltage of -5V and 5V, respectively.

At lower temperatures, the gate presents a larger effect on the channel resistance. A full gate sweep from -10 to 10 V is performed at approximately 1.5 K (Fig 6.6 b). The gate after reaching a voltage higher than 10 V showed a large leak current of almost 10<sup>-9</sup>A. A semi-ambipolar effect is observed for the Bi<sub>2</sub>Se<sub>3</sub> resistance as a function of the gate voltage. The resistance is slowly increasing with the application of negative voltages. A sharp increase starts for voltage lower than -5 V, meaning that the Fermi level is approaching the conduction band minimum<sup>133,153</sup> and the band gap, close to the central neutrality point as observed in the literature by a peak maximum in the resistance<sup>142,143,146,147</sup>. However, in our FET device, the ambipolar behavior is not achieved due to the limitation of the maximum

gate voltage of -10 V. Nevertheless, a resistance modulation of approximately 55% is achieved with a negative voltage of -10 V. Furthermore, the resistance slowly decreases by applying positive voltages, because the application of a positive gate voltage leads to the n-type doping of the topological insulator and consequently a more metallic film. Additionally, a Bi<sub>2</sub>Se<sub>3</sub> resistance curve is shown as a function of the gate voltage, but with the presence of the magnetic field of 2 T. The magnetic field shows a shift in the channel resistance to higher resistances as expected from the WAL effect.

In conclusion, the enhancement of the channel resistance with gating suggests that the Fermi level tuning is successfully achieved in the FET device.

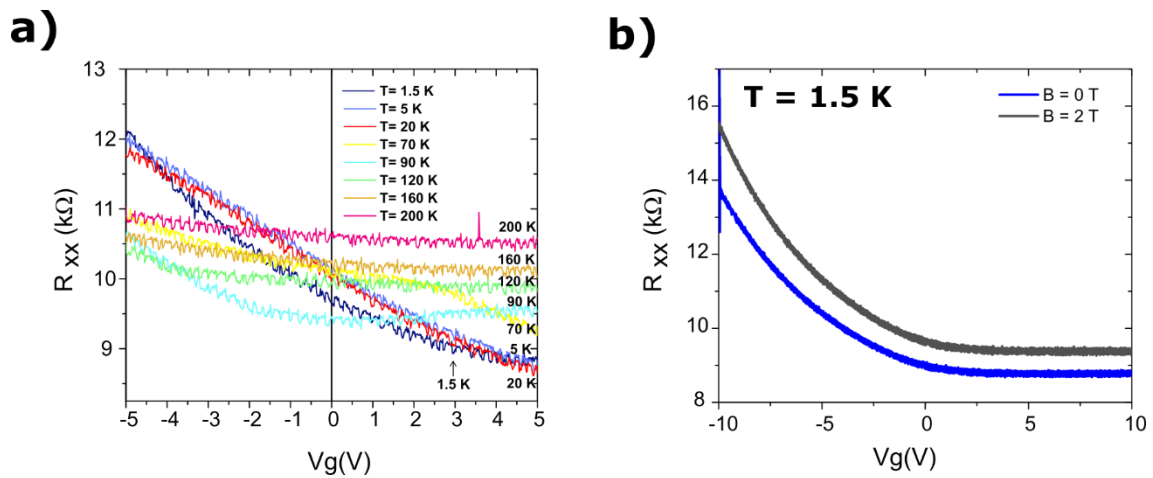


**Figure 6.6** Bi<sub>2</sub>Se<sub>3</sub> channel resistance as a function of the gate voltage for a) temperatures from 200 K to 1.55 K and b) different magnetic fields of 0 and 2 T at 1.5 K.

### 6.2.2. Gate Dependence of Weak Antilocalization

WAL is observed in the FET device at 1.5 K as a function of the magnetic field (Fig 6.7) for two different gate voltages of 0 V and -6 V. A clear sharp cusp of the magnetoconductance is visible at both voltages which confirms the existence of the WAL, which indicates the potential existence of surface states in the TI.

Surprisingly, the WAL behavior is identical for both gate voltages even though a large channel resistance is observed at a gate voltage ( $V_g$ ) of -6 V. The bulk contribution is minimized as the channel becomes more insulating, which should lead to a more pronounced cusp and ideally decoupled surface states from both surfaces (top and bottom). A small deviation in the magnetoconductance is observed at higher magnetic fields than 2T which comes from the contribution of the magnetic field background.

The Bi<sub>2</sub>Se<sub>3</sub> WAL effect for both gate voltages is fitted with the HLN model (Eq. 1.4) with the fitting parameters shown in Table 6.1. An  $\alpha$  close to -0.1 at  $V_g = 0$  V and  $V_g = -6$  V is obtained, meaning that the gate voltage does not have a clear influence on the prefactor, as

observed in <sup>37,149</sup>. At the same time, the prefactor is smaller than the expected -0.5 from coupled surface states, as observed previously for thicker films (section 4.3.2). The reduced prefactor values can be attributed to the small thickness of the Bi<sub>2</sub>Se<sub>3</sub> layer. The prefactor was also observed to decrease as the thickness was decreasing in TIs <sup>109,154,155</sup>. It was also observed after the maintenance of the MBE system (March 2024) that the In shutter was uncalibrated (partially open when it should be closed) and consequently, could present a small percentage of In in the Bi<sub>2</sub>Se<sub>3</sub> layer, which might lead to a weaker WAL.

On the other hand, the coherence length seems to be improved as the negative voltage is applied, from 582 nm to 657 nm. However, a large experimental error might imply that the observed value is statistically consistent with no significant change. The bulk carriers have a reduced contribution to the overall 2D conductivity of the system and, therefore an improved coherence length<sup>133</sup>. Moreover, the negative voltages reduce the bulk conduction channels by the gate modulation which reduces the surface to bulk scattering.

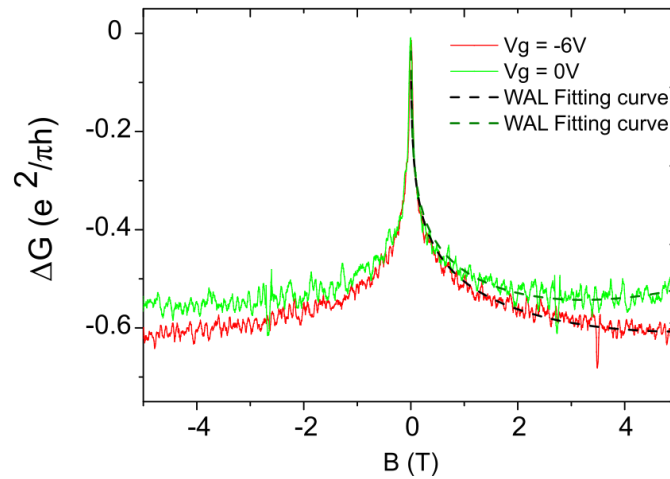


**Figure 6.7** Gate dependence of the WAL in the Bi<sub>2</sub>Se<sub>3</sub> device for the gate voltage of 0 and -6 V as a function of the magnetic field. The fitting is shown as dashed lines for each gate voltage.

**Table 6.1** Estimated WAL fitting values from the Bi<sub>2</sub>Se<sub>3</sub> device at 1.5 K for different gate voltages of 0 and -6 V.

Gate (V)	Prefactor ( $\alpha$ )	Coherence length (nm)	$\beta$
0	$-0.08 \pm 0.02$	$582 \pm 353$	$0.004 \pm 0.002$
-6	$-0.09 \pm 0.02$	$657 \pm 432$	$0.002 \pm 0.002$

### 6.2.3. Bi<sub>2</sub>Se<sub>3</sub> transport properties modulation with gate voltage

Finally, the Bi<sub>2</sub>Se<sub>3</sub> transport properties are extracted for the different gate voltages. This characterization of the material is a direct method to prove the effectiveness of the gate effect. The gate dependence of the Hall carrier density ( $n$ ) is obtained from  $n = \frac{1}{R_H e}$ , where  $R_H$  is the Hall slope. The Hall resistance ( $R_{xy}$ ) is shown in Fig 6.8 a) for different gate voltages from -10 up to 10 V.  $R_{xy}$  shows a linear behavior with the magnetic field as expected, where the Hall slope is extracted to estimate the carrier concentration.

The extracted values, electron density, and mobility are shown in Fig 6.8 b) as a function of the gate voltage. The carrier density is reduced as the gate voltage decreases to negative voltages, which is indicative of a n-type material. Even though the In<sub>2</sub>Se<sub>3</sub> capping layer is introduced to prevent oxygen diffusion and at the same time, protect the Bi<sub>2</sub>Se<sub>3</sub> layer, the n-type degeneracy can be worsened from unintentional environmental contaminations<sup>156</sup> and by the fabrication process through the chemical reaction between the Bi<sub>2</sub>Se<sub>3</sub> and the solvents. At  $V_g$  of 0 V, an electron concentration of approximately  $6 \times 10^{12} \text{ cm}^{-2}$  is obtained, comparable to the previously observed Bi<sub>2</sub>Se<sub>3</sub> with the same buffer layer at RT (section 3.4.2). There is a slight difference from  $6 \times 10^{12} \text{ cm}^{-2}$  (1.5 K) to  $1.6 \times 10^{13} \text{ cm}^{-2}$  (RT), which is attributed to the temperature since the Bi<sub>2</sub>Se<sub>3</sub> electron concentration tends to increase with temperature. The Bi<sub>2</sub>Se<sub>3</sub> FET obtained mobility of almost  $550 \text{ m}^2 \text{ V}^{-1} \text{ s}^{-1}$ . The reduced mobility, compared to the previous Bi<sub>2</sub>Se<sub>3</sub> on an IS-BIS buffer layer (section 3.4.2:  $600 \text{ m}^2 \text{ V}^{-1} \text{ s}^{-1}$ ) could be associated with the reduced thickness reinforcing the significant effect of the thickness present on the mobility<sup>40</sup>.

In terms of the transport properties modulation with the gate voltage, the electron concentration is reduced from  $6 \times 10^{12} \text{ cm}^{-2}$  to  $4 \times 10^{12} \text{ cm}^{-2}$  by sweeping the  $V_g$  to -10 V, this effect is similarly observed in<sup>43,133</sup>. Likewise, the mobility is improved from 550 to  $750 \text{ m}^2 \text{ V}^{-1} \text{ s}^{-1}$  with a  $V_g$  of -10 V. The electron concentration decreasing with the gate voltage is also an indication of an n-type material as stated in the literature<sup>133,150</sup>. The transport properties have a linear tendency with the gate voltage applied.

In conclusion, the gate voltage is shown to affect the Bi<sub>2</sub>Se<sub>3</sub> channel by modulating its transport properties, which can be understood as the Fermi level being closer to the band gap or closer to the conduction band minimum.

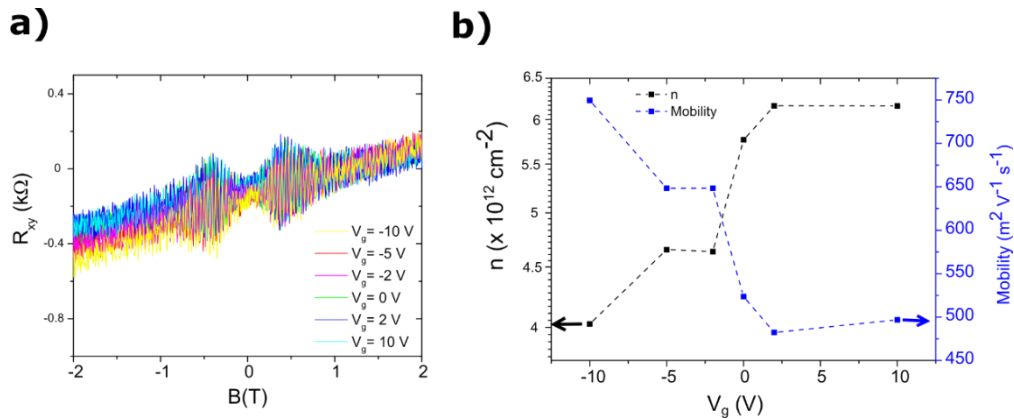


**Figure 6.8** a) Linear response of the transverse resistance ( $R_{xy}$ ) as a function of the magnetic field for different gate voltages. b) Extracted electron concentration and mobility for the different gate voltages. The measurements are performed at a temperature of 1.5 K.

### 6.3. Summary

In summary, the fabrication of FET devices based on thin-layer MBE-grown Bi<sub>2</sub>Se<sub>3</sub> with IS-BIS buffer and In<sub>2</sub>Se<sub>3</sub> capping layers is developed at a wafer scale level. Selective In<sub>2</sub>Se<sub>3</sub> etching is achieved to allow the ohmic contact with the Bi<sub>2</sub>Se<sub>3</sub> with minimal air exposure. A functional gate field effect transistor is achieved by a dielectric behavior of the gate I-V. The negative gate voltage was shown to have a beneficial effect by improving the insulating bulk contributions while improving the transport properties, such as electron concentration and mobility. Furthermore, the WAL was maintained after the fabrication process with a cusp in the magneto conductance.

## Conclusion and outlook

In this thesis, MBE was demonstrated to be a robust technique for the deposition of high-quality  $\text{Bi}_2\text{Se}_3$  thin films. Epitaxial growth on sapphire (0001) substrates has proven feasible for the growth of  $\text{Bi}_2\text{Se}_3$  at relatively low growth temperatures (310 °C), Se overpressures ( $\text{BEP} = 2.5 \times 10^{-5}$  mBar) and slow growth rates (1-1.4 nm/min). Notably, defects created, such as twinning and dislocations, could be mitigated by a substrate surface treatment with two-step growth or by the implementation of an  $\text{In}_2\text{Se}_3$ - $(\text{Bi}, \text{In})_2\text{Se}_3$  buffer layer with improved chemical compatibility.  $\text{Bi}_2\text{Se}_3$  demonstrated high single crystallography and relatively good electrical and transport properties of the topological insulator with the highest mobility of  $592.5 \text{ cm}^2/\text{Vs}$  and lowest sheet concentration of  $1.69 \times 10^{13} \text{ cm}^{-2}$  at room temperature. Furthermore, the topological properties were confirmed by the existence of surface states crossing the band gap (ARPES) and the presence of a weak antilocalization effect cusp in the magnetoconductance. However, the n-type degeneracy obtained after the growth of the TI could not be avoided during growth or after air exposure, impairing the exploitation of the dissipationless surface states at room temperature.

Ga and Cu doping of  $\text{Bi}_2\text{Se}_3$  was investigated to counterbalance the n-type degeneracy. Ga doping resulted in an expansion of the  $\text{Bi}_2\text{Se}_3$  crystal lattice parameter by the introduction of Ga atoms in the unit cell. The  $\text{Bi}_2\text{Se}_3$  lattice parameter  $c$  changed from  $28.66 \text{ \AA}$  (reference) to the highest value of  $28.92 \text{ \AA}$  (Ga: 2 at.%). This expansion suggests the Ga intercalation in the van der Waals gap at low Ga concentrations. N-type doping was consistently observed for Ga doping with a sixfold increase of the electron concentration to  $\sim 6 \times 10^{19} \text{ cm}^{-3}$  for Ga percentages of 2 at.% and 7 at.%, which supports the interpretation of the intercalation of Ga atoms into the material. ARPES measurements showed an upward Fermi level shift, and consequently, an increase in the electron concentration, which is in agreement with the transport measurements. Moreover, the surface states characteristics of the topological insulator survived upon the lowest concentration of Ga (2 at.%), whereas for the highest concentration of Ga (7 at.%), a destruction of the surface states was observed. Similar conclusions were extracted from the inexistent WAL effect for the doping of the 7 at.% doping with Ga.

In contrast, Cu doping leads to the contraction of the crystal volume as observed by XRD. Moreover, STEM images and energy-dispersive X-rays showed a random distribution of Cu atoms in the crystal. These observations indicate that Cu occupies the Bi sites in the crystal. In terms of transport, Cu doping exhibits characteristics of a good acceptor impurity leading to a two-fold reduction in the carrier concentration by the substitution of Bi atoms. ARPES measurements on Cu-doped  $\text{Bi}_2\text{Se}_3$  revealed a downward Fermi level shift and consequently, an improved topological transport with a reduction of bulk contributions. Moreover, the surface states are not destroyed upon the highest Cu concentration of 7 at.%.

As an alternative approach to tuning the Fermi level into the band gap, the investigation was extended to the fabrication of FET devices based on epitaxial  $\text{Bi}_2\text{Se}_3$ , emphasizing the preservation of the TI surface quality by the incorporation of a  $\beta\text{-In}_2\text{Se}_3$  capping layer. The fabrication process was developed and successfully achieved, enabling the Fermi level

tuning, closer to the conduction band minimum by the application of negative gate voltages. Tuning of the Fermi level can be seen by the improved transport properties and the semi-ambipolar behavior of the channel resistance while preserving the WAL effect, though with a reduced cusp at low temperatures.

Overall, no evidence of topological superconductivity was found in MBE-grown  $\text{Bi}_2\text{Se}_3$  doped with Cu atoms. The main reason is attributed to the high-quality thin films provided by MBE growth. The known TSC found in Cu-doped  $\text{Bi}_2\text{Se}_3$  is achieved by less “cleaner” growth techniques (melt-growth), increasing the concentration of defects in the material, which might be the key to obtaining the TSC. The high-quality growth provided by MBE could thus be a disadvantage for the appearance of TSC.

In addition, Ga doping at low concentrations preserved the topological behavior. Moreover, the possibility of Ga being intercalated in the Van der Waals gap and the plateau-like behavior observed in the WAL effect could indicate that Ga might be a possible new dopant for the TSC family. However, high concentrations of Ga doping led to a topological phase transition by the destruction of the surface states since the WAL cusp vanished.

As an outlook for future projects, the growth of the topological insulator  $\text{Bi}_2\text{Se}_3$  with reduced intrinsic defects and an insulating bulk should be a main goal. The use of different substrates or buffer layers with minimal lattice mismatch should be reconsidered because of the presence of twin domains in the thin-film material and the existence of defects that lead to n-type degeneracy. An interesting approach involves the use of  $\text{SrTiO}_3$  (STO) substrates. Despite the larger lattice mismatch of -25% (Table 3.1) compared to sapphire substrates,  $\text{SrTiO}_3$  (111) substrates could be used for back-gating, allowing a Fermi-level tuning of the bottom surface<sup>37</sup>. STO is a dielectric material similar to the  $\text{Al}_2\text{O}_3$  (sapphire), but with a higher dielectric constant ( $\epsilon_r = 300$  at RT<sup>157</sup>) compared to the sapphire ( $\epsilon_r = 9.3$ ). Furthermore, the dielectric constant of STO increases at low temperatures ( $\epsilon_r = 24000$  at 3K<sup>157</sup>), which allows the bottom gate tuning of the Fermi level at low temperatures. The use of both top and bottom gating of the topological insulator can lead to a higher reduction in the carrier concentration and, consequently, the tuning of the Fermi level into the band gap.

The top-gate FET devices developed in this thesis still have room to be improved and achieve an ambipolar behavior characteristic of a Fermi level transition from the conduction band to the valence band. The reduced Fermi level tuning in the FET device is linked to the poor dielectric material used and the deposition technique of  $\text{Al}_2\text{O}_3$  by sputtering. The use of an ionic liquid gate (TEME-DFSI) would be the focus of the next approach, where a significant tuning effect is achieved even at low gate voltages<sup>150,158</sup>. Although Ga and Cu-doped  $\text{Bi}_2\text{Se}_3$  device fabrication was accomplished, the electrical characterization of these devices was not feasible due to time constraints and dedicated tool limitations at the research institute.

## References

- Kane, C. L. & Mele, E. J. Quantum Spin hall effect in graphene. *Phys. Rev. Lett.* **95**, 226801 (2005).
- Klitzing, K. V., Dorda, G. & Pepper, M. New method for high-accuracy determination of the fine-structure constant based on quantized hall resistance. *Phys. Rev. Lett.* **45**, 494–497 (1980).
- König, M. *et al.* Quantum Spin Hall Insulator State in HgTe Quantum Wells. *Science* **318**, 766–770 (2007).
- Zhang, H. *et al.* Topological insulators in Bi<sub>2</sub>Se<sub>3</sub>, Bi<sub>2</sub>Te<sub>3</sub> and Sb<sub>2</sub>Te<sub>3</sub> with a single Dirac cone on the surface. *Nat. Phys.* **5**, 438–442 (2009).
- Hasan, M. Z. & Kane, C. L. Colloquium: Topological insulators. *Rev. Mod. Phys.* **82**, 3045–3067 (2010).
- Laughlin, R. B. Quantized Hall conductivity in two dimensions. *Phys. Rev. B* **23**, 5632–5633 (1981).
- Halperin, B. I. Quantized Hall conductance, current-carrying edge states, and the existence of extended states in a two-dimensional disordered potential. *Phys. Rev. B* **25**, 2185–2190 (1982).
- den Nijs, M. Quantized Hall conductance in a two dimensional periodic potential. *Phys. A Stat. Mech. its Appl.* **124**, 199–210 (1984).
- Kane, C. L. & Mele, E. J. Z<sub>2</sub> topological order and the quantum spin hall effect. *Phys. Rev. Lett.* **95**, 146802 (2005).
- Ortmann, F., Roche, S. & Valenzuela, S. O. Topological Insulators Fundamentals and Perspectives. in 1–400 (2015).
- Vanderbilt, D. *Berry Phases in Electronic Structure Theory: Electric Polarization, Orbital Magnetization and Topological Insulators*. (Cambridge University Press, 2018). doi:10.1017/9781316662205.
- Xia, Y. *et al.* Observation of a large-gap topological-insulator class with a single Dirac cone on the surface. *Nat. Phys.* **5**, 398–402 (2009).
- Chen, Y. L. *et al.* Experimental realization of a three-dimensional topological insulator, Bi<sub>2</sub>Te<sub>3</sub>. *Science* **325**, 178–181 (2009).
- Hikami, S., Larkin, A. I. & Nagaoka, Y. Spin-Orbit Interaction and Magnetoresistance in the Two Dimensional Random System. *Prog. Theor. Phys.* **63**, 707–710 (1980).
- Ginley, T. P., Wang, Y. & Law, S. Topological insulator film growth by molecular beam epitaxy: A review. *Crystals* **6**, 154 (2016).
- Kenjiro Oura, Lifshits, V. G., Saranin, A. A., Zotov, A. V. & Katayama, M. *Surface Science- An Introduction*. Springer vol. 125 (2004).
- Editors, S., Klitzing, P. A. K. Von & Wiesendanger, H. S. R. *NANOSCIENCE AND TECHNOLOGY Springer-Verlag Berlin Heidelberg GmbH Physics and Astronomy*.
- Claro, M. S., Grzonka, J., Nicoara, N., Ferreira, P. J. & Sadewasser, S. Wafer-Scale Fabrication of 2D β-In<sub>2</sub> Se<sub>3</sub> Photodetectors. *Adv. Opt. Mater.* **9**, 2001034 (2021).
- Vignaud, G. & Gibaud, A. REFLEX : a program for the analysis of specular X-ray and neutron reflectivity data. *J. Appl. Crystallogr.* **52**, 201–213 (2019).
- Mambakkam, S. V. & Law, S. Spectroscopy of van der Waals nanomaterials: Opportunities and challenges. *J. Appl. Phys.* **134**, 1–28 (2023).
- Shailja Sharma, Shiv Kumar, Amit Kumar, Kenya Shimada, and C. S. Y. Electronic transport studies of Ag-doped Bi<sub>2</sub>Se<sub>3</sub> topological insulator Electronic transport studies of Ag-doped Bi<sub>2</sub>Se<sub>3</sub> topological insulator. *J. Appl. Phys.* **132**, 105108 (2022).
- Pereira, V. M. M. In situ studies of Bi<sub>2</sub>Te<sub>3</sub> thin films and interfaces grown by molecular beam epitaxy. (Universit'at Dresden, 2021).
- Kremer, G. *et al.* Quantum Confinement and Electronic Structure at the Surface of van der Waals Ferroelectric α-In<sub>2</sub>Se<sub>3</sub>. *ACS Nano* **17**, 18924–18931 (2023).
- Crisol, A.; Bisti, F.; Coldelram, C.; Llonch, M.; Molas, B.; Monge, R.; Nicolás, J.; Nikitina, L.; Quispe, M.; Ribó, L.; Tallarida, M. ALBA BL20 New Monochromator Design. *Proc. MEDSI'20* 14–16 (2021).
- Fan, C., Sakamoto, K. & Krüger, P. Carrier doping of Bi<sub>2</sub> Se<sub>3</sub> surface by chemical adsorption—A DFT study. *Appl. Surf. Sci.* **643**, 158699 (2024).
- He, L., Kou, X. & Wang, K. L. Review of 3D topological insulator thin-film growth by molecular beam epitaxy and potential applications. *Phys. Status Solidi - Rapid Res. Lett.* **7**, 50–63 (2013).
- Ginley, T. P. & Law, S. Growth of Bi<sub>2</sub> Se<sub>3</sub> topological insulator films using a selenium cracker source. *J. Vac. Sci. Technol. B, Nanotechnol. Microelectron. Mater. Process. Meas. Phenom.* **34**, 02L105 (2016).
- Levy, I., Garcia, T. A., Shafique, S. & Tamargo, M. C. Reduced twinning and surface roughness of Bi<sub>2</sub> Se<sub>3</sub> and Bi<sub>2</sub> Te<sub>3</sub> layers grown by molecular beam epitaxy on sapphire substrates. *J. Vac. Sci. Technol. B, Nanotechnol. Microelectron. Mater. Process. Meas. Phenom.* **36**, 02D107 (2018).
- Walsh, L. A. *et al.* Fermi Level Manipulation through Native Doping in the Topological Insulator Bi<sub>2</sub> Se<sub>3</sub>. *ACS Nano* **12**, 6310–6318 (2018).
- Bai, A., Hilde, M., Patil, P. D., Engel-Herbet, R. & Peiris, F. Probing the growth quality of molecular beam epitaxy-grown Bi<sub>2</sub> Se<sub>3</sub> films via in-situ spectroscopic ellipsometry. *J. Cryst. Growth* **591**, 126714 (2022).
- He, L. *et al.* Epitaxial growth of Bi<sub>2</sub> Se<sub>3</sub> topological insulator thin films on Si (111). *J. Appl. Phys.* **109**, 103702 (2011).
- Hasan, M. Z. & Moore, J. E. Three-Dimensional Topological Insulators. *Annu. Rev. Condens. Matter Phys.* **2**, 55–78 (2011).
- Schreyeck, S. *et al.* Molecular beam epitaxy of high structural quality Bi<sub>2</sub> Se<sub>3</sub> on lattice matched InP(111) substrates. *Appl. Phys. Lett.* **102**, 041914 (2013).
- Bansal, B. N. *et al.* Epitaxial growth of topological insulator Bi<sub>2</sub> Se<sub>3</sub> film on Si(111) with atomically sharp interface. *Thin Solid Films* **520**, 224–229 (2011).
- Li, H. *et al.* Growth and band alignment of Bi<sub>2</sub> Se<sub>3</sub> topological insulator on H-terminated Si(111) van der Waals surface. *Appl. Phys. Lett.* **102**, 074106 (2013).
- Claro, M. S., Levy, I., Gangopadhyay, A., Smith, D. J. & Tamargo, M. C. Self-assembled Bismuth Selenide (Bi<sub>2</sub> Se<sub>3</sub>) quantum dots grown by molecular beam epitaxy. *Sci. Rep.* **39**, 3370 (2019).

37. Chen, J. *et al.* Gate-voltage control of chemical potential and weak antilocalization in Bi<sub>2</sub>Se<sub>3</sub>. *Phys. Rev. Lett.* **105**, 176602 (2010).
38. Brom, J. E. *et al.* Structural and electrical properties of epitaxial Bi<sub>2</sub>Se<sub>3</sub> thin films grown by hybrid physical-chemical vapor deposition. *Appl. Phys. Lett.* **100**, 161110 (2012).
39. Wang, Y., Ginley, T. P., Zhang, C. & Law, S. Transport properties of Bi<sub>2</sub>(Se<sub>1-x</sub>Te<sub>x</sub>)<sub>3</sub> thin films grown by molecular beam epitaxy. *J. Vac. Sci. Technol. B, Nanotechnol. Microelectron. Mater. Process. Meas. Phenom.* **35**, 02B106 (2017).
40. Wickramasinghe, K. S., Forrester, C. & Tamargo, M. C. Molecular Beam Epitaxy of Twin-Free Bi<sub>2</sub>Se<sub>3</sub> and Sb<sub>2</sub>Te<sub>3</sub> on In<sub>2</sub>Se<sub>3</sub>/InP(111)B Virtual Substrates. *Crystals* **13**, 677 (2023).
41. Hasegawa, S. Reflection High-Energy Electron Diffraction. in *Characterization of Materials* (ed. Wiley) 1925–1937 (Wiley, 2012). doi:10.1002/0471266965.com139.
42. Tang, F., Parker, T., Wang, G. & Lu, T. Surface texture evolution of polycrystalline and nanostructured films: RHEED surface pole figure analysis. *J. Phys. D Appl. Phys.* **40**, R427–R439 (2007).
43. Bansal, N. *et al.* Robust topological surface states of Bi<sub>2</sub>Se<sub>3</sub> thin films on amorphous SiO<sub>2</sub>/Si substrate and a large ambipolar gating effect. *Appl. Phys. Lett.* **104**, 241606 (2014).
44. Guillet, T. *et al.* Magnetotransport in Bi<sub>2</sub>Se<sub>3</sub> thin films epitaxially grown on Ge(111). *AIP Adv.* **8**, 115125 (2018).
45. Lee, J. J. *et al.* Intrinsic ultrathin topological insulators grown via molecular beam epitaxy characterized by in-situ angle resolved photoemission spectroscopy. *Appl. Phys. Lett.* **101**, 013118 (2012).
46. Hu, J. *et al.* Disorder-induced linear magnetoresistance in Sr-doped Bi<sub>2</sub>Se<sub>3</sub> thin films. *arXiv Prepr. arXiv* 2202.08110 (2022).
47. Wang, M. *et al.* Growth and structural characterisation of Sr-doped Bi<sub>2</sub>Se<sub>3</sub> thin films. *Sci. Rep.* **8**, 2192 (2018).
48. Liu, Y., Weinert, M. & Li, L. Spiral growth without dislocations: Molecular beam epitaxy of the topological insulator Bi<sub>2</sub>Se<sub>3</sub> on epitaxial graphene/SiC(0001). *Phys. Rev. Lett.* **108**, 115501 (2012).
49. Lin, Y. C. *et al.* A study on the epitaxial Bi<sub>2</sub>Se<sub>3</sub> thin film grown by vapor phase epitaxy. *AIP Adv.* **6**, 065218 (2016).
50. Richardella, A., Kandala, A., Lee, J. S. & Samarth, N. Characterizing the structure of topological insulator thin films. *APL Mater.* **3**, 083303 (2015).
51. Lee, Y. F., Kumar, R., Hunte, F., Narayan, J. & Schwartz, J. Microstructure and transport properties of epitaxial topological insulator Bi<sub>2</sub>Se<sub>3</sub> thin films grown on MgO (100), Cr<sub>2</sub>O<sub>3</sub> (0001), and Al<sub>2</sub>O<sub>3</sub> (0001) templates. *J. Appl. Phys.* **118**, 125309 (2015).
52. Volosheniuk, S. O., Selivanov, Y. G., Bryzgalov, M. A., Martovitskii, V. P. & Kuntsevich, A. Y. Effect of Sr doping on structure, morphology, and transport properties of Bi<sub>2</sub>Se<sub>3</sub> epitaxial thin films. *J. Appl. Phys.* **125**, 095103 (2019).
53. Mortelmans, W. Epitaxy of van der Waals materials a fundamental and exploratory study focused on molecular beam epitaxy of WSe<sub>2</sub>. (Ku Leuven, 2020).
54. Yao, X., Moon, J., Cheong, S. W. & Oh, S. Structurally and chemically compatible BiInSe<sub>3</sub> substrate for topological insulator thin films. *Nano Res.* **13**, 2541–2545 (2020).
55. Koirala, N. *et al.* Record Surface State Mobility and Quantum Hall Effect in Topological Insulator Thin Films via Interface Engineering. *Nano Lett.* **15**, 8245–8249 (2015).
56. Wang, Y., Ginley, T. P. & Law, S. Growth of high-quality Bi<sub>2</sub>Se<sub>3</sub> topological insulators using (Bi<sub>1-x</sub>In<sub>x</sub>)<sub>2</sub>Se<sub>3</sub> buffer layers. *J. Vac. Sci. Technol. B, Nanotechnol. Microelectron. Mater. Process. Meas. Phenom.* **36**, 02D101 (2018).
57. Singh, B., Gautam, S., Aggarwal, V., Tawale, J. S. & Kushvaha, S. S. Growth and characterization of crystalline Bi<sub>2</sub>Se<sub>3</sub> thin films on flexible metal foils by magnetron sputtering system. *Mater. Today Proc.* **64**, 1701–1706 (2022).
58. Riney, L. *et al.* Introduction of Sr into Bi<sub>2</sub>Se<sub>3</sub> thin films by molecular beam epitaxy. *J. Appl. Phys.* **129**, 085107 (2021).
59. Jafarpisheh, S. *et al.* Reducing the Impact of Bulk Doping on Transport Properties of Bi-Based 3D Topological Insulators. *Phys. status solidi* **258**, 2000021 (2021).
60. Zhang, H., Zhang, X., Liu, C., Lee, S.-T. & Jie, J. High-Responsivity, High-Detectivity, Ultrafast Topological Insulator Bi<sub>2</sub>Se<sub>3</sub>/Silicon Heterostructure Broadband Photodetectors. *ACS Nano* **10**, 5113–5122 (2016).
61. Corbae, P. *et al.* Observation of spin-momentum locked surface states in amorphous Bi<sub>2</sub>Se<sub>3</sub>. *Nat. Mater.* **22**, 200–206 (2023).
62. Sultana, R., Gurjar, G., Patnaik, S. & Awana, V. P. S. Growth, Characterization and High-Field Magneto-Conductivity. *J. Supercond. Nov. Magn.* **32**, 769–777 (2019).
63. Wang, C. C., Shieu, F. S. & Shih, H. C. Photosensing and characterizing of the pristine and In-, Sn-doped Bi<sub>2</sub>Se<sub>3</sub> nanoplatelets fabricated by thermal V-S process. *Nanomaterials* **11**, 1352 (2021).
64. Wang, Y. & Law, S. Optical properties of (Bi<sub>1-x</sub>In<sub>x</sub>)<sub>2</sub>Se<sub>3</sub> thin films. *Opt. Mater. Express* **8**, 2570 (2018).
65. Selivanov, Y. G., Martovitskii, V. P., Bannikov, M. I. & Kuntsevich, A. Y. Effect of sr doping on structural and transport properties of Bi<sub>2</sub>Se<sub>3</sub>. *Materials* **14**, 7528 (2021).
66. Brahlek, M. *et al.* Topological-metal to band-insulator transition in (Bi<sub>1-x</sub>In<sub>x</sub>)<sub>2</sub>Se<sub>3</sub> thin films. *Phys. Rev. Lett.* **109**, 186403 (2012).
67. Stephen, G. M. *et al.* Effect of Sn Doping on Surface States of Bi<sub>2</sub>Se<sub>3</sub> Thin Films. *J. Phys. Chem. C* **124**, 27082–27088 (2020).
68. Zhang, M. & Wei, Z. T. Effect of Silver Doping on Transport Properties of Bi<sub>2</sub>Se<sub>3</sub>: Ag<sub>x</sub>Bi<sub>2-x</sub>Se<sub>3</sub> and Bi<sub>2-x</sub>Ag<sub>x</sub>Se<sub>3</sub>. *Electron. Mater. Lett.* **14**, 298–304 (2018).
69. Uesugi, E. *et al.* Fermi level tuning of Ag-doped Bi<sub>2</sub>Se<sub>3</sub> topological insulator. *Sci. Rep.* **9**, 5376 (2019).
70. Shi, T., Kushnir, K., Wang, Z., Law, S. & Titova, L. V. Photoexcited Free Carrier Dynamics in Bi<sub>2</sub>Se<sub>3</sub>, (Bi<sub>0.75</sub>In<sub>0.25</sub>)<sub>2</sub>Se<sub>3</sub>, and (Bi<sub>0.5</sub>In<sub>0.5</sub>)<sub>2</sub>Se<sub>3</sub>: From Topological to Band Insulator. *ACS Photonics* **7**, 2778–2786 (2020).
71. Brahlek, M. Criteria for Realizing Room-Temperature Electrical Transport Applications of Topological Materials. *Adv. Mater.* **32**, 2005698 (2020).
72. Pilidi, A. & Speliotis, T. Anomalous hall effect in a magnetic topological insulator (BiMn)(Bi<sub>0.75</sub>In<sub>0.25</sub>)<sub>2</sub>Te<sub>3</sub>. *IEEE Trans. Magn.* **55**, 1–7 (2019).
73. Collins-Mcintyre, L. J. *et al.* Magnetic ordering in Cr-doped Bi<sub>2</sub>Se<sub>3</sub> thin films. *EPL* **107**, 57009 (2014).
74. Liu, L., Zhang, M. & Liu, Q. The Raman Spectra of Co-, Fe-, and Mn-doped Bi<sub>2</sub>Se<sub>3</sub> Single Crystals. *crystals* **13**, 456 (2023).
75. Hor, Y. S. *et al.* Superconductivity in Cu<sub>x</sub>Bi<sub>2-x</sub>Se<sub>3</sub> and its implications for pairing in the undoped topological insulator. *Phys. Rev. Lett.* **104**, 057001 (2010).

76. Kriener, M. *et al.* Electrochemical synthesis and superconducting phase diagram of  $\text{Cu}_x\text{Bi}_2\text{Se}_3$ . *Phys. Rev. B - Condens. Matter Mater. Phys.* **84**, 054513 (2011).
77. Han, C. Q. *et al.* Electronic structure of a superconducting topological insulator Sr-doped  $\text{Bi}_2\text{Se}_3$ . *Appl. Phys. Lett.* **107**, 171602 (2015).
78. Liu, Z. *et al.* Superconductivity with Topological Surface State in  $\text{Sr}_x\text{Bi}_2\text{Se}_3$ . *J. Am. Chem. Soc.* **137**, 10512–10515 (2015).
79. Kevy, S. M. *et al.* Structural and electronic inhomogeneity of superconducting Nb-doped  $\text{Bi}_2\text{Se}_3$ . *Phys. Rev. B* **103**, 085107 (2021).
80. Dalgaard, K. J. *et al.* Local structure of Nb in superconducting Nb-doped  $\text{Bi}_2\text{Se}_3$ . *Phys. Rev. B* **103**, 184103 (2021).
81. Fu, L. & Kane, C. L. Superconducting proximity effect and majorana fermions at the surface of a topological insulator. *Phys. Rev. Lett.* **100**, 096407 (2008).
82. Mourik, V. *et al.* Signatures of majorana fermions in hybrid superconductor-semiconductor nanowire devices. *Science* **336**, 1003–1007 (2012).
83. Iyengar, S. A., Puthirath, A. B. & Swaminathan, V. Realizing Quantum Technologies in Nanomaterials and Nanoscience. *Adv. Mater.* **35**, 2107839 (2023).
84. Wiendlocha, B. Resonant Levels, Vacancies, and Doping in  $\text{Bi}_2\text{Te}_3$ ,  $\text{Bi}_2\text{Te}_2\text{Se}$ , and  $\text{Bi}_2\text{Se}_3$  Tetradymites. *J. Electron. Mater.* **45**, 3515–3531 (2016).
85. Phutela, A., Bhumla, P., Jain, M. & Bhattacharya, S. Exploring strong and weak topological states on isostructural substitutions in  $\text{TlBiSe}_2$ . *Sci. Rep.* **12**, 21970 (2022).
86. Shirasawa, T. *et al.* Structure and transport properties of Cu-doped  $\text{Bi}_2\text{Se}_3$  films. *Phys. Rev. B - Condens. Matter Mater. Phys.* **89**, 195311 (2014).
87. Hecker, M. & Schmalian, J. Vestigial nematic order and superconductivity in the doped topological insulator  $\text{Cu}_x\text{Bi}_2\text{Se}_3$ . *npj Quantum Mater.* **3**, 26 (2018).
88. Zhang, Y. *et al.* Doping effects of Sb and Pb in epitaxial topological insulator  $\text{Bi}_2\text{Se}_3$  thin films: An in situ angle-resolved photoemission spectroscopy study. *Appl. Phys. Lett.* **97**, 194102 (2010).
89. Matano, K., Kriener, M., Segawa, K., Ando, Y. & Zheng, G. Structural and Electronic Characterization of  $\text{Cu}_x\text{Bi}_2\text{Se}_3$ . *J. Mex. Chem. Soc.* **60**(3), 101–107 (2016).
90. Bapi Pradhan. Solution Phase Synthesis of Large- area Ultra-thin Two Dimensional Layered  $\text{Bi}_2\text{Se}_3$ : Role of Cu intercalated ans substitution. *Mater. Res. Express* **6**, 124005 (2019).
91. Li, Y., Smith, N. P., Rexhausen, W., Schofield, M. A. & Guptasarma, P. Possible lattice and charge order in  $\text{Cu}_x\text{Bi}_2\text{Te}_2\text{Se}$ . *J. Phys. Mater.* **3**, 015008 (2020).
92. Yu, S. H., Hung, T. L., Ou, M. N., Chou, M. M. C. & Chen, Y. Y. Zero Cu valence and superconductivity in high-quality  $\text{Cu}_x\text{Bi}_2\text{Se}_3$  crystal. *Phys. Rev. B* **100**, 174502 (2019).
93. Wang, Z., Han, D., Gao, X. P. A. & Zhang, Z. Influence of dopant uniformity on electron transport in  $\text{Cu}_x\text{Bi}_2\text{Se}_3$  films. *Cryst. Growth Des.* **21**, 608–616 (2021).
94. Grzonka, J., Claro, M. S., Molina-Sánchez, A., Sadewasser, S. & Ferreira, P. J. Novel Polymorph of GaSe. *Adv. Funct. Mater.* **31**, 2104965 (2021).
95. Li, M. *et al.* Electron delocalization and relaxation behavior in Cu-doped  $\text{Bi}_2\text{Se}_3$  films. *Phys. Rev. B* **96**, 075152 (2017).
96. Shannon, B. Ionic Radii and Systematic Studies of Interatomic Distances in Halides and Chalcogenides Central Research and Development Department, Experimental. *Acta Crystallogr. A* **32**, 751–767 (1976).
97. Li, M. *et al.* Transition from weak antilocalization to linear magnetoresistance by tuning structure geometry and chemical potential in nanostructured  $\text{Bi}_2\text{Se}_3$  films. *J. Solid State Chem.* **328**, 124315 (2023).
98. Zhu, J. *et al.* Absorption edge, urbach tail, and electron-phonon interactions in topological insulator  $\text{Bi}_2\text{Se}_3$  and band insulator  $(\text{Bi}_{0.89}\text{In}_{0.11})_2\text{Se}_3$ . *Appl. Phys. Lett.* **114**, 162105 (2019).
99. Dixon, A. K., Bowden, D. J., Ellis, H. & Logan, B. M. Point Defects in Ga-Doped  $\text{Bi}_2\text{Se}_3$  Single Crystals. *H Phys. Status Solidi B-basic Solid State Phys.* **119**, K17–K19 (1983).
100. Sharma, S. & Yadav, C. S. Anisotropic Upper Critical Field, Seebeck and Nernst Coefficient in  $\text{Nb}_{0.2}\text{Bi}_2\text{Se}_3$  Topological Superconductor. *Supercond. Sci. Technol* **35**, 075015 (2022).
101. Shrutii, Maurya, V. K., Neha, P., Srivastava, P. & Patnaik, S. Superconductivity by Sr intercalation in the layered topological insulator  $\text{Bi}_2\text{Se}_3$ . *Phys. Rev. B - Condens. Matter Mater. Phys.* **92**, 020506(R) (2015).
102. Hu, J. *et al.* Manipulating the magneto-resistance of  $\text{Bi}_2\text{Se}_3$  thin films by strontium doping. *J. Appl. Phys.* **132**, 095302 (2022).
103. Li, M., Wang, Z., Yang, L., Gao, X. P. A. & Zhang, Z. From linear magnetoresistance to parabolic magnetoresistance in Cu and Cr-doped topological insulator  $\text{Bi}_2\text{Se}_3$  films. *J. Phys. Chem. Solids* **128**, 331–336 (2019).
104. Kašparová, J. *et al.* n-type to p-type crossover in quaternary  $\text{Bi}_x\text{Sb}_y\text{Pb}_z\text{Se}_3$  single crystals. *J. Appl. Phys.* **97**, 103720 (2005).
105. Garate, I. & Glazman, L. Weak localization and antilocalization in topological insulator thin films with coherent bulk-surface coupling. *Phys. Rev. B - Condens. Matter Mater. Phys.* **86**, 035422 (2012).
106. Chen, J. *et al.* Tunable surface conductivity in  $\text{Bi}_2\text{Se}_3$  revealed in diffusive electron transport. *Phys. Rev. B - Condens. Matter Mater. Phys.* **83**, 241304 (2011).
107. Banerjee, A., Ganesan, R. & Anil Kumar, P. S. Enhanced coherence and decoupled surface states in topological insulators through structural disorder. *Appl. Phys. Lett.* **113**, 072105 (2018).
108. Brahlek, M., Koirala, N., Salehi, M., Bansal, N. & Oh, S. Emergence of decoupled surface transport channels in bulk insulating  $\text{Bi}_2\text{Se}_3$  thin films. *Phys. Rev. Lett.* **113**, 026801 (2014).
109. Malasi, M., Rathod, S., Lakhani, A. & Kumar, D. Evidence of surface delocalization in ultrathin films of topological insulator in presence of intersurface hybridization and disorder. *Appl. Phys. Lett.* **121**, 093101 (2022).
110. Al-Tawhid, A. H. *et al.* Superconductivity and Weak Anti-localization at  $\text{KTaO}_3$  (111) Interfaces. *J. Electron. Mater.* **51**, 6305–6309 (2022).
111. Shen, J., Xie, Y. & Cha, J. J. Revealing Surface States in In-Doped  $\text{SnTe}$  Nanoplates with Low Bulk Mobility. *Nano Lett.* **15**, 3827–3832 (2015).
112. Vijay Narayan, Thuy-Anh Nguyen, Rhodri Mansell, David Ritchie, and G. M. Interplay of spin-orbit coupling and superconducting correlations in germanium telluride thin films. *Phy. Status Solidi R* **10**, 253–259 (2016).

113. S. de Castro, B. Kawata, G. R. F. L. Weak antilocalization effect and multi-channel transport in SnTe quantum well. *Appl. Phys. Lett.* **120**, 203102 (2022).
114. El-Sherif, H. *et al.* Scalable Characterization of 2D Gallium-Intercalated Epitaxial Graphene. *ACS Appl. Mater. Interfaces* **13**, 55428–55439 (2021).
115. Li, C. *et al.* Proximity-induced superconductivity in epitaxial topological insulator/graphene/gallium heterostructures. *Nat. Mater.* **22**, 570–575 (2023).
116. Briggs, N. *et al.* Atomically thin half-van der Waals metals enabled by confinement heteroepitaxy. *Nat. Mater.* **19**, 637–643 (2020).
117. Wetherington, M. T. *et al.* 2-dimensional polar metals: a low-frequency Raman scattering study. *2D Mater.* **8**, 041003 (2021).
118. Jens Bardarson. "Topological Electronics and Bosonics : from Concepts to devices". Winter school (2024).
119. Lahoud, E. *et al.* Evolution of the Fermi surface of a doped topological insulator with carrier concentration. *Phys. Rev. B - Condens. Matter Mater. Phys.* **88**, 1–9 (2013).
120. Brito, D., Pérez-rodriguez, A., Khatri, I. & Diez, E. Effect of gallium doping on structural and transport properties of the topological insulator Bi<sub>2</sub>Se<sub>3</sub> grown by molecular beam epitaxy. *Phys. J Appl* **132**, 115107 (2022).
121. Changdar, S., Sultana, R., Banik, S., Awana, V. P. S. & Thirupathiah, S. Angle resolved photoemission spectroscopy study on electronic band structure of topological insulator Bi<sub>2</sub>Se<sub>3</sub> in the presence of magnetic impurities. in *AIP Conference Proceedings* vol. 2265 030355 (2020).
122. Muñiz Cano, B. *et al.* Experimental Demonstration of a Magnetically Induced Warping Transition in a Topological Insulator Mediated by Rare-Earth Surface Dopants. *Nano Lett.* **23**, 6249–6258 (2023).
123. Richard, P., Qian, T. & Ding, H. ARPES measurements of the superconducting gap of Fe-based superconductors and their implications to the pairing mechanism. *J. Phys. Condens. Matter* **27**, 293203 (2015).
124. Wray, L. A. *et al.* Observation of topological order in a superconducting doped topological insulator. *Nat. Phys.* **6**, 855–859 (2010).
125. Tanaka, Y. *et al.* Evolution of electronic structure upon Cu doping in the topological insulator Bi<sub>2</sub>Se<sub>3</sub>. *Phys. Rev. B* **85**, 125111 (2012).
126. Wang, Y.-L. *et al.* Structural defects and electronic properties of the Cu-doped topological insulator Bi<sub>2</sub>Se<sub>3</sub>. *Phys. Rev. B* **84**, 075335 (2011).
127. Wang, H. *et al.* Crossover between weak antilocalization and weak localization of bulk states in ultrathin Bi<sub>2</sub>Se<sub>3</sub> films. *Sci. Rep.* **4**, 5817 (2014).
128. Whitcher, T. J. *et al.* Correlated plasmons in the topological insulator Bi<sub>2</sub>Se<sub>3</sub> induced by long-range electron correlations. *NPG Asia Mater.* **12**, 37 (2020).
129. Bianchi, M. *et al.* Coexistence of the topological state and a two-dimensional electron gas on the surface of Bi<sub>2</sub>Se<sub>3</sub>. *Nat. Commun.* **1**, 128 (2010).
130. Kuroda, K. *et al.* Hexagonally deformed fermi surface of the 3D topological insulator Bi<sub>2</sub>Se<sub>3</sub>. *Phys. Rev. Lett.* **105**, 076802 (2010).
131. Bianchi, M. *et al.* The electronic structure of clean and adsorbate-covered Bi<sub>2</sub>Se<sub>3</sub> : an angle-resolved photoemission study. *Semicond. Sci. Technol.* **27**, 124001 (2012).
132. Liu, J. *et al.* Surface coupling in Bi<sub>2</sub>Se<sub>3</sub> ultrathin films by screened Coulomb interaction. *Nat. Commun.* **14**, 4424 (2023).
133. Lang, M. *et al.* Revelation of topological surface states in Bi<sub>2</sub>Se<sub>3</sub> thin films by in situ Al passivation. *ACS Nano* **6**, 295–302 (2012).
134. Nowak, K. *et al.* Influence of Doping on the Topological Surface States of Crystalline Bi<sub>2</sub>Se<sub>3</sub> Topological Insulators. *Materials* **15**, 2083 (2022).
135. Gross, A. L. *et al.* Copper migration and surface oxidation of Cu<sub>x</sub>Bi<sub>2</sub>Se<sub>3</sub> in ambient pressure environments. (2022).
136. Gross, A. L. *et al.* Copper migration and surface oxidation of Cu<sub>x</sub>Bi<sub>2</sub>Se<sub>3</sub> in ambient pressure environments. *J. Phys. Mater.* **5**, 044005 (2022).
137. Takagaki, Y., Jenichen, B., Jahn, U., Ramsteiner, M. & Friedland, K.-J. Weak antilocalization and electron-electron interaction effects in Cu-doped Bi<sub>2</sub>Se<sub>3</sub> films. *Phys. Rev. B* **85**, 115314 (2012).
138. Huang, J. & Č. P. Multi-band magnetotransport in exfoliated thin films of Cu<sub>x</sub>Bi<sub>2</sub>Se<sub>3</sub>. *J. Phys. Condens. Matter* **30**, 155302 (2018).
139. Chrobak, M., Maćkosz, K., Nowak, K., Naumov, A. & Przybylski, M. Magnetoresistance vs. electronic structure in Cu doped single crystalline Bi<sub>2</sub>Se<sub>3</sub> 3D topological insulator. *J. Magn. Magn. Mater.* **589**, 171548 (2024).
140. Edmonds, M. T. *et al.* Stability and Surface Reconstruction of Topological Insulator Bi<sub>2</sub>Se<sub>3</sub> on Exposure to Atmosphere. *J. Phys. Chem. C* **118**, 20413–20419 (2014).
141. Kong, D. *et al.* Rapid surface oxidation as a source of surface degradation factor for Bi<sub>2</sub>Se<sub>3</sub>. *ACS Nano* **5**, 4698–4703 (2011).
142. Koirala, N., Salehi, M., Moon, J. & Oh, S. Gate-tunable quantum Hall effects in defect-suppressed Bi<sub>2</sub>Se<sub>3</sub> films. *Phys. Rev. B* **100**, 085404 (2019).
143. Matthias, R. *et al.* Top-Down Fabrication of Bulk-Insulating Topological Insulator Nanowires for Quantum Devices. *Nano Lett.* **23**, 2846–2853 (2023).
144. Uchiyama, T. *et al.* Semiconductor–metal transition in Bi<sub>2</sub>Se<sub>3</sub> caused by impurity doping. *Sci. Rep.* **13**, 537 (2023).
145. Xiu, F. *et al.* Quantum Capacitance in Topological Insulators. *Sci. Rep.* **2**, 669 (2012).
146. Steinberg, H., Gardner, D. R., Lee, Y. S. & Jarillo-Herrero, P. Surface state transport and ambipolar electric field effect in Bi<sub>2</sub>Se<sub>3</sub> nanodevices. *Nano Lett.* **10**, 5032–5036 (2010).
147. Yoshimi, R. *et al.* Quantum Hall effect on top and bottom surface states of topological insulator (Bi<sub>1-x</sub>Sb<sub>x</sub>)<sub>2</sub>Te<sub>3</sub> films. *Nat. Commun.* **6**, 6627 (2015).
148. Clark, O. J., Freyse, F., Yashina, L. V., Rader, O. & Sánchez-Barriga, J. Robust behavior and spin-texture stability of the topological surface state in Bi<sub>2</sub>Se<sub>3</sub> upon deposition of gold. *npj Quantum Mater.* **7**, 36 (2022).
149. Checkelsky, J. G., Hor, Y. S., Cava, R. J. & Ong, N. P. Bulk band gap and surface state conduction observed in voltage-tuned crystals of the topological insulator Bi<sub>2</sub>Se<sub>3</sub>. *Phys. Rev. Lett.* **106**, 196801 (2011).
150. Son, J. *et al.* Conductance modulation in topological insulator Bi<sub>2</sub>Se<sub>3</sub> thin films with ionic liquid gating. *Appl. Phys. Lett.* **103**, 213114 (2013).

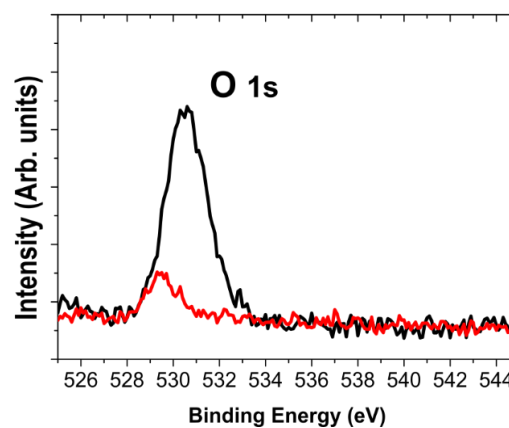
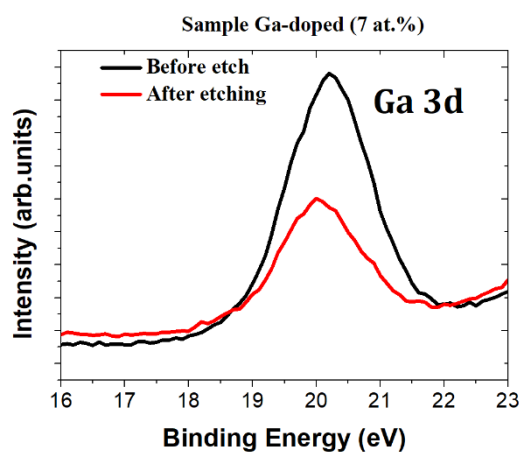
151. Yang, F. *et al.* Dual-Gated Topological Insulator Thin-Film Device for Efficient Fermi-Level Tuning. *ACS Nano* **9**, 4050–4055 (2015).
152. Lee, J., Park, J., Lee, J.-H., Kim, J. S. & Lee, H.-J. Gate-tuned differentiation of surface-conducting states in  $\text{Bi}_{1.5}\text{Sb}_{0.5}\text{Te}_{1.7}\text{Se}_{1.3}$  topological-insulator thin crystals. *Phys. Rev. B* **86**, 245321 (2012).
153. Steinberg, H., Laloë, J. B., Fatemi, V., Moodera, J. S. & Jarillo-Herrero, P. Electrically tunable surface-to-bulk coherent coupling in topological insulator thin films. *Phys. Rev. B - Condens. Matter Mater. Phys.* **84**, 5–8 (2011).
154. Gautam, S. *et al.* Signature of weak-antilocalization in sputtered topological insulator  $\text{Bi}_2\text{Se}_3$  thin films with varying thickness. *Sci. Rep.* **12**, 9770 (2022).
155. Ferreira-teixeira, S. *et al.* Electronic Conduction Channels Engineered in Topological Insulator Sputtered Thin Films. *Appl. Electron. Mater.* **4**, 5789–5798 (2022).
156. Hellerstedt, J. *et al.* Thickness and growth-condition dependence of in-situ mobility and carrier density of epitaxial thin-film  $\text{Bi}_2\text{Se}_3$ . *Appl. Phys. Lett.* **105**, 173506 (2014).
157. Müller, K. A. & Burkard, H.  $\text{SrTiO}_3$ : An intrinsic quantum paraelectric below 4 K. *Phys. Rev. B* **19**, 3593–3602 (1979).
158. Yuan, H. *et al.* Liquid-gated ambipolar transport in ultrathin films of a topological insulator  $\text{Bi}_2\text{Te}_3$ . *Nano Lett.* **11**, 2601–2605 (2011).
159. Ando, Y. Topological insulator materials. *J. Phys. Soc. Japan* **82**, 1–32 (2013).
160. Shen, S.-Q. *Topological Insulators: Dirac equations in condensed matters*. Springer vol. 168 (Springer, 2012).
161. Fitzpatrick, M. E. *et al.* Determination of Residual Stresses by X-ray Diffraction. *Natl. Phys. Lab.* **52**, (2005).
162. Tougaard, S. SURFACE ANALYSIS | X-Ray Photoelectron Spectroscopy. in *Encyclopedia of Analytical Science* 446–456 (Elsevier, 2005). doi:10.1016/B0-12-369397-7/00589-6.

## Annex

### S1. Gallium and oxygen segregation towards the surface

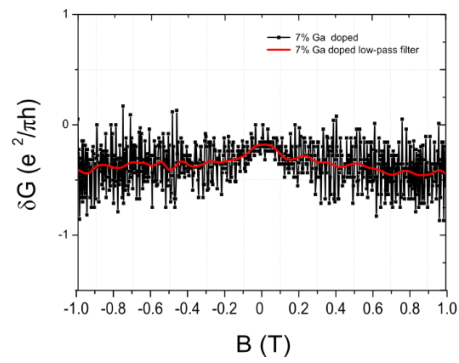
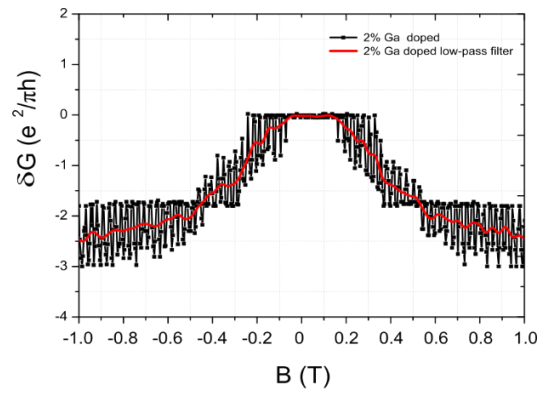
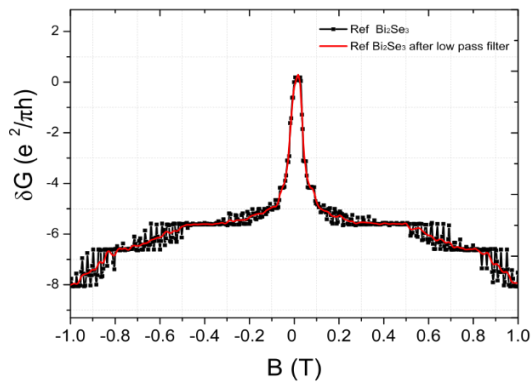
Before performing the etch of the material surface, to remove the oxides, it was observed that there was a higher concentration of Ga atoms in the surface. There is a segregation of Ga atoms towards the surface. The signal before and after the etch is shown in the following image. The signal difference is more perceptible for high compositions of Ga.

Moreover, it was also measured the oxygen signal before and after the etch to confirm that the first layer was oxidized. After the Ar<sup>+</sup> etching, the signal of oxides was minimal.

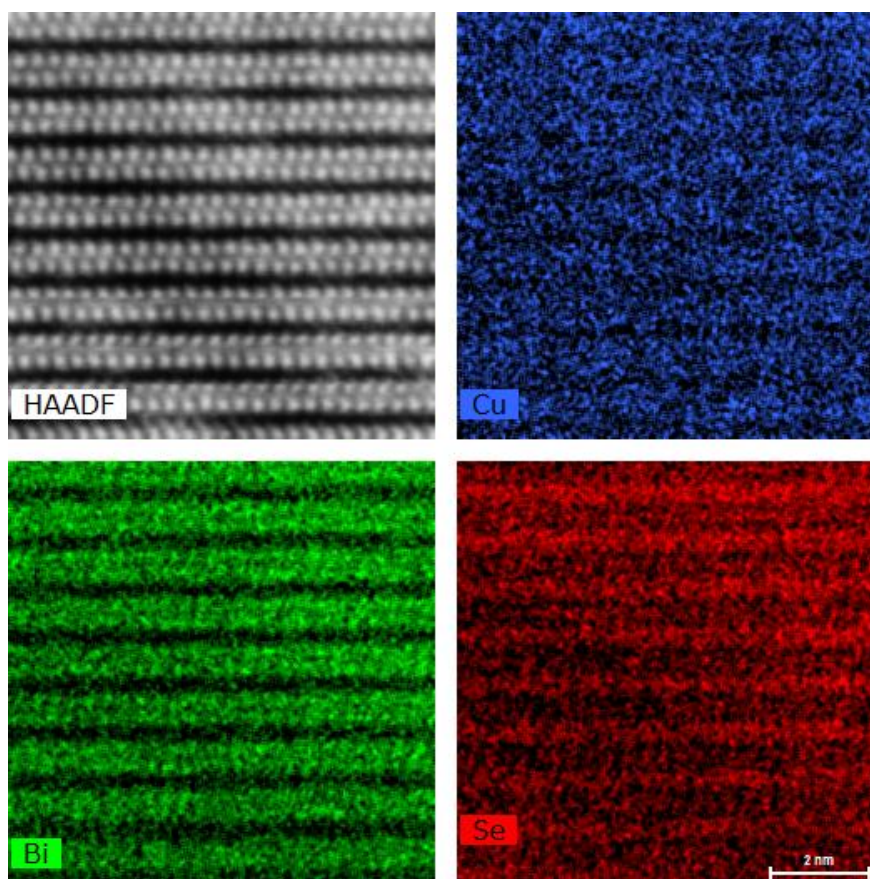


## S2. WAL filters and analysis

Application of lowpass filter to remove high frequency noise.



### S3. Energy-dispersive x-ray spectroscopy of (7 at.%) Cu-doped $\text{Bi}_2\text{Se}_3$



Energy-dispersive x-ray analysis showed an atomic percentage of Cu between 6-7 at.%.

## S4. ARPES python code for image creation, analysis and fitting profile

```

from nexusformat.nexus import *
import numpy as np
import matplotlib.pyplot as plt
import matplotlib.colors as mcolors
from ipywidgets import interact, widgets, Layout

def momentum_function(angles,energy):
    # This is just a simple example function, you should replace it with your actual function
    # In this example, we'll assume a linear relationship for demonstration purposes
    return 0.512*(np.sqrt(energy))*np.sin(np.pi*angles/180.0)

from scipy.optimize import curve_fit

# Fermi-Dirac distribution function
def fermi_dirac(E, E_F):
    return 1 / (np.exp((E - E_F) / (8.617333262145e-05 * 10)) + 1)

```

### Single band structure energy dispersion

```

[2]: # Define a function that correlates scattering angle with momentum

from nexusformat.nexus import *
import numpy as np

# Import data
a=nxload('C:/Users/Utilizador/Desktop/Things to do/Python/DATA/new_ref/003_new_ref.nxs')

def momentum_function(angles,energy):
    # This is just a simple example function, you should replace it with your actual function
    # In this example, we'll assume a linear relationship for demonstration purposes
    return 0.512*(np.sqrt(energy))*np.sin(np.pi*angles/180.0)

value = np.array(a.entry1.data.data)
angles = np.array(a.entry1.data.angles)
energies = np.array(a.entry1.data.energies)

# Create a new axis for momentum using the defined function
momentum_last = momentum_function(angles,energies[-1])

# Create a new y-axis for momentum
#new_y_axis = np.linspace(np.min(momentum_last), np.max(momentum_last), len(angles))

# Initialize an array to store the remapped values
remapped_values = np.zeros((len(angles), len(energies)))

# Perform the remapping
for i in range(len(energies)):
    momentum = momentum_function(angles,energies[i])
    remapped_values[:, i] = np.interp(momentum_last, momentum, value[:, i],left=0.0,right=0.0)

```

```

[3]: import matplotlib.pyplot as plt
import matplotlib.colors as mcolors
from ipywidgets import interact, widgets, Layout

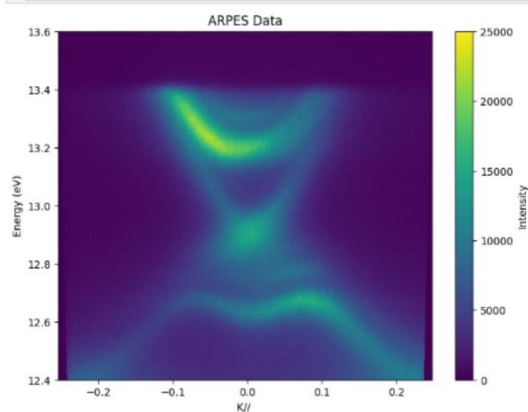
# Define the range for the color map scale (adjust these values)
custom_min_intensity = 0
custom_max_intensity = 25000
norm = mcolors.Normalize(vmin=custom_min_intensity, vmax=custom_max_intensity)

# Create a heatmap using Matplotlib
plt.figure(figsize=(8, 6))
plt.imshow(remapped_values.T, cmap='viridis', aspect='auto', origin='lower', extent=[min(momentum_function(angles,energies[-1])), max(momentum_function(angles,energies[-1]))], max(momentum_function(angles,energies[-1]))])
plt.colorbar(label='Intensity')
plt.title('2D Map with Momentum as Y-Axis')
plt.ylabel('Energy (eV)')
plt.xlabel('K//')
plt.title('ARPES Data')

# Save the plot as a PNG image
#plt.savefig('sample_plot_cu.png', format='png', dpi=300) # 'sample_plot.png' is the desired file name

plt.show()

```



## Fitting Fermi dirac function

```
[8]: # Fermi-Dirac distribution function
def fermi_dirac(E, E_F):
    return 1 / (np.exp((E - E_F) / (8.61733262145e-05 * 10)) + 1)

# Example data
actual_E_F = 13.4 # actual Fermi Level for generating example data

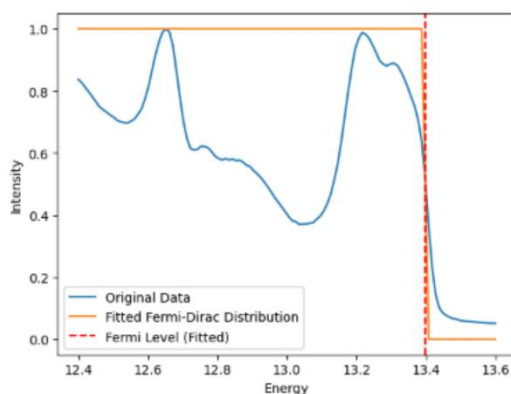
# data integrated
int=np.sum(renapped_values,axis=0)
data=int/max(int)

# Fit Fermi-Dirac distribution to the data
initial_guess = [actual_E_F] # initial guess for fitting parameters
fit_params, Conv = curve_fit(fermi_dirac, energies, data, p0=initial_guess)

# Extract Fermi Level from the fitted parameters
fitted_E_F = fit_params[0]

# Plot the results
plt.plot(energies, data, label='Original Data')
plt.plot(energies, fermi_dirac(energies, *fit_params), label='Fitted Fermi-Dirac Distribution')
plt.axvline(fitted_E_F, color='red', linestyle='--', label='Fermi Level (Fitted)')
plt.xlabel('Energy')
plt.ylabel('Intensity')
plt.legend()
plt.show()

error=np.sqrt(Conv)
print(f"Fitted Fermi Level: {fitted_E_F}")
print(f"Fermi Level error: {error}")
```

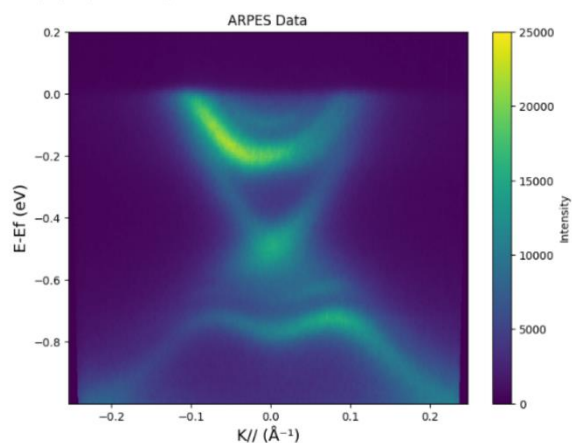


Fitted Fermi Level: 13.398376558002218  
Fermi Level error: [[0.001171]]

```
[23]: # Define the range for the color map scale (adjust these values)
#custom_min_intensity = 0
#custom_max_intensity = 35000
#norm = mcolors.Normalize(vmin=custom_min_intensity, vmax=custom_max_intensity)
# Create a heatmap using Matplotlib
plt.figure(figsize=(8, 6))
plt.imshow(renapped_values.T, cmap='viridis', aspect='auto', origin='lower', extent=(min(momentum_function(angles,energies[-1])), max(momentum_function(angles,energies[-1])), min(momentum_function(angles,energies[-1])), max(momentum_function(angles,energies[-1]))))

plt.colorbar(label='Intensity')
plt.title('2D Map with Momentum as Y-Axis')
plt.ylabel('E-Ef (eV)', fontsize=14)
plt.xlabel('K// (Å⁻¹)', fontsize=14)
plt.title('ARPES Data')
plt.savefig('sample_plot_2D.png', format='png', dpi=300) # 'sample_plot.png' is the desired file name
```

[23]: Text(0.5, 1.0, 'ARPES Data')



## For fitting curve

### Fitting model

```
[22]: #gen_values = np.zeros((Len(angles), Len(energies)))
def dograp(Edirac,vel_f,Eval,m_val,Econd,m_cond,momentum_last,energies,remapped_values):

    fitted_E_F=13.4
    x, y = np.meshgrid(momentum_last,energies-fitted_E_F)

    # Parameters for the Lorentzian curve
    linewidth = 0.05 # Lorentzian linewidth
    amplitude = 800.0 # Peak amplitude

    # Create a 2D curve (Line)
    line1 = vel_f * momentum_last + Edirac

    # Calculate the Lorentzian profile perpendicular to the line
    perpendicular_distance = np.abs(y - line1)
    lorentzian = amplitude / (np.pi * linewidth * (1 + ((perpendicular_distance) / linewidth) ** 2.0))

    line2 = -vel_f * momentum_last + Edirac
    perpendicular_distance = np.abs(y - line2)
    lorentzian += amplitude / (np.pi * linewidth * (1 + ((perpendicular_distance) / linewidth) ** 2.0))

    line3 = Eval - (3.807/m_val) * momentum_last**2 + rash * np.abs(momentum_last) #+ (1/(4*e_dept)) * ( (3.807/m_val) * momentum_last**2 )**2
    linewidth = 0.05
    perpendicular_distance = np.abs(y - line3)
    lorentzian += amplitude / (np.pi * linewidth * (1 + ((perpendicular_distance) / linewidth) ** 2.0))

    line4 = Econd + 3.807/m_cond * momentum_last**2
    perpendicular_distance = np.abs(y - line4)
    lorentzian += amplitude / (np.pi * linewidth * (1 + ((perpendicular_distance) / linewidth) ** 2.0))

    # New bands
    extravalen = (Eval+0.1) - (3.807/m_val) * momentum_last**2 + rash * np.abs(momentum_last) #from fitting
    extracond = (Econd+0.1) + 3.807/m_cond * momentum_last**2 #From fittings

    # Optionally, visualize the 2D Lorentzian profile perpendicular to the line
    plt.figure(figsize=(8, 6))
    plt.pcolormesh(x,y,lorentzian)
    plt.colorbar()
    plt.show()

    # Create a heatmap using Matplotlib
    plt.figure(figsize=(8, 6))
    plt.pcolormesh(x,y,remapped_values.transpose(), cmap='viridis')
    plt.colorbar(label='Value at Momentum')
    plt.plot(momentum_last, line1, color='red',linestyle='--')
    plt.plot(momentum_last, line2, color='red',linestyle='--')
    plt.plot(momentum_last, line3, color='white',linestyle='--')
    plt.plot(momentum_last, line4, color='black',linestyle='--')
    plt.plot(momentum_last, extravalen, color='yellow',linestyle='--')
    plt.plot(momentum_last, extracond, color='yellow',linestyle='--')
    plt.ylabel('E-Ef (eV)',fontsize=14)
    plt.xlabel('k// (Å⁻¹)',fontsize=14)
    plt.ylim(-1,0)
    #plt.title('2D Map with Momentum as Y-Axis')
    plt.savefig('sample_plot_REF fitting with all bands.png', format='png', dpi=300) # 'sample_plot.png' is the desired file name
    plt.show()
    return

def curvesfitting(ky,vel_f,Edirac,m_val,m_cond,Eval,Econd):

    linewidth=0.05
    k,y = ky
    amplitude= 1000
    fitted_E_F = 13.4

    # Create a 2D curve (Line)
    line1 = vel_f * k + Edirac

    # Calculate the Lorentzian profile perpendicular to the line
    perpendicular_distance = np.abs(y - line1)
    lorentzian = amplitude / (np.pi * linewidth * (1 + ((perpendicular_distance) / linewidth) ** 2.0))

    line2 = -vel_f * k + Edirac
    perpendicular_distance = np.abs(y - line2)
    lorentzian += amplitude / (np.pi * linewidth * (1 + ((perpendicular_distance) / linewidth) ** 2.0))

    line3 = Eval - (3.807/m_val) * k**2 + rash * np.abs(k)
    perpendicular_distance = np.abs(y - line3)
    lorentzian += amplitude / (np.pi * linewidth * (1 + ((perpendicular_distance) / linewidth) ** 2.0))

    line4 = Econd + 3.807/m_cond * k**2
    perpendicular_distance = np.abs(y - line4)
    lorentzian += amplitude / (np.pi * linewidth * (1 + ((perpendicular_distance) / linewidth) ** 2.0))
    return lorentzian.ravel()
```

```

amplitude=800
fitted_E_F=13.4
mat = np.meshgrid(momentum_last, energies-fitted_E_F)

# Parameters for the Lorentzian curve
x, y = np.meshgrid(momentum_last, energies-fitted_E_F)
linewidth = 0.05 # Lorentzian linewidth
Edirac = -0.5
vel_f = 4
Eval = -0.5
m_val = 0.25
e_sept = 0.01
rash = 2
fcond = -0.2
m_cond = 0.19

# Flatten the input arrays
x_data_flat = (mat[0]).ravel()
y_data_flat = (mat[1]).ravel()
z_data_flat = (renapped_values.transpose()).ravel()

# Define the region of interest
roi_condition = (x_data_flat > -0.15) & (x_data_flat < 0.15) & (y_data_flat > -1) & (y_data_flat < 0)

# Subset the data
x_roi = x_data_flat[roi_condition]
y_roi = y_data_flat[roi_condition]
z_roi = z_data_flat[roi_condition]

# Bounds
bounds = [(3.5, -0.6, 0.2, 0.1, -0.9, -0.2), [5, -0.5, 0.35, 0.25, -0.4, -0.05]]

# Fit Fermi-Dirac distribution to the data
initial_guess = [vel_f, Edirac, m_val, m_cond, Eval, fcond] # initial guess for fitting parameters
fit_params, covariance = curve_fit(curvesfitting, (x_roi, y_roi), z_roi, p0=initial_guess, bounds=bounds)

# Extract Fermi level from the fitted parameters
# Create a 2D curve (line)
line1 = vel_f * momentum_last + Edirac

# Calculate the Lorentzian profile perpendicular to the line
perpendicular_distance = np.abs(y - line1)
lorentzian = amplitude / (np.pi * linewidth * (1 + ((perpendicular_distance) / linewidth) ** 2.0))

line2 = -vel_f * momentum_last + Edirac
perpendicular_distance = np.abs(y - line2)
lorentzian += amplitude / (np.pi * linewidth * (1 + ((perpendicular_distance) / linewidth) ** 2.0))

line3 = Eval - (3.887/m_val) * momentum_last**2 + rash * np.abs(momentum_last) # (1/(4*e_sept)) * ((3.887/m_val) * momentum_last**2)**2
linewidth = 0.05
perpendicular_distance = np.abs(y - line3)
lorentzian += amplitude / (np.pi * linewidth * (1 + ((perpendicular_distance) / linewidth) ** 2.0))

line4 = fcond + 3.887/m_cond * momentum_last**2
perpendicular_distance = np.abs(y - line4)
lorentzian += amplitude / (np.pi * linewidth * (1 + ((perpendicular_distance) / linewidth) ** 2.0))

vel_f=fit_params[0]
Edirac=fit_params[1]
m_val=fit_params[2]
m_cond=fit_params[3]
Eval=fit_params[4]
fcond=fit_params[5]

print("Fitted Fermi velocity: {fit_params[0]}")
print("Fitted Dirac point: {fit_params[1]}")
print("Fitted linewidth: {fit_params[2]}")
print("Fitted Electron mass Valence: {fit_params[2]}")
print("Fitted Electron mass conduction: {fit_params[3]}")
print("Fitted Valence point: {fit_params[4]}")
print("Fitted Conduction point: {fit_params[5]}")

# for i in range(len(fit_params)):
#     for j in range(len(fit_params)):
#         if i<=j:
#             print(covariance[i,j])

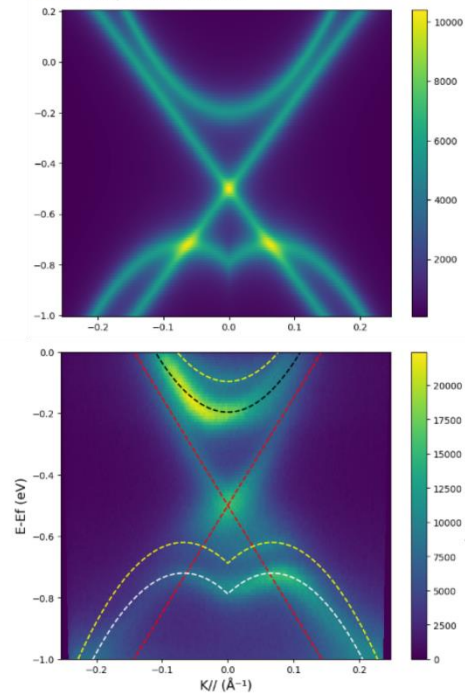
diagrap(Edirac, vel_f, Eval, m_val, fcond, m_cond, momentum_last, energies, renapped_values)

```

```

Fitted Fermi velocity: 3.50000000000000057
Fitted Dirac point: -0.50000000000000001
Fitted Electron mass Valence: 0.25711758019306135
Fitted Electron mass conduction: 0.237118497462933
Fitted Valence point: -0.7881174126331106
Fitted Conduction point: -0.19624385592749668

```



## Core Levels

```

[2]: #Import data
core = xarray.open_dataset('C:/Users/Utilizador/Desktop/Things to do/Python/DATA/new_ref/005_new_ref.ncx') # REF
core2 = xarray.open_dataset('C:/Users/Utilizador/Desktop/Things to do/Python/DATA/Flashed_ref/182_f1_ref.ncx') # REF REF
core3 = xarray.open_dataset('C:/Users/Utilizador/Desktop/Things to do/Python/DATA/Flashed_Ga_2pc/857_f1_Ga_2pc_core.ncx') # CoreLevels of Ga2%
core4 = xarray.open_dataset('C:/Users/Utilizador/Desktop/Things to do/Python/DATA/Flashed_Ga_2pc/818_f1_Cu_2pc.ncx') # CoreLevels of Cu 2%
core5 = xarray.open_dataset('C:/Users/Utilizador/Desktop/Things to do/Python/DATA/Cu_7pc/829_Cu_7pc.ncx') # CoreLevels of Cu 7%
core6 = xarray.open_dataset('C:/Users/Utilizador/Desktop/Things to do/Python/DATA/Ga_7pc/884_Ga_7pc.ncx') # CoreLevels of Ga 7%

anglesc = np.array(core6.entry1.data.angles)
energisc = np.array(core6.entry1.data.energisc)

valuec = np.array(core.entry1.data.data)
valuec2 = np.array(core2.entry1.data.data)
valuec3 = np.array(core3.entry1.data.data)
valuec4 = np.array(core4.entry1.data.data)
valuec5 = np.array(core5.entry1.data.data)
valuec6 = np.array(core6.entry1.data.data)
valuec7 = np.array(core6.entry1.data.data)

# Sum along rows (axis 1)
all = np.sum(valuec, axis=0)

REF = np.sum(valuec, axis=0)
REALREF = np.sum(valuec2, axis=0)
ga2one = np.sum(valuec3, axis=0)
cu2one = np.sum(valuec4, axis=0)
cu7one = np.sum(valuec5, axis=0)
ga7one = np.sum(valuec6, axis=0)

#x-axis
xc = np.zeros(len(energisc))
for i in range(len(energisc)):
    xc[i] = energisc[i] - energisc[-1] + 1.23 # where is work function -4.6 eV

# Invert the vector using slicing
# Inverted_vector = energisc[::-1]

# Define energy ranges for Bi and Ga peaks
bi_peak_range = (-30, -24)
ga_peak_range = (-21, -19)
in_peak_range = (-19, -17)

# Find indices corresponding to the energy ranges
bi_indices = np.where((xc >= bi_peak_range[0]) & (xc <= bi_peak_range[1]))[0]
ga_indices = np.where((xc >= ga_peak_range[0]) & (xc <= ga_peak_range[1]))[0]
in_indices = np.where((xc >= in_peak_range[0]) & (xc <= in_peak_range[1]))[0]

# Integrate the intensity within the specified energy ranges
bi_intensity = np.trapezoid(all[bi_indices], xc[bi_indices])
ga_intensity = np.trapezoid(all[ga_indices], xc[ga_indices])
in_intensity = np.trapezoid(all[in_indices], xc[in_indices])

ev = bi_intensity + ga_intensity + in_intensity
bipercentage_element = (bi_intensity / ev) * 40
gapercentage_element = (ga_intensity / ev) * 40
inpercentage_element = (in_intensity / ev) * 40

# Print the integrated intensities
print(f"Integrated intensity for Bi (-30 to -24 eV): {bipercentage_element}")
print(f"Integrated intensity for Ga (-21 to -19 eV): {gapercentage_element}")
print(f"Integrated intensity for In (-18 to -17 eV): {inpercentage_element}")

Integrated intensity for Bi (-30 to -24 eV): 36.476294591595696
Integrated intensity for Ga (-21 to -19 eV): 1.9099561621575822
Integrated intensity for In (-18 to -17 eV): 1.6137492462467162

# Last x digits of an array all[-40:]

# Create core levels
plt.figure(figsize=(8, 6))
plt.xticks(())
plt.yticks(())
plt.ylabel('Intensity [Arb. Units]', fontsize=14)
plt.xlabel('Binding energies (eV)', fontsize=14)
plt.title('Core levels')
plt.xlim(-30, 0)

Offset = 500000
# plt.plot(xc[150:600], all[150:600])
plt.plot(xc, REF, label='Reference Bi,Se')
plt.plot(xc, REALREF*Offset, label='Referencia Bi,Se')
plt.plot(xc, ga2one*Offset, label='Ga-doped 2 at.%')
plt.plot(xc, cu2one*Offset, label='Cu-doped 2 at.%')
plt.plot(xc, cu7one*Offset, label='Cu-doped 7 at.%')
plt.plot(xc, ga7one*Offset, label='Ga-doped 7 at.%')
plt.plot(xc, cu7one*Offset, label='Cu-doped 7 at.%')

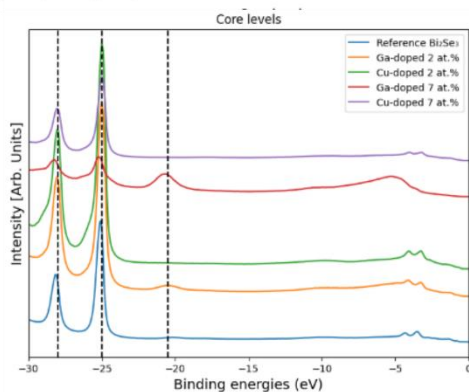
# I cannot believe someone is reading my code! You didn't give up? I would be tired already

# Add a vertical line at x = -25
plt.axvline(x=-25, color='black', linestyle='--')
plt.axvline(x=-28, color='black', linestyle='--')
plt.axvline(x=-18, color='black', linestyle='--')
plt.axvline(x=-20.5, color='black', linestyle='--')
plt.legend()

#
# plt.savefig('C:/Users/Utilizador/Desktop/Things to do/Python/DATA/Analysis/CL/CL.png', format='png', dpi=300)

[3]: <matplotlib.legend.Legend at 0x109d1795730>

```



## SEVERAL points

```
[4]: a=mxload('C:/Users/Utilizador/Desktop/Things to do/Python/DATA/flashed_ref/001_f1_ref.nxs')
value = np.array(a.entry1.data.data)
angles = np.array(a.entry1.data.angles)
energies = np.array(a.entry1.data.energies)

# All data points?
ss=np.zeros(value[0,0,0,:].shape)
print(value.shape)

for i in range(9):
    for j in range(9):
        ss+=value[1,1,0,:]

# Create a new axis for momentum using the defined function
momentum_last = momentum_function(angles,energies[-1])

# Initialize an array to store the remapped values
remapped_values = np.zeros((len(angles), len(energies)))

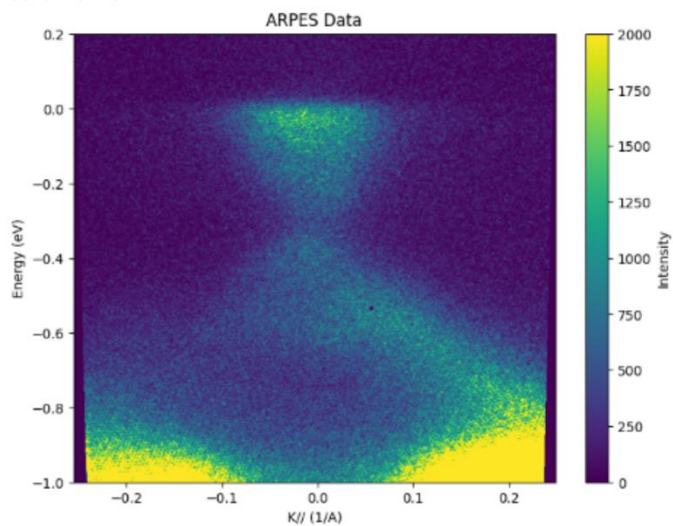
# Perform the remapping
for i in range(len(energies)):
    momentum = momentum_function(angles,energies[i])
    remapped_values[:, i] = np.interp(momentum_last, momentum, ss[:, i],left=0.0,right=0.0)

# Define the range for the color map scale (adjust these values)
fitted_F_F=13.4
custom_min_intensity = 0
custom_max_intensity = 2000
norm = mcolors.Normalize(vmin=custom_min_intensity, vmax=custom_max_intensity)

# Create a heatmap using Matplotlib
plt.figure(figsize=(8, 6))
plt.imshow((remapped_values.T), cmap='viridis', aspect='auto', origin='lower', extent=[min(momentum_function(angles,energies[-1])), max(momentum_function(angles,energies[-1]))])
plt.colorbar(label='Intensity')
plt.title('2D Map with Momentum as Y-Axis')
plt.ylabel('Energy (eV)')
plt.xlabel('K// (1/Å)')
plt.title('ARPES Data')
plt.ylim(-1,0.2)

# Save the plot as a PNG image
#plt.savefig('Band disperston_REF several points.png', format='png', dpi=300) # 'sample_plot.png' is the desired file name

plt.show()
(9, 9, 617, 943)
```



## Mapping

```

import matplotlib.pyplot as plt
import matplotlib.colors as mcolors
from ipywidgets import interact, widgets, Layout
from IPython.display import display
from nexusformat.nexus import *
import numpy as np
from nexusformat.nexus import *

#Import data
b=nxload('C:/Users/Utilizador/Desktop/Things to do/Python/DATA/flashed_Cu_2pc/004_f1_Cu_2pc.nxs')

def momentum_function(angles,ener):
    # This is just a simple example function, you should replace it with your actual function
    # In this example, we'll assume a linear relationship for demonstration purposes
    return 0.512*np.sqrt(ener)*np.sin(np.deg2rad(angles))

value = np.array(b.entry1.data.data)
anglesx = np.array(b.entry1.data.angles)
anglesy = np.array(b.entry1.data.defl_angles)
energies = np.array(b.entry1.data.energies)

#debug the matrix sizes
print(value.shape)
print(anglesx.shape)
print(anglesy.shape)
print(energies.shape)

# Create a new axis for momentum using the defined function
# Create a new axis for momentum using the defined function
momentum_last_x = momentum_function(anglesx,energies[-1])
momentum_last_y = momentum_function(anglesy,energies[-1])

remapped_values = np.zeros((len(anglesy),len(anglesx), len(energies)))

# Perform the remapping
for i in range(len(energies)):
    momentum_x = momentum_function(anglesx,energies[i])
    momentum_y = momentum_function(anglesy,energies[i])
    for k in range(len(anglesy)):
        remapped_values[k,:, i] = np.interp(momentum_last_x, momentum_x, value[k,:, i],left=0.0,right=0.0)
    for l in range(len(anglesx)):
        remapped_values[:,l, i] = np.interp(momentum_last_y, momentum_y, value[:,l, i],left=0.0,right=0.0)

x, y = np.meshgrid(momentum_last_x,momentum_last_y)

print(remapped_values[:, :,5].shape)

# Perform the remapping onto the 2D grid
def update_plot(c=742):
    intensity_data = value[:, :,c] # Intensity data

# At this point, 'remapped_map' contains the Fermi surface map data

# Create a heatmap using Matplotlib
# plt.figure(figsize=(8, ))
plt.pcolormesh(y,x,remapped_values[:, :,c], cmap='viridis')
plt.colorbar(Label='Intensity')
plt.ylabel('ky (Å-1)')
plt.xlabel('kx (Å-1)')
plt.xlim(-0.22,0.24)
plt.ylim(-0.18,0.18)
plt.title(f'ARPES Data for energy: {energies[c]-13.4} eV')
plt.savefig('Map Cu 2% 0 eV .png', format='png', dpi=300) # 'sample_plot.png' is the desired file name
plt.show()

# Create an interactive slider for Enval
slider_layout = Layout(width='100%') # Adjust the width as needed
enval_slider = widgets.IntSlider(value=742, min=0, max=943, step=1, description='c', layout=slider_layout)

# Create an interactive plot using ipywidgets
interactive_plot = interact(update_plot, c=enval_slider)
display(interactive_plot)

(161, 617, 943)
(617,)
(161,)
(943,)
(161, 617)
Error displaying widget: model not found
<function __main__.update_plot(c=742)>

plt.pcolormesh(y,x,remapped_values[:, :,520], cmap='viridis')
plt.ylim(-0.18,0.18)
plt.xlim(-0.24,0.24)
plt.savefig('Max Cu 0.4 .png', format='png', dpi=300) # 'sample_plot.png' is the desired file name
plt.show()

```